

# UC Berkeley

## UC Berkeley Electronic Theses and Dissertations

### Title

Classification, Follow-Up, and Analysis of Gamma-Ray Bursts and their Early-Time Near-Infrared/Optical Afterglows

### Permalink

<https://escholarship.org/uc/item/37f0c759>

### Author

Morgan, Adam Nolan

### Publication Date

2014

Peer reviewed|Thesis/dissertation

Classification, Follow-Up, and Analysis of Gamma-Ray Bursts and their Early-Time  
Near-Infrared/Optical Afterglows

By

Adam Nolan Morgan

A dissertation submitted in partial satisfaction of the

requirements for the degree of

Doctor of Philosophy

in

Astrophysics

in the

Graduate Division

of the

University of California, Berkeley

Committee in charge:

Joshua S. Bloom, Chair  
Alexei V. Filippenko  
John Rice

Spring 2014

Classification, Follow-Up, and Analysis of Gamma-Ray Bursts and their Early-Time  
Near-Infrared/Optical Afterglows

Copyright 2014  
by  
Adam Nolan Morgan

## Abstract

Classification, Follow-Up, and Analysis of Gamma-Ray Bursts and their Early-Time Near-Infrared/Optical Afterglows

by

Adam Nolan Morgan

Doctor of Philosophy in Astrophysics

University of California, Berkeley

Joshua S. Bloom, Chair

In the study of astronomical transients, deriving knowledge from discovery is a multifaceted process that includes real-time classification to identify new events of interest, deep, multi-wavelength follow-up of individual events, and the global analysis of multi-event catalogs. Here we present a body of work encompassing each of these steps as applied to the study of gamma-ray bursts (GRBs). First, we present our work on utilizing machine-learning algorithms on early-time metrics from the *Swift* satellite to inform the resource allocation of follow-up telescopes in order to optimize time spent on high-redshift GRB candidates. Next, we show broadband observations and analysis of the early-time afterglow of GRB 120119A, utilizing data obtained with a dozen telescope facilities both in space and on the ground. This event exhibits extreme red-to-blue color change in the first few minutes after the trigger at levels unseen in prior afterglows, and our model fits of this phenomenon reveal the best support yet for the direct detection of dust destruction in the local environment of a GRB. Finally, we present results from the PAIRITEL early-time near-infrared (NIR) afterglow catalog. The 1.3 meter PAIRITEL has autonomously observed 14 GRBs in under 3 minutes after the burst, yielding a homogenous sample of early-time  $JHK_s$  light curves. Our analysis of these events provides constraints on the early-time NIR GRB afterglow luminosity function and gives insight into the importance of dust extinction in the suppression of some optical afterglows.



I dedicate this dissertation to my family.

# Contents

<b>List of Figures</b>	<b>v</b>
<b>Acknowledgments</b>	<b>vii</b>
<b>1 Introduction</b>	<b>1</b>
1.1 Classification and Follow-Up of GRBs . . . . .	1
1.2 The Role of Dust Extinction . . . . .	2
1.2.1 Historical Overview . . . . .	2
1.2.2 Introduction to Dust Destruction . . . . .	5
1.2.3 Testing for Dust Destruction . . . . .	6
1.3 Thesis Outline . . . . .	7
<b>2 Rapid, Machine-Learned Resource Allocation: Application to High-redshift GRB Follow-up</b>	<b>9</b>
2.1 Introduction . . . . .	10
2.2 Data Collection . . . . .	11
2.3 Classification Methodology . . . . .	15
2.3.1 Random Forest classification . . . . .	16
2.3.2 RATE GRB- $z$ : Random forest Automated Triage Estimator for GRB redshifts . . . . .	19
2.4 Validation of Classifier Performance . . . . .	20
2.4.1 Comparison of Weight Choices . . . . .	21
2.4.2 Effects of Feature Selection . . . . .	21
2.4.3 Final Classifier . . . . .	22
2.4.4 Feature Importance of Classifier . . . . .	24
2.5 Discussion . . . . .	25
2.5.1 Calibration on GRBs with unknown redshifts . . . . .	25
2.5.2 Validation Set: Application to Recent GRBs . . . . .	27
2.5.3 Comparison to Previous Efforts . . . . .	31
2.6 Conclusions . . . . .	32

<b>3</b>	<b>Evidence for Dust Destruction from the Early-time Color Change of GRB 120119A</b>	<b>47</b>
3.1	Introduction . . . . .	48
3.2	Observations . . . . .	49
3.2.1	<i>Swift</i> Observations . . . . .	49
3.2.2	PROMPT Observations . . . . .	50
3.2.3	PAIRITEL Observations . . . . .	50
3.2.4	KAIT Observations . . . . .	51
3.2.5	Liverpool Observations . . . . .	51
3.2.6	SMARTS Observations . . . . .	52
3.2.7	P60 Observations . . . . .	52
3.2.8	Gemini-S spectroscopy . . . . .	53
3.2.9	Gemini-N Observations . . . . .	53
3.2.10	Keck Observations . . . . .	54
3.2.11	<i>Hubble Space Telescope</i> Observations . . . . .	55
3.2.12	CARMA Millimeter Observations . . . . .	55
3.3	Analysis . . . . .	55
3.3.1	Optical/NIR Light Curve . . . . .	55
3.3.2	Late-Time SED and Extinction Profile . . . . .	56
3.3.3	Construction of Early-time SEDs . . . . .	62
3.3.4	Modelling Color Change . . . . .	63
3.3.5	Optical Rise and Shock Constraints . . . . .	67
3.3.6	Host-Galaxy Properties . . . . .	71
3.4	Discussion and Conclusions . . . . .	73
<b>4</b>	<b>The PAIRITEL Early-time Near-infrared GRB Afterglow Catalog</b>	<b>84</b>
4.1	Introduction . . . . .	84
4.2	Methodology . . . . .	85
4.2.1	Data Collection . . . . .	85
4.2.2	Data Reduction . . . . .	87
4.2.3	Photometry . . . . .	88
4.3	Observations . . . . .	90
4.3.1	GRB 051109A . . . . .	90
4.3.2	GRB 061126 . . . . .	90
4.3.3	GRB 061222A . . . . .	91
4.3.4	GRB 070208 . . . . .	93
4.3.5	GRB 071025 . . . . .	93
4.3.6	GRB 080319A . . . . .	94
4.3.7	GRB 080319B . . . . .	94
4.3.8	GRB 080319C . . . . .	95
4.3.9	GRB 080320 . . . . .	95
4.3.10	GRB 080604 . . . . .	97

---

4.3.11	GRB 080607 . . . . .	98
4.3.12	GRB 090530 . . . . .	98
4.3.13	GRB 090618 . . . . .	99
4.3.14	GRB 090709A . . . . .	99
4.4	Discussion . . . . .	102
4.4.1	Detection Rates and the Role of Dust Extinction . . . . .	102
4.4.2	Brightness and Luminosity Distributions . . . . .	103
	<b>Bibliography</b>	<b>115</b>
	<b>A Software and Web Products for GRB Follow-Up and Analysis</b>	<b>125</b>

# List of Figures

1.1	SED Dependence on Absorption $A_V$ . . . . .	3
1.2	SED Dependence on $R_V$ . . . . .	3
1.3	SED Dependence on Extinction Law . . . . .	4
1.4	SED Dependence on Spectral Index $\beta$ . . . . .	6
1.5	Optical Rise in GRB Afterglow from Dust Destruction . . . . .	7
2.1	Redshift distribution of long-duration <i>Swift</i> GRBs. . . . .	12
2.2	Correlations of Early-time <i>Swift</i> Features . . . . .	16
2.3	Illustration of the RATE GRB- $z$ Process. . . . .	20
2.4	Cross-validated Ranking Predictions of Training Data . . . . .	22
2.5	Sensitivity of Efficiency and Purity to Classifier Weight . . . . .	23
2.6	Sensitivity of Efficiency and Purity to Useless Features . . . . .	24
2.7	Efficiency and Purity of Classifier for $z \geq 4.0$ Cutoff . . . . .	25
2.8	Efficiency and Purity of Classifier for $z \geq 3.5$ Cutoff . . . . .	26
2.9	Efficiency and Purity of Classifier for $z \geq 3.0$ Cutoff . . . . .	27
2.10	Feature Importance . . . . .	28
2.11	Calibration of Follow-up Criterion $Q$ . . . . .	29
3.1	GMOS-South Spectrum of GRB 120119A . . . . .	53
3.2	First-day Optical/NIR Light Curve of GRB 120119A . . . . .	57
3.3	XRT Light Curve of GRB 120119A . . . . .	58
3.4	Late-time SED of GRB 120119A . . . . .	59
3.5	PAIRITEL Light Curve Interpolation . . . . .	64
3.6	Time-varying Spectral Energy Distribution . . . . .	66
3.7	Best-fit Model Values for $A_V(t)$ (mag) and $\beta(t)$ . . . . .	68
3.8	Covariance Between $\Delta A_V$ and $\Delta\beta$ . . . . .	69
3.9	False-color NIR <i>HST</i> Imaging of the Field of GRB 120119A . . . . .	72
4.1	Histogram of PAIRITEL response times to <i>Swift</i> triggers. . . . .	86
4.2	False color ( $J,H,K_s$ ) PAIRITEL image of the field of GRB 090709A . . . . .	88
4.3	Optimal Aperture Determination . . . . .	89
4.4	PAIRITEL Light Curve of GRB 051109A . . . . .	91
4.5	PAIRITEL Light Curve of GRB 061126 . . . . .	92

---

4.6	PAIRITEL Light Curve of GRB 061222A . . . . .	92
4.7	PAIRITEL Light Curve of GRB 070208 . . . . .	93
4.8	PAIRITEL Light Curve of GRB 071025 . . . . .	94
4.9	PAIRITEL Light Curve of GRB 080319A . . . . .	95
4.10	PAIRITEL Light Curve of GRB 080319B . . . . .	96
4.11	PAIRITEL Light Curve of GRB 080319C . . . . .	96
4.12	PAIRITEL Light Curve of GRB 080320 . . . . .	97
4.13	PAIRITEL Light Curve of GRB 080607 . . . . .	98
4.14	PAIRITEL Light Curve of GRB 090530 . . . . .	99
4.15	PAIRITEL Light Curve of GRB 090618 . . . . .	100
4.16	PAIRITEL Light Curve of GRB 090709A . . . . .	100
4.17	PAIRITEL Brightness Distribution at $t = 3$ minutes (observer frame) . . . . .	104
4.18	PAIRITEL Luminosity Distribution at $t = 3$ minutes (rest frame) . . . . .	107
A.1	Screenshot of the RATE GRB- $z$ Webpage . . . . .	126
A.2	Screenshot of a Sample GRB Summary Page . . . . .	127
A.3	Screenshot of Finding Chart Generator Page . . . . .	128

# Acknowledgments

The completion of this body of work would not have been possible without the numerous contributions from many amazing people to whom I owe a great deal of gratitude. The journey that culminated in this thesis has been a long one, beginning over eleven years ago when the wonderful folks at the *Swift* Mission Operations Center at Penn State sparked my love of gamma-ray bursts and welcomed me into this exciting field.

For the past six years I have had the great fortune of working under the supervision of my research advisor, Professor Joshua Bloom. Josh has been tremendously supportive, providing me with encouragement, fantastic research opportunities, financial support, and many of the tools I need to be successful in my next stages of life. I would also like to offer my sincere thanks to my other committee members, Alex Filippenko and John Rice. It has been great to work more closely with Alex over the last few years on the KAIT GRB project, and I've also greatly appreciated the opportunity to work with him as a GSI for his excellent introduction to astronomy course. John has been a great liaison into the world of statistics, and I'm grateful for the stimulating discussions we've had on the subject.

I've had the pleasure of collaborating with many others during my time at Berkeley, all of whom have assisted me in ways too numerous to list. However, none have had quite as much of an impact on my development over the past six years as Dan Perley. Dan has been a great mentor to me in many ways, and his paw prints can be found on nearly every aspect of this thesis. Not only has he helped me innumerable times with navigating the science of GRBs, but he has been and continues to be a wonderful and supportive friend.

I also owe a great deal of thanks to Pierre Christian, who worked closely with me during his last two years as an undergraduate at Berkeley. His tireless efforts were instrumental in the preparation of the final chapter of this thesis, and he was an absolute delight to work with. Special thanks are also due to classmate and friend Chris Klein, who not only wrote the PAIRITEL image reduction software upon which the last two chapters of this thesis rely, but has also provided me with more brownies than I care to quantify.

Furthermore, I would also like to extend my thanks to collaborators Tamara Broderick, Nat Butler, Brad Cenko, Bethany Cobb, Nino Cucchiara, Berian James, James Long, Adam Miller, Joey Richards, and Dan Starr, all of whom have provided important contributions to this work. I'm also indebted to the amazing staff in the Berkeley astronomy department, and in particular Dexter Stewart. Their amazing efforts behind the scenes kept all the administrative aspects of my graduate career running smoothly.

---

On the funding side of things, I'm grateful to have received an NSF graduate research fellowship which supported me for three years. Many other grants from NASA and the NSF have been vital in funding the resources necessary to complete this work. In particular, the construction and operation of PAIRITEL was made possible by the support of the Harvard University Milton Fund, a camera loan from the University of Virginia, and the support of the Smithsonian Astrophysical Observatory SAO, UC Berkeley, and *Swift* Guest Investigator grants.

I am extremely grateful to all of the many friends I've had the pleasure of knowing during my time at Berkeley. All the other graduate students in our department have been incredibly kind and supportive. To my amazing housemates Chat Hull, James Gao, and Helene Moorman, thank you for making our house a home. We've truly become a family, and I will dearly miss seeing you all every night. In addition, to everyone over at #DC, thank you for your constant companionship over the years. I'm honored to call you all my friends.

Infinite thanks go to my parents, Kathleen Nolan and Glen Morgan, and my brother, Tyler for a lifetime of love and support. I am so incredibly fortunate to have such a wonderful family. Finally, to my lovely wife and best friend Mariana Garcia, thanks for the cake. I couldn't have done this without you, and I'm so excited to continue our journey through life together.



# Chapter 1

## Introduction

### 1.1 Classification and Follow-Up of GRBs

As we approach the 10th anniversary of the launch of *Swift*, the changing goals of the study of gamma-ray bursts (GRBs) field are apparent. With 870 *Swift* bursts as of this writing<sup>a</sup>, far less emphasis is placed on individual events both in terms of telescope time and exerted manpower. As the sample size continues to increase, concerted efforts to study single events is giving way to statistical analyses on large catalogs, unveiling global trends of the underlying properties of GRBs.

Nevertheless, deep analysis of single events continues to provide surprises and yield great insights even today. March 2011 saw the discovery of the tidal disruption of a star by a supermassive black hole, Swift J1644+57 (initially designated GRB 110328A), unveiling a new class of explosive transients (Bloom et al. 2011). The ultra-long GRB 111209A lasted over 7 hours, breaking duration records and possibly indicating a different progenitor (Gendre et al. 2013). And just over a year ago, the *Fermi*/*Swift* GRB 130427A yielded the detection of the highest energy photon (95 GeV) seen from a GRB, and was the brightest (in fluence) GRB of the previous 29 years (Vestrand et al. 2014; Ackermann et al. 2014; Perley et al. 2014, e.g.). My own contribution in this vein is the study of GRB 120119A, where we found the strongest evidence thus far for dust destruction in the local environment of a GRB (see Chapter 3).

Cases like these are, of course, rare exceptions, and while the examples above were easily identifiable as unique and interesting events from their high-energy properties, whether or not a new GRB is going to prove to be “interesting” is not always so immediately obvious. In particular, extracting insight on the redshift of a GRB solely from its rapidly available high-energy properties is an exceptionally difficult problem with many subtle complexities (see Chapter 2).

A drive towards automation, removing pipeline-clogging humans from the process as much as possible, has been getting stronger in the study of astronomical transients (and

<sup>a</sup>[http://swift.gsfc.nasa.gov/archive/grb\\_table/stats/](http://swift.gsfc.nasa.gov/archive/grb_table/stats/)

indeed in many aspects of our daily lives) out of a simple necessity: we simply do not have the resources to devote deep attention to every newly discovered event. Huge discovery engines are unveiling more events than we can afford to follow-up, and the discovery rate will only continue to increase in the future. The Large Synoptic Survey Telescope (LSST; [LSST Science Collaboration et al. 2009](#)) is expected to generate over 30 Tb of multi-wavelength images per night and observe billions of both static and time-varying objects over more than half of the sky. The looming challenges of “big data” are driving a paradigm shift in astronomical research, leading to the development of machine-learned classification frameworks to tackle the data deluge (see [Bloom & Richards 2012](#) for a review).

## 1.2 The Role of Dust Extinction

Extragalactic dust affects all ultra-violet/optical/infrared (UVOIR) measurements of objects outside our galaxy, though it is notoriously difficult to measure as it requires precise knowledge the spectrum of the background source. GRBs, with their relatively simple intrinsic power-law spectra, are proving to be very useful in unveiling the diverse nature of extragalactic dust (see [Perley 2011](#) for a review). Here we provide a brief overview of extragalactic dust extinction and its importance in the study of GRBs, which is of particular relevance for Chapters 3 and 4 of this thesis.

### 1.2.1 Historical Overview

Traditionally, the basic empirical extinction law was not parameterized in terms of total absorption, but rather in terms of reddening, due to the relative ease of measuring reddening from an observer standpoint. Thus instead of measuring the total amount of absorption, one instead measures the extent of absorption relative to the  $V$ -band ( $\lambda_V \simeq 5500\text{\AA}$ ), leading to an extinction law  $E(\lambda - V)$ . The relatively larger uncertainty inherent in the translation from reddening to total absorption is characterized by the  $R_V$  parameter, which is normalized to the  $B$ -band:  $A_V = R_V E(B - V)$ . Figure 1.1 shows the SED dependence of a varying  $A_V$  for SMC-like dust.

The  $R_V$  parameter is intrinsic to practically every extinction law that is based on measurements<sup>b</sup>, and is typically measured through observations in an infrared band where there should be very little extinction, such as the  $K$ -band.  $R_V$  can vary largely in the Milky Way, with values ranging from about 2 to 6 and an average value of about  $R_V = 3.1$ . It also varies widely for different LMC sightlines (with an average of about 3.2; [Misselt et al. 1999](#)), and SMC sightlines (with an average of 2.74; [Gordon et al. 2003](#)). Since  $R_V$  varies internally in every galaxy, a certain measured value does not map to a particular dust law. Figure 1.2 demonstrates the SED dependence on this parameter.

<sup>b</sup>An exception is the extinction described in [Maiolino et al. \(2004\)](#), which comes from supernova dust theory, and has likely been observed toward the sightline of GRB 071025 ([Perley et al. 2010a](#)).

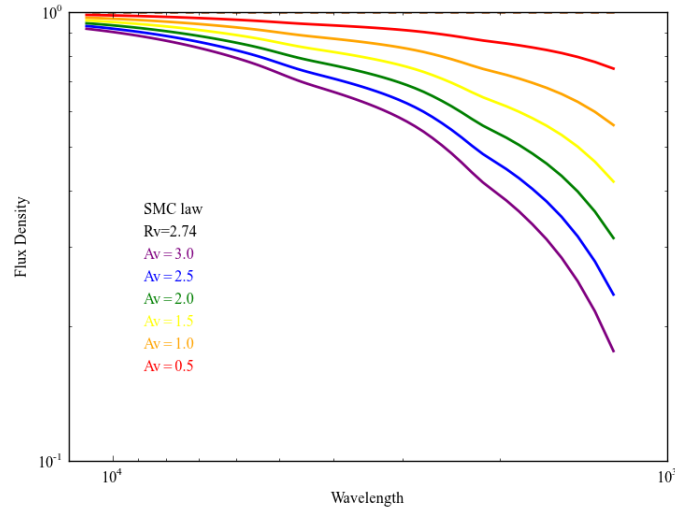


Figure 1.1: SED dependence on absorption  $A_V$ , assuming SMC-like dust with  $R_V = 2.74$ .

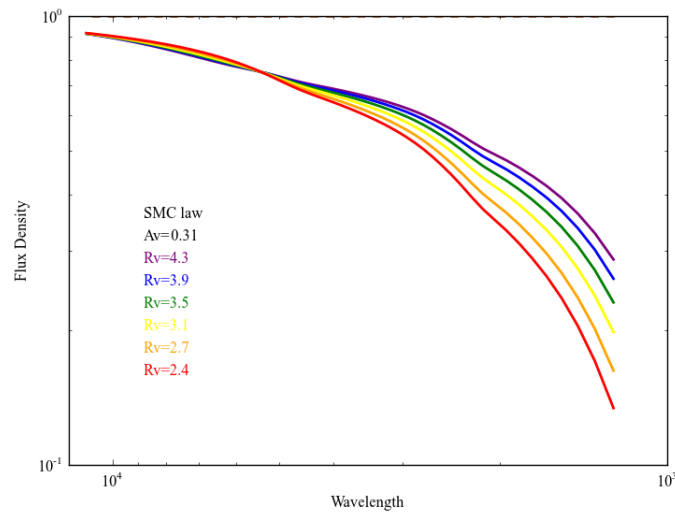


Figure 1.2: SED dependence on the ratio of total to selective extinction  $R_V$ , assuming SMC-like dust with  $A_V = 0.31$ .

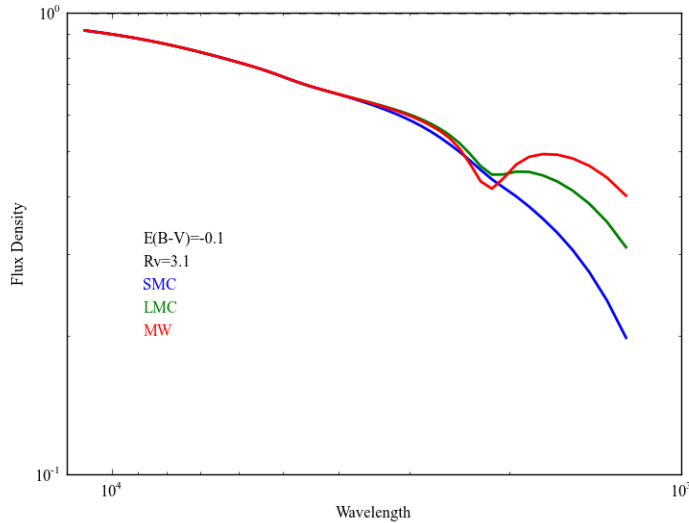


Figure 1.3: SED Dependence on Extinction Law

In the optical regime, simple interpolation between measured values of  $E(\lambda - V)$  at different wavelengths yields a good estimate for a particular  $\lambda$  (e.g. [Seaton 1979](#) for the Milky Way and [Pei 1992](#) for the LMC/SMC). Slight variances in  $R_V$  seen in the IR led to the development of functional forms to more accurately estimate  $E(\lambda - V)$  across a range of wavelengths (e.g. [Cardelli et al. 1989](#)). In the UV, however, large variations are seen along different sightlines, and especially between the three well studied galaxies of the Milky Way, LMC, and SMC. Notably, a large absorption feature at 2175 Ångstroms is seen in the Milky Way and LMC, but not in the SMC (Figure 1.3). The complexities seen in the UV were parameterized by [Fitzpatrick \(1999\)](#) in terms of six parameters:  $c_1$  and  $c_2$  are the intercept and slope of the linear part of the UV component in  $E(\lambda - V)$ ,  $c_3$  is the strength of the 2175 Å bump,  $c_4$  is the strength of the rise in the FUV,  $x_0$  is the centroid of the 2175 Å bump in inverse microns ( $x_0 \simeq 1/0.2175$ ), and  $\gamma$  is the width of that feature<sup>c</sup>. In the local group, nearly every sightline can be fit with these six parameters and  $R_V$ <sup>d</sup>.

For galaxies outside the local group, the standard methods no longer apply since it is no longer possible to obtain spectra of individual stars. Instead, one must take the integrated light from all the stars and compare it to the idealized integrated light that would be seen if there was no dust based on population synthesis models (see [Perley et al. 2013](#)). This is more difficult, as, in addition to the uncertainty in the modeling itself, there are geometrical effects such as sizes of clouds and the varying optical depth to different stars. Furthermore, scattering of photons is no longer equivalent to their absorption. [Calzetti et al. \(2000\)](#)

<sup>c</sup>The parameters  $x_0$  and  $\gamma$  are not expected to vary much, but could in principle, as the origin of the 2175 Å bump is likely due to some complex organic molecule with complicated behavior.

<sup>d</sup>[Reichart \(2001\)](#) found an empirical relation between  $c_1, c_2$ , and  $R_V$ , which removes some of the degeneracy between them.

determined an attenuation law for nearby starburst galaxies, finding that massive stars dominate the radiation output.

### 1.2.2 Introduction to Dust Destruction

The photodestruction of dust in the nearby environment of GRBs is expected at early times (Waxman & Draine 2000; Draine & Hao 2002), but, until our work shown in Chapter 3, unambiguous evidence was not seen from afterglow observations. As the bulk of the destruction is likely due to bright X-rays during the prompt emission phase, contemporaneous optical observations are needed in order to observe time-variability in the light curve (e.g., Fruchter et al. 2001; Perna et al. 2003).

Early observational evidence for or against dust destruction in early GRB afterglows had been varied and inconclusive. In GRB 030418, a dearth of optical emission seen in their observations starting  $\sim 200$  seconds after the start of the burst ( $> 1$  minute after the prompt phase ended, and thus after dust destruction would have occurred) is interpreted as absorption of optical photons by dust inside a massive stellar wind medium (Rykoff et al. 2004). In this interpretation, local dust must have persisted in order for the attenuation to occur, but other models can be invoked to explain this early-rise and subsequent decay that is now commonly seen in early optical afterglows.

In the case of GRB 061126, Perley et al. (2008c) explore the possibility that grey dust could explain the observed deficit of optical flux to X-rays at late times. In this event, optical absorption was observed without the expected reddening of normal dust observed in the local universe. While the presence of grey dust was not conclusively seen, a possible interpretation of its existence would be the sublimation of smaller grains in the local environment due to early photoionization of dust by the prompt X-ray emission.

Simultaneous, multi-color imaging of the afterglow during the prompt emission is necessary to observe both the decrease in opacity and red-to-blue color change associated with dust destruction. Perley et al. (2010b) tested for this in the case of GRB 071025 with simultaneous  $JHK_s$  and unfiltered optical data (which resembled the  $I$ -band due to the redness of the afterglow). The optical and near-infrared (NIR) measurements were binned to temporally match, and dust models were fit at each four-point SED, allowing both the extinction and intrinsic spectral index  $\beta$  to vary. No evidence for a change in absorption was seen, even during the first bin, which coincides with the end of the prompt X-ray emission, ruling out dust destruction after the start of the NIR observations ( $\sim 150$  s after the burst).

GRB 120119A (Chapter 3) offered a fantastic opportunity to test for dust destruction signatures in the optical afterglow, with multi-color optical/NIR observations beginning less than one minute after the burst trigger. Several detections in each of 6 bands ( $JHK_s$ ,  $R$ ,  $I$ , and Unfiltered) coincide with the end of the prompt X-ray emission, when dust sublimation is expected to occur. A significant red-to-blue color change is observed during this time, but careful testing is needed to disambiguate between dust destruction and other sources of de-reddening, such as a change in the intrinsic spectral index  $\beta$  (Figure 1.4) due to the evolution of the GRB afterglow.

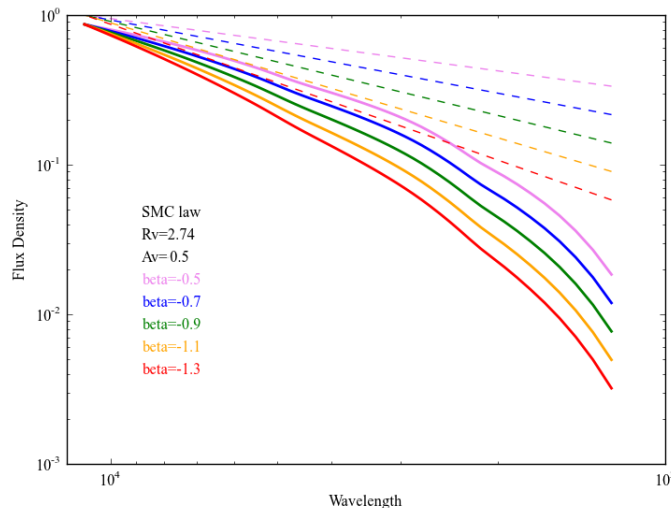


Figure 1.4: SED dependence on the intrinsic power-law spectral index  $\beta$ , assuming SMC-like dust with  $R_V = 2.74$  and  $A_V = 0.5$ .

### 1.2.3 Testing for Dust Destruction

To test whether dust destruction signatures can be significantly separated from other sources of color change, it is useful to consider the effects of a varying optical depth  $\tau$  with time. After correcting for Galactic extinction and redshift, the flux of a GRB afterglow can be parameterized as

$$f(\nu, t) = f_0 \left( \frac{t}{t_0} \right)^{-\alpha} \left( \frac{\nu}{\nu_0} \right)^{-\beta} e^{-\tau(\lambda_{em}, t)},$$

In the simplest case, one can assume a single, unbroken temporal power law decay with index  $\alpha$  and fixed intrinsic spectral index  $\beta$  (which could be inferred from an extrapolation of the XRT photon index combined with the NIR SED), and test how changes in optical depth as a function of time would affect the resultant light curve. These are not at all robust assumptions, as both the temporal and intrinsic spectral indices are known to evolve with time during the early stages of the GRB, and any deduced variation in  $\tau$  could easily be due to either or both of these. Nevertheless, as an illustration of how dust destruction might manifest, Figure 1.5 shows a toy model of an afterglow with a fixed  $\alpha$  and  $\beta$  and a trivially varying  $\tau$  (decaying as  $1/t$ ). Broad properties are evident in this simple case, most notably the chromatic rise in the bluer filters during the early afterglow.

However, identifying a robust parametric model for  $\tau(t)$  is a complicated pursuit. The distribution of dust grains (which give rise to the various dust laws) is expected to change in non-trivial ways under the influence of a high-intensity, high-energy radiation field, as, for example, smaller grains are more preferentially destroyed Fruchter et al. (2001). Detailed dust-destruction simulations by Perna et al. (2003) present the time evolution of extinction

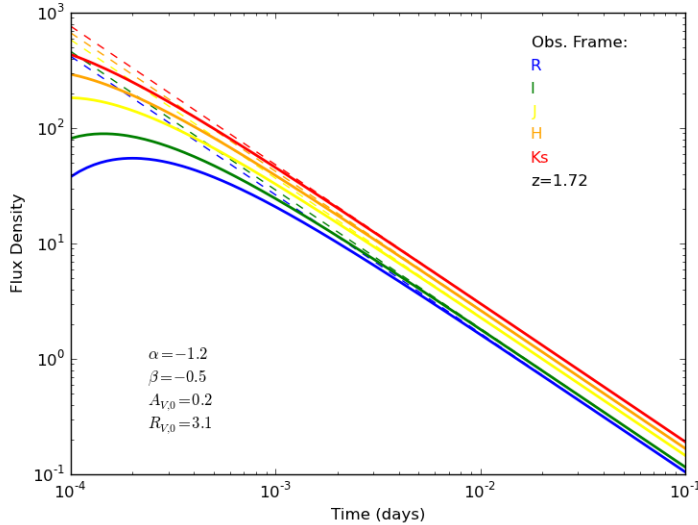


Figure 1.5: Optical rise in GRB afterglow from dust destruction for a model afterglow at  $z = 1.728$  assuming the parameterization  $f(\nu, t) = f_0 \left(\frac{t}{t_0}\right)^{-\alpha} \left(\frac{\nu}{\nu_0}\right)^{-\beta} e^{-\tau(\lambda_{em}, t)}$ , assuming  $\tau \propto 1/t$ .

and reddening for a variety of environments (density and radius), dust distributions, and dust-to-gas ratios. These simulations highlight the complex interplay between changes in  $A_V$  and  $E(B - V)$  with time and are highly dependent on the local environment. Note also that these simulations assume a constant luminosity from the X-ray source, and a set spectral index ( $\beta = 0.5$ ). A changing luminosity, as is present in GRB prompt emission, further complicates the issue.

Without a densely sampled light curve over a broad range of colors, it is unlikely that details on the level of dust-grain distribution can be accurately distinguished. However, by assuming the bulk of color-change due to dust destruction manifests as a change in the absorption  $A_V$ , it is still possible to investigate whether observed color-change in a GRB afterglow is the result of changes in the dust environment or intrinsic to the GRB itself (Chapter 3).

### 1.3 Thesis Outline

The work presented in this thesis focuses on three core elements in the broader context of transient astronomy as applied to the study of GRBs: classification to inform action, insight from deep multi-wavelength follow-up of individual events, and the construction and analysis of survey catalogs. In Chapter 2 we present our work on utilizing Random

---

Forests on rapidly-available *Swift* metrics to inform telescope follow-up decisions in order to optimize time spent on high-redshift GRB candidates. The results of this work have broad applicability to informing automated follow-up of astronomical transients, and presents a framework to handle the general problem of optimized resource allocation. In Chapter 3, we present broadband observations and analysis of the early-time afterglow of GRB 120119A, which showed extreme red-to-blue color change in the first few minutes after the burst. Our modeling of this event revealed among the best support yet for dust destruction in the local environment of a GRB. Finally, in Chapter 4, we present the results of a multi-year campaign to observe the early-time near-infrared light curves of GRB afterglows with the robotic Peters Automatic Infrared Imaging Telescope (PAIRITEL). Our homogenous sample of fourteen  $JHK_s$  provides an estimate of the early-time NIR luminosity distribution of GRB afterglows and yields insight into the importance of dust extinction for optically suppressed events.



## Chapter 2

# Rapid, Machine-Learned Resource Allocation: Application to High-redshift GRB Follow-up

As the number of observed Gamma-Ray Bursts (GRBs) continues to grow, follow-up resources need to be used more efficiently in order to maximize science output from limited telescope time. As such, it is becoming increasingly important to rapidly identify bursts of interest as soon as possible after the event, before the afterglows fade beyond detectability. Studying the most distant (highest redshift) events, for instance, remains a primary goal for many in the field. Here we present our Random forest Automated Triage Estimator for GRB redshifts (**RATE GRB- $z$** ) for rapid identification of high-redshift candidates using early-time metrics from the three telescopes onboard *Swift*. While the basic **RATE** methodology is generalizable to a number of resource allocation problems, here we demonstrate its utility for telescope-constrained follow-up efforts with the primary goal of identifying and studying high- $z$  GRBs. For each new GRB, **RATE GRB- $z$**  provides a recommendation—based on the available telescope time—of whether the event warrants additional follow-up resources. We train **RATE GRB- $z$**  using a set consisting of 135 *Swift* bursts with known redshifts, only 18 of which are  $z > 4$ . Cross-validated performance metrics on this training data suggest that  $\sim 56\%$  of high- $z$  bursts can be captured from following up the top 20% of the ranked candidates, and  $\sim 84\%$  of high- $z$  bursts are identified after following up the top  $\sim 40\%$  of candidates. We further use the method to rank 200+ *Swift* bursts with unknown redshifts according to their likelihood of being high- $z$ .

A version of this chapter was previously published as Morgan, Long, Richards, Broderick, Butler, and Bloom, *Rapid, Machine-learned Resource Allocation: Application to High-redshift Gamma-Ray Burst Follow-up*, The Astrophysical Journal, vol. 746, p. 170, 2012.

## 2.1 Introduction

As the most luminous electromagnetic explosions, gamma-ray bursts (GRBs) offer a unique probe into the distant universe—but only if their rapidly fading afterglows are observed before dimming beyond detectability (e.g., [Wijers et al. 1998](#); [Miralda-Escude 1998](#); [Lamb & Reichart 2000](#); [Kawai 2008](#); [McQuinn et al. 2008](#)). Since the launch of the *Swift* satellite in November 2004 ([Gehrels et al. 2004](#)), more than 170 long duration *Swift* gamma-ray bursts have had measured redshifts, but only a handful fall into the highest redshift range that allow for the probing of the earliest ages of the universe, up to less than a billion years after the Big Bang (Fig. 2.1). With a limited budget of large-aperture telescope time accessible for deep follow-up, it is becoming increasingly important to rapidly identify these GRBs of interest in order to capture the most interesting events without spending available resources on more mundane events.

Along with quasars (e.g., [Mortlock et al. 2011](#)) and NIR-dropout Lyman-break galaxies (e.g., [Bouwens et al. 2010, 2011](#)), GRBs have been established as among the most distant objects detectable in the universe, with a spectroscopically confirmed event at  $z = 8.2$  (GRB 090423; [Tanvir et al. 2009](#); [Salvaterra et al. 2009](#)) and a photometric candidate at  $z \sim 9.4$  (GRB 090429B; [Cucchiara et al. 2011b](#)). Such observations can provide valuable constraints on star formation in the early universe, illuminate the locations and properties of some of the earliest galaxies and stars, and probe the epoch of reionization. (e.g., [Tanvir & Jakobsson 2007](#), and references therein). Further, the relatively simple spectra of GRB afterglows compared to other cosmic lighthouses makes it easier to both identify their redshifts and extract useful spectral features such as neutral hydrogen absorption signatures for the study of cosmic reionization. (e.g., [Miralda-Escude 1998](#); [Barkana & Loeb 2004](#); [Totani et al. 2006](#); [McQuinn et al. 2008](#)). However, such benefits can only be realized if spectra are obtained with large-aperture telescopes before the afterglow fades beyond the level required to obtain a useful signal, typically within a day after the GRB.

As such, there has been a long-standing effort to extract a measure of a GRB’s redshift from its early time, high-energy signal, with a primary goal of the rapid identification of high- $z$  candidates. This might appear in principle to be a straightforward exercise; for instance, distant GRBs should on average appear fainter and longer-duration than nearby events due to distance and cosmological time dilation, respectively. In practice, however, the large intrinsic diversity of GRBs, as well as thresholding effects, confounds the straightforward use of early-time observations in divulging redshift and other important properties. While much effort has gone into tightening the correlations between high-energy properties in order to homogenize the sample for use as a luminosity (and hence distance/redshift) predictor (e.g., [Amati et al. 2002](#); [Ghirlanda et al. 2004](#); [Firmani et al. 2006](#); [Schaefer 2007](#)), there has been significant debate as to whether some of these relations are actually due to thresholding effects specific to the detectors rather than intrinsic physical properties of the GRBs (e.g., [Friedman & Bloom 2005](#); [Butler et al. 2007, 2009](#)). Regardless, whether or not these inferred relationships are actually physical or simply detector effects would not affect their utility as a *detector-specific* parameter prediction tool. By restricting ourselves to *Swift* events only, we

avoid the uncertainty of whether certain correlations remain when using different detectors.

With this in mind, we set out to search for indications of high-redshift GRBs in the rich, mostly homogeneous dataset provided by 6+ years of GRB observations by the three telescopes onboard *Swift* (BAT; Barthelmy et al. 2005, XRT; Burrows et al. 2005, UVOT; Roming et al. 2005). Past studies exploring high- $z$  indicators have used hard cuts on certain features such as UVOT afterglow detection, burst duration, and inferred hydrogen column density (e.g., Grupe et al. 2007; vanden Berk et al. 2008; Ukwatta et al. 2009), regression on such features (Koen 2009, 2010), and combinations of potential GRB luminosity indicators (Xiao & Schaefer 2009, 2011). In this work, we take a different approach by utilizing supervised machine learning algorithms, specifically Random Forest classification, to make follow-up recommendations for each event automatically and in real time. Particular attention is paid to careful treatment of performance evaluation by using cross-validation (§2.4), a robust methodology to guard against over-fitting and the circular practice of testing hypotheses using the same data that suggested (and constrained) them.

The primary driving force of this study is simple: *given limited follow-up time available on telescopes, we want to maximize the time spent on high- $z$  GRBs*<sup>a</sup>. To this end, we provide a deliverable metric, explained in §2.3.2, to assist in the decision-making process on whether to follow up a new GRB. Real-time distribution of this metric is available for each new *Swift* trigger via website<sup>b</sup> and RSS feed<sup>c</sup>.

The structure of this chapter is as follows: in §2.2 we outline the collation of the data, and describe the particular GRB features utilized in redshift classification. In §2.3, the Random Forest algorithm is detailed, along with some specific challenges posed by this particular data set. Performance metrics of the classifiers are presented in §2.4, and in §2.5 we discuss the results of testing the classifiers on additional GRBs, both with and without known redshifts. Finally, our conclusions are given in §2.6.

## 2.2 Data Collection

The *Swift* BAT constantly monitors 1.4 steradians on the sky over the energy range 15 – 150 keV. GRB triggering can occur either by a detection of a large gamma-ray rate increase in the BAT detectors (“rate trigger”), or a fainter, long-duration event recovered after on-board source reconstruction reveals a new significant source (“image trigger”). A rough ( $\sim 3$  arcmin) position is determined, and if there are no overriding observing constraints, the spacecraft slews to allow the XRT and UVOT to begin observations, typically between 1 and 2 minutes after the trigger. The XRT observes between the energy range of 0.2 – 10 keV and detects nearly all of the GRBs it can observe rapidly enough, providing positional

<sup>a</sup>For the purposes of this study, “high-redshift” corresponds to all  $z > 4.0$ : a compromise between only keeping the most interesting events and having enough data to train on. However, we have explored performance of different redshift cuts; see §2.4.3.

<sup>b</sup><http://rate.grbz.info/>

<sup>c</sup><http://rate.grbz.info/rss.xml>

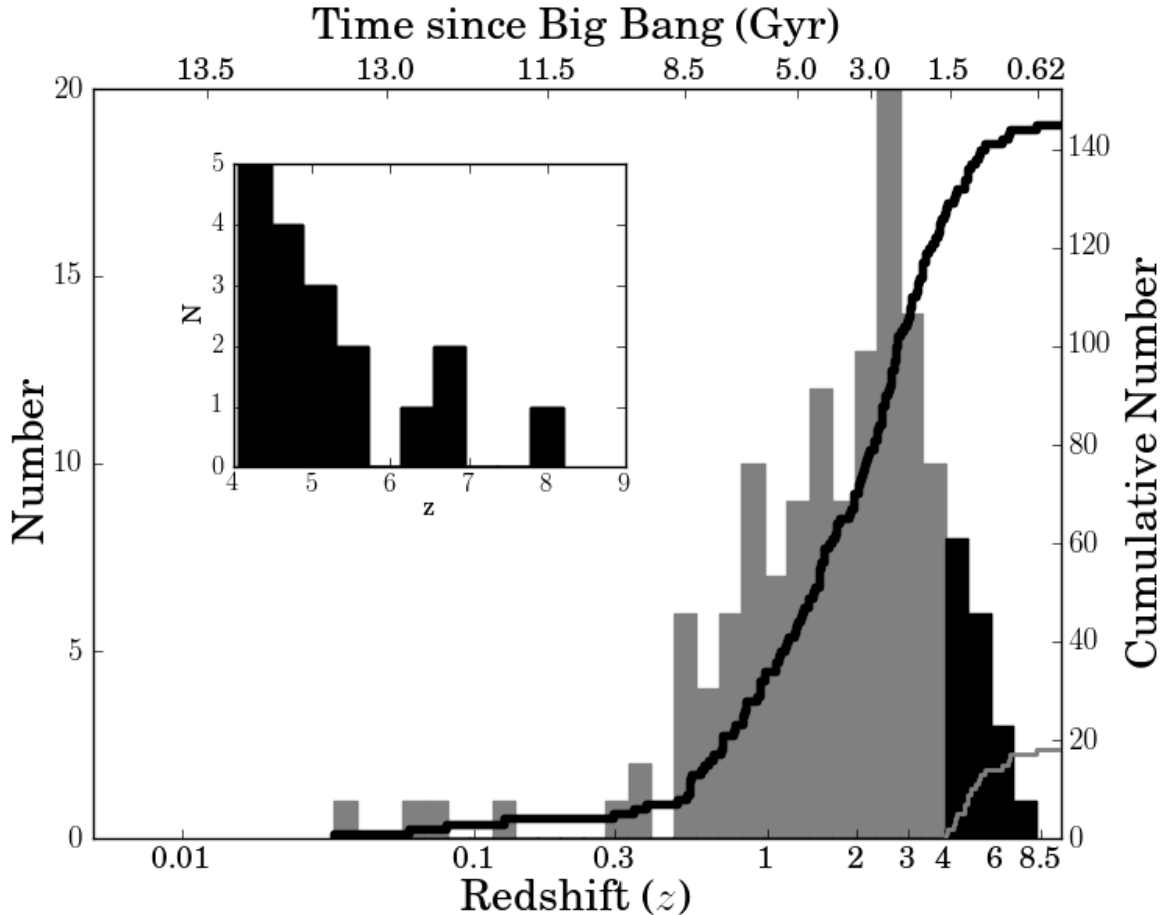


*Figure 2.1:* Redshift distribution of the 135 long-duration *Swift* GRBs in our sample (Table 2.4). For the purposes of this study, “high” redshift is defined as those bursts with redshifts larger than  $z = 4$ , which corresponds to approximately  $1\text{-}\sigma$  above the mean of the distribution. In our sample, 18 bursts fall into this category (black, and in inset). In determining age since the Big Bang, we assume a cosmology with  $h = 0.71$ ,  $\Omega_m = 0.3$ , and  $\Omega_\Lambda = 0.7$ . Solid lines show the cumulative number of GRBs as a function of redshift for high- $z$  bursts (grey) and all bursts (black).

accuracies of 2 – 5 arcseconds within minutes. The UVOT is a 30 cm aperture telescope that can observe in the range of 170–650 nm. Due to the relatively blue response of this telescope, it cannot detect highly reddened sources due to either dusty environments or (more relevant to this analysis) high-redshift origins.

At each stage in the data collection process, information is sent to astronomers on the ground via the Gamma-ray bursts Coordinates Network (GCN<sup>d</sup>) providing rapid early-time metrics. The more detailed full data are sent to the ground in  $\sim 90$  minute intervals starting

<sup>d</sup><http://gcn.gsfc.nasa.gov/>

between roughly 1 – 2 hours after the burst. For our dataset, we have collected data after various levels of processing directly from GCN notices, online tables<sup>e</sup> and automated pipelines (Butler & Kocevski 2007; Butler et al. 2007) that process and refine the data into more useful metrics. Tens of attributes and their estimated uncertainties (when available) are parsed from the various sources and collated into a common format.

In order to evaluate our full dataset in an unbiased way, we restricted ourselves to using features that have been generated for all possible<sup>f</sup> past events and are automatically generated for future events. This is the primary reason we do not include potentially useful features such as relative spectral lag (e.g., Ukwatta et al. 2010, 2011, and references therein) which has been utilized as a redshift indicator with smaller and pre-*Swift* datasets (Murakami et al. 2003; Band et al. 2004; Zhang et al. 2006; Schaefer 2007) but requires a larger spectral coverage than *Swift* alone can provide. However, our technique is easily extendable to include additional useful features should they be homogeneously determined for past GRBs and automatically available in real-time for new events, and therefore we strongly encourage the automated distribution of any such data products.

Because the addition of too many features causes a decrease in classifier performance (see §2.4.2), a total of 12 features were kept for our final classifier (Table 2.1), 10 of which were derived from BAT gamma-ray measurements, one from XRT observations, and one from UVOT observations. Of the 10 BAT features, 4 were parsed directly from GCN Notices, the most rapidly available (and thus unrefined) source of information on GRBs<sup>g</sup>. The parameter  $t_{BAT}$  is a rough measurement of the duration of the BAT trigger event and thus a lower limit on the total duration of the GRB. The binary feature of whether or not the event was a rate trigger is an indicator of the signal-to-noise of an event, for only the brighter events are detected as rate triggers, while those on the threshold of detection are image triggers. The final two GCN features are also rough indicators of brightness:  $\sigma_{BAT}$  is the significance (in sigma) of the detected source in the on-board reconstruction of the BAT image, and  $R_{peak,BAT}$  is the peak count rate observed during the duration of the event.

Five higher-level BAT-derived attributes were pulled from online tables automatically updated by the pipeline described in Butler et al. (2007). The feature  $\alpha$  is the power-law index before the peak of the Band-function fit to the gamma-ray spectrum (typically clustered around  $-1$ ). Another parameter in the Band-function fit,  $E_{peak}$ , is the energy at which most of the photons are emitted. The fluence,  $S$ , is the total gamma-ray flux (15–350 keV) integrated over the duration of the burst.  $S/N_{max}$  is simply the maximum signal-to-noise achieved over the duration of the light curve. Finally,  $T_{90}$  is a measure of the burst duration, defined to be the time interval over which the middle 90% of the total

<sup>e</sup>[http://swift.gsfc.nasa.gov/docs/swift/archive/grb\\_table.html/](http://swift.gsfc.nasa.gov/docs/swift/archive/grb_table.html/)

<sup>f</sup>Even with the restriction of observation by all 3 *Swift* telescopes, certain features derived from model fits are nonetheless incalculable for certain GRBs from the available data. See §2.3.1 for how our algorithm treats missing values.

<sup>g</sup>For 14 events in our test set, the SWIFT\_BAT\_POSITION notice was not available on the online repository, primarily due to satellite downlink problems at the time of discovery. For these events, the relevant parameters were extracted directly from the *Swift* TDRSS database (<http://heasarc.nasa.gov/W3Browse/all/swiftdrssl.html>).

Table 2.1: List of Features Utilized

Feature	Type	Reference
BAT Rate Trigger?	BAT Prompt	GCN Notices
$\sigma_{BAT}$	BAT Prompt	GCN Notices
$R_{peak,BAT}$	BAT Prompt	GCN Notices
$t_{BAT}$	BAT Prompt	GCN Notices
UVOT Detection?	NFI Prompt	GCN Notices
$N_{H,pc}$	Processed	Butler & Kocevski (2007)
$\alpha$	Processed	Butler et al. (2007)
$E_{peak}$	Processed	Butler et al. (2007)
$S$	Processed	Butler et al. (2007)
$S/N_{max}$	Processed	Butler et al. (2007)
$T_{90}$	Processed	Butler et al. (2007)
$P_{z>4}$	Processed	Butler et al. (2010)

background-subtracted flux is emitted.

One additional “metafeature” is derived from the BAT data. In principle, if we knew in detail the intrinsic distributions of GRB observables (fluence, hardness, duration; see Butler et al. 2007) as a function of redshift, measurements of these observables for a new event could be used to directly evaluate the expected redshift. A detailed fitting of the intrinsic distributions for *Swift* is presented in Butler et al. (2010), and we use the parametrized intrinsic distributions there to calculate the posterior probability redshift distributions for each GRB in our sample (see, e.g., Figure 8 in Butler et al. 2010). Here, we further condense this distribution into one useful feature:  $P_{z>4}$ , the fraction of posterior probability at  $z > 4$ .

Finally, two features are extracted from data taken by the two narrow-field instruments onboard *Swift*, one each from the XRT and UVOT. The feature  $N_{H,pc}$  is the excess neutral hydrogen column (above the galactic value) inferred from the XRT PC (Photon-counting mode) data, obtained from the Butler & Kocevski (2007) pipeline. The last feature is simply a binary measure of whether or not the GRB afterglow was detected by the UVOT.

While most of these features have associated uncertainties, the proper treatment of uncertainties in attributes is an area of ongoing research in machine learning (e.g. Carroll et al. 2006). Some methods call for the uncertainties to be treated as attributes in and of themselves, but we found that the addition of these relatively weak features were actually detrimental for our small dataset (see, e.g., Fig. 2.6). We also considered an approach by which features with large uncertainties were considered poor measurements and were instead marked as missing values. However, this had a negligible effect on our final classifier performance, so for simplicity we treat all values as precisely known.

We collated data on all *Swift* GRBs with rapidly available BAT data up to and including GRB 100621A - 471 in total. Specifically, this excludes bursts that were not identified in real-time due to the event being below the standard triggering threshold or occurring while the satellite was slewing to a new location. Of these, 39 are short GRBs (defined for the purposes of this study to be those with  $T_{90} < 2.0$  s<sup>h</sup>), which are believed to arise from a

<sup>h</sup>  $T_{90}$  alone is not a strong enough discriminator to definitively assign a particular GRB to one class or

different physical process and are thus removed from the sample. For further uniformity in the sample, bursts without rapid ( $< 1$  hour) XRT/UVOT follow-up are also removed, leaving 347 events<sup>i</sup>. Of the remaining long bursts in our sample, 135 had reliable redshifts (Table 2.4) and were thus included in our training data set (Table 2.5). The additional 212 long bursts without secure redshift determinations are explored further in §2.5.1. Exploratory data analysis shows preliminary indications of which of these features will be most useful for classification. Figure 2.2 shows several 2D slices of the feature space, with the high- $z$  bursts highlighted.

## 2.3 Classification Methodology

The resource allocation approach we have taken here naturally manifests itself as a classification problem: deciding whether or not to follow up a new event is simply a two-class problem of “observe” or “do not observe,” and the methodology presented here can be applied to any problem that can be broken up in this way. This was the primary motivation for using classification instead of a regression or “pseudo- $z$ ” approach for this study. The primary disadvantage of classification for the particular problem of high-redshift identification is that all instances above and below the class division (chosen here to be  $z = 4$ ) are treated equally; e.g., a burst with  $z = 4.01$  has the same influence on our inference about “high” bursts as a burst with  $z = 8$ <sup>j</sup>. However, classification has advantages over regression in that it is a conceptually much simpler problem, and most of the difficulties encountered due to the unbalanced, small dataset of interest here would only be aggravated by an extension to regression. Further, our approach capitalizes on the fact that one of our predictors (lack of UVOT detection) is itself a binary feature with an understood physical connection to redshift<sup>k</sup>.

another (“short” versus “long”; see Levesque et al. 2010 for discussion). In this study, we will accept the few errant bursts from the “short” class included in our sample as additional noise in our method.

<sup>i</sup>The reason for this missing data is almost always due to observing constraints from the GRB being too close to the Sun, Moon, or Earth at the time of discovery. Not removing these bursts would introduce a bias in the sample due to the fact that events without a rapid XRT position are far less likely to lead to an afterglow discovery, and hence, redshift determination. A total of 15 bursts with known- $z$  were removed for this reason.

<sup>j</sup>This of course would not be an issue when applying the RATE methodology to a problem with more well-defined class boundaries, such as prioritizing follow-up of a particular rare class of transient event.

<sup>k</sup>Bursts with a UVOT detection must be  $z < 5$  due to the Lyman cutoff. This is due to the fact that photons with wavelengths smaller (thus higher energy) than the Lyman limit of  $\lambda = 912\text{\AA}$  would be almost completely absorbed by neutral gas in the host galaxy and intergalactic star forming regions. A redshift of  $z = 5$  might therefore be considered a natural cutoff point for the high- $z$  class, but due to so few training events at this high redshift ( $N_{z>5} = 8$ ), we opted for the more conservative cutoff point of  $z = 4$  ( $N_{z>4} = 18$ ).



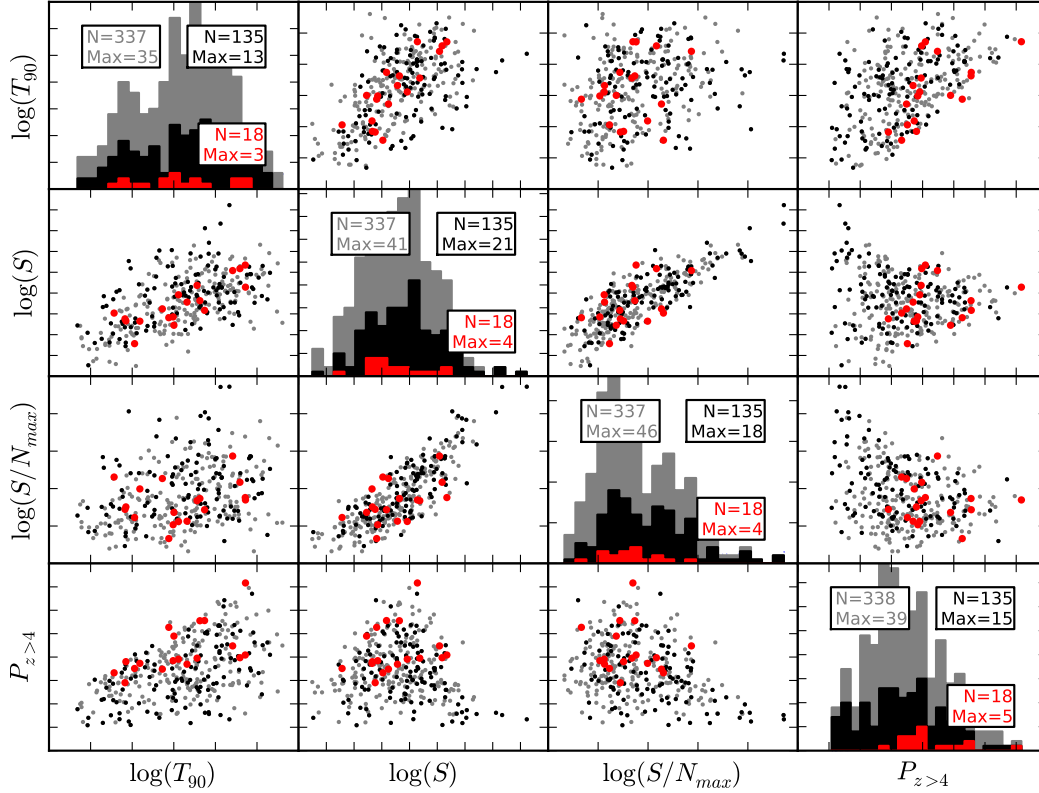


Figure 2.2: Plot of a selection of early-time *Swift* features (Table 2.1) against each other. The grey points show the full distribution of *Swift* GRBs. Bursts with known redshifts are black, and the 18 known events with redshifts greater than 4 are overplotted in red. In the histogram text boxes,  $N$  shows how many instances of that feature in total are shown (anything less than the full number of instances is due to the value of that feature being unknown for certain instances), and Max shows the maximum number of instances in any particular bin.

### 2.3.1 Random Forest classification

A supervised classification algorithm uses a set of training data of known class to estimate a function for assigning data points to classes based on their features. The statistics and machine learning communities have developed many classification algorithms, including Support Vector Machines (SVM), Naïve Bayes, Neural Networks, and Gaussian Mixture Models. We use Random Forest (RF [Breiman 2001](#)) for its ability to select important features, resist overfitting the data, model nonlinear relationships, handle categorical variables, and produce probabilistic output. These strengths, along with a record of attaining very high classifica-



tion accuracy relative to other algorithms have led to widespread use of Random Forest in the astronomy community (e.g., Bailey et al. 2007; Carliles et al. 2010; Dubath et al. 2011; O’Keefe et al. 2009; Richards et al. 2011). In this work, we utilized custom R software built around the `randomForest` package to generate classifiers and evaluate performance.

Random Forest is an ensemble classifier that averages together the outputs from many decision trees, a common example of which is Classification and Regression Trees (CART, Breiman 1984). In RF, the decision trees are constructed by recursive binary splitting of the high-dimensional feature space, where each split is performed with respect to a particular feature. For example, the decision tree might split the data on feature  $S/N_{\max}$  using value 100, in which case all observations with  $S/N_{\max} > 100$  are placed in one group and the rest placed in the second group. As these are binary splits, for convenience we henceforth refer to observations going “left” or “right” of each split as an analogue for the decision made at that split.

For each split, the feature and specific split-point are chosen so as to best separate the observations into the classes, by using some objective function. We use the Gini Index, a standard objective function for classification (Breiman 1984). At any given node in a tree and some proposed split  $s$ , let  $N_{l,h}$  = number of high-priority (in our case, high- $z$ ) events that go to the left of the split,  $N_{l,l}$  = number of low-priority events that go left. Define  $N_{r,h}$  and  $N_{r,l}$  similarly, replacing left with right. Let  $N_l = N_{l,l} + N_{l,h}$ , the total number of observations that go left. Similarly define,  $N_r = N_{r,l} + N_{r,h}$ , for the total number of observations that go right. The Gini criterion is defined as

$$\frac{N_l}{N_l + N_r} \left( \frac{N_{l,h}}{N_l} \right) \left( \frac{N_{l,r}}{N_l} \right) + \frac{N_r}{N_l + N_r} \left( \frac{N_{r,h}}{N_r} \right) \left( \frac{N_{r,l}}{N_r} \right), \quad (2.1)$$

and the split that minimizes this value over the random subset of features considered at each node<sup>1</sup> is chosen. For instance, in the ideal case where the split on a particular feature completely separates all the instances of the two classes from each other, the Gini index reaches a minimum of 0. The splitting is done recursively, continuing down each subgroup until all of the observations in each final group (“terminal node”) are of a single class. The process is known as “growing a tree” because each split can be visualized as generating two branches from a single branch to produce a tree-like structure. Once a tree is constructed from the training data, each new observation starts at the root node (the top split in the tree) and, recursively, the splitting rules determine the terminal node to which the observation belongs. The observation is assigned to the class of the terminal node.

To create the RF classifier, a sufficiently large<sup>m</sup> number of decision trees are constructed, resulting in a “forest”. Each decision tree is generated from an independent bootstrap sample (Efron 1982); Samples are drawn with replacement from the original data set, resulting in a

<sup>1</sup>At each node,  $m = 3$  features were considered, guided by the default practice in the `randomForest` routine of  $m = \text{floor}(\sqrt{p})$ , where  $p$  is the total number of features.

<sup>m</sup>With enough trees, error rates will converge and growing additional trees will result in no further performance improvements. Our forests are grown to 5000 trees throughout this work in order to ensure consistency in the rankings of unknown events.

new data set of the same size as the original, with on average 2/3 of the original observations present at least once. Additionally, only a random subset of the features is eligible for splitting at each node. Many decision trees are grown with each tree slightly different due to the bootstrap sampling and random selection of features at each split. RF classifies new observations by averaging the outputs of each tree in the ensemble.

Training observations can be classified by using all trees where that observation was not used in the bootstrap sampling stage. This produces estimates of error rates and class probabilities for each observation that are not overfit to the training data. Error rates and probabilities computed using this method are known as “out-of-bag” estimates.

### Missing feature values

As mentioned in §2.2, certain features, namely  $\alpha$  and  $N_{\text{H,pc}}$ , were occasionally unable to be determined from model fits to the data and are thus missing for certain observations. We handle missing values by imputation, where missing values for features are assigned estimated values. For missing values of continuous features, we assigned the median of all observations for which that feature is non-missing. Missing categorical features are assigned the mode of all observations for which the feature is non-missing. This is one of the simplest imputation methods and has the advantage of being transparent and computationally cheap. We experimented with a more sophisticated imputation method, `MissForest`, that iteratively predicts the missing values of each feature given all the other features (Stekhoven & Bühlmann 2011), but as it produced similar error rates to median imputation, we opted for latter, simpler approach in our final classifier.

### Class imbalance

A further challenge in this data set is the imbalance between classes. We are training on 135 bursts, only 18 of which are in the high- $z$  class — an asymmetry present in many resource allocation problems where the goal is to prioritize the rarer events. Without modification, standard machine learning classification algorithms applied to imbalanced data sets attain notoriously suboptimal performance (Chawla et al. 2004), and often result in simply classifying all unknown events as the more common class. As we care more about correctly classifying the rarer events, misclassifications of high- $z$  events must be punished more strongly than vice versa. In Random Forest, classes may be weighted in order to overcome the imbalance by altering the splits chosen by Gini and the probabilities assigned to classes in the terminal nodes of each tree (Chen et al. 2004).

We utilized the `classwt` option in the `randomForest` package, which accounts for class weights in the Gini index calculation (Eq. 2.1) when splitting at the nodes (Liaw 2011, private communication), similar to weighting techniques used in single CART trees (Breiman 1984). If we are weighting high-priority observations (e.g.  $z > 4$  GRBs) by  $w_h$  and low-priority

observations by  $w_l$ , we let,

$$\begin{aligned} N'_{l,h} &= w_h N_{l,h} \\ N'_{l,l} &= w_l N_{l,l} \\ N'_{r,h} &= w_h N_{r,h} \\ N'_{r,l} &= w_l N_{r,l} \end{aligned}$$

Let  $N'_l = N'_{l,l} + N'_{l,h}$ , the weighted total number of observations that go left. Similarly define,  $N'_r = N'_{r,l} + N'_{r,h}$ , for the weighted total number of observations that go right. The Gini criterion (Eq. 2.1) is evaluated with the weighted values, and the split that minimizes this value is chosen. We tested a variety of weight choices by fixing  $w_l$  to be unity and varying  $w_h$  over a range of values. The results of this test are presented in §2.4.1, which demonstrates the effects of class weight choice on classifier performance.

### 2.3.2 RATE GRB- $z$ : Random forest Automated Triage Estimator for GRB redshifts

With the background above in hand, we now describe our resource allocation algorithm and its utility for the prioritization of high- $z$  GRB follow-up. In our application, the data are described in §2.2 and the classes are high- and low-redshift GRBs, with  $z = 4$  as the boundary between the classes. Our primary goal is to provide a decision for each new GRB: should we devote further resources to this event or not? This decision may be different for each astronomer, as it is dependent on the amount of follow-up time available. Implicit in this goal is the desire to follow up on as many truly high-redshift bursts as possible, under a set of given telescope time constraints. Directly using the results of an off-the-shelf classifier for this task (i.e., strictly following-up on events labeled as “high-priority”) is suboptimal. If too few events are labeled as high-priority, there would be an under-utilization of available resources. If too many are being labeled as high priority, simply following up on the first ones available would preclude any prioritization of events within this high-priority class.

These issues can be avoided by instead tailoring the follow-up decision to the resources available (in this case, the available telescope time devoted to high- $z$  GRB observations). The RATE method works as follows: Let  $\mathcal{Q}$  be the fraction of events one has resources to follow up on<sup>n</sup>. First we construct a Random Forest classifier using the training data with known response (in this case redshift). We compute the probability of each training event being high-priority using out-of-bag probabilities (See §2.3.1). For each new event, we obtain a probability of it being high priority using the Random Forest classifier, and compute the fraction of training bursts that received a higher probability of being high-priority than this

<sup>n</sup>As telescope resources are allocated by number of hours and not number of objects, we implicitly assume here that an equal amount of resource time will be allocated to each follow-up event. This is not in general the case, as objects that turn out to be particularly interesting may have additional resources spent on them. However, a user’s estimate of  $\mathcal{Q}$  can always be adjusted without penalty as available resources change.

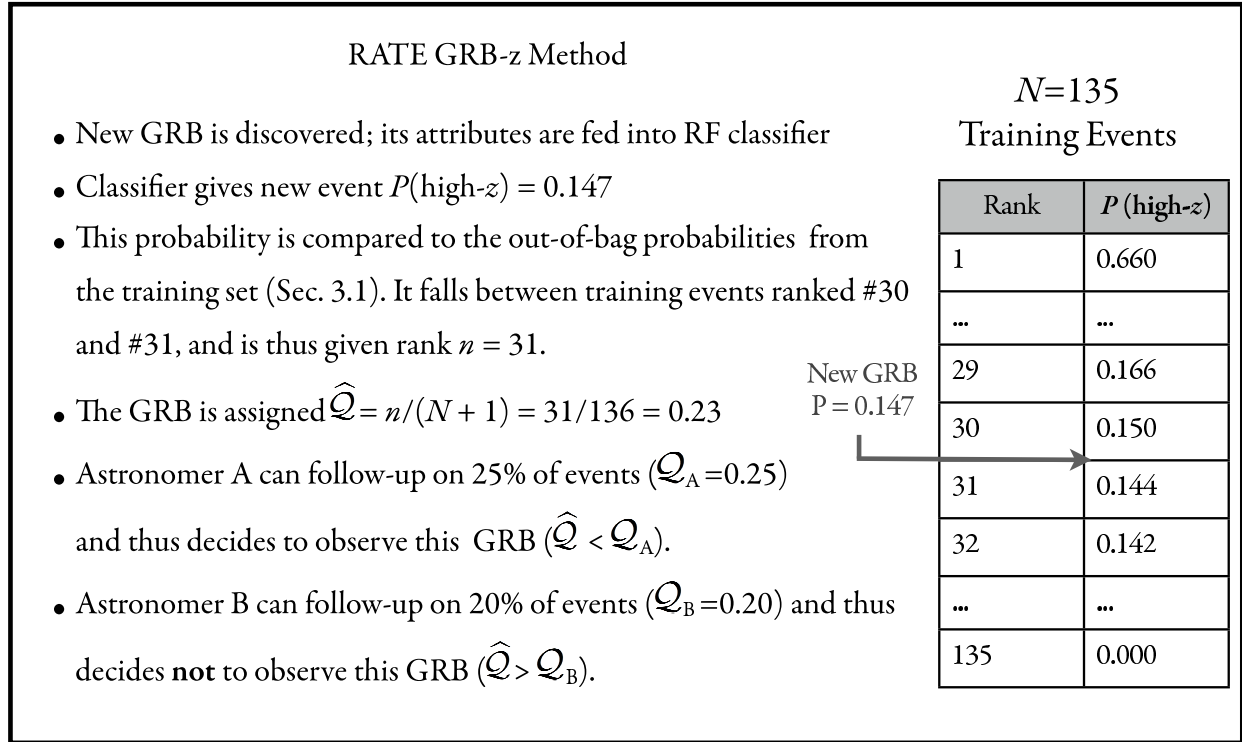


Figure 2.3: Example of the RATE GRB- $z$  process.

new burst. A new burst is assigned rank  $n$ , with  $n - 1$  training events having a lower probability of being high priority. Then, for  $N$  total training bursts, we obtain a learned probability rank for the new event of  $\hat{Q} := n/(N + 1)$ . This leads to a simple decision metric for each new event: If  $\hat{Q}$  is less than the desired fraction of events a particular observer wishes to follow up ( $\hat{Q} < Q$ ), follow-up observations are recommended. For instance, if one can afford to follow up on  $\sim 30\%$  of all observable GRBs, then the desired follow-up fraction is  $Q = 0.3$ , and follow-up would be recommended for all events assigned a  $\hat{Q} < 0.3$ . An illustration of this process in action is shown in Figure 2.3. The desired fraction of follow-up events  $Q$  can be dynamically changed without penalty; if the amount of available resources changes, one simply needs to raise or lower this cut-off value accordingly.

## 2.4 Validation of Classifier Performance

Our training data consist of 135 bursts, 18 of which are high-redshift ( $> 4$ ). Our primary measure of performance is efficiency, defined here as the fraction of high bursts that we that we follow up on relative to the number of total high- $z$  GRBs that occurred ( $N_{\text{high observed}}/N_{\text{total high}}$ ). A secondary performance measure is purity, the number of followed-

up events that were actually high- $z$  ( $N_{\text{high observed}}/N_{\text{total observed}}$ ). We measure performance using 10-fold cross-validation (Kohavi 1995), where 90% of the data is used to construct a classifier and predict on the remaining 10% of events. Each line in the following performance plots is the cross-validated performance averaged across 100 trials of 10-fold cross-validation in order to reduce variability due to randomness in training/test subset selection.

### 2.4.1 Comparison of Weight Choices

As described in §2.3.1, one of the primary challenges in learning on this dataset is the simple fact that there are comparatively few high- $z$  events on which to train. If simply getting the most classifications correct were the primary performance metric, as it is in many classification problems, classifying *all* new events as low-redshift would be considered a strong classifier since so few events are in the high- $z$  class. However, since our objective is to identify the best candidates of this rare class, we punish misclassifications of high- $z$  GRBs more heavily to achieve higher efficiency and purity (outlined above) for a given fraction of followed-up events.

Thus, in selecting the best weight for our classifier, we compared the efficiency and purity of high- $z$  classification for various choices of the weight  $w_h$  using the feature set shown in Table 2.1. While the relative probability ranking of the GRBs stayed relatively stable over weight choices (Figure 2.4), a clear trend emerges when comparing classification performance (Figure 2.5). As expected, punishing misclassifications of the smaller, more desirable high- $z$  class cause more of these rare events to be correctly identified. Beyond a weight of 10, however, a ceiling is reached where further weight increases show zero change in classification performance. This is therefore the weight chosen for all subsequent performance comparisons.

### 2.4.2 Effects of Feature Selection

As mentioned in §2.2, early testing indicated that the addition of too many features rapidly degraded the predictive power of the final classifier. This is due to a manifestation of the so-called “curse of dimensionality” known as Hughes Phenomenon (Hughes 1968), where for a fixed number of training instances, the predictive power decreases as the dimensionality increases. This appears to contradict the conventional wisdom that Random Forest does not overfit, and thus it is better to use many features. However, we note that resistance to overfitting is different from signal being drowned in noise. With enough noisy features, correlations between class and a useless feature will happen purely by chance, preventing true relationships from being found.

To visualize this effect for our data, we took our nominal feature set and continually added features with no predictive power (random samples from the uniform distribution) to quantify the degradation in performance of the resultant classifiers. The random features were re-generated for each of the 100 trials, and the cross-validated results are shown in Figure 2.6. The fact that even a small number of useless features causes a noticeable decrease in performance highlights the importance of attribute selection. However, we note that too

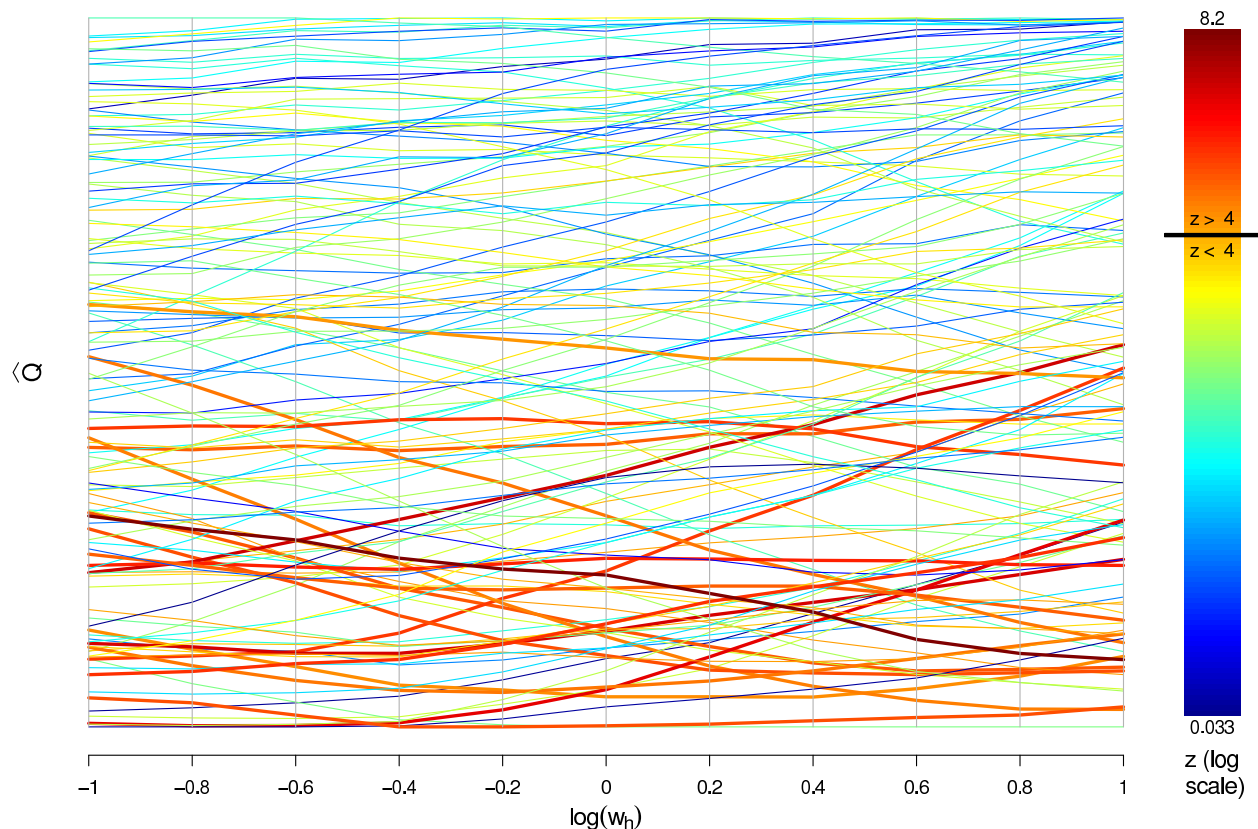


Figure 2.4: Bumps plot showing the cross-validated ranking prediction  $\hat{Q}$  for each GRB in the training set over a variety of weight choices. Each line corresponds to an individual GRB, colored by its observed redshift. Bursts with  $z > 4$  are plotted with a thicker line. The clustering of high- $z$  events towards low  $\hat{Q}$  is clear, illustrating the predictive power of the classifier. The relative ranking of events remains largely stable over different penalization weights, but performance improvements at higher weights are apparent in Figure 2.5, which level off after a weight of 10.

much fine tuning of attribute feature selection choices — such as testing all combinations of features and seeing which one gives the best performance — would overfit to the data and give an underestimate of the true error.

### 2.4.3 Final Classifier

Taking into account the above issues of multiple feature set choices, the deleterious effect of useless features, and the performance with various weight choices to help with imbalance, we have developed a classifier which we believe to be robust and powerful. The full feature set utilized is shown in Table 2.1, and the weight chosen is described in §2.4.1. The final cross-validated estimates of  $\hat{Q}$  for the training data are shown alongside the corresponding



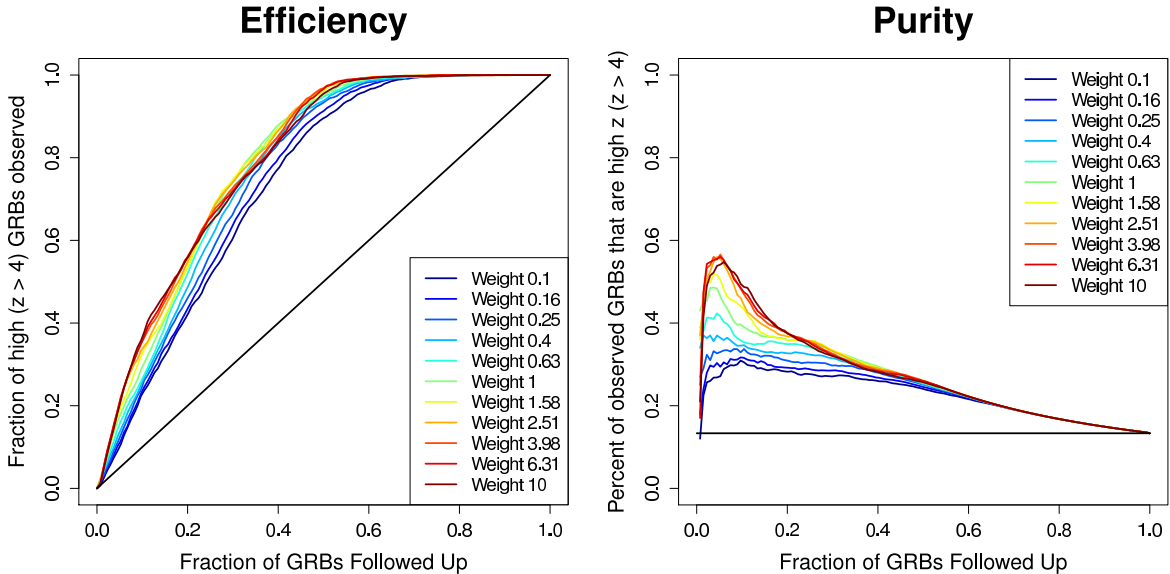


*Figure 2.5:* The effects of different weights on classifier performance are shown via plots of efficiency ( $N_{\text{high observed}}/N_{\text{total high}}$ ; left panel) and purity ( $N_{\text{high observed}}/N_{\text{total observed}}$ ; right panel) versus fraction of GRBs followed-up (see Figure 2.11 for how our decision criterion  $\mathcal{Q}$  corresponds to actual fraction followed-up). Solid black lines show expected results if selecting events by random guessing alone. Cross validated performances of the classifier trained with different weights are shown. Weights above 1.0 penalize misclassifications of high- $z$  events more strongly, and vice versa. Efficiency and purity were calculated at each fraction of followed-up GRBs ( $\mathcal{Q}$ , broken down into  $N = 135$  bins) and averaged over 100 random number generator seeds to account for variance between Random Forest runs. Clear performance increases for both metrics are shown for higher weights, but beyond a weight of 10, identical results are achieved. For clarity, estimates of uncertainties in the curves are not shown, but are of order those plotted in Figure 2.7.

redshifts in Table 2.4. By referencing a particular point on the  $x$ -axis of Figure 2.7 (left panel) one can determine what fraction of high bursts can be detected for a particular amount of telescope follow-up time. For example, if we are able to follow up on 20% of all GRBs detected by *Swift*, then the bursts recommended for follow-up by our classifier will contain on average  $56\% \pm 6\%$  of all GRBs with redshift greater than 4 that occur. Following-up on  $\sim 40\%$  of all bursts will yield  $84\% \pm 6\%$  of all GRBs with redshift greater than 4, and following-up on the top 50% of candidates will result in nearly all of the high- $z$  events being observed ( $96\% \pm 4\%$ ).

Purity is shown in the right panel of Figure 2.7, which describes how many of the followed-up bursts will actually be high-redshift. Following up on 20% of all bursts would result in  $37\% \pm 4\%$  of the followed-up events being high-redshift, and  $28\% \pm 2\%$  of followed up bursts would be high-redshift if 40% of GRBs were followed-up on.

As the high/low class division of  $z = 4$  was relatively arbitrary, for completeness we also

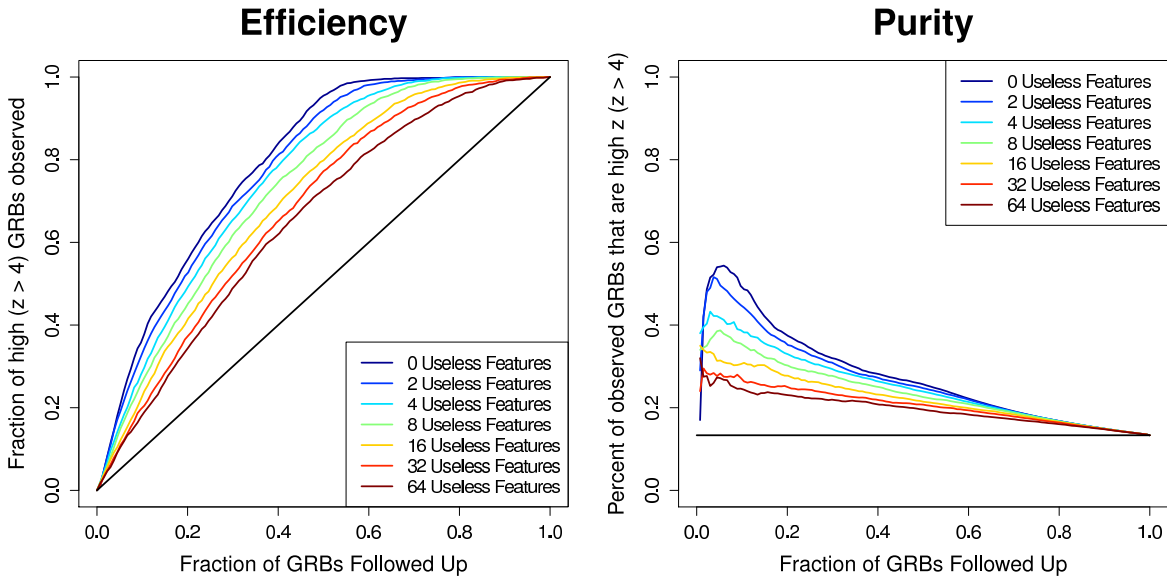


*Figure 2.6:* The effects of the addition of useless features on classifier performance are shown via plots of efficiency ( $N_{\text{high observed}}/N_{\text{total high}}$ ; left panel) and purity ( $N_{\text{high observed}}/N_{\text{total observed}}$ ; right panel) versus fraction of GRBs followed up according to our decision criterion ( $\mathcal{Q}$ ). Solid black lines show expected results if selecting events by random guessing alone. Cross validated performances of the classifier trained with different amounts of useless, randomly generated features are shown. Degradation in both efficiency and purity becomes clear with the addition of only a few useless features, highlighting the importance of feature selection for small, imbalanced datasets such as this one.

re-trained the classifier and calculated performance results using cutoff values of  $z = 3.5$  (Fig. 2.8) and  $z = 3$  (Fig. 2.9). Note that while the sample size of ‘high’ events more than doubles by lowering the cutoff value to  $z = 3$ , the resultant efficiency decreases significantly. We attribute this effect to a decrease in the predictive power of certain attributes at lower redshift. For instance, the  $z > 3$  population has proportionally many more instances of UVOT detections in its ‘high- $z$ ’ class than the  $z > 4$  population, which reduces its effectiveness as a discriminating feature.

#### 2.4.4 Feature Importance of Classifier

There are several complications in identifying the relative importance of features in contributing to selecting high- $z$  candidates. To an extent, simple scatter plots such as those in Figure 2.2 can give an indication as to what features are best at separating the classes, but these fail to account for the complex interactions between features occurring within the RF classification. The effects of removing features from the dataset and then re-constructing the classifier give another indication of feature importance, but fail to account for redundancy



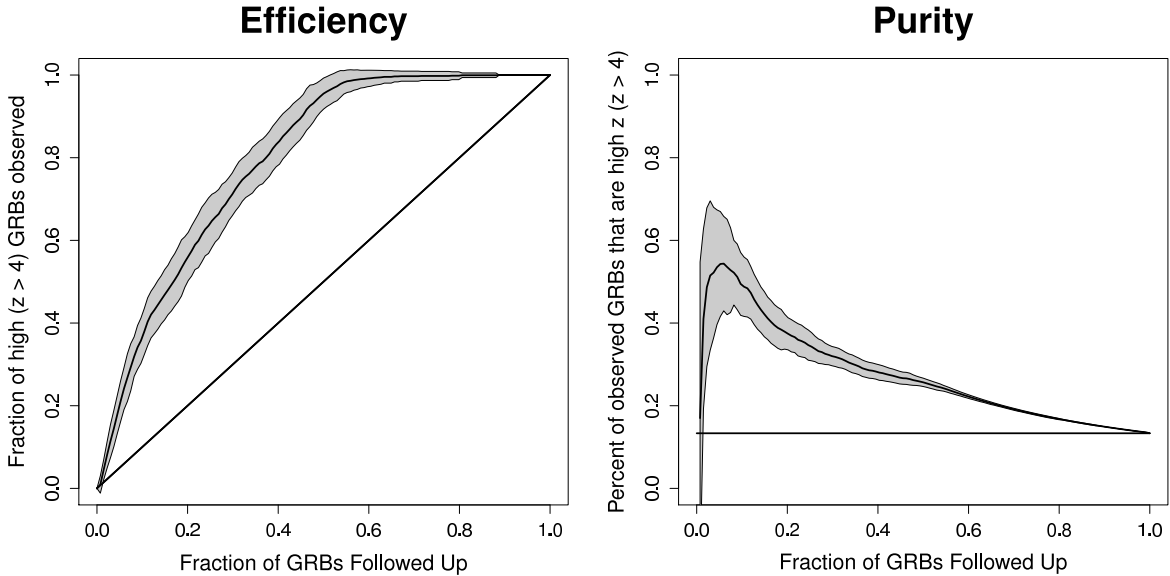


Figure 2.7: Efficiency ( $N_{\text{high observed}}/N_{\text{total high}}$ ; left panel) and purity ( $N_{\text{high observed}}/N_{\text{total observed}}$ ; right panel) versus fraction of GRBs followed up according to our decision criterion ( $\mathcal{Q}$ ) with a high- $z$  cutoff of  $z = 4$ . 18 bursts ( $\sim 13\%$  of our training set) are  $z \geq 4.0$ . The curve uncertainties shown are  $1\sigma$  standard deviations from the mean value across all seeds.

in the features; if two features have similar predictive properties, removing one will just cause the other to take its place. Nevertheless, such an experiment can be illustrative, and the results are shown in Figure 2.10. In general, the removal of an individual feature does not cause a significant change in performance, and the small changes that do occur trend toward a degradation in the number of high- $z$  bursts identified, implying that few if any of the features in the dataset are useless. The features that cause the largest degradation in performance upon their removal are  $\alpha$ ,  $R_{\text{peak,BAT}}$ , and  $S/N_{\text{max}}$ , indicating that these features are both useful predictors and are not fully redundant with other features. Note that the slight improvement in performance from the removal of the temporal features  $T_{90}$  and  $t_{\text{BAT}}$  is consistent with these values having little-to-no predictive power, in agreement with the recent findings of Kocevski & Petrosian (2013) showing a lack of time dilation signatures in GRB light curves.

## 2.5 Discussion

### 2.5.1 Calibration on GRBs with unknown redshifts

A natural application of our methodology is to use it to predict the follow-up metric  $\hat{\mathcal{Q}}$  for the remaining majority of long-duration *Swift* GRBs with no known redshift, providing

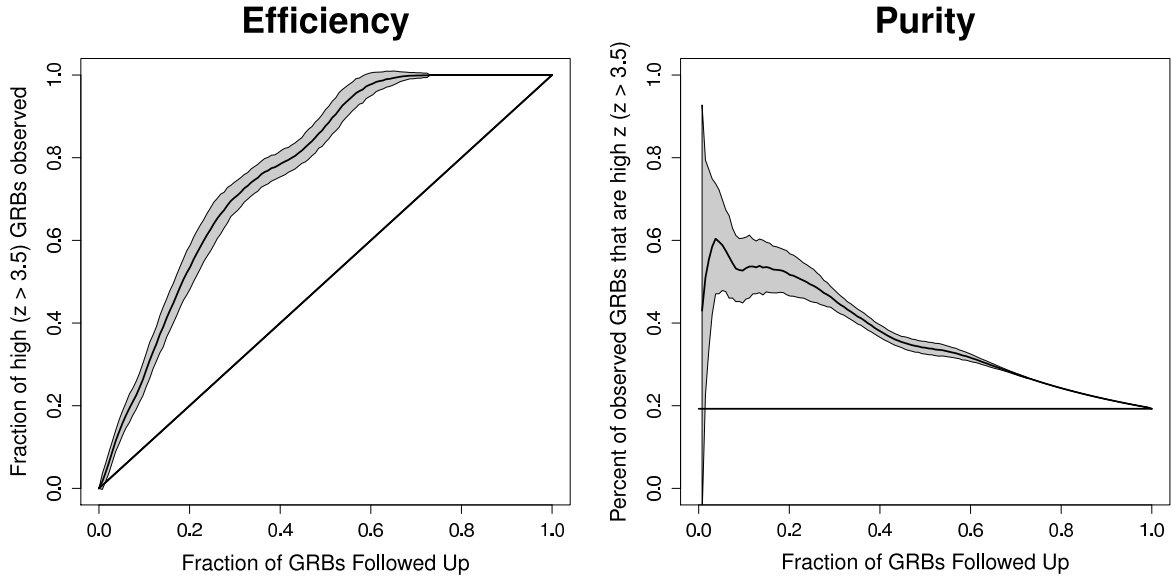


*Figure 2.8:* Efficiency ( $N_{\text{high observed}}/N_{\text{total high}}$ ; left panel) and purity ( $N_{\text{high observed}}/N_{\text{total observed}}$ ; right panel) versus fraction of GRBs followed up according to our decision criterion ( $\mathcal{Q}$ ) with a high- $z$  cutoff of  $z = 3.5$ . 26 bursts ( $\sim 19\%$  of our training set) are  $z \geq 3.5$ . The curve uncertainties shown are  $1\sigma$  standard deviations from the mean value across all seeds.

a list of the top candidates predicted to be high- $z$ . This application is precisely how RATE GRB- $z$  could be used in practice on new events, albeit one-at-a-time rather than on many at once. We caution that due to the natural selection effect of GRBs with measured redshifts having a higher likelihood of being brighter events, the bursts with unknown redshifts are likely to comprise a somewhat different redshift distribution than our training dataset. The primary consequence of this is the interpretation of the user-desired follow-up fraction  $\mathcal{Q}$  and the prioritization parameter  $\hat{\mathcal{Q}}$ . In principle, the classifier was calibrated such that, over time, a fraction  $\mathcal{Q}$  of new events will have affirmative follow-up recommendations (that is, events such that  $\hat{\mathcal{Q}} \leq \mathcal{Q}$ ). However, this will not necessarily be the case if the full redshift distribution of GRBs makes up a different population than our training data.

To test this, we calculated  $\hat{\mathcal{Q}}$  for each of the remaining 212 GRBs with unknown redshift that met our culling criteria outlined in §2.2. From this we could calculate the fraction of GRBs followed up ( $\hat{\mathcal{Q}} \leq \mathcal{Q}$ ) for each cutoff value of  $\mathcal{Q}$ . The results of this test are shown in Figure 2.11. For the chosen weight of 10 (see §2.4.1), the  $\mathcal{Q}$ -values are well calibrated with the final follow-up recommendations. The resultant  $\hat{\mathcal{Q}}$  priorities are listed in Table 2.6. These values can be interpreted as a ranking of which of these past events without secure redshift determinations are most likely to be at high-redshift.

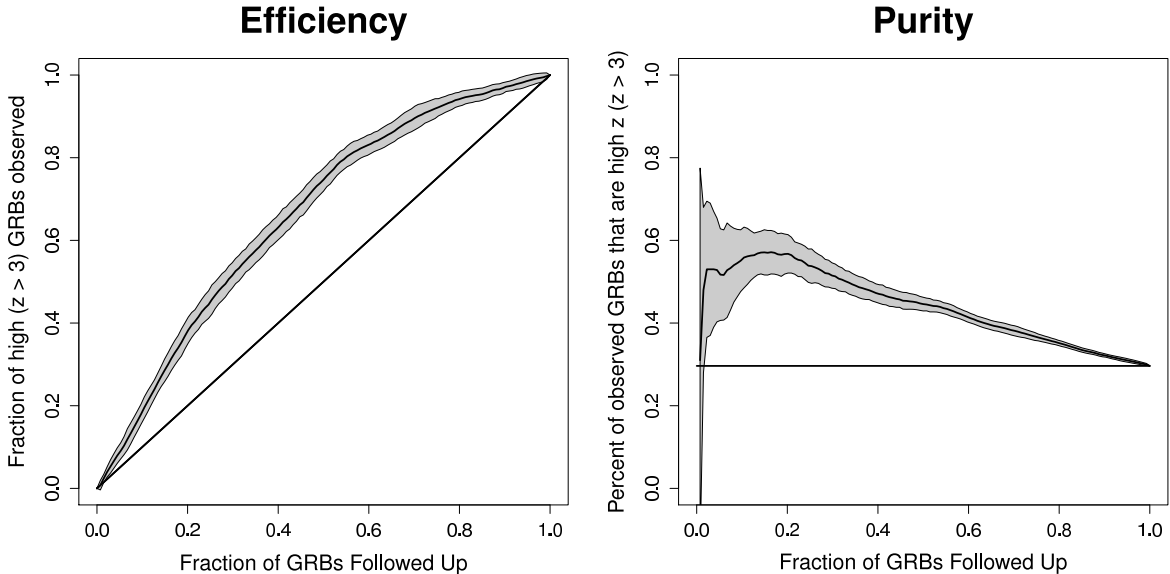


Figure 2.9: Efficiency ( $N_{\text{high observed}}/N_{\text{total high}}$ ; left panel) and purity ( $N_{\text{high observed}}/N_{\text{total observed}}$ ; right panel) versus fraction of GRBs followed up according to our decision criterion ( $\mathcal{Q}$ ) with a high- $z$  cutoff of  $z = 3.0$ . 40 bursts ( $\sim 30\%$  of our training set) are  $z \geq 3.0$ . The curve uncertainties shown are  $1\sigma$  standard deviations from the mean value across all seeds.

## 2.5.2 Validation Set: Application to Recent GRBs

Since the cutoff date in our training set (June 21, 2010) until Sept. 1, 2011, there have been 15 long duration *Swift* GRBs with reliable redshifts from which we constructed an independent validation set to test our method<sup>o</sup>. The feature values for these GRBs are presented in Table 2.2. While none of these events were over our high-redshift cutoff value of  $z = 4$ , it is still possible, though challenging, to use low- $z$  events (either by direct redshift measurement or by the identification of a coincident blue host galaxy) as a consistency test. We would expect that the purity at a given  $\mathcal{Q}$  would be lower than the fraction of recommended follow-up events ( $\hat{\mathcal{Q}} \leq \mathcal{Q}$ ) *without* a secure low- $z$  determination. For instance,  $\mathcal{Q} = 0.2$  has a purity of  $37\% \pm 4\%$ , so no more than  $\sim 63\%$  of events with  $\hat{\mathcal{Q}} < 0.2$  should be definitively low-redshift.

The validation GRBs were run through the RATE GRB- $z$  classifier, and their resultant  $\hat{\mathcal{Q}}$  values are shown in Table 2.3 along with their corresponding redshifts. The smallest  $\hat{\mathcal{Q}}$  value of these events is  $\sim 0.3$ , meaning that none of these events would have been recommended for high- $z$  follow-up for anyone wishing to observe fewer than 30% of events. While these values are certainly consistent with our expected purity, it is not particularly constraining,

<sup>o</sup>One of the bursts with a measured redshift, GRB 110328A, had very unusual properties and was determined to be a potential Tidal Disruption Event (Bloom et al. 2011; Levan et al. 2011b), and was thus also excluded from the validation set.

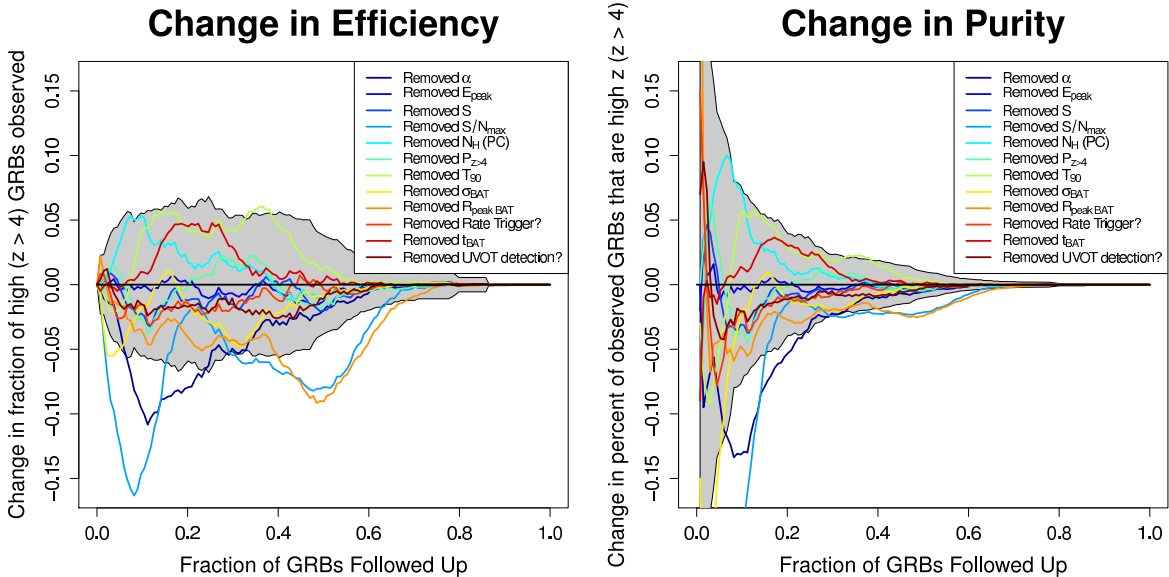


*Figure 2.10:* Change in efficiency (left) and purity (right) by removing individual features from the default feature set listed in Table 2.1. The standard deviation from the mean value across all seeds for the default dataset is shown in grey. The lack of degradation in performance by the removal of a feature does not necessarily imply that it has no predictive power, only that it may be redundant with other features. Most of the features do not cause a significant change in performance once removed from the dataset. However, the removal of a few of the individual features does cause a degradation in performance larger than what would be expected by random, implying that these features are both important and not completely redundant. Note that the relative change in both purity and efficiency are equal in both plots, as only the numerator of each metric is changing ( $N_{\text{high observed}}$ ), but we show both values for consistency.

as it would have been very unlikely for this almost-random selection of GRBs to violate this constraint by chance alone, even if the classifier had no predictive power.

A more constraining test is the identification of high- $z$  events with high  $\hat{Q}$  for comparison with the expected efficiency. Two events not included in our training set have had recent high- $z$  identifications: GRB 090429B with strong photometric evidence for being  $z \simeq 9.4$  (Cucchiara et al. 2011b), and the spectroscopic identification of GRB 111008A at  $z = 4.99$  (Levan et al. 2011a; Wiersema et al. 2011). The former has a  $\hat{Q}$  value of  $\sim 0.185$ , consistent with the expected efficiency. However, GRB 111008A has a  $\hat{Q}$  of  $\sim 0.637$ , a value above which we would have expected to find no more than 1% of high- $z$  events. This outlier seems likely due to the extreme brightness of the event (among the brightest  $\sim 10\%$  of *Swift* bursts in the observer frame, and top  $\sim 3\%$  in the rest frame). Indeed, compared to all 18 high- $z$  events in the training set, GRB 111008A has the most extreme values towards the ‘wrong’ end of three of the highly important features identified in §2.4.4 ( $\alpha$ ,  $P_{z>4}$ , and  $R_{\text{peak},\text{BAT}}$ )

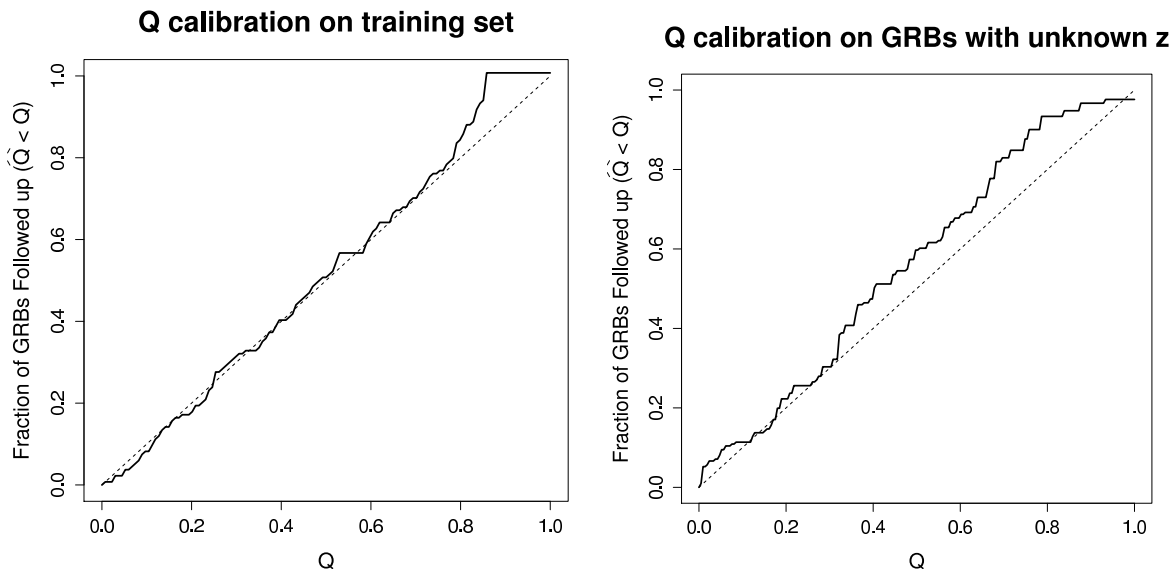


*Figure 2.11:* Here we quantify the calibration of  $Q$ ; namely, how well does the user-desired follow-up fraction  $Q$  correspond to the actual number of bursts recommended to be followed up by the algorithm ( $\hat{Q} \leq Q$ ). The left figure shows the self-calibration of the cross-validated training set, which aligns as expected. The right plot shows the calibration on the test set is good, especially at low  $Q$ . At larger  $Q$ , there is a slight departure from the diagonal, implying a follow-up recommendation of more events than expected at these values. This can be attributed to the differing populations between the training set (with measured redshifts) and test set (with unknown redshifts), as illustrated in Figure 2.2. This slight discrepancy is not surprising, as low brightness events without UVOT detections are naturally more difficult to obtain redshifts for.

and also has the fourth largest  $S/N_{max}$ . In later iterations of `RATE GRB-z`, this event (and all new GRBs with secure redshifts) will be added to the training data to re-generate the classifier and further improve its robustness against such outliers.

Table 2.2: Validation Data

GRB	$\hat{Q}$	$\alpha$	$E_{peak}$ (keV)	$S$ (erg/cm <sup>2</sup> )	$S/N_{max}$	$N_{H,pc}$ (10 <sup>22</sup> cm <sup>-2</sup> )	$T_{90}$ (s)	$\sigma_{BAT}$	$R_{peak,BAT}$ (ct/s)	Rate trigger	$t_{BAT}$ (s)	UVOT detect	$P_{z>4}$
100728B	6.07e-01	-1.64e+00	8.19e+01	2.54e-06	2.06e+01	3.90e-02	1.15e+01	9.07e+00	1.47e+02	yes	1.02e+00	yes	1.01e-01
100814A	6.81e-01	-1.11e+00	1.35e+02	9.33e-06	9.80e+01	?	1.77e+02	1.91e+01	8.34e+02	yes	1.02e+00	yes	1.80e-01
100816A	9.33e-01	-5.71e-01	1.42e+02	2.71e-06	5.80e+01	1.13e-01	2.50e+00	2.29e+01	1.42e+03	yes	1.02e+00	yes	5.55e-02
100901A	4.00e-01	-1.55e+00	1.28e+02	3.41e-06	1.78e+01	4.00e-02	4.59e+02	7.70e+00	4.50e+02	yes	8.19e+00	yes	2.25e-01
100906A	1.00e+00	-1.66e+00	1.57e+02	1.37e-05	1.36e+02	?	1.17e+02	1.05e+01	1.91e+02	yes	5.12e-01	yes	7.39e-02
101219B	6.30e-01	-1.89e+00	4.97e+01	3.75e-06	1.00e+01	-8.00e-03	4.18e+01	7.63e+00	8.44e+02	no	6.40e+01	yes	1.07e-01
110205A	3.19e-01	-1.39e+00	9.75e+01	1.98e-05	1.50e+02	1.10e-02	2.77e+02	1.00e+01	1.48e+03	no	6.40e+01	yes	1.45e-01
110213A	9.33e-01	-1.82e+00	6.70e+01	8.77e-06	3.10e+01	4.00e-02	4.31e+01	1.21e+01	2.05e+02	yes	1.02e+00	yes	5.32e-02
110422A	1.00e+00	-6.23e-01	1.11e+02	5.17e-05	2.10e+02	1.58e-01	2.67e+01	7.19e+00	8.20e+01	yes	1.28e-01	yes	2.49e-02
110503A	9.33e-01	-8.18e-01	1.42e+02	1.43e-05	6.27e+01	2.60e-02	9.31e+00	2.04e+01	1.26e+03	yes	1.02e+00	yes	1.89e-02
110715A	9.33e-01	-1.06e+00	8.94e+01	1.40e-05	2.02e+02	1.64e-01	1.31e+01	1.19e+01	1.47e+02	yes	1.28e-01	yes	9.70e-03
110726A	5.04e-01	-2.97e-01	4.27e+01	2.07e-07	1.51e+01	-4.90e-02	5.40e+00	8.60e+00	2.24e+02	yes	1.02e+00	yes	1.14e-01
110731A	1.00e+00	-1.19e+00	4.06e+02	1.25e-05	1.30e+02	7.20e-02	4.66e+01	2.46e+01	2.32e+03	yes	1.02e+00	yes	5.09e-02
110801A	9.33e-01	-1.84e+00	6.07e+01	6.85e-06	3.56e+01	2.90e-02	4.00e+02	7.83e+00	3.50e+02	yes	4.10e+00	yes	1.98e-01
110808A	5.56e-01	?	2.59e+01	4.27e-07	1.01e+01	2.17e-01	3.94e+01	7.19e+00	4.26e+02	yes	8.19e+00	yes	1.06e-01

Table 2.3: Validation Redshifts and Predictions

GRB	$\hat{Q}$	$z$	References
100728B	5.63e-01	2.106	<a href="#">Flores et al. 2010</a>
100814A	7.04e-01	1.44	<a href="#">O’Meara et al. 2010</a>
100816A	9.33e-01	0.8035	<a href="#">Tanvir et al. 2010a,c</a>
100901A	4.22e-01	1.408	<a href="#">Chornock et al. 2010a</a>
100906A	9.19e-01	1.727	<a href="#">Tanvir et al. 2010b</a>
101219B	6.07e-01	0.5519	<a href="#">de Ugarte Postigo et al. 2011c</a>
110205A	3.19e-01	2.22	<a href="#">Cenko et al. 2011</a>
110213A	8.89e-01	1.46	<a href="#">Milne &amp; Cenko 2011</a>
110422A	9.33e-01	1.770	<a href="#">Malesani et al. 2011; de Ugarte Postigo et al. 2011a</a>
110503A	9.33e-01	1.613	<a href="#">de Ugarte Postigo et al. 2011b</a>
110715A	8.89e-01	0.82	<a href="#">Piranomonte et al. 2011</a>
110726A	5.56e-01	1.036	<a href="#">Cucchiara et al. 2011a</a>
110731A	9.33e-01	2.83	<a href="#">Tanvir et al. 2011</a>
110801A	8.67e-01	1.858	<a href="#">Cabrera Lavers et al. 2011</a>
110808A	5.63e-01	1.348	<a href="#">de Ugarte Postigo et al. 2011d</a>

### 2.5.3 Comparison to Previous Efforts

Extracting indications of redshift from promptly available information has been a continuing goal of GRB studies since their cosmological origins were discovered nearly 15 years ago. Several potential luminosity indicators were pursued with the optimistic goal of using GRBs as standard candles for cosmological studies. The efficacy of individual indicators toward this goal proved to be limited, and a physical origin of the relations has been contested, with authors attributing them instead to detector thresholding or other selection effects ([Butler et al. 2007, 2009, 2010; Shahmoradi & Nemiroff 2011](#)). While these studies have ruled out the majority of such relations as intrinsic to GRBs themselves, prompt properties can still be used as redshift indicators if the systematics are properly accounted for.

Several recent studies have attempted to use combinations of features to determine “pseudo-redshifts” for GRBs. In an extension of work by [Schaefer \(2007\)](#), [Xiao & Schaefer \(2009, 2011\)](#) used a combination of six purported luminosity relations. Further, [Koen \(2009, 2010\)](#) has explored linear regression as a tool for predicting GRB redshifts using the dataset from [Schaefer \(2007\)](#). As data derived from multiple satellites were used, these studies are particularly vulnerable to the detector selection effects mentioned above.

Some works avoided the complications of regression and instead focused upon the simple selection of high- $z$  candidates for follow-up purposes. [Campana et al. \(2007\)](#) utilized a sample of *Swift*-only bursts (thus avoiding detector effect biases) and used hard cuts on three features ( $T_{90}$ , lack of UVOT detection, and high-galactic latitude) for high- $z$  candidate selection. [Salvaterra et al. \(2007\)](#) extended upon this work with the additional feature of peak photon flux.

Several issues prevent a direct comparison among the various methods of the effectiveness at separating high- $z$  events. These include the usage of different features from each study, which is complicated by the lack of uniformity of features being created for each. Further, the techniques above strictly constrain the manner in which each feature influences the output,

whereas our method is fully non-parametric and therefore more flexible. However, the largest concern is accurate reporting of predictive performance. In particular, we caution against the circular practice of measuring the performance of methods by applying them to the same events from which the luminosity relations were formed. In order to prevent over-estimating the accuracy of a predictive model, one needs to test on data independent from the training set, such as with cross-validation.

Finally, the RATE method differs from previous efforts in that it casts the problem as one of optimal resource allocation under limited follow-up time. Prior techniques are not explicitly calibrated to suit this purpose. Direct classification methods will either under or over-utilize available resources. Past regression or “pseudo- $z$ ” methods are not explicitly calibrated to a particular follow-up decision (i.e., at what “pseudo- $z$ ” does one decide to follow up?), though it would be possible in principle to correct for this using a transformation which ensures that the desired follow-up fraction corresponds to the actual fraction of bursts followed up (e.g., Figure 2.11). In contrast, the RATE technique is by design applicable to any available resource reserves, and is generally extendable to any transient follow-up prioritization problem.

## 2.6 Conclusions

In this chapter, we presented the RATE GRB- $z$  method for allocating follow-up telescope resources to high-redshift GRB candidates using Random Forest classification on early-time *Swift* metrics. The RATE method is generalizable to any prioritization problem that can be parameterized as “observe” or “don’t observe”, and accommodates statistical challenges such as small datasets, imbalanced classes, and missing feature values. The issue of resource allocation is becoming increasingly important in the era of data-driven transient surveys such as PTF, Pan-STARRS, and LSST which provide extremely high discovery rates without a significant increase in follow-up resources. With enough training instances of any object of interest for a given transient survey, the RATE method can be applied to prioritize follow-up of future high-priority candidates.

In the RATE GRB- $z$  application, our robust, cross-validated performance metrics indicate that by observing just 20% of bursts, one can capture  $56\% \pm 6\%$  of  $z > 4$  events with a sample purity of  $37\% \pm 4\%$ . Further, following up on half of all events will yield nearly all ( $96\% \pm 4\%$ ) of the high- $z$  events. The method provides a simple decision point for each new event: if the prioritization value  $\hat{Q}$  is smaller than the percent of events a user wishes to allocate resources to, then follow-up is recommended. These rapid predictions, combined with the more traditional photometric dropout technique from simultaneous multi-filter NIR observatories (such as PAIRITEL, GROND, and the upcoming RATIR), offer a robust tool in more efficiently informing GRB follow-up decisions. To facilitate the dissemination of high-redshift GRB predictions to the community, we have set up a website (<http://rate.grbz.info>) with  $\hat{Q}$  values for past bursts, and an RSS feed (<http://rate.grbz.info/rss.xml>) to provide real-time results from our classifier on new events.



## Acknowledgments

This work was sponsored by an NSF-CDI grant (award #0941742) “Real-time Classification of Massive Time-series Data Streams” (PI: Bloom). This publication has made use of data obtained from the *Swift* interface of the High-Energy Astrophysics Archive (HEASARC), provided by NASA’s Goddard Space Flight Center. A. Morgan gratefully acknowledges support from an NSF Graduate Research Fellowship. T. Broderick was funded by a National Science Foundation Graduate Research Fellowship. We are extremely grateful to the *Swift* team for the rapid public dissemination, calibration, and analysis of the *Swift* data. We thank Daniel Perley for useful conversations and for the creation and maintenance of the very useful <http://grbox.net> website. We also thank Scott Barthelmy for his invaluable efforts in creating and maintaining the GCN system.

Table 2.4: Training Data Redshifts

GRB	$\widehat{Q}_{train}$	$z$	References
050223	4.30e-01	0.5915	Berger & Shin 2006
050315	3.57e-01	1.949	Kelson & Berger 2005
050318	6.86e-01	1.44	Berger & Mulchaey 2005
050319	5.90e-01	3.2425	Fynbo et al. 2005a; Jakobsson et al. 2006c; Fynbo et al. 2009b
050416A	7.68e-01	0.6535	Lenz et al. 2005
050505	2.46e-02	4.27	Berger et al. 2005
050525A	7.90e-01	0.606	Foley et al. 2005
050730	6.66e-02	3.969	Chen et al. 2005; D’Elia et al. 2007
050801	6.49e-01	1.38	Fynbo et al. 2009b; Oates et al. 2009
050802	9.43e-02	1.71	Fynbo et al. 2005b
050814	2.32e-01	5.3	Jakobsson et al. 2006b
050820A	7.52e-01	2.6147	Ledoux et al. 2005
050826	2.05e-01	0.296	Mirabal et al. 2007
050904	2.53e-01	6.29	Kawai et al. 2005; Price et al. 2006b
050908	4.76e-01	3.35	Fugazza et al. 2005
050922C	7.94e-01	2.1995	D’Elia et al. 2005; Jakobsson et al. 2006c; Fynbo et al. 2009b
051109A	6.09e-01	2.346	Quimby et al. 2005
051109B	1.10e-01	0.080	Perley et al. 2006
060108	3.58e-03	2.03	Melandri et al. 2006
060115	1.54e-01	3.5328	Piranomonte et al. 2006b; Fynbo et al. 2009b
060116	2.05e-01	6.60	Grazian et al. 2006
060124	5.17e-01	2.296	Prochaska et al. 2006
060206	4.24e-01	4.0559	Fynbo et al. 2006b
060210	1.20e-01	3.913	Cucchiara et al. 2006a
060218	2.98e-01	0.0331	Mirabal & Halpern 2006
060223A	1.05e-01	4.41	Berger et al. 2006
060418	5.85e-01	1.49	Vreeswijk et al. 2007
060502A	2.44e-01	1.5026	Cucchiara et al. 2006b; Fynbo et al. 2009b
060510B	2.77e-02	4.9	Price 2006
060512	7.03e-01	2.1	Starling et al. 2006; Fynbo et al. 2009b
060522	3.19e-01	5.11	Lenz et al. 2006a
060526	7.36e-01	3.2213	Berger & Gladders 2006; Jakobsson et al. 2006c; Fynbo et al. 2009b
060605	1.16e-01	3.78	Savaglio et al. 2007
060607A	5.10e-01	3.082	Ledoux et al. 2006
060614	8.53e-01	0.1257	Price et al. 2006a; Della Valle et al. 2006
060707	1.41e-01	3.4240	Jakobsson et al. 2006c; Fynbo et al. 2009b
060708	2.34e-01	1.92	Fynbo et al. 2009b; Schady & Moretti 2006
060714	6.67e-01	2.7108	Jakobsson et al. 2006c; Fynbo et al. 2009b
060729	7.28e-01	0.5428	Thoene et al. 2006b; Fynbo et al. 2009b
060807	1.29e-01	3.28	Fynbo et al. 2009b
060904B	3.72e-01	0.7029	Fynbo et al. 2009b; Fugazza et al. 2006
060906	4.17e-01	3.6856	Vreeswijk et al. 2006; Jakobsson et al. 2006c; Fynbo et al. 2009b
060908	2.63e-01	1.8836	Fynbo et al. 2009b
060912	8.36e-01	0.937	Jakobsson et al. 2006a
060926	6.81e-01	3.2086	Piranomonte et al. 2006a; D’Elia et al. 2006; Fynbo et al. 2009b
060927	1.98e-01	5.4636	Ruiz-Velasco et al. 2007; Fynbo et al. 2009b
061007	8.56e-01	1.2622	Osip et al. 2006; Fynbo et al. 2009b
061021	8.42e-01	0.3463	Fynbo et al. 2009b
061110A	1.60e-01	0.7578	Thoene et al. 2006a; Fynbo et al. 2009b
061110B	5.07e-01	3.4344	Fynbo et al. 2006a, 2009b
061121	8.54e-01	1.3145	Bloom et al. 2006a; Fynbo et al. 2009b
061126	8.53e-01	1.1588	Perley et al. 2008c
061222A	6.47e-01	2.088	Perley et al. 2009b
061222B	2.72e-01	3.355	Berger 2006

Table 2.4 (cont'd): Training Data Redshifts

GRB	$\hat{Q}_{train}$	$z$	References
070110	4.67e-02	2.3521	Jaunsen et al. 2007b; Fynbo et al. 2009b
070208	1.76e-01	1.165	Cucchiara et al. 2007b
070306	2.78e-01	1.49594	Jaunsen et al. 2008
070318	4.83e-01	0.8397	Jaunsen et al. 2007a; Fynbo et al. 2009b
070411	6.92e-01	2.9538	Jakobsson et al. 2007b; Fynbo et al. 2009b
070419A	3.89e-01	0.9705	Cenko et al. 2007; Fynbo et al. 2009b
070506	4.61e-01	2.3090	Thoene et al. 2007b; Fynbo et al. 2009b
070508	8.53e-01	0.82	Jakobsson et al. 2007c; Fynbo et al. 2009b
070518	5.22e-01	0.7	Cucchiara et al. 2007c
070529	2.49e-01	2.4996	Berger et al. 2007
070611	2.23e-01	2.0394	Thoene et al. 2007a; Fynbo et al. 2009b
070714B	6.47e-01	0.92	Graham et al. 2007
070721B	4.65e-01	3.6298	Malesani et al. 2007; Fynbo et al. 2009b
070802	2.99e-01	2.4541	Prochaska et al. 2007; Fynbo et al. 2009b
070810A	5.92e-01	2.17	Thoene et al. 2007c
071025	4.36e-01	5.2	Fynbo et al. 2009b; Perley et al. 2010a
071031	2.26e-01	2.6918	Ledoux et al. 2007; Fynbo et al. 2009b
071117	6.46e-01	1.3308	Jakobsson et al. 2007a; Fynbo et al. 2009b
071122	2.47e-01	1.14	Cucchiara et al. 2007a
071227	6.15e-01	0.383	D'Avanzo et al. 2007
080129	1.16e-01	4.349	Greiner et al. 2009a
080210	5.23e-01	2.6419	Jakobsson et al. 2008d; Fynbo et al. 2009b
080310	8.01e-01	2.4274	Prochaska et al. 2008a; Fynbo et al. 2009b
080319B	8.46e-01	0.9382	Vreeswijk et al. 2008e,c; Fynbo et al. 2009b
080319C	7.03e-01	1.9492	Wiersema et al. 2008b; Fynbo et al. 2009b
080330	8.39e-01	1.5119	Malesani et al. 2008; Fynbo et al. 2009b
080413A	5.88e-01	2.433	Thoene et al. 2008b; Fynbo et al. 2009b
080413B	8.30e-01	1.1014	Vreeswijk et al. 2008d; Fynbo et al. 2009b
080430	7.21e-01	0.767	Cucchiara & Fox 2008
080520	8.28e-01	1.5457	Jakobsson et al. 2008a; Fynbo et al. 2009b
080603B	7.71e-01	2.6892	Fynbo et al. 2008a, 2009b
080604	3.61e-01	1.4171	Wiersema et al. 2008a; Fynbo et al. 2009b
080605	8.56e-01	1.6403	Jakobsson et al. 2008e; Fynbo et al. 2009b
080607	8.56e-01	3.0363	Prochaska et al. 2009; Fynbo et al. 2009b
080707	4.29e-01	1.2322	Fynbo et al. 2008c, 2009b
080710	4.32e-01	0.8454	Perley et al. 2008a; Fynbo et al. 2009b
080721	7.62e-01	2.5914	D'Avanzo et al. 2008b; Jakobsson et al. 2008f; Fynbo et al. 2009b
080804	8.05e-01	2.2045	Thoene et al. 2008a; Cucchiara et al. 2008d; Fynbo et al. 2009b
080805	2.54e-01	1.5042	Jakobsson et al. 2008c,b; Fynbo et al. 2009b
080810	7.14e-01	3.3604	Prochaska et al. 2008b; Fynbo et al. 2009b
080905B	3.92e-01	2.3739	Vreeswijk et al. 2008b; Fynbo et al. 2009b
080913	4.64e-01	6.7	Greiner et al. 2009b
080916A	6.02e-01	0.6887	Fynbo et al. 2008b, 2009b
080928	5.99e-01	1.6919	Vreeswijk et al. 2008a; Fynbo et al. 2009b
081007	7.86e-01	0.5295	Berger et al. 2008b
081008	3.47e-01	1.967	Cucchiara et al. 2008a; D'Avanzo et al. 2008a
081028A	3.83e-01	3.038	Berger et al. 2008a
081029	1.51e-01	3.8479	D'Elia et al. 2008a; Cucchiara et al. 2008b
081118	2.37e-01	2.58	D'Elia et al. 2008b
081121	5.82e-01	2.512	Berger & Rauch 2008
081203A	7.19e-01	2.05	Kuin et al. 2009
081222	8.12e-01	2.77	Cucchiara et al. 2008c
090102	8.13e-01	1.547	de Ugarte Postigo et al. 2009c
090205	3.87e-01	4.6503	D'Avanzo et al. 2010

Table 2.4 (cont'd): Training Data Redshifts

GRB	$\hat{Q}_{train}$	$z$	References
090418A	8.09e-01	1.608	<a href="#">Chornock et al. 2009a</a>
090423	8.46e-02	8.2	<a href="#">Salvaterra et al. 2009</a> ; <a href="#">Tanvir et al. 2009</a>
090424	8.30e-01	0.544	<a href="#">Chornock et al. 2009b</a>
090516A	8.85e-02	4.109	<a href="#">de Ugarte Postigo et al. 2009b</a>
090519	2.86e-01	3.85	<a href="#">Levan et al. 2009b</a>
090529	4.91e-02	2.625	<a href="#">Malesani et al. 2009b</a>
090618	8.58e-01	0.54	<a href="#">Cenko et al. 2009a</a>
090715B	6.13e-01	3.00	<a href="#">Wiersema et al. 2009</a>
090809	5.23e-01	2.737	<a href="#">Malesani et al. 2009a</a>
090812	4.49e-01	2.452	<a href="#">de Ugarte Postigo et al. 2009a</a>
090814A	3.53e-01	0.696	<a href="#">Jakobsson et al. 2009</a>
090926B	4.44e-01	1.24	<a href="#">Fynbo et al. 2009a</a>
090927	7.89e-01	1.37	<a href="#">Levan et al. 2009a</a>
091018	7.86e-01	0.971	<a href="#">Chen et al. 2009</a>
091020	7.80e-01	1.71	<a href="#">Xu et al. 2009</a>
091029	4.89e-01	2.752	<a href="#">Chornock et al. 2009c</a>
091109A	3.69e-01	3.076	<a href="#">Rau et al. 2010</a>
091127	8.36e-01	0.490	<a href="#">Cucchiara et al. 2009a</a>
091208B	7.89e-01	1.0633	<a href="#">Perley et al. 2009a</a>
100219A	1.32e-01	4.6667	<a href="#">de Ugarte Postigo et al. 2010</a> ; <a href="#">Cenko et al. 2010a</a>
100302A	7.10e-02	4.813	<a href="#">Chornock et al. 2010b</a>
100316B	7.26e-01	1.063	<a href="#">Vergani et al. 2010</a>
100316D	2.50e-01	0.0593	<a href="#">Chornock et al. 2010c</a>
100418A	5.15e-01	0.6235	<a href="#">Antonelli et al. 2010</a> ; <a href="#">Cucchiara &amp; Fox 2010</a>
100425A	5.27e-01	1.755	<a href="#">Goldoni et al. 2010</a>
100513A	7.56e-02	4.772	<a href="#">Cenko et al. 2010b</a>
100621A	8.53e-01	0.542	<a href="#">Milvang-Jensen et al. 2010</a>

Table 2.5: Training Data: Early-Time Metrics from *Swift* GRBs with Known Redshifts.

GRB	$\alpha$	$E_{peak}$	$S$	$S/N_{max}$	$N_{H,pc}$	$T_{90}$	$\sigma_{BAT}$	$R_{peak,BAT}$	Rate trigger	$t_{BAT}$	UVOT detect	$P_{z>4}$
050223	-1.74e+00	6.70e+01	8.75e-07	1.34e+01	-2.37e-01	1.74e+01	9.00e+00	7.26e+02	yes	8.19e+00	no	1.74e-01
050315	?	4.33e+01	4.32e-06	4.37e+01	9.60e-02	9.46e+01	8.00e+00	2.60e+02	yes	1.02e+00	no	9.27e-02
050318	-1.22e+00	5.01e+01	1.41e-06	4.90e+01	1.80e-02	3.10e+01	9.00e+00	2.05e+02	yes	5.12e-01	yes	6.29e-02
050319	-2.00e+00	4.47e+01	1.87e-06	1.82e+01	1.50e-02	1.54e+02	1.00e+01	2.63e+02	yes	1.02e+00	yes	1.48e-01
050416A	-7.24e-01	1.50e+01	3.40e-07	1.75e+01	2.34e-01	2.91e+00	1.10e+01	1.65e+02	yes	5.12e-01	yes	4.35e-03
050505	-1.41e+00	1.40e+02	4.84e-06	2.18e+01	4.80e-02	6.02e+01	1.00e+01	2.28e+02	yes	2.05e+00	no	1.48e-01
050525A	-8.30e-01	8.19e+01	1.86e-05	3.40e+02	4.90e-02	9.10e+00	1.80e+01	3.47e+02	yes	6.40e-02	yes	1.23e-02
050730	-1.39e+00	1.65e+02	2.55e-06	1.32e+01	5.00e-03	6.05e+01	1.10e+01	1.02e+03	yes	1.22e+01	yes	1.75e-01
050801	-1.96e+00	4.27e+01	3.26e-07	1.82e+01	-2.30e-02	5.88e+00	1.03e+01	2.21e+02	yes	5.12e-01	yes	9.31e-02
050802	-1.59e+00	9.51e+01	2.73e-06	1.86e+01	2.70e-02	1.43e+01	8.05e+00	2.06e+02	yes	1.02e+00	yes	1.28e-01
050814	-3.43e-01	6.07e+01	7.74e-07	6.80e+00	5.00e-03	2.75e+01	6.81e+00	6.08e+02	yes	1.64e+01	no	2.14e-01
050820A	-1.17e+00	4.94e+02	8.69e-06	4.14e+01	2.10e-02	2.40e+02	8.38e+00	2.34e+02	yes	1.02e+00	yes	8.94e-02
050826	-1.22e+00	3.40e+02	1.03e-06	1.25e+01	2.35e-01	3.44e+01	8.16e+00	5.33e+02	yes	8.19e+00	no	1.02e-01
050904	-1.17e+00	5.32e+02	1.22e-05	3.84e+01	8.00e-03	1.97e+02	1.33e+01	2.82e+03	no	6.40e+01	no	1.49e-01
050908	-1.72e+00	6.70e+01	6.00e-07	1.25e+01	-2.40e-02	1.08e+01	9.29e+00	3.11e+02	yes	2.05e+00	yes	1.56e-01
050922C	-9.92e-01	1.83e+02	2.66e-06	6.00e+01	2.40e-02	4.56e+00	2.28e+01	1.49e+03	yes	1.02e+00	yes	6.03e-02
051109A	1.41e+00	1.05e+02	1.54e-06	1.41e+01	5.00e-02	4.90e+00	1.15e+01	2.64e+02	yes	2.05e+00	yes	8.46e-02
051109B	-2.72e-01	5.87e+01	1.67e-07	7.30e+00	1.10e-02	8.32e+00	9.84e+00	5.27e+02	yes	4.10e+00	no	1.34e-01
060108	?	4.40e+01	5.12e-07	2.05e+01	6.20e-02	1.53e+01	8.51e+00	2.42e+02	yes	1.02e+00	no	1.42e-01
060115	-1.15e+00	6.75e+01	1.87e-06	2.74e+01	-4.80e-02	1.10e+02	1.05e+01	7.75e+02	yes	8.19e+00	no	2.18e-01
060116	-1.42e+00	1.65e+02	2.82e-06	1.15e+01	7.62e-01	3.60e+01	6.58e+00	4.54e+02	yes	1.64e+01	no	1.45e-01
060124	5.00e+00	8.28e+01	4.76e-07	5.40e+00	5.80e-02	8.16e+00	6.59e+00	1.66e+02	yes	1.02e+00	yes	1.25e-01
060206	-1.18e+00	8.35e+01	1.04e-06	4.51e+01	3.70e-02	6.06e+00	1.02e+01	1.99e+02	yes	5.12e-01	yes	1.16e-01
060210	-1.47e+00	1.36e+02	1.42e-05	4.28e+01	7.20e-02	3.70e+02	8.42e+00	2.04e+02	yes	1.02e+00	no	1.75e-01
060218	-8.44e-01	4.05e+01	7.85e-07	6.30e+00	3.72e-01	1.28e+02	7.84e+00	2.11e+03	no	8.00e+01	yes	2.71e-01
060223A	-1.01e+00	7.45e+01	6.76e-07	1.80e+01	-1.50e-02	8.40e+00	9.99e+00	2.69e+02	yes	1.02e+00	yes	1.40e-01
060418	-1.61e+00	1.35e+02	1.31e-05	8.06e+01	6.40e-02	1.03e+02	1.08e+01	2.95e+02	yes	1.02e+00	yes	9.42e-02
060502A	-1.43e+00	1.82e+02	4.43e-06	4.57e+01	4.10e-02	3.02e+01	1.27e+01	3.32e+02	yes	1.02e+00	yes	1.26e-01
060510B	-1.41e+00	7.60e+01	4.38e-06	2.23e+01	2.70e-02	2.30e+02	1.05e+01	2.19e+03	no	6.40e+01	no	3.08e-01
060512	-4.67e-01	2.26e+01	2.03e-07	8.10e+00	-5.40e-02	8.37e+00	9.39e+00	4.37e+02	yes	4.10e+00	yes	5.25e-02
060522	-6.85e-01	9.04e+01	1.22e-06	1.65e+01	-1.00e-03	7.41e+01	1.34e+01	3.11e+03	no	6.40e+01	yes	2.28e-01
060526	-1.88e+00	7.33e+01	1.85e-06	2.35e+01	-2.10e-02	2.96e+02	9.05e+00	1.79e+02	yes	5.12e-01	yes	1.81e-01
060605	-2.86e-01	1.28e+02	5.59e-07	1.64e+01	2.00e-02	1.85e+01	7.96e+00	3.63e+02	yes	3.07e+00	yes	1.34e-01
060607A	-1.01e+00	1.39e+02	3.68e-06	5.07e+01	2.00e-02	1.03e+02	1.48e+01	4.90e+02	yes	1.02e+00	yes	1.72e-01
060614	-1.90e+00	3.93e+02	2.82e-05	1.92e+02	1.40e-02	1.09e+02	1.85e+01	5.63e+02	yes	1.02e+00	yes	6.40e-02
060707	-6.56e-01	6.43e+01	1.88e-06	2.01e+01	2.40e-02	7.51e+01	8.58e+00	3.80e+02	yes	4.10e+00	yes	2.01e-01
060708	-9.34e-01	9.05e+01	6.05e-07	3.01e+01	2.80e-02	7.50e+00	8.22e+00	1.61e+02	yes	5.12e-01	yes	1.17e-01
060714	-1.90e+00	5.32e+01	4.30e-06	4.40e+01	5.60e-02	1.19e+02	8.78e+00	3.63e+02	yes	4.10e+00	yes	1.47e-01
060729	-1.79e+00	6.68e+01	4.32e-06	4.47e+01	7.60e-02	1.20e+02	7.13e+00	2.43e+02	yes	4.10e+00	yes	1.74e-01
060807	-1.37e+00	1.65e+02	7.54e-07	9.30e+00	1.06e-01	1.09e+01	1.11e+01	6.14e+02	yes	4.10e+00	no	1.09e-01

Table 2.5 (cont'd): Training Data: Early-Time Metrics from *Swift* GRBs with Known Redshifts.

GRB	$\alpha$	$E_{peak}$	$S$	$S/N_{max}$	$N_{H,pc}$	$T_{90}$	$\sigma_{BAT}$	$R_{peak,BAT}$	Rate trigger	$t_{BAT}$	UVOT detect	$P_{z>4}$
060904B	-9.96e-01	8.32e+01	1.88e-06	3.42e+01	1.30e-01	1.71e+02	8.68e+00	1.62e+02	yes	5.12e-01	yes	1.43e-01
060906	-1.97e+00	4.66e+01	3.56e-06	3.05e+01	2.10e-02	7.30e+01	7.96e+00	1.46e+03	no	6.40e+01	no	1.02e-01
060908	-7.29e-01	1.42e+02	3.81e-06	4.74e+01	1.80e-02	1.85e+01	8.73e+00	2.40e+02	yes	1.02e+00	yes	1.21e-01
060912	-1.70e+00	2.02e+02	2.25e-06	4.35e+01	1.36e-01	5.92e+00	1.99e+01	9.27e+02	yes	1.02e+00	yes	5.79e-02
060926	?	2.02e+01	2.42e-07	1.70e+01	1.62e-01	7.05e+00	1.16e+01	3.71e+02	yes	1.02e+00	no	2.99e-02
060927	-8.20e-01	7.31e+01	1.32e-06	4.31e+01	-2.20e-02	2.30e+01	1.21e+01	2.20e+02	yes	2.56e-01	no	1.24e-01
061007	-9.57e-01	8.38e+02	1.15e-04	3.30e+02	1.18e-01	7.49e+01	1.56e+01	3.84e+02	yes	1.02e+00	yes	3.09e-02
061021	-1.27e+00	4.06e+02	4.95e-06	5.09e+01	4.50e-02	1.21e+01	9.12e+00	2.46e+02	yes	1.02e+00	yes	5.13e-02
061110A	-1.56e+00	1.06e+02	2.01e-06	2.41e+01	-4.70e-02	4.70e+01	7.33e+00	2.86e+02	yes	2.05e+00	no	1.94e-01
061110B	-7.07e-01	5.47e+02	2.46e-06	1.58e+01	1.68e-01	3.24e+01	8.14e+00	3.61e+02	yes	4.10e+00	no	7.19e-02
061121	-1.37e+00	3.46e+02	2.79e-05	2.74e+02	1.18e-01	8.30e+01	8.08e+00	1.10e+02	yes	2.56e-01	yes	3.22e-02
061126	-1.16e+00	3.89e+02	1.39e-05	8.57e+01	1.33e-01	2.68e+01	8.76e+00	2.19e+02	yes	1.02e+00	yes	6.41e-02
061222A	-1.07e+00	2.30e+02	1.45e-05	1.40e+02	3.07e-01	8.17e+01	7.21e+00	3.19e+02	yes	4.10e+00	no	7.98e-02
061222B	-1.94e+00	5.18e+01	3.28e-06	2.26e+01	5.50e-02	4.20e+01	1.08e+01	1.51e+03	no	6.40e+01	no	1.19e-01
070110	-1.15e+00	1.00e+02	1.82e-06	2.59e+01	-3.00e-03	4.77e+01	1.02e+01	4.91e+02	yes	3.07e+00	yes	2.09e-01
070208	-4.46e-01	6.60e+01	5.67e-07	1.03e+01	1.82e-01	5.25e+01	7.29e+00	1.87e+02	yes	1.41e+00	no	1.64e-01
070306	-1.67e+00	1.20e+02	9.04e-06	8.54e+01	3.16e-01	2.61e+02	9.85e+00	7.05e+02	yes	1.22e+01	no	1.26e-01
070318	-1.41e+00	1.96e+02	4.41e-06	4.81e+01	2.30e-01	5.10e+01	1.00e+01	2.01e+02	yes	5.12e-01	yes	1.29e-01
070411	-1.70e+00	1.20e+02	4.23e-06	3.04e+01	-2.80e-02	1.09e+02	1.05e+01	6.00e+02	yes	4.10e+00	yes	2.17e-01
070419A	-2.75e-01	2.69e+01	5.42e-07	1.25e+01	1.60e-01	1.61e+02	1.08e+01	2.49e+03	no	6.40e+01	yes	1.99e-01
070506	5.00e+00	7.08e+01	1.99e-07	8.60e+00	1.52e-01	3.55e+00	8.48e+00	2.08e+03	no	6.40e+01	yes	1.02e-01
070508	-1.00e+00	2.08e+02	3.34e-05	2.62e+02	2.45e-01	2.12e+01	1.99e+01	8.82e+02	yes	1.02e+00	yes	2.03e-02
070518	?	3.50e+01	2.06e-07	1.01e+01	9.10e-02	5.34e+00	7.22e+00	1.97e+02	yes	1.02e+00	yes	9.92e-02
070529	-1.35e+00	2.46e+02	5.22e-06	1.35e+01	1.19e-01	1.12e+02	6.76e+00	4.19e+02	yes	1.22e+01	yes	1.63e-01
070611	6.91e-02	6.70e+01	3.42e-07	1.04e+01	1.20e-02	1.13e+01	9.07e+00	3.84e+02	yes	4.10e+00	yes	1.42e-01
070714B	-1.33e+00	1.65e+02	1.43e-06	3.58e+01	7.30e-02	6.42e+01	1.21e+01	2.25e+02	yes	1.28e-01	yes	7.60e-02
070721B	-1.18e+00	4.06e+02	7.45e-06	2.68e+01	-2.00e-03	3.31e+02	8.36e+00	2.32e+02	yes	2.05e+00	yes	1.16e-01
070802	-1.82e+00	5.49e+01	3.96e-07	7.30e+00	1.40e-02	1.47e+01	7.15e+00	1.47e+03	no	6.40e+01	no	1.59e-01
070810A	-7.46e-01	4.17e+01	5.74e-07	2.46e+01	6.80e-02	7.68e+00	1.27e+01	3.42e+02	yes	1.02e+00	yes	8.05e-02
071025	-1.67e+00	1.65e+02	1.10e-05	8.60e+01	7.30e-02	1.61e+02	1.09e+01	2.04e+03	no	6.40e+01	no	1.74e-01
071031	?	1.23e+01	1.10e-06	1.59e+01	2.40e-02	1.87e+02	9.48e+00	4.55e+02	yes	4.10e+00	yes	1.52e-01
071117	-1.16e+00	1.28e+02	3.40e-06	7.64e+01	1.02e-01	6.48e+00	2.56e+01	2.18e+03	yes	1.02e+00	no	5.35e-02
071122	-1.57e+00	1.11e+02	1.04e-06	1.00e+01	-4.70e-02	7.92e+01	7.13e+00	1.49e+03	no	6.40e+01	yes	2.04e-01
071227	-1.12e+00	3.32e+02	5.26e-07	1.38e+01	2.60e-02	2.20e+00	8.54e+00	2.01e+02	yes	1.02e+00	yes	3.86e-02
080129	-1.22e+00	2.46e+02	1.92e-06	1.16e+01	1.65e-01	4.56e+01	7.51e+00	1.32e+03	no	6.40e+01	no	1.35e-01
080210	-1.75e+00	9.05e+01	2.74e-06	3.66e+01	1.17e-01	4.39e+01	1.79e+01	4.51e+03	no	8.00e+01	yes	1.53e-01
080310	?	2.23e+01	2.69e-06	2.75e+01	5.00e-03	3.62e+02	7.40e+00	2.15e+02	yes	1.02e+00	yes	7.03e-02
080319B	-1.09e+00	1.22e+03	4.11e-04	7.25e+02	5.30e-02	1.47e+02	2.25e+01	1.91e+03	yes	1.02e+00	yes	1.70e-02
080319C	-1.03e+00	1.57e+02	5.38e-06	6.05e+01	7.30e-02	3.29e+01	1.51e+01	4.59e+02	yes	1.02e+00	yes	9.71e-02
080330	?	2.02e+01	4.41e-07	1.34e+01	8.10e-02	6.61e+01	7.58e+00	1.87e+02	yes	1.02e+00	yes	8.62e-02

Table 2.5 (cont'd): Training Data: Early-Time Metrics from *Swift* GRBs with Known Redshifts.

GRB	$\alpha$	$E_{peak}$	$S$	$S/N_{max}$	$N_{H,pc}$	$T_{90}$	$\sigma_{BAT}$	$R_{peak,BAT}$	Rate trigger	$t_{BAT}$	UVOT detect	$P_{z>4}$
080413A	-1.56e+00	1.49e+02	5.88e-06	7.48e+01	6.60e-02	4.66e+01	9.06e+00	2.09e+02	yes	5.12e-01	yes	9.54e-02
080413B	-1.19e+00	6.70e+01	3.70e-06	6.44e+01	9.50e-02	7.04e+00	2.30e+01	1.45e+03	yes	1.02e+00	yes	1.73e-02
080430	-1.74e+00	1.22e+02	1.86e-06	5.27e+01	1.48e-01	1.62e+01	1.08e+01	2.62e+02	yes	5.12e-01	yes	1.07e-01
080520	?	1.11e+01	5.81e-08	8.30e+00	2.05e-01	2.97e+00	8.70e+00	3.48e+02	yes	2.05e+00	yes	2.02e-02
080603B	-1.22e+00	7.05e+01	2.87e-06	7.00e+01	7.10e-02	5.95e+01	1.06e+01	2.13e+02	yes	5.12e-01	yes	8.55e-02
080604	-1.72e+00	7.41e+01	1.45e-06	1.61e+01	-1.80e-02	1.25e+02	1.17e+01	2.76e+03	no	6.40e+01	yes	2.58e-01
080605	-1.13e+00	2.23e+02	2.23e-05	1.58e+02	1.52e-01	1.96e+01	2.58e+01	1.60e+03	yes	1.02e+00	yes	2.90e-02
080607	-1.17e+00	9.03e+02	5.12e-05	1.23e+02	1.42e-01	8.37e+01	1.79e+01	7.41e+02	yes	1.02e+00	yes	2.83e-02
080707	-1.71e+00	7.41e+01	9.67e-07	1.72e+01	-3.20e-02	3.03e+01	9.84e+00	2.88e+02	yes	1.02e+00	yes	1.39e-01
080710	-1.26e+00	3.00e+02	3.24e-06	1.26e+01	4.20e-02	1.39e+02	8.57e+00	3.87e+02	yes	4.10e+00	yes	1.77e-01
080721	-9.51e-01	6.05e+02	3.41e-05	3.72e+01	5.80e-02	2.99e+01	1.02e+01	2.71e+02	yes	1.02e+00	yes	3.66e-02
080804	-1.03e+00	4.06e+02	9.02e-06	3.11e+01	9.00e-03	6.17e+01	7.49e+00	1.43e+02	yes	1.02e+00	yes	8.18e-02
080805	-1.54e+00	3.00e+02	4.47e-06	4.97e+01	1.94e-01	1.12e+02	8.81e+00	2.24e+02	yes	1.02e+00	no	1.59e-01
080810	-1.31e+00	3.67e+02	9.71e-06	5.79e+01	1.40e-02	4.53e+02	7.59e+00	1.96e+02	yes	1.02e+00	yes	1.55e-01
080905B	-1.67e+00	8.19e+01	2.78e-06	2.28e+01	1.93e-01	1.04e+02	8.01e+00	2.59e+02	yes	2.05e+00	yes	1.98e-01
080913	-4.05e-01	1.35e+02	7.60e-07	1.67e+01	3.80e-02	8.19e+00	9.39e+00	2.00e+02	yes	1.02e+00	no	9.52e-02
080916A	-1.08e+00	1.05e+02	5.55e-06	8.93e+01	1.84e-01	6.25e+01	2.03e+01	8.60e+02	yes	1.02e+00	yes	1.41e-01
080928	-1.73e+00	7.41e+01	3.96e-06	3.98e+01	6.40e-02	2.85e+02	8.92e+00	2.44e+03	no	1.12e+02	yes	2.02e-01
081007	-1.35e+00	2.73e+01	5.91e-07	1.96e+01	2.67e-01	5.55e+00	9.43e+00	2.21e+02	yes	1.02e+00	yes	2.56e-02
081008	-1.30e+00	9.05e+01	5.61e-06	5.07e+01	4.40e-02	1.99e+02	1.00e+01	3.82e+02	yes	2.05e+00	yes	2.06e-01
081028A	-1.31e+00	6.70e+01	4.32e-06	4.20e+01	1.80e-02	2.76e+02	1.80e+01	6.72e+03	no	1.28e+02	yes	2.85e-01
081029	-1.43e+00	3.00e+02	3.34e-06	1.60e+01	1.90e-02	1.69e+02	1.15e+01	2.14e+03	no	6.40e+01	yes	2.18e-01
081118	?	3.68e+01	1.57e-06	1.98e+01	-4.10e-02	6.66e+01	1.50e+01	3.30e+03	no	6.40e+01	no	1.54e-01
081121	-5.21e-01	1.82e+02	7.88e-06	2.44e+01	2.60e-02	1.94e+01	9.79e+00	2.41e+02	yes	4.10e+00	yes	8.97e-02
081203A	-1.44e+00	2.01e+02	1.36e-05	8.03e+01	5.80e-02	2.54e+02	7.56e+00	1.87e+02	yes	1.02e+00	yes	1.58e-01
081222	-1.04e+00	1.35e+02	7.31e-06	1.48e+02	3.10e-02	3.35e+01	8.08e+00	1.15e+02	yes	2.56e-01	yes	5.65e-02
090102	-1.36e+00	3.67e+02	1.42e-05	3.55e+01	7.90e-02	3.07e+01	9.37e+00	2.39e+02	yes	2.05e+00	yes	7.98e-02
090205	-8.90e-01	3.33e+01	1.92e-07	1.30e+01	4.10e-02	1.07e+01	8.16e+00	3.97e+02	yes	4.10e+00	no	1.26e-01
090418A	-1.39e+00	3.32e+02	8.70e-06	5.24e+01	1.95e-01	5.80e+01	8.16e+00	1.63e+02	yes	1.02e+00	yes	1.26e-01
090423	-7.00e-01	5.22e+01	6.66e-07	3.13e+01	7.10e-02	1.24e+01	8.16e+00	2.03e+02	yes	1.02e+00	no	1.37e-01
090424	-1.08e+00	1.28e+02	2.84e-05	1.32e+02	1.95e-01	5.03e+01	2.33e+01	3.35e+03	yes	1.02e+00	yes	9.01e-03
090516A	-1.56e+00	1.35e+02	1.49e-05	2.40e+01	5.50e-02	2.28e+02	8.83e+00	5.54e+02	yes	2.69e+01	no	1.54e-01
090519	-9.81e-01	4.06e+02	3.25e-06	1.52e+01	-3.20e-02	8.18e+01	8.61e+00	6.47e+02	yes	1.22e+01	no	1.08e-01
090529	-8.03e-01	4.27e+01	1.10e-06	1.77e+01	7.00e-03	7.98e+01	8.87e+00	1.73e+03	no	6.40e+01	yes	2.00e-01
090618	-1.29e+00	1.38e+02	1.48e-04	7.20e+02	9.70e-02	1.15e+02	2.26e+01	1.10e+03	yes	1.02e+00	yes	2.61e-02
090715B	-1.61e+00	1.82e+02	8.99e-06	8.49e+01	7.10e-02	2.68e+02	1.15e+01	3.32e+02	yes	1.02e+00	yes	1.21e-01
090809	-1.70e+00	7.41e+01	9.22e-07	1.18e+01	7.30e-02	1.93e+02	8.62e+00	3.39e+02	yes	4.10e+00	yes	1.23e-01
090812	-1.29e+00	2.72e+02	1.17e-05	7.85e+01	2.30e-02	9.98e+01	1.03e+01	2.60e+02	yes	1.02e+00	yes	1.29e-01
090814A	-6.80e-01	4.49e+01	1.29e-06	1.37e+01	-7.90e-02	1.13e+02	1.00e+01	1.84e+03	no	8.80e+01	yes	2.17e-01
090926B	-4.64e-01	8.19e+01	7.75e-06	6.33e+01	1.68e-01	1.26e+02	6.74e+00	1.56e+02	yes	1.02e+00	no	1.07e-01

Table 2.5 (cont'd): Training Data: Early-Time Metrics from *Swift* GRBs with Known Redshifts.

GRB	$\alpha$	$E_{peak}$	$S$	$S/N_{max}$	$N_{H,pc}$	$T_{90}$	$\sigma_{BAT}$	$R_{peak,BAT}$	Rate trigger	$t_{BAT}$	UVOT detect	$P_{z>4}$
090927	-1.77e+00	6.07e+01	4.94e-07	1.43e+01	7.10e-02	1.84e+01	1.14e+01	2.36e+02	yes	5.12e-01	yes	8.05e-02
091018	-1.69e+00	2.86e+01	1.46e-06	8.33e+01	5.50e-02	4.44e+00	1.15e+01	2.00e+02	yes	2.56e-01	yes	9.35e-03
091020	-1.24e+00	1.22e+02	5.17e-06	5.58e+01	7.90e-02	3.90e+01	1.77e+01	5.20e+02	yes	1.02e+00	yes	1.04e-01
091029	-1.40e+00	5.63e+01	2.84e-06	6.84e+01	4.00e-02	4.00e+01	9.18e+00	2.43e+02	yes	1.02e+00	yes	9.92e-02
091109A	-1.23e+00	4.48e+02	3.62e-06	1.30e+01	6.90e-02	4.97e+01	7.64e+00	4.94e+02	yes	1.64e+01	yes	1.01e-01
091127	?	2.73e+01	1.24e-05	5.07e+01	3.60e-02	9.57e+00	1.80e+01	6.60e+02	yes	1.02e+00	yes	4.87e-03
091208B	-1.28e+00	7.05e+01	3.83e-06	2.95e+01	2.19e-01	1.52e+01	9.31e+00	1.68e+02	yes	1.02e+00	yes	3.32e-02
100219A	-1.37e+00	1.22e+02	8.45e-07	1.04e+01	-1.20e-02	3.10e+01	7.44e+00	1.43e+03	no	6.40e+01	yes	1.42e-01
100302A	?	4.27e+01	5.32e-07	1.52e+01	1.80e-02	3.17e+01	7.73e+00	1.50e+03	no	6.40e+01	no	1.95e-01
100316B	?	2.86e+01	2.51e-07	1.80e+01	-5.50e-02	4.30e+00	9.10e+00	1.89e+02	yes	5.12e-01	yes	5.86e-02
100316D	?	2.73e+01	2.23e-06	7.60e+00	1.13e+00	4.22e+02	7.83e+00	1.84e+03	no	6.40e+01	no	1.81e-01
100418A	?	3.68e+01	4.78e-07	1.33e+01	4.70e-02	9.63e+00	7.06e+00	1.77e+02	yes	1.02e+00	yes	1.04e-01
100425A	-5.26e-01	2.35e+01	4.11e-07	1.48e+01	5.40e-02	4.36e+01	9.39e+00	2.38e+02	yes	1.02e+00	no	4.16e-02
100513A	-1.65e+00	8.19e+01	2.08e-06	2.33e+01	1.40e-02	6.51e+01	1.04e+01	9.28e+02	yes	1.22e+01	no	2.28e-01
100621A	-1.59e+00	6.70e+01	2.38e-05	2.95e+02	5.94e-01	6.63e+01	1.87e+01	8.13e+02	yes	1.02e+00	yes	4.88e-02



Table 2.6: Test Data: Early-Time Metrics from *Swift* GRBs with unknown Redshifts.

GRB	$\hat{Q}$	$\alpha$	$E_{peak}$	$S$	$S/N_{max}$	$N_{H,pc}$	$T_{90}$	$\sigma_{BAT}$	$N_{peak,BAT}$	Rate trigger	$t_{BAT}$	UVOT detect	$P_{z>4}$
050215A	3.19e-01	-1.29e+00	4.14e+02	1.34e-06	1.02e+01	?	6.65e+01	9.00e+00	6.94e+02	yes	8.19e+00	no	9.81e-02
050215B	1.78e-01	?	3.01e+01	2.86e-07	1.44e+01	5.70e-02	8.50e+00	8.00e+00	3.00e+02	yes	2.05e+00	no	1.06e-01
050219A	4.22e-01	1.87e-02	1.00e+02	4.91e-06	5.08e+01	9.10e-02	2.50e+01	8.00e+00	1.93e+02	yes	1.02e+00	no	1.12e-01
050219B	7.33e-01	-8.94e-01	1.12e+02	1.94e-05	7.19e+01	8.80e-02	2.09e+01	1.70e+01	4.09e+02	yes	1.02e+00	no	2.73e-02
050326	7.04e-01	-1.04e+00	3.41e+02	1.70e-05	1.33e+02	3.80e-02	3.02e+01	2.10e+01	1.84e+04	yes	5.12e-01	no	5.67e-02
050406	8.44e-01	2.68e+00	2.47e+01	7.05e-08	8.00e+00	-8.10e-02	5.34e+00	8.00e+00	2.97e+02	yes	2.05e+00	yes	8.68e-02
050412	6.59e-01	-6.56e-01	6.05e+02	1.67e-06	1.37e+01	-3.00e-02	1.39e+01	9.00e+00	3.29e+02	yes	2.05e+00	no	5.38e-02
050421	7.11e-01	-1.27e+00	1.82e+02	1.67e-07	5.00e+00	3.73e-01	5.32e+00	6.00e+00	3.79e+02	yes	5.50e+00	no	7.93e-02
050422	1.85e-01	-1.36e+00	1.50e+02	1.23e-06	1.40e+01	-5.52e-01	5.95e+01	8.00e+00	7.84e+02	yes	1.22e+01	no	1.33e-01
050502B	5.93e-02	-1.58e+00	1.00e+02	8.06e-07	2.53e+01	-3.00e-03	1.74e+01	1.30e+01	5.00e+02	yes	1.02e+00	no	1.09e-01
050509A	1.63e-01	?	4.20e+01	4.57e-07	2.33e+01	1.11e+00	1.18e+01	9.00e+00	3.19e+02	yes	1.02e+00	no	1.24e-01
050712	1.33e-01	-1.44e+00	1.83e+02	2.19e-06	1.63e+01	4.20e-02	5.73e+01	8.89e+00	1.24e+03	yes	2.69e+01	yes	1.64e-01
050713A	6.59e-01	-1.46e+00	2.35e+02	9.36e-06	7.28e+01	2.27e-01	1.25e+02	1.13e+01	2.15e+02	yes	5.12e-01	no	9.01e-02
050713B	3.70e-02	-1.34e+00	1.65e+02	9.39e-06	1.43e+01	2.33e-01	1.33e+02	7.04e+00	2.66e+02	yes	1.22e+01	no	1.68e-01
050714B	3.19e-01	?	2.42e+01	7.43e-07	1.02e+01	2.28e-01	6.06e+01	1.01e+01	1.63e+03	no	6.40e+01	no	1.03e-01
050716	7.41e-03	-7.99e-01	1.36e+02	8.66e-06	2.07e+01	5.90e-02	6.42e+01	8.00e+00	2.03e+02	yes	2.05e+00	no	1.73e-01
050717	8.37e-01	-1.15e+00	8.32e+02	1.36e-05	8.07e+01	9.10e-02	7.94e+01	8.53e+00	6.30e+01	yes	6.40e-02	no	5.68e-02
050726	4.44e-01	-1.08e+00	4.03e+02	5.40e-06	1.43e+01	2.20e-02	1.91e+02	8.32e+00	3.85e+02	yes	8.19e+00	yes	1.19e-01
050815	8.74e-01	-1.99e+00	4.20e+01	1.42e-07	9.60e+00	-1.59e-01	3.03e+00	8.78e+00	3.70e+02	yes	2.05e+00	no	9.21e-02
050819	6.59e-01	-6.58e-01	2.04e+01	3.29e-07	1.10e+01	-2.70e-02	4.68e+01	8.79e+00	1.31e+03	yes	2.69e+01	no	8.39e-02
050820B	3.04e-01	-5.74e-01	1.16e+02	2.84e-06	8.07e+01	2.88e-01	1.27e+01	8.76e+00	2.65e+02	yes	1.02e+00	no	1.10e-01
050822	6.37e-01	?	2.79e+01	3.13e-06	3.17e+01	7.60e-02	1.05e+02	9.73e+00	4.25e+02	yes	2.05e+00	no	5.77e-02
050915A	2.00e-01	-1.31e+00	1.65e+02	1.28e-06	1.26e+01	8.80e-02	2.14e+01	7.68e+00	1.86e+02	yes	1.02e+00	no	1.15e-01
050915B	5.63e-01	-1.30e+00	6.17e+01	3.94e-06	6.06e+01	-1.89e-01	4.12e+01	2.34e+01	9.11e+03	no	6.40e+01	no	1.08e-01
050916	4.07e-01	-1.79e+00	5.49e+01	1.23e-06	8.50e+00	3.21e-01	4.26e+01	8.77e+00	2.19e+03	no	1.20e+02	no	2.13e-01
050922B	2.07e-01	?	3.85e+01	3.27e-06	1.46e+01	6.60e-02	2.52e+02	8.66e+00	1.87e+03	no	1.68e+02	no	9.60e-02
051001	7.41e-03	-1.12e+00	4.27e+01	9.91e-07	2.11e+01	1.59e-01	5.59e+01	7.29e+00	1.40e+03	no	6.40e+01	no	2.06e-01
051006	2.00e-01	-1.42e+00	2.69e+02	2.31e-06	1.73e+01	5.48e-01	2.65e+01	7.25e+00	2.54e+02	yes	4.10e+00	no	9.85e-02
051008	3.78e-01	-7.98e-01	2.66e+02	1.02e-05	6.21e+01	3.12e-01	4.51e+01	9.65e+00	2.20e+02	yes	1.02e+00	no	9.55e-02
051016A	1.26e-01	-1.57e+00	1.01e+02	1.15e-06	1.20e+01	1.46e-01	7.44e+00	9.72e+00	3.19e+02	yes	4.10e+00	no	1.08e-01
051021B	4.00e-01	-3.58e-01	9.88e+01	9.15e-07	1.88e+01	-1.58e-01	3.35e+01	6.77e+00	1.81e+02	yes	1.02e+00	no	1.75e-01
051117A	7.33e-01	-1.76e+00	7.57e+01	7.38e-06	5.38e+01	9.20e-02	2.38e+02	1.28e+01	6.43e+02	yes	4.10e+00	yes	2.33e-01
051117B	4.52e-01	-1.72e+00	7.24e+01	3.02e-07	8.40e+00	3.20e-01	1.04e+01	6.47e+00	3.52e+02	yes	5.50e+00	no	1.26e-01
051221B	7.41e-03	-1.42e+00	1.35e+02	2.11e-06	1.40e+01	4.25e-01	5.88e+01	7.45e+00	2.39e+03	no	1.92e+02	no	1.73e-01
060105	8.74e-01	-1.07e+00	6.20e+02	4.39e-05	1.34e+02	1.78e-01	5.52e+01	1.44e+01	4.50e+02	yes	1.02e+00	no	5.92e-02
060109	1.63e-01	4.41e+00	4.97e+01	7.09e-07	1.31e+01	2.45e-01	1.13e+02	7.10e+00	5.45e+02	yes	8.19e+00	no	1.99e-01
060111A	5.63e-01	-7.87e-01	8.31e+01	1.49e-06	4.92e+01	1.25e-01	1.53e+01	7.47e+00	1.49e+02	yes	5.12e-01	yes	1.58e-01
060111B	9.41e-01	-8.58e-01	5.41e+02	4.93e-06	1.98e+01	2.46e-01	6.14e+01	6.97e+00	1.45e+02	yes	1.02e+00	yes	7.91e-02
060203	7.41e-03	-1.51e+00	1.05e+02	1.66e-06	1.20e+01	5.40e-02	8.37e+01	8.16e+00	1.57e+03	no	8.00e+01	no	2.08e-01
060204B	2.96e-01	-6.92e-01	1.11e+02	3.16e-06	4.32e+01	1.10e-01	4.07e+01	8.49e+00	3.17e+02	yes	2.05e+00	yes	1.90e-01

Table 2.6 (cont'd): Test Data: Early-Time Metrics from *Swift* GRBs with unknown Redshifts.

GRB	$\hat{Q}$	$\alpha$	$E_{peak}$	$S$	$S/N_{max}$	$N_{H,pc}$	$T_{90}$	$\sigma_{BAT}$	$N_{peak,BAT}$	Rate trigger	$t_{BAT}$	UVOT detect	$P_{z>4}$
060211A	1.26e-01	-9.91e-01	4.27e+01	5.22e-07	8.30e+00	6.00e-02	2.86e+01	1.26e+01	4.08e+03	no	1.28e+02	no	2.24e-01
060211B	3.33e-01	-1.74e+00	6.07e+01	4.42e-07	1.19e+01	-2.00e-03	1.11e+01	9.03e+00	3.15e+02	yes	2.05e+00	no	1.46e-01
060219	7.11e-01	2.48e-01	2.12e+01	1.31e-07	6.60e+00	2.92e-01	8.84e+00	7.20e+00	5.37e+02	yes	8.19e+00	no	9.20e-02
060306	6.96e-01	-1.13e+00	6.38e+01	2.36e-06	4.25e+01	2.89e-01	6.10e+01	2.00e+01	8.25e+02	yes	1.02e+00	no	6.71e-02
060319	6.89e-01	?	2.47e+01	2.34e-07	1.32e+01	3.51e-01	5.28e+00	9.87e+00	1.98e+03	no	7.20e+01	no	6.70e-02
060323	1.63e-01	-1.47e+00	1.46e+02	1.03e-06	6.80e+00	6.50e-02	1.76e+01	9.72e+00	4.75e+02	yes	4.10e+00	yes	1.21e-01
060403	3.19e-01	-4.41e-01	2.47e+02	2.23e-06	2.22e+01	-1.90e-01	2.64e+01	9.60e+00	2.24e+02	yes	1.02e+00	no	1.02e-01
060413	5.19e-02	-1.66e+00	1.11e+02	6.00e-06	5.84e+01	1.20e+00	1.21e+02	7.26e+00	1.71e+03	no	6.40e+01	no	2.08e-01
060421	3.26e-01	-1.11e+00	1.18e+02	1.67e-06	4.21e+01	9.40e-02	1.11e+01	8.34e+00	1.33e+02	yes	2.56e-01	no	1.08e-01
060427	3.19e-01	-1.75e+00	6.93e+01	6.46e-07	6.20e+00	7.50e-02	4.31e+01	9.47e+00	1.80e+03	no	6.40e+01	no	2.08e-01
060428A	6.81e-01	-1.49e+00	4.54e+01	1.61e-06	3.79e+01	1.79e-01	5.26e+01	7.35e+00	1.89e+02	yes	1.02e+00	no	8.63e-02
060501	5.63e-01	-1.23e+00	2.17e+02	2.63e-06	2.23e+01	5.13e-01	1.22e+01	1.11e+01	2.63e+02	yes	1.02e+00	no	8.72e-02
060507	3.63e-01	-1.68e+00	8.19e+01	3.22e-06	1.57e+01	4.80e-02	5.21e+01	7.19e+00	1.42e+02	yes	1.02e+00	no	2.16e-01
060510A	8.15e-01	-1.77e+00	7.40e+01	1.67e-05	2.78e+01	-9.00e-03	2.19e+01	9.16e+00	1.96e+02	yes	1.02e+00	yes	2.83e-02
060515	3.41e-01	5.60e-03	2.40e+02	2.04e-06	1.73e+01	-1.09e-01	5.98e+01	7.76e+00	3.97e+02	yes	8.19e+00	no	1.33e-01
060728	5.19e-02	-1.52e+00	9.53e+01	3.21e-07	5.50e+00	?	3.90e+01	7.18e+00	1.45e+03	no	6.40e+01	no	1.46e-01
060804	2.67e-01	-1.67e+00	7.41e+01	7.23e-07	8.60e+00	-8.00e-03	8.41e+00	8.92e+00	3.95e+02	yes	8.19e+00	yes	1.35e-01
060805A	4.96e-01	5.00e+00	3.01e+01	5.45e-08	6.70e+00	1.01e-01	1.11e+01	7.64e+00	4.11e+02	yes	4.10e+00	no	9.66e-02
060813	7.56e-01	-9.54e-01	1.88e+02	9.11e-06	1.02e+02	1.02e-01	1.58e+01	7.17e+00	8.30e+01	yes	2.56e-01	no	5.80e-02
060814	7.48e-01	-1.29e+00	2.01e+02	2.38e-05	1.74e+02	2.85e-01	1.59e+02	1.56e+01	4.92e+02	yes	1.02e+00	no	9.01e-02
060825	2.07e-01	-1.23e+00	8.05e+01	1.28e-06	4.73e+01	-1.70e-02	8.55e+00	2.01e+01	9.50e+02	yes	1.02e+00	no	1.31e-01
060904A	3.63e-01	-1.27e+00	1.73e+02	1.17e-05	1.27e+02	1.84e-01	7.52e+01	7.71e+00	2.10e+02	yes	1.02e+00	no	1.01e-01
060919	4.52e-01	-1.78e+00	6.61e+01	7.67e-07	1.72e+01	6.00e-01	4.70e+00	9.13e+00	2.22e+02	yes	1.02e+00	no	1.04e-01
060923A	2.15e-01	-3.71e-01	4.97e+01	8.40e-07	1.06e+01	6.40e-02	5.70e+01	7.22e+00	1.62e+02	yes	1.02e+00	no	1.40e-01
060923B	5.78e-01	?	2.14e+01	5.68e-07	1.30e+01	-5.00e-03	8.91e+00	9.40e+00	4.64e+02	yes	4.10e+00	no	3.29e-02
060929	5.19e-01	-1.94e+00	4.48e+01	1.13e-06	1.10e+01	3.70e-02	5.50e+02	8.67e+00	4.40e+02	yes	4.10e+00	no	1.98e-01
061002	7.41e-03	-1.65e+00	9.82e+01	1.40e-06	1.30e+01	1.73e-01	2.26e+01	8.16e+00	4.53e+02	yes	8.19e+00	no	1.60e-01
061019	4.00e-01	?	4.62e+01	3.49e-06	1.26e+01	5.69e-01	1.90e+02	7.37e+00	1.92e+02	yes	4.10e+00	no	9.86e-02
061027	5.63e-01	-1.79e+00	1.19e+02	4.40e-07	4.60e+00	?	1.08e+01	7.05e+00	1.45e+03	no	6.40e+01	no	1.11e-01
061028	3.04e-01	-1.69e+00	7.94e+01	1.64e-06	1.05e+01	2.94e-01	1.22e+02	8.10e+00	1.82e+03	no	1.28e+02	no	2.27e-01
061102	2.52e-01	5.00e+00	1.00e+02	2.79e-07	6.10e+00	4.28e-01	2.45e+01	6.75e+00	5.67e+02	yes	1.22e+01	no	1.48e-01
061202	1.63e-01	-1.20e+00	1.16e+02	5.09e-06	8.55e+01	4.13e-01	1.25e+02	6.94e+00	3.45e+02	yes	4.10e+00	no	1.45e-01
061218	7.63e-01	?	1.31e+01	6.22e-08	5.30e+00	?	6.36e+00	6.71e+00	3.81e+02	yes	4.10e+00	no	7.42e-02
070103	6.37e-01	-1.82e+00	5.82e+01	3.37e-07	9.10e+00	1.95e-01	1.09e+01	9.86e+00	1.96e+02	yes	5.12e-01	no	1.17e-01
070107	6.59e-01	-1.13e+00	6.31e+02	1.20e-05	4.82e+01	8.50e-02	3.58e+02	1.73e+01	4.81e+03	no	9.60e+01	yes	9.53e-02
070126	4.07e-01	2.23e+00	3.30e+01	1.24e-07	4.60e+00	?	8.90e+00	7.04e+00	1.37e+03	no	6.40e+01	no	1.01e-01
070219	4.74e-01	-1.87e+00	5.65e+01	3.61e-07	1.23e+01	3.05e-01	9.60e+00	7.61e+00	2.80e+02	yes	2.05e+00	no	1.44e-01
070220	7.48e-01	-1.29e+00	4.92e+02	2.08e-05	1.15e+02	1.87e-01	1.51e+02	1.05e+01	2.96e+02	yes	1.02e+00	no	9.05e-02
070223	5.19e-02	-1.21e+00	6.11e+01	1.74e-06	1.46e+01	6.06e-01	7.63e+01	7.24e+00	3.36e+02	yes	3.07e+00	no	2.41e-01
070224	3.48e-01	?	2.96e+01	3.33e-07	9.50e+00	-7.70e-02	2.40e+01	7.50e+00	1.51e+03	no	6.40e+01	no	1.48e-01

Table 2.6 (cont'd): Test Data: Early-Time Metrics from *Swift* GRBs with unknown Redshifts.

GRB	$\hat{Q}$	$\alpha$	$E_{peak}$	$S$	$S/N_{max}$	$N_{H,pc}$	$T_{90}$	$\sigma_{BAT}$	$N_{peak,BAT}$	Rate trigger	$t_{BAT}$	UVOT detect	$P_{z>4}$
070328	8.30e-01	-1.14e+00	4.59e+02	1.96e-05	1.10e+02	1.78e-01	4.96e+01	1.65e+01	6.55e+02	yes	1.02e+00	no	7.94e-02
070330	5.63e-01	3.40e+00	3.33e+01	1.92e-07	1.11e+01	2.20e-02	6.79e+00	1.03e+01	3.08e+02	yes	1.02e+00	yes	9.41e-02
070412	3.04e-01	-1.46e+00	1.15e+02	9.14e-07	1.49e+01	2.00e-01	3.43e+01	7.32e+00	1.50e+02	yes	5.12e-01	no	1.30e-01
070419B	3.26e-01	-1.36e+00	1.49e+02	1.00e-05	8.46e+01	7.00e-02	1.34e+02	7.02e+00	1.73e+02	yes	1.02e+00	no	1.92e-01
070420	9.33e-01	-9.98e-01	1.58e+02	2.42e-05	6.37e+01	?	9.59e+01	1.09e+01	3.31e+02	yes	2.05e+00	yes	7.89e-02
070429A	7.41e-03	?	3.29e+01	7.05e-07	1.28e+01	5.00e-02	3.58e+01	1.21e+01	3.01e+03	no	8.00e+01	no	1.52e-01
070509	3.56e-01	?	3.85e+01	1.79e-07	1.08e+01	2.69e-01	4.75e+00	8.66e+00	2.45e+02	yes	1.02e+00	no	1.09e-01
070520A	1.78e-01	-1.94e-01	7.41e+01	3.31e-07	7.50e+00	1.25e-01	3.14e+01	7.99e+00	1.84e+03	no	8.80e+01	no	1.68e-01
070520B	3.93e-01	-1.13e+00	3.67e+02	2.48e-06	8.50e+00	2.87e-01	3.13e+01	7.32e+00	3.07e+02	yes	4.10e+00	no	1.12e-01
070521	8.59e-01	-1.35e+00	3.00e+02	1.64e-05	1.19e+02	5.22e-01	5.61e+02	1.15e+01	3.31e+02	yes	1.02e+00	no	7.65e-02
070531	2.07e-01	-1.36e+00	1.65e+02	2.04e-06	1.44e+01	-2.95e-01	3.72e+01	1.02e+01	4.93e+02	yes	4.10e+00	no	1.26e-01
070612B	1.78e-01	-8.01e-01	9.05e+01	2.09e-06	2.42e+01	4.62e-01	1.55e+01	9.09e+00	1.82e+02	yes	1.02e+00	no	1.27e-01
070616	4.00e-01	-1.33e+00	1.49e+02	2.89e-05	1.49e+02	7.70e-02	4.44e+02	8.92e+00	1.71e+03	no	6.40e+01	yes	1.81e-01
070621	3.04e-01	-1.55e+00	1.57e+02	7.79e-06	4.88e+01	3.76e-01	3.61e+01	9.01e+00	1.95e+02	yes	1.02e+00	no	1.38e-01
070628	9.48e-01	-1.90e+00	6.38e+01	5.11e-06	5.05e+01	6.60e-02	1.33e+01	1.21e+01	4.66e+02	yes	1.02e+00	yes	6.53e-02
070704	3.19e-01	-1.59e+00	2.23e+02	9.61e-06	7.42e+01	1.17e-01	3.85e+02	1.61e+01	2.91e+03	no	6.40e+01	no	1.66e-01
070714A	8.74e-01	?	1.74e+01	1.68e-07	2.15e+01	5.46e-01	2.56e+00	1.24e+01	2.98e+02	yes	5.12e-01	no	1.13e-02
070721A	9.33e-01	?	1.50e+01	7.29e-08	6.90e+00	1.60e-01	3.40e+00	8.23e+00	2.17e+02	yes	1.02e+00	yes	3.16e-02
070805	1.11e-01	-1.55e+00	2.01e+02	1.13e-06	6.90e+00	2.27e-01	2.25e+01	9.19e+00	4.41e+02	yes	4.10e+00	no	1.29e-01
070808	3.70e-02	-1.47e+00	1.35e+02	2.33e-06	2.43e+01	5.59e-01	5.72e+01	1.32e+01	3.60e+02	yes	1.02e+00	no	1.24e-01
071028A	1.11e-01	-1.19e-01	5.77e+01	3.29e-07	1.09e+01	1.10e-02	3.63e+01	8.74e+00	1.96e+03	no	6.40e+01	no	2.01e-01
071101	7.48e-01	?	3.01e+01	8.36e-08	7.80e+00	1.05e-01	3.72e+00	6.51e+00	2.55e+02	yes	2.05e+00	no	7.46e-02
071118	3.48e-01	-1.67e+00	7.41e+01	6.79e-07	8.30e+00	1.57e-01	5.66e+01	7.67e+00	1.68e+03	no	6.40e+01	yes	1.86e-01
080123	5.56e-01	?	4.49e+01	1.80e-07	5.30e+00	1.98e-01	2.57e+01	7.04e+00	5.20e+01	yes	6.40e-02	no	1.41e-01
080205	9.19e-01	-1.96e+00	4.97e+01	2.93e-06	3.36e+01	9.90e-02	1.13e+02	8.53e+00	1.89e+02	yes	1.02e+00	yes	1.60e-01
080207	3.56e-01	-1.05e+00	1.00e+02	8.69e-06	6.19e+01	6.16e-01	3.11e+02	1.58e+01	3.86e+03	no	6.40e+01	no	2.41e-01
080212	3.93e-01	-3.56e-01	7.41e+01	3.61e-06	2.47e+01	1.29e-01	1.32e+02	7.18e+00	3.01e+02	yes	4.10e+00	yes	2.42e-01
080218B	7.56e-01	7.88e-01	1.65e+01	5.07e-07	1.11e+01	3.49e-01	6.30e+00	7.25e+00	2.08e+02	yes	4.10e+00	no	1.04e-02
080229A	7.93e-01	-1.87e+00	9.51e+01	1.28e-05	1.12e+02	1.85e-01	5.02e+01	1.03e+01	1.94e+02	yes	1.02e+00	no	4.86e-02
080303	4.96e-01	-1.55e+00	1.82e+02	9.76e-07	1.75e+01	-1.00e-03	4.47e+01	7.67e+00	1.33e+02	yes	5.12e-01	yes	1.02e-01
080307	2.67e-01	-1.68e+00	9.05e+01	1.37e-06	1.69e+01	1.21e-01	9.78e+01	7.15e+00	4.48e+02	yes	8.19e+00	no	2.20e-01
080315	7.33e-01	5.00e+00	1.65e+01	1.02e-07	4.70e+00	?	4.15e+00	7.51e+00	1.57e+03	no	6.40e+01	no	5.32e-02
080319A	2.07e-01	-1.64e+00	1.05e+02	7.19e-06	2.39e+01	9.40e-02	4.56e+01	7.23e+00	3.95e+02	yes	1.22e+01	yes	1.44e-01
080319D	4.00e-01	3.93e+00	3.68e+01	2.16e-07	8.30e+00	7.50e-02	3.04e+01	7.22e+00	1.60e+03	no	6.40e+01	yes	1.72e-01
080320	7.41e-03	-1.61e+00	9.51e+01	5.64e-07	1.36e+01	5.30e-02	2.14e+01	7.64e+00	2.45e+02	yes	1.41e+00	no	1.40e-01
080325	2.96e-02	-1.67e+00	1.11e+02	7.67e-06	1.81e+01	-4.00e-03	1.84e+02	7.46e+00	9.87e+02	no	6.40e+01	no	2.23e-01
080328	9.78e-01	-1.36e+00	6.05e+02	1.79e-05	8.37e+01	1.21e-01	9.10e+01	1.53e+01	4.87e+02	yes	1.02e+00	yes	8.16e-02
080409	6.89e-01	-1.15e+00	4.07e+01	5.17e-07	2.47e+01	1.89e-01	9.94e+00	1.41e+01	2.60e+02	yes	5.12e-01	no	4.08e-02
080503	7.19e-01	-1.94e+00	4.97e+01	2.75e-06	3.45e+01	-8.40e-02	1.79e+02	8.79e+00	7.50e+01	yes	6.40e-02	no	1.91e-01
080506	7.19e-01	-1.74e+00	6.70e+01	1.97e-06	1.93e+01	-2.80e-02	1.52e+02	7.18e+00	1.48e+03	no	6.40e+01	yes	2.61e-01

Table 2.6 (cont'd): Test Data: Early-Time Metrics from *Swift* GRBs with unknown Redshifts.

GRB	$\hat{Q}$	$\alpha$	$E_{peak}$	$S$	$S/N_{max}$	$N_{H,pc}$	$T_{90}$	$\sigma_{BAT}$	$N_{peak,BAT}$	Rate trigger	$t_{BAT}$	UVOT detect	$P_{z>4}$
080516	6.59e-01	-1.78e+00	6.70e+01	5.01e-07	1.19e+01	6.40e-01	6.84e+00	8.61e+00	1.49e+02	yes	5.12e-01	no	9.54e-02
080517	7.41e-03	-1.51e+00	1.00e+02	8.68e-07	1.12e+01	2.56e-01	2.69e+01	9.81e+00	6.15e+02	yes	8.19e+00	no	1.36e-01
080602	3.70e-02	-1.51e+00	1.16e+02	6.09e-06	3.95e+01	1.12e-01	8.51e+01	8.11e+00	2.33e+02	yes	2.05e+00	no	1.22e-01
080613B	5.63e-01	-1.36e+00	5.47e+02	1.06e-05	9.44e+01	-1.70e-02	8.32e+01	1.13e+01	2.41e+02	yes	2.56e-01	no	8.76e-02
080623	5.63e-01	-1.36e+00	1.82e+02	2.04e-06	2.15e+01	1.08e-01	1.61e+01	7.53e+00	1.16e+02	yes	5.12e-01	no	9.23e-02
080701	6.67e-01	?	4.27e+01	9.15e-07	2.67e+01	6.08e-01	9.35e+00	1.61e+01	4.49e+02	yes	1.02e+00	no	6.85e-02
080703	7.93e-01	-1.72e+00	6.38e+01	3.49e-07	1.08e+01	1.80e-02	4.20e+00	7.30e+00	1.68e+02	yes	1.02e+00	yes	9.61e-02
080714	4.96e-01	-1.44e+00	1.49e+02	4.79e-06	4.49e+01	-1.20e-02	3.42e+01	1.74e+01	5.76e+02	yes	1.02e+00	yes	1.06e-01
080723A	2.07e-01	5.00e+00	7.41e+01	5.22e-07	1.40e+01	5.70e-01	2.49e+01	8.42e+00	2.50e+02	yes	1.02e+00	no	1.55e-01
080727A	6.07e-01	-1.23e+00	2.23e+02	2.82e-07	7.90e+00	4.00e-02	5.64e+00	7.30e+00	4.12e+02	yes	5.50e+00	no	6.75e-02
080727B	8.07e-01	-1.05e+00	3.67e+02	8.11e-06	8.14e+01	5.33e-01	1.83e+01	1.07e+01	1.12e+02	yes	6.40e-02	no	5.02e-02
080727C	2.44e-01	-9.45e-01	1.92e+02	8.75e-06	7.62e+01	6.26e-01	9.98e+01	7.95e+00	2.05e+02	yes	1.02e+00	no	1.45e-01
080802	3.93e-01	-1.74e+00	6.07e+01	2.06e-06	1.80e+01	2.58e-01	1.74e+02	7.06e+00	3.75e+02	yes	4.10e+00	no	2.67e-01
080903	4.52e-01	-9.27e-01	6.38e+01	1.77e-06	3.75e+01	-3.80e-02	6.93e+01	8.95e+00	2.85e+02	yes	1.02e+00	yes	2.05e-01
080906	7.56e-01	-1.58e+00	1.05e+02	6.38e-06	4.72e+01	1.57e-01	1.59e+02	6.72e+00	1.66e+02	yes	1.02e+00	yes	2.16e-01
080916B	1.85e-01	-1.45e+00	1.00e+02	1.13e-06	1.15e+01	-3.10e-02	3.38e+01	7.33e+00	3.38e+02	yes	4.10e+00	yes	1.54e-01
081011	1.85e-01	-1.56e+00	8.19e+01	3.88e-07	1.00e+01	-2.30e-02	1.87e+01	7.49e+00	3.90e+02	yes	4.10e+00	yes	1.33e-01
081012	6.00e-01	-8.83e-01	4.48e+02	3.48e-06	1.63e+01	?	3.20e+01	7.78e+00	2.32e+02	yes	2.05e+00	no	7.67e-02
081102	3.33e-01	-1.66e+00	7.79e+01	3.75e-06	2.54e+01	-2.39e-01	6.30e+01	8.52e+00	3.18e+02	yes	2.05e+00	no	1.80e-01
081104	3.85e-01	-1.86e+00	6.07e+01	2.66e-06	2.24e+01	1.43e+00	4.14e+01	9.32e+00	5.14e+02	yes	8.19e+00	no	1.82e-01
081109A	5.63e-01	-1.28e+00	1.05e+02	4.35e-06	5.87e+01	2.85e-01	7.01e+01	9.10e+00	2.27e+02	yes	1.02e+00	yes	1.85e-01
081126	8.59e-01	-9.37e-01	2.46e+02	6.01e-06	5.29e+01	6.10e-02	5.96e+01	1.44e+01	4.65e+02	yes	1.02e+00	yes	9.53e-02
081127	3.93e-01	-1.98e+00	4.97e+01	6.48e-07	1.03e+01	?	2.21e+01	7.25e+00	4.92e+02	yes	8.19e+00	no	1.53e-01
081128	1.63e-01	-8.59e-01	4.61e+01	2.47e-06	3.62e+01	8.00e-03	1.08e+02	2.02e+01	7.71e+03	no	8.80e+01	no	1.31e-01
081210	3.26e-01	-1.36e+00	2.23e+02	3.75e-06	3.59e+01	?	1.51e+02	8.20e+00	3.31e+02	yes	2.05e+00	yes	1.39e-01
081211A	6.89e-01	?	3.68e+01	1.93e-07	7.50e+00	1.35e-01	4.76e+00	6.53e+00	2.07e+02	yes	2.05e+00	yes	9.33e-02
081221	8.15e-01	-1.10e+00	8.19e+01	2.24e-05	2.79e+02	3.50e-01	3.42e+01	8.37e+00	1.52e+02	yes	5.12e-01	no	2.87e-02
081228	7.93e-01	-1.99e+00	3.87e+01	1.43e-07	9.70e+00	5.00e-02	3.78e+00	7.61e+00	1.94e+02	yes	1.02e+00	no	7.83e-02
081230	1.85e-01	-9.56e-01	5.22e+01	8.38e-07	2.22e+01	6.30e-02	5.51e+01	1.68e+01	3.95e+03	no	6.40e+01	yes	2.21e-01
090111	7.56e-01	?	2.23e+01	8.01e-07	2.00e+01	2.04e-01	2.97e+01	7.11e+00	1.91e+02	yes	1.02e+00	no	6.49e-02
090113	5.63e-01	-1.52e+00	1.28e+02	1.32e-06	3.23e+01	1.55e-01	8.80e+00	7.58e+00	6.80e+01	yes	1.28e-01	no	9.19e-02
090123	5.63e-01	-1.59e+00	1.16e+02	4.67e-06	2.46e+01	-1.00e-02	1.42e+02	7.15e+00	1.55e+02	yes	1.02e+00	yes	2.07e-01
090307A	4.96e-01	5.00e+00	3.32e+02	3.24e-07	6.00e+00	3.81e-01	2.18e+01	5.73e+00	4.98e+02	yes	1.22e+01	no	9.72e-02
090308A	5.63e-01	-1.94e+00	4.72e+01	6.46e-07	9.00e+00	2.60e-01	2.64e+02	8.92e+00	1.95e+03	no	6.40e+01	no	1.98e-01
090309A	8.59e-01	-1.29e+00	3.00e+02	2.74e-07	9.60e+00	1.83e-01	2.46e+00	7.07e+00	1.82e+02	yes	1.02e+00	no	5.23e-02
090401B	9.33e-01	-1.24e+00	4.48e+02	2.14e-05	1.57e+02	1.56e-01	2.28e+02	1.01e+01	1.09e+02	yes	6.40e-02	yes	2.94e-02
090404	9.04e-01	-1.82e+00	3.17e+01	3.13e-06	6.17e+01	4.51e-01	8.58e+01	8.91e+00	3.37e+02	yes	2.05e+00	no	6.74e-02
090407	5.19e-02	-1.48e+00	1.00e+02	1.07e-06	1.35e+01	2.31e-01	1.48e+02	8.43e+00	3.12e+02	yes	2.05e+00	no	1.56e-01
090417B	4.07e-01	-1.74e+00	1.11e+02	3.13e-06	2.51e+01	8.96e-01	2.52e+02	9.81e+00	4.85e+03	no	3.20e+02	no	2.98e-01
090419	4.00e-01	-1.35e+00	1.82e+02	4.74e-06	1.43e+01	4.74e-01	4.33e+02	8.88e+00	2.11e+03	no	6.40e+01	yes	2.49e-01

Table 2.6 (cont'd): Test Data: Early-Time Metrics from *Swift* GRBs with unknown Redshifts.

GRB	$\hat{Q}$	$\alpha$	$E_{peak}$	$S$	$S/N_{max}$	$N_{H,pc}$	$T_{90}$	$\sigma_{BAT}$	$N_{peak,BAT}$	Rate trigger	$t_{BAT}$	UVOT detect	$P_{z>4}$
090422	6.30e-01	-1.61e+00	9.05e+01	5.98e-07	1.61e+01	8.60e-02	5.58e+01	7.00e+00	5.20e+01	yes	6.40e-02	no	8.83e-02
090429A	2.81e-01	-6.92e-01	1.11e+02	8.09e-07	2.04e+01	1.98e-01	2.75e+01	5.64e+00	1.40e+02	yes	1.02e+00	no	1.60e-01
090429B	1.85e-01	-6.85e-01	4.72e+01	3.40e-07	2.21e+01	8.70e-02	5.80e+00	1.29e+01	3.69e+02	yes	1.02e+00	no	1.07e-01
090518	6.00e-01	-1.45e+00	1.35e+02	1.05e-06	2.41e+01	4.91e-01	4.58e+01	9.03e+00	1.20e+02	yes	2.56e-01	no	9.13e-02
090530	5.63e-01	-1.57e+00	9.05e+01	1.84e-06	2.37e+01	8.10e-02	4.08e+01	9.41e+00	1.32e+02	yes	2.56e-01	yes	1.15e-01
090607	6.89e-01	-1.19e+00	3.00e+02	2.57e-07	1.13e+01	5.10e-02	2.46e+00	6.44e+00	1.17e+02	yes	5.12e-01	no	4.31e-02
090628	3.19e-01	-1.44e+00	2.01e+02	1.35e-06	1.82e+01	-8.50e-02	2.77e+01	1.00e+01	2.58e+02	yes	1.02e+00	no	9.50e-02
090709A	8.74e-01	-1.06e+00	3.00e+02	4.59e-05	2.52e+02	1.83e-01	3.45e+02	1.73e+01	6.68e+02	yes	1.02e+00	no	6.44e-02
090727	1.56e-01	-1.34e+00	1.65e+02	2.57e-06	1.23e+01	3.40e-02	3.01e+02	8.11e+00	2.72e+02	yes	2.05e+00	no	1.74e-01
090728	3.19e-01	-1.82e+00	6.07e+01	1.43e-06	1.50e+01	2.20e-02	3.28e+01	9.64e+00	3.73e+02	yes	4.10e+00	no	1.74e-01
090807	1.78e-01	-1.43e+00	2.73e+01	1.87e-06	2.13e+01	2.62e-01	1.52e+02	1.32e+01	3.09e+03	no	6.40e+01	no	1.19e-01
090813	6.67e-01	-1.64e+00	1.65e+02	2.45e-06	2.80e+01	1.66e-01	7.92e+00	7.75e+00	5.40e+01	yes	6.40e-02	no	5.37e-02
090831C	6.30e-01	-1.24e+00	3.00e+02	4.19e-07	9.60e+00	8.00e-03	7.28e+00	8.36e+00	4.60e+02	yes	5.50e+00	no	7.02e-02
090904A	6.37e-01	-2.00e+00	4.38e+01	4.11e-06	5.01e+01	-2.00e-02	1.62e+02	1.08e+01	2.04e+03	no	6.40e+01	no	9.44e-02
090904B	5.26e-01	-1.58e+00	1.82e+02	2.12e-05	4.26e+01	8.60e-01	5.82e+01	7.98e+00	2.39e+02	yes	4.10e+00	no	9.28e-02
090912	3.26e-01	-7.91e-01	6.38e+01	4.94e-06	3.33e+01	4.39e-01	1.51e+02	6.62e+00	1.27e+02	yes	1.02e+00	no	1.49e-01
090929B	9.19e-01	-1.83e+00	6.07e+01	8.90e-06	5.21e+01	5.60e-02	3.71e+02	7.72e+00	1.20e+02	yes	2.56e-01	yes	1.18e-01
091026	3.26e-01	-1.70e+00	7.41e+01	2.98e-06	3.00e+01	1.86e-01	7.74e+01	1.21e+01	2.67e+02	yes	1.02e+00	no	1.39e-01
091102	6.37e-01	-1.13e+00	3.67e+02	1.21e-06	2.33e+01	1.42e-01	7.07e+00	1.30e+01	3.62e+02	yes	1.02e+00	no	5.62e-02
091104	3.04e-01	-1.78e+00	5.49e+01	1.08e-06	1.15e+01	5.60e-02	1.06e+02	7.72e+00	1.49e+03	no	6.40e+01	no	2.68e-01
091221	6.37e-01	-1.62e+00	1.65e+02	9.49e-06	8.51e+01	-1.70e-02	6.90e+01	7.54e+00	1.83e+02	yes	1.02e+00	yes	1.15e-01
100111A	4.96e-01	-1.79e+00	6.07e+01	1.00e-06	2.29e+01	8.20e-02	1.51e+01	1.21e+01	2.58e+02	yes	5.12e-01	yes	1.34e-01
100117A	4.52e-01	?	1.00e+02	6.10e-07	1.11e+01	8.20e-02	6.39e+02	7.19e+00	5.70e+01	yes	6.40e-02	no	1.75e-01
100205A	1.85e-01	-1.73e+00	7.41e+01	5.97e-07	1.17e+01	5.00e-02	3.28e+01	8.08e+00	7.18e+02	yes	1.22e+01	no	1.82e-01
100212A	7.56e-01	-1.02e+00	2.86e+01	1.00e-06	1.63e+01	-4.00e-02	1.69e+02	1.45e+01	3.71e+02	yes	5.12e-01	no	4.08e-02
100213A	7.04e-01	-1.40e+00	1.35e+02	5.16e-07	1.94e+01	8.80e-02	2.37e+00	7.01e+00	4.70e+01	yes	6.40e-02	no	4.98e-02
100213B	7.19e-01	?	2.86e+01	1.37e-06	2.47e+01	-3.06e-01	3.66e+01	1.09e+01	5.16e+02	yes	4.10e+00	no	8.29e-02
100305A	0.00e+00	-1.33e+00	1.82e+02	3.54e-06	1.39e+01	4.80e-02	1.70e+02	8.24e+00	1.14e+03	no	6.40e+01	no	1.93e-01
100316A	2.67e-01	-1.54e+00	1.28e+02	1.60e-06	1.49e+01	-3.20e-02	1.10e+01	8.09e+00	2.03e+02	yes	2.05e+00	no	9.59e-02
100316C	2.00e-01	-1.54e+00	1.00e+02	3.23e-07	1.13e+01	2.28e-01	1.00e+01	7.19e+00	3.72e+02	yes	4.10e+00	no	1.11e-01
100413A	1.63e-01	-1.11e+00	4.48e+02	1.40e-05	4.77e+01	2.03e-01	1.97e+02	1.06e+01	8.76e+02	yes	1.64e+01	no	1.46e-01
100420A	7.41e-03	-1.27e+00	1.65e+02	9.39e-07	8.80e+00	1.17e-01	5.04e+01	7.37e+00	1.52e+03	no	6.40e+01	no	1.56e-01
100424A	3.26e-01	-1.87e+00	5.49e+01	2.13e-06	2.43e+01	1.16e-01	1.10e+02	1.05e+01	2.02e+03	no	6.40e+01	no	2.63e-01
100504A	4.81e-01	-1.79e+00	6.70e+01	3.36e-06	4.56e+01	6.91e-01	9.81e+01	1.29e+01	3.99e+02	yes	1.02e+00	no	1.48e-01
100508A	5.19e-02	-1.23e+00	2.01e+02	1.74e-06	1.15e+01	6.80e-02	5.98e+01	7.47e+00	1.45e+03	no	6.40e+01	yes	1.48e-01
100514A	4.44e-01	-3.32e-01	4.97e+01	3.62e-07	1.27e+01	-1.45e-01	2.13e+01	7.06e+00	2.84e+02	yes	3.07e+00	yes	1.65e-01
100522A	7.63e-01	-1.46e+00	4.97e+01	2.19e-06	6.08e+01	3.44e-01	3.52e+01	1.10e+01	1.31e+02	yes	1.28e-01	no	3.10e-02
100526A	3.63e-01	-1.95e+00	4.97e+01	3.52e-06	1.85e+01	1.60e-01	1.31e+02	7.19e+00	1.13e+03	no	6.40e+01	no	2.20e-01
100526B	7.41e-03	-1.52e+00	9.51e+01	7.88e-07	1.09e+01	1.45e-01	5.45e+01	6.89e+00	9.03e+02	yes	2.69e+01	no	1.78e-01
100606A	4.96e-01	-1.12e+00	5.47e+02	1.28e-05	4.19e+01	1.00e-01	1.92e+02	1.06e+01	2.38e+02	yes	1.02e+00	no	9.39e-02

Table 2.6 (cont'd): Test Data: Early-Time Metrics from *Swift* GRBs with unknown Redshifts.

GRB	$\hat{Q}$	$\alpha$	$E_{peak}$	$S$	$S/N_{max}$	$N_{H,pc}$	$T_{90}$	$\sigma_{BAT}$	$N_{peak,BAT}$	Rate trigger	$t_{BAT}$	UVOT detect	$P_{z>4}$
100614A	4.00e-01	-1.85e+00	5.49e+01	3.55e-06	2.10e+01	7.00e-02	1.80e+02	1.44e+01	2.92e+03	no	6.40e+01	no	2.58e-01
100615A	6.59e-01	-1.51e+00	6.54e+01	5.70e-06	1.07e+02	9.05e-01	4.35e+01	1.05e+01	2.19e+02	yes	5.12e-01	no	6.28e-02
100619A	7.93e-01	-1.47e+00	7.79e+01	5.34e-06	8.27e+01	3.56e-01	9.79e+01	7.94e+00	1.04e+02	yes	2.56e-01	no	7.78e-02

## Chapter 3

# Evidence for Dust Destruction from the Early-time Color Change of GRB 120119A

We present broadband observations and analysis of *Swift* gamma-ray burst (GRB) 120119A. Our early-time afterglow detections began under 15 s after the burst in the host frame (redshift  $z = 1.73$ ), and they yield constraints on the burst energetics and local environment. Late-time afterglow observations of the burst show evidence for a moderate column of dust ( $A_V \approx 1.1$  mag) similar to, but statistically distinct from, dust seen along Small Magellanic Cloud sightlines. Deep late-time observations reveal a dusty, rapidly star-forming host galaxy. Most notably, our early-time observations exhibit a significant red-to-blue color change in the first  $\sim 200$  s after the trigger at levels heretofore unseen in GRB afterglows. This color change, which is coincident with the final phases of the prompt emission, is a hallmark prediction of the photodestruction of dust in GRB afterglows. We test whether dust-destruction signatures are significantly distinct from other sources of color change, namely a change in the intrinsic spectral index  $\beta$ . We find that a time-varying power-law spectrum alone cannot adequately describe the observed color change, and allowing for dust destruction (via a time-varying  $A_V$ ) significantly improves the fit. While not definitively ruling out other possibilities, this event provides the best support yet for the direct detection of dust destruction in the local environment of a GRB.

A version of this chapter was previously published as Morgan, Perley, Cenko, Bloom, Cucchiara, Richards, Filippenko, Haislip, LaCluyze, Corsi, Melandri, Cobb, Gomboc, Horesh, James, Li, Mundell, Reichart, and Steele, *Evidence for Dust Destruction from the Early-time Colour Change of GRB 120119A*, Monthly Notices of the Royal Astronomical Society, vol. 440, p. 1810, 2014.

## 3.1 Introduction

More than seven years after the launch of *Swift* (Gehrels et al. 2004), a rich collection of optical light curves of gamma-ray bursts (GRBs) has been amassed. While global similarities in light-curve behaviors are becoming well established (e.g., Kann et al. 2010, 2011), thorough studies of individual bursts nevertheless continue to yield important insights into the details of the explosions and their environments. In particular, there remain relatively few examples of very early-time optical light curves when the prompt phase of the high-energy emission is still ongoing (for some examples, see Panaitescu & Vestrand 2008; Melandri et al. 2008; Cenko et al. 2009b; Rykoff et al. 2009; Oates et al. 2009) due to the small but significant delays in relaying positional information to the ground, and the nonzero response times of even the fastest robotic telescopes.

Furthermore, the majority of the earliest-time light curves are of a single color (often unfiltered), which can provide only limited information on the evolution of the GRB emission and interactions with its surrounding environment. Contemporaneous, multi-color observations are needed to identify and characterize any color change that may occur in the early afterglow.

Strong color change is expected to occur for at least some events owing to the photodestruction of dust in the nearby environment of GRBs at early times (Waxman & Draine 2000; Draine & Hao 2002). Given the association of massive-star progenitors with long-duration GRBs, it is natural to expect GRBs to explode in dusty environments. However, only a small fraction ( $\sim 25\%$ ) exhibit evidence for significant ( $A_V > 1$  mag) dust obscuration in late-time optical/ultraviolet (UV) spectral energy distributions (SEDs) (Covino et al. 2013). One potential explanation of this apparent discrepancy is the photodestruction of dust in GRB environments by prompt high-energy emission.

So far, however, unambiguous evidence for or against dust destruction in early GRB afterglows has been varied and inconclusive. As the bulk of the destruction is likely produced by bright X-rays during the prompt emission, optical observations contemporaneous with the high-energy radiation are needed in order to observe time variability in the SED (e.g., Fruchter et al. 2001; Perna et al. 2003).

Indirect evidence for or against dust destruction has been explored in observations of a few individual GRBs. In GRB 030418, an optical rise following a dearth of emission seen in images beginning  $\sim 200$  s after the start of the burst ( $> 1$  min after the prompt phase ended, and thus after dust destruction would have occurred) is interpreted as absorption of optical photons by dust inside a massive stellar wind medium (Rykoff et al. 2004). In this interpretation, complete destruction of the local dust did not occur, as some must have persisted to produce the attenuation. However, other models can be invoked to explain this early rise and subsequent decay that is now commonly seen in early-time optical afterglows (see, e.g., §3.3.5).

In the case of GRB 061126, Perley et al. (2008c) and Gomboc et al. (2008) explore the possibility that grey dust could explain the observed deficit of optical flux to X-rays at late times. The optical dimness of this event was interpreted as optical absorption without the



expected reddening by normal dust observed in the local universe. While the presence of grey dust was not conclusively seen, a possible interpretation of its existence would be the sublimation of smaller grains in the local environment due to early photoionization of dust by the prompt X-ray emission. However, a significant change of  $A_V$  was not reported, so the grey dust might have been pre-existing.

In order to unambiguously identify the signatures of dust destruction, simultaneous, multi-color imaging of the afterglow (especially during the high-intensity high-energy emission) is necessary. With well-sampled, multi-color optical/near-infrared (NIR) observations beginning less than 1 min after the burst trigger, GRB 120119A offers one of the best cases yet to study the nature of an early-time GRB afterglow. The afterglow exhibits an appreciable red-to-blue color change coincident with the end of the prompt high-energy emission, making this event an excellent candidate to test for the signatures of dust destruction. However, careful modelling of the SED as a function of time is needed to disambiguate between changes in the dust-absorption properties and other sources of color change, such as a change in the intrinsic spectral index  $\beta$ .

In this study, we present observations and analysis of the broadband afterglow of GRB 120119A. Details of the observations and data reduction are given in §3.2. Next, we present modelling and analysis, including general properties of the afterglow behavior in §3.3.1, modelling of the late-time extinction profile in §3.3.2, details of the construction of early-time SEDs in §3.3.3, modelling of the early-time color change in §3.3.4, constraints on the origin of the early emission in §3.3.5, and details of the host-galaxy properties in §3.3.6. To conclude, we discuss the implications of the results in §3.4. Throughout the paper we adopt the specific flux convention of  $F(\nu, t) \propto \nu^\beta t^\alpha$ . All quoted uncertainties are  $1\sigma$  unless stated otherwise, and dates and times are given in UT.

## 3.2 Observations

### 3.2.1 *Swift* Observations

GRB 120119A triggered the Burst Alert Telescope (BAT; Barthelmy et al. 2005) onboard *Swift* (Gehrels et al. 2004) at 04:04:30.21. *Swift* slewed immediately to the source and began observations with the X-Ray Telescope (XRT; Burrows et al. 2005) and UltraViolet/Optical Telescope (UVOT; Roming et al. 2005) at 53.3 s and 61 s after the trigger, respectively.

We processed the BAT data using the formalism of Butler et al. (2007). The BAT data show a duration of  $T_{90} = 70 \pm 4$  s and a total fluence (15–350 keV) of  $S = (2.3 \pm 0.1) \times 10^{-5}$  erg cm $^{-2}$ . The XRT data were reduced using the pipeline described by Butler & Kocevski (2007), and they were corrected for Galactic neutral hydrogen (assuming the standard associated absorption from other elements) using the maps of Kalberla et al. (2005). The XRT bandwidth covers the energies 0.2–10 keV; all flux values quoted herein are converted to an effective energy of 1 keV.

The beginning of the XRT observations marginally overlaps with the end of the observed

BAT emission; this initial steep decline of X-ray emission ( $\alpha = -2.71 \pm 0.09$ ) is consistent with an extrapolation of the tail of the BAT emission to lower energies, as has been seen in many previous bursts (e.g., O’Brien et al. 2006).

The optical afterglow was clearly detected with the White filter onboard the UVOT in the initial finding-chart exposure taken  $\sim 140$  s after the burst ( $m_{\text{white}} = 19.5 \pm 0.1$  mag), and was again marginally detected in the  $B$  band  $\sim 1800$  s after the trigger ( $B = 19.4 \pm 0.3$  mag; Chester & Beardmore 2012). It was undetected in all other filters, including the first  $U$ -band exposure  $\sim 290$  s after the trigger ( $m_U > 18.7$  mag).

### 3.2.2 PROMPT Observations

Observations of GRB 120119A were taken by the Skynet robotic telescope network using 5 PROMPT telescopes at Cerro Tololo Inter-American Observatory (CTIO) in Chile. Observations began at 04:05:08, 38 s after the burst. Observations in  $I, R, V, B$ , and open filters were taken beginning at different starting times, but nearly simultaneous multi-color observations were performed when possible. Unfortunately, the images taken in the  $V$  band suffered from a previously unknown detector issue, and thus were not used in the analysis. The exposure of each observation increases with time since the GRB, with a minimum of 5 s to a maximum of 80 s in the  $I, R, B$ , and open filters. Additional late-time exposures were obtained with the Sloan  $g'$  and  $z'$  filters. Stacking is done manually as necessary to increase the signal-to-noise ratio (S/N), with an aim of obtaining photometric uncertainties of approximately  $\pm 0.1$  mag.

Photometry was performed using a custom pipeline written in C and Python, based upon IRAF<sup>a</sup> aperture photometry. Photometric calibration was performed using a selection of 7 SDSS stars. For filters not in SDSS, color transformations were performed using the prescription of Jester et al. (2005). The results are shown in Table 3.6, where magnitudes are in the Vega system.

### 3.2.3 PAIRITEL Observations

The robotic Peters Automatic Infrared Imaging Telescope (PAIRITEL; Bloom et al. 2006b) began automatic observations of GRB 120119A at 04:05:23, 53 s after the BAT trigger. PAIRITEL consists of the 1.3 m Peters Telescope at Mt. Hopkins, AZ, which was formerly used for the Two Micron All Sky Survey (2MASS; Skrutskie et al. 2006) but was subsequently refurbished with the southern 2MASS camera. PAIRITEL uses two dichroics to image in the NIR  $J, H$ , and  $K_s$  filters simultaneously every 7.8 s. Three images are taken at each dither position and then median combined into 23.4 s “triplestacks.” Images are then resampled to  $1''$  pixel<sup>-1</sup> from its native  $2''$  pixel scale and coadded using SWarp (Bertin et al. 2002).

<sup>a</sup>IRAF is distributed by the National Optical Astronomy Observatory, which is operated by the Association of Universities for Research in Astronomy (AURA), Inc., under cooperative agreement with the US National Science Foundation (NSF).

Aperture photometry was performed using custom Python software, utilizing Source Extractor (SExtractor; Bertin & Arnouts 1996) as a back end. The optimal aperture of  $5.5''$  diameter was determined by minimizing the absolute error relative to 2MASS magnitudes of our calibration stars. Calibration was performed by redetermining the zeropoint for each image individually by comparison to 2MASS magnitudes with the calibration stars. The resulting statistical uncertainty in the zeropoint is negligible relative to other sources of error. Additional, systematic sources of error are addressed in detail by Perley et al. (2010b); we use a similar procedure here to determine the total uncertainty of each point. The results are shown in Table 3.6, where magnitudes are in the Vega system.

### 3.2.4 KAIT Observations

The Katzman Automatic Imaging Telescope (KAIT; Filippenko et al. 2001) began observations of GRB120119A at 04:06:33, 2.05 min after the BAT trigger. KAIT is a 0.76 m telescope located at Lick Observatory dedicated to discovering and observing supernovae and other transients; it has been autonomously responding to GRB triggers since 2002 (Li et al. 2003b).

KAIT began observations by cycling through 20 s exposures in  $V$ ,  $I$ , and unfiltered images, later switching to alternating  $I$  and unfiltered exposures, and finally (when the source was faint) just unfiltered images. Automatic bias subtraction and flat-fielding is performed at the telescope. Coaddition with SWarp is then performed as necessary to obtain significant detections of the afterglow.

Aperture photometry with a  $2''$  radius was performed on the coadded images via a custom IDL wrapper based on the GSFC IDL Astronomy User's library `aper` routine. Calibration was done relative to field stars from the Sloan Digital Sky Survey Data Release 8 (SDSS DR8; Aihara et al. 2011), where magnitudes were converted into  $V, R, I$  using the transformation equations of Lupton (2005)<sup>b</sup>. Unfiltered observations were calibrated relative to  $R$ -band magnitudes following the procedure of Li et al. (2003a). The results are shown in Table 3.6, where magnitudes are in the Vega system.

### 3.2.5 Liverpool Observations

The 2 m Liverpool Telescope<sup>c</sup> (LT) robotically responded to the BAT trigger under its automatic GRB follow-up program (Guidorzi et al. 2006) and began observations  $\sim 2.6$  min after the burst. The first  $\sim 10$  min of observations were obtained with the RINGO2 polarimeter, which were coadded into a total of seven 80 s frames and then calibrated against the SDSS  $r'$  filter. Subsequent observations were acquired by alternating SDSS  $r'i'z'$  filters from 14.5 min to 53 min after the burst, with a pre-determined sequence of increasing exposures. Differential photometry was performed with respect to 5 SDSS field stars with the

<sup>b</sup><http://www.sdss.org/DR7/algorithms/sdssUBVRITransform.html#Lupton2005>

<sup>c</sup><http://telescope.livjm.ac.uk/>

Graphical Astronomy and Image Analysis Tool (GAIA). The results are shown in Table 3.6, where magnitudes are in the AB system.

### 3.2.6 SMARTS Observations

Beginning at 04:41:41 ( $\sim 0.64$  hr after the burst), data were obtained using the ANDICAM (A Novel Dual Imaging CAMera) instrument mounted on the 1.3 m telescope at CTIO<sup>d</sup>. This telescope is operated as part of the Small and Moderate Aperture Research Telescope System (SMARTS) consortium<sup>e</sup>. The ANDICAM detector consists of a dual-channel camera that allows for simultaneous optical and IR imaging.

During each epoch, multiple dithered images were obtained with an image cadence designed to ensure that the final combined frames in each filter are referenced to the same time of mid-exposure. Thus, afterglow measurements are obtained at a single reference time for all filters, without any need for temporal extrapolation. Standard IRAF data reduction was performed on these images, including bias subtraction, flat-fielding, and sky subtraction. The images were then aligned and averaged to produce a single master frame for each epoch. During the first epoch, total summed exposure times equaled 180 s in *BRIJK* and 120 s in *HV*. For all other epochs, the total summed exposure times amounted to 15 min in *IV* and 12 min in *JK*.

The afterglow brightness was measured using seeing-matched, relative aperture photometry, with the relative magnitude of the afterglow determined by comparison with a set of field stars. The relative magnitudes were converted to apparent magnitudes by comparison with the Rubin 149 standard star (Landolt 1992) in the optical and with 2MASS stars in the IR.

### 3.2.7 P60 Observations

We began observations of the afterglow of GRB 120119A with the automated Palomar 60 inch (1.5 m) telescope (P60; Cenko et al. 2006b) beginning at 7:33 on 2012 January 19 (3.48 hr after the *Swift*-BAT trigger). Images were obtained in the Sloan *g'*, *r'*, and *i'* filters, and individual frames were automatically reduced using our custom IRAF software pipeline. To increase the S/N, individual frames were astrometrically aligned using the Scamp software package and coadded using SWarp (Bertin et al. 2002).

We used aperture photometry to extract the flux of the afterglow from these coadded frames with the aperture radius roughly matched to the FWHM of the point-spread function (PSF). Aperture magnitudes were then calibrated relative to field sources from SDSS DR8. Imaging continued on the following night, but by then the afterglow had faded below our detection threshold. The results are shown in Table 3.6, where magnitudes are in the AB system.

<sup>d</sup><http://www.astronomy.ohio-state.edu/ANDICAM>

<sup>e</sup><http://www.astro.yale.edu/smarts>

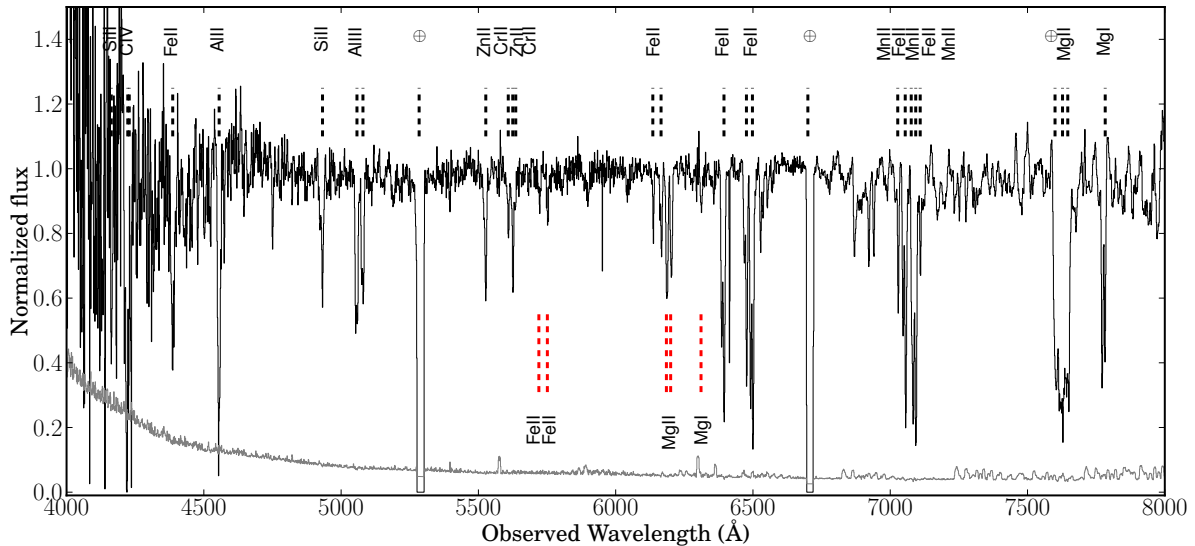


*Figure 3.1:* Normalized, combined spectrum of GRB 120119A obtained with GMOS-South. Two systems of absorption features are clearly identified. Indicated in black are the host-galaxy ( $z = 1.728$ ) metal lines, while in red we see a strong Mg II absorber at  $z = 1.212$ , based on Mg II and Fe transitions. At the bottom, we show the noise spectrum.

### 3.2.8 Gemini-S spectroscopy

On January 19.20, 53 min after the BAT trigger, we utilized our rapid Target-of-Opportunity program (GS-2011B-Q-9, P.I. Cucchiara) to observe the optical afterglow with GMOS-S on the Gemini South telescope. We obtained two spectra of 900s each, with the R400 grating (corresponding to a resolving power of  $R \approx 1200$  at  $6000 \text{ \AA}$ ) and a  $1''$  slit, spanning the  $4000\text{--}8000 \text{ \AA}$  wavelength range. Flat-field and Cu-Ar lamp calibration files were obtained immediately after the target observation.

The data were reduced using the **Gemini** and **GMOS** packages available under the IRAF environment. Cosmic-ray rejection was performed using the `lacos-spec` routine (van Dokkum 2001). The extracted 1-dimensional spectra were combined and normalized using the routines `long_combspec`, `x_continuum`, and `x_nrmspec` available under the XIDL package.

The final result is shown in Figure 3.1. The spectrum reveals several metal absorption features, which are associated with a host galaxy at redshift  $z = 1.728 \pm 0.05$ . In addition, a strong Mg II system at lower redshift ( $z = 1.212$ ) is present (as is common in GRB afterglow spectra; e.g., Vergani et al. 2009; Cucchiara et al. 2009b; Prochter et al. 2006).

### 3.2.9 Gemini-N Observations

On January 21.28 (2.1 days after the burst) we observed the field of GRB 120119A with the Gemini Multi-Object Spectrograph (GMOS; Hook et al. 2004) and Near InfraRed Imager

and Spectrometer (NIRI; Hodapp et al. 2003) as part of our rapid ToO program GN-2011B-Q-34 (P.I. Tanvir) in order to continue monitoring the late-time behavior of the afterglow. We performed a series of short ( $\sim 3$  min) exposures in the optical  $g'$ ,  $r'$ , and  $i'$  bands. These data were obtained with a dithered random pattern around the GRB location to improve the subsequent reductions. Data were flat-fielded and coadded using the Gemini-GMOS tasks under the IRAF environment. The final coadded images consist of a total of 26 min ( $i'$ ) and 20 min ( $r'$  and  $g'$ ), with a scale of  $0.14''$  pixel $^{-1}$ .

The IR observations consist of 20 dithered images of 80 s each ( $4 \times 20$  s exposures) in the  $J$  band, 18 dithered images of 80 s each ( $16 \times 5$  s exposures) in the  $H$  band, and 19 dithered images of 128 s each ( $16 \times 8$  s exposures) in the  $K$  band. Each sequence was obtained with dithering patterns similar to those for the GMOS data. Reduction, including cosmic-ray rejection, flat-fielding, and coaddition, was performed using the NIRI package. The afterglow is detected in all of the final coadded images.

We obtained two additional NIRI  $K$ -band imaging epochs of the field of GRB 120119A using our standard ToO program (GN-2011B-Q-10, P.I. Fox) on January 25 ( $\sim 6$  days post trigger) and April 2 ( $\sim 74$  days post trigger), with total integration times of 29 min and 34 min, respectively. Seeing conditions were exceptional during both integrations ( $0.35''$ ). Images were reduced and combined following the procedures above. In both of these coadds we detect a faint, marginally extended ( $\sim 0.3''$ ), nonfading ( $< 0.15$  mag at 95% confidence) source underlying the GRB position; we suggest that it is the GRB host galaxy.

### 3.2.10 Keck Observations

We imaged the location of GRB 120119A with the Low Resolution Imaging Spectrometer (LRIS; Oke et al. 1995) on the Keck-I 10, telescope at three different epochs. The first epoch was carried out on January 26 between 10:42 and 11:07 (7.3 days post-trigger) with the  $g$ ,  $R$ , and  $I$  filters. While seeing conditions for most of that night were generally poor, these data were taken within a brief window of good seeing ( $\sim 0.7''$ ). An object is well detected at the afterglow position at a magnitude only slightly fainter than in the GMOS imaging several days earlier.

A second epoch of imaging was taken on February 21 (33 days post-trigger), but seeing conditions were poor ( $1.7''$ ) and the position of the GRB is blended with the neighboring galaxy  $3''$  to the south. Nevertheless, a source is still clearly present at the GRB location. Photometry of this object was complicated by the poor seeing and blending, but we do not see any clear evidence of fading from the previous LRIS epoch.

A final epoch of imaging was performed on 2012 December 11 (0.89 yr after the burst) under relatively good seeing conditions ( $\sim 1.0''$ ). Images were taken with the  $B$ ,  $R$ , and RG850 (roughly  $z'$ ) filters. The host galaxy is clearly detected in all three bands.



### 3.2.11 *Hubble Space Telescope* Observations

The position around GRB 120119A was observed in the NIR with the Wide Field Camera 3 (WFC3) on the *Hubble Space Telescope* (*HST*) as part of our Cycle 20 program (GO-12949, PI D. Perley) to investigate the host galaxies of dust-obscured GRBs. Observations were obtained in the F125W (wide *J*) and F160W (wide *H*) filters on 2012 October 28 ( $\sim 283$  days post trigger). The exposure time totaled 1209 s in each filter, taken in both cases at three dithered positions.

We downloaded the reduced observations from the Hubble Legacy Archive. The host-galaxy candidate from our Keck and Gemini observations is clearly extended (see Section 3.3.6). It is easily detected ( $S/N \approx 30$ ) in both frames, and it shows a morphology consistent with a bright, compact core ( $r < 0.3''$ ) surrounded by a disk of lower surface brightness ( $r \approx 0.8''$ ). There is no clear evidence of tidal features or ongoing interaction.

Photometry of the host galaxy was performed using a custom IDL aperture photometry routine using a circular aperture of  $1.0''$  radius centered on the host position. We used the zeropoints in the WFC3 handbook and aperture corrections of 0.07 mag (F125W) and 0.09 mag (F160W) measured from stars elsewhere in the images. The corresponding AB magnitudes of the host galaxy are  $F125W = 23.13 \pm 0.04$  mag and  $F160W = 23.34 \pm 0.07$  mag.

### 3.2.12 CARMA Millimeter Observations

We observed the location of GRB 120119A with the Combined Array for Research in Millimeter-wave Astronomy (CARMA) for 2.2 hr on 2012 January 19, beginning at 11:47:42. The observation were undertaken at a frequency of 95 GHz with a bandwidth of 8 GHz, while the telescope was in the C configuration. We used the compact source J0744-064 as a phase calibrator and observed Mars for flux calibration. The data were reduced using the MIRIAD software<sup>f</sup>. The mid-epoch of the CARMA observation,  $\sim 8.9$  hr since the burst, is close to the last optical/NIR observations that yielded a detection (at  $t \approx 5.6$  hr since the burst; see Fig. 3.2). The  $3\sigma$  upper limit derived from the CARMA nondetection is 0.99 mJy at 95 GHz.

## 3.3 Analysis

### 3.3.1 Optical/NIR Light Curve

A complete list of our afterglow photometry (uncorrected for Galactic extinction) is presented in Table 3.6. All flux values used for modelling in this work have been corrected for the expected Galactic extinction of  $E(B - V) = 0.093$  mag along the line of sight using the dust maps of Schlegel et al. (1998) and correcting for the  $\sim 14\%$  recalibration of these maps reported by Schlafly & Finkbeiner (2011). The first day of optical/NIR photometry is

<sup>f</sup><http://bima.astro.umd.edu/miriad/>

plotted in Figure 3.2, and some features are easily apparent. First, a significant red-to-blue color change is observed during the first 200 s after the trigger. We note that the bulk of this color evolution occurs coincident with the end of the prompt high-energy emission (see Fig. 3.3). We explore the details and implications of this color change in §3.3.4.

After the significant color change ceased, the afterglow is seen to achromatically rise, peaking at roughly 800 s (observer frame). Minor oscillations are seen in some features during this peak, though coverage is limited and detailed modelling of these features is not presented here. We will explore the implications of the optical rise in §3.3.5.

The XRT afterglow (plotted in Fig. 3.3) is well fit by a series of power-law decays. The afterglow is initially caught in a rapid decay which is consistent with a lower-energy extension of the tail end of the prompt gamma-ray emission seen by the BAT. The light curve then slows to a shallower decay of  $\alpha_X = -1.27 \pm 0.02$  by the onset of the second epoch of observations. To compare this afterglow with that at lower energies (Fig. 3.3), we fit the optical/NIR light curve from the time of the onset of the second epoch of XRT observations until the end of the early-time optical observations ( $\sim 0.4$  to 5.6 hr after the burst). While a single power-law component appears to dominate the light curve at this time, an additional excess of emission is seen at early times. We fit the light curve using a combination of a single power law plus a [Beuermann et al. \(1999\)](#) component (see [Perley et al. 2008b](#), for a description of our light-curve fitting code). The power-law component has a decay index  $\alpha_{\text{oir}} = -1.30 \pm 0.01$ , consistent with the XRT decay at this time, indicating that the flux originates from the same synchrotron spectral component. The minor rising component had a fixed rising index of  $\alpha_{1,a} = 1.0$ , and a best-fit decay of  $\alpha_{1,b} = 3.9 \pm 0.2$ .

### 3.3.2 Late-Time SED and Extinction Profile

At the time of the onset of the second epoch of XRT observations  $\sim 20$  min after the burst, the complex evolution of the light curve ceased and given way to a simple power-law decay as the primary emission component (§3.3.1). At this late stage, no evidence for further significant color change is seen. To construct an SED from which to model the late-time dust extinction, we extracted the flux values in each band from our light-curve fit (§3.3.1) to the time of the first SMARTS observation 38.7 min post burst. The resultant  $1\sigma$  uncertainties on the fit parameters were multiplied by  $\sqrt{(\chi^2/\text{dof})}$  for each corresponding filter to weight the uncertainty in each color by an estimate of the individual light-curve fit qualities (which is particularly important for the  $z$  and  $V$  bands because of the relatively small number observations in these filters). Estimated systematic uncertainties of 0.03 mag in the NIR and 0.04 mag in the optical were then added in quadrature. The resultant SED is given in Table 3.1 and plotted in Figure 3.4.

The SED clearly shows a significant dust component. We fit various extinction laws to the SED using a custom Python implementation of the [Fitzpatrick \(1999\)](#) parameterization based upon the GSFC IDL Astronomy User’s library. Average parameter values were extracted from [Gordon et al. \(2003\)](#) for the Small Magellanic Cloud (SMC) and [Misselt et al. \(1999\)](#) for the Large Magellanic Cloud (LMC). Flux values and colors were corrected for the observed



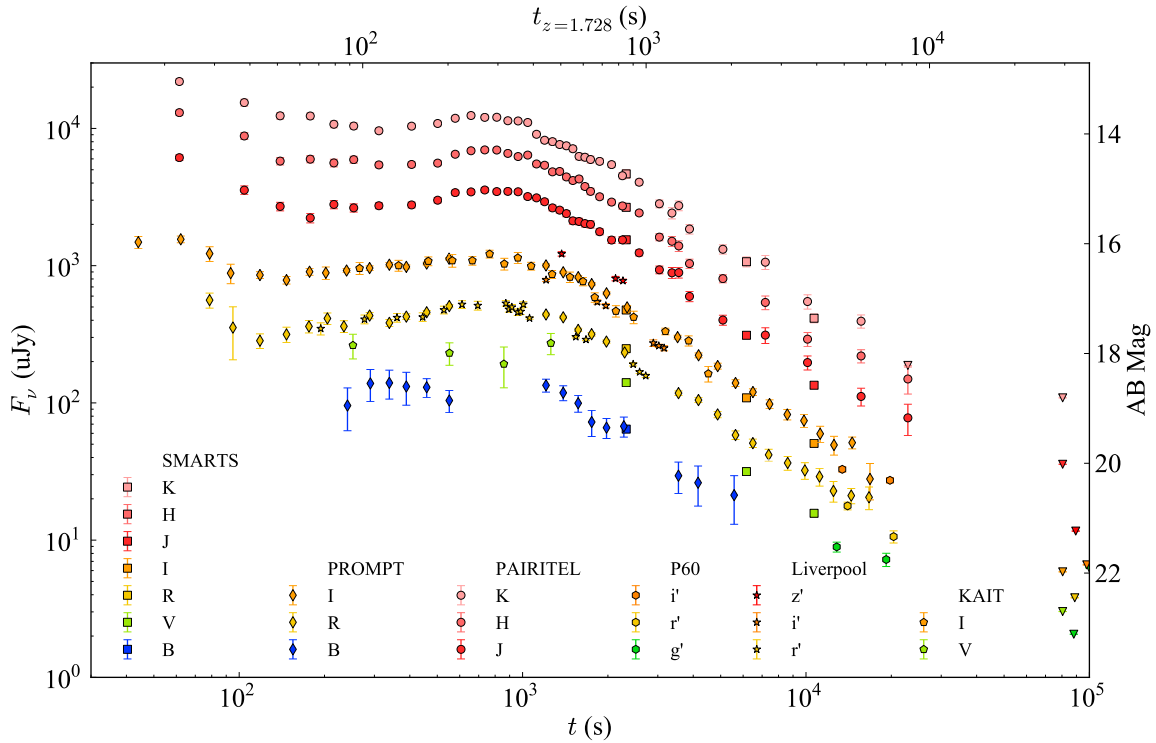
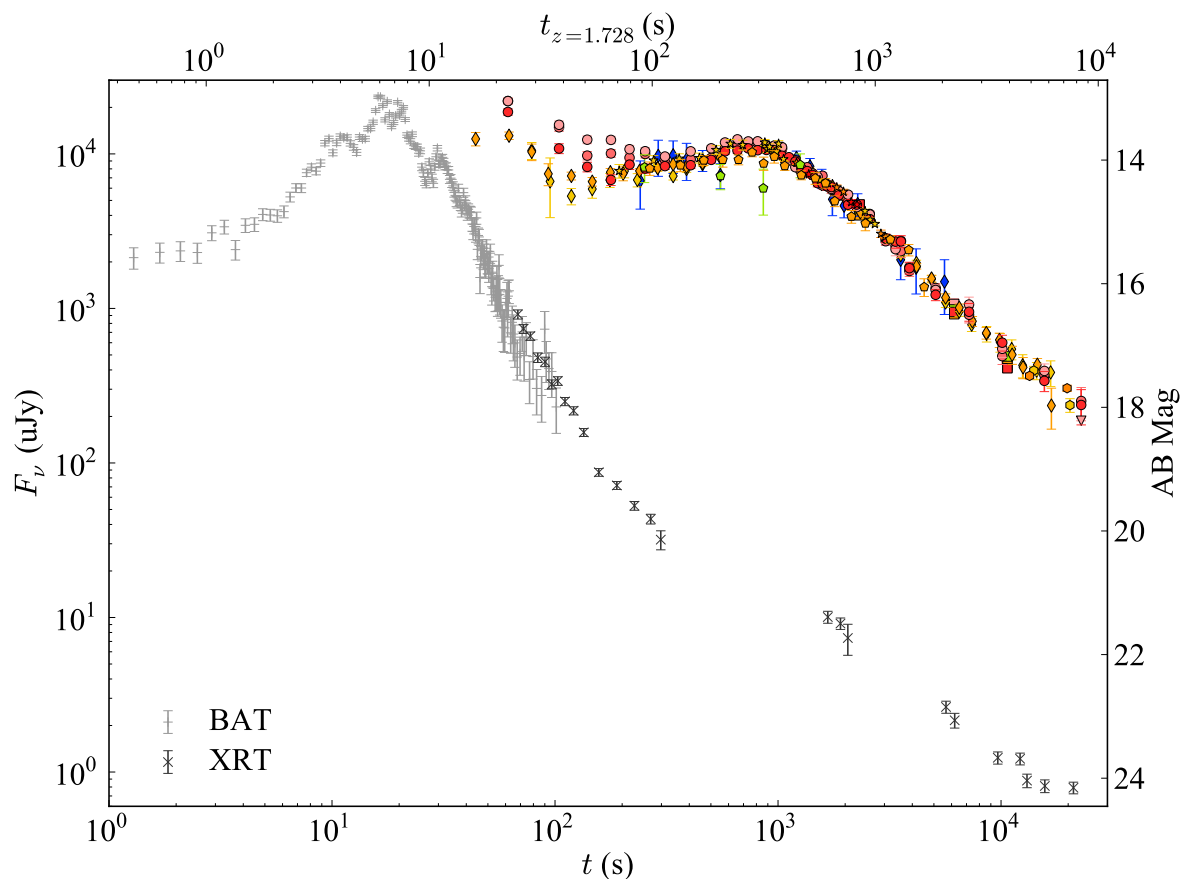


Figure 3.2: First-day optical/NIR light curve of GRB 120119A. A significant red-to-blue color change is observed during the first 200s after the trigger. An achromatic rise is seen around 800s after the trigger, followed by some mild undulations before settling to a single power-law decay with index  $\alpha_{\text{oir}} = -1.30 \pm 0.01$ . Unfiltered data are not included in this plot. The upper and lower time-axis scales refer to the rest frame and the observed frame, respectively.

Table 3.1: GRB 120119A Afterglow SED

Filter	Flux ( $\mu\text{Jy}$ )	$1\sigma$ Uncertainty ( $\mu\text{Jy}$ )
<i>B</i>	45.0	2.5
<i>V</i>	109.9	5.0
<i>r'</i>	160.6	6.6
<i>R</i>	193.7	8.2
<i>i'</i>	340.6	15.9
<i>I</i>	456.1	19.2
<i>z'</i>	654.0	26.2
<i>J</i>	1358.6	44.9
<i>H</i>	2522.7	80.8
<i>K</i>	4312.1	144.5

Note. — Afterglow fluxes were extrapolated to  $t = 38.7$  min after the burst using our light-curve model. Values have not been corrected for Galactic extinction.



*Figure 3.3:* XRT light curve highlighting the overlap between the initial high-energy X-ray emission and the beginning of the optical observations during which significant color change is seen for the first 200 s. The optical/NIR observations have all been scaled to the  $K_s$  band based on their late-time SED (§3.3.2) to highlight the early-time color change. The optical/NIR markers are the same as in Figure 3.2. The BAT data have been scaled up to match the XRT and are consistent with an extrapolation of the tail of the prompt BAT emission to lower energies. The upper and lower time-axis scales refer to the rest frame and the observed frame, respectively.

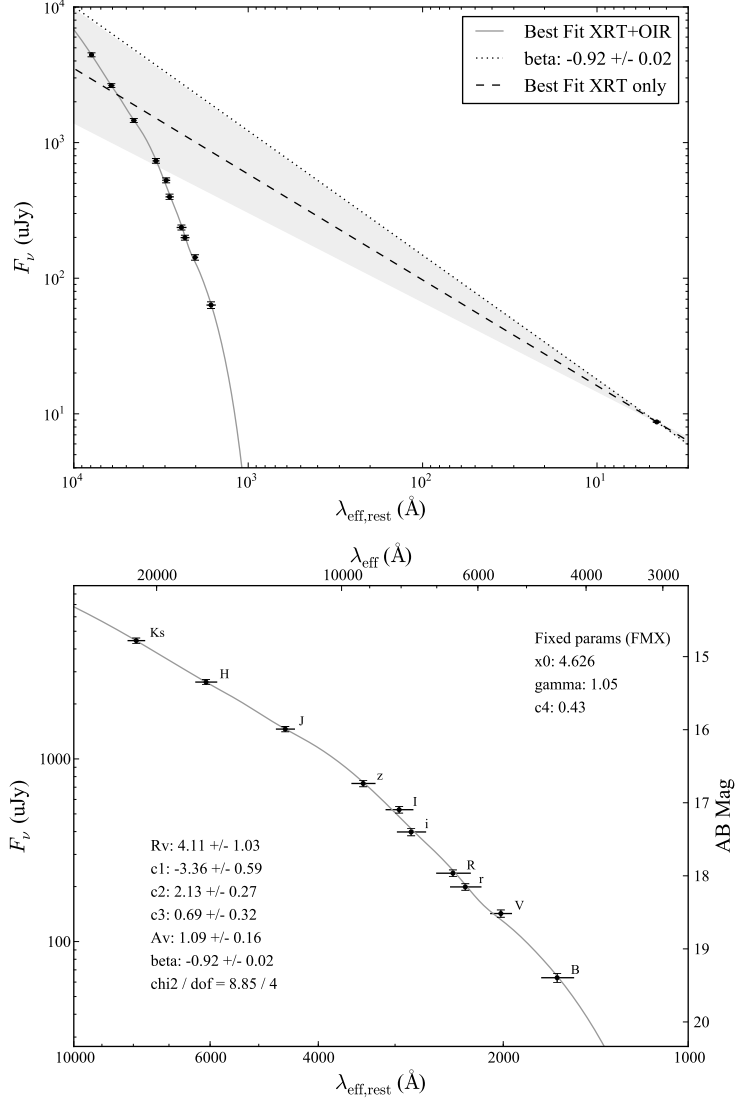


*Figure 3.4:* Late-time SED of GRB 120119A inferred from our light-curve model extrapolated to 38.7 min after the burst (Table 3.1). Values were corrected for the host redshift ( $z = 1.728$ ) and Galactic extinction ( $A_V = 0.288$  mag). *Top panel:* The dashed line and light grey cone represent the best-fit value and uncertainty (respectively) of  $\beta$  inferred from the XRT spectrum alone using the products of Butler & Kocevski (2007):  $\beta_{\text{XRT}} = 0.78 \pm 0.12$ . The solid grey curve shows the best-fit dust model (FMX;  $\chi^2/\text{dof} = 8.9/4$ ), and the dotted line is the  $\beta$  inferred from that fit. *Bottom panel:* Zoomed in SED highlighting the Optical/NIR points. The horizontal bars at each point show the FWHM of the corresponding filter. The solid grey curve shows the best-fit dust model (FMX).

redshift ( $z = 1.728$ ; §3.2.8) and Galactic extinction ( $A_V = 0.288$  mag, assuming  $R_V = 3.1$  for the Milky Way, MW), and the intrinsic spectral index  $\beta$  was allowed to be free in all fits.

Of the three standard local dust extinction laws (MW, LMC, SMC), the SED is by far best fit by an SMC curve ( $\chi^2/\text{dof} = 23.5/7$ ), using the average value of the ratio of total to selective extinction  $R_V = 2.74$  from Gordon et al. (2003). Fits with  $R_V$  as a free parameter were attempted, but lacking UV detections this parameter could not be well constrained. For SMC dust, the best-fit values for extinction and spectral index are  $A_V = 0.62 \pm 0.06$  mag and  $\beta = -1.39 \pm 0.11$ . The resultant fits are shown in Table 3.2.

We can further constrain the value of  $\beta$  by including the interpolated, unabsorbed XRT flux in the SED fit ( $E_{\text{xrt,eff}} = 1$  keV; see §3.2.1). We note that the resultant best-fit value of  $\beta$  from the optical/NIR data alone is somewhat large for this stage in the evolution and is inconsistent with the XRT observations under the assumption of a synchrotron-emission origin (e.g., Sari et al. 1998). As the X-ray and optical/NIR afterglows are fading at approximately the same rate at the SED extrapolation time ( $\alpha_X = -1.27 \pm 0.02$ ,  $\alpha_{\text{oir}} = -1.30 \pm 0.01$ ; see §3.3.1), we can assume they originate from the same component of the synchrotron spectrum. With the inclusion of the XRT data in the SMC dust fit, we obtain best-fit values of  $A_V = 0.88 \pm 0.01$  mag and  $\beta = -0.89 \pm 0.01$ .

That the SMC curve gives the best fit among the standard dust laws is consistent with the findings of previous studies (e.g., Schady et al. 2012; Covino et al. 2013). However, the goodness of fit is still poor ( $\chi^2/\text{dof} = 44.0/8$ ) given the quality of the data. We thus attempted a more general fit using the full parameterization of Fitzpatrick (1999), which is described by six parameters:  $c_1$  and  $c_2$  are (respectively) the intercept and slope of the linear part of the UV component in  $E(\lambda - V)$ ,  $c_3$  is the strength of the 2175 Å bump,  $c_4$  is the strength of the rise in the FUV,  $x_0$  is the centroid of the 2175 Å bump in inverse microns ( $x_0 \approx 1/0.2175$ ), and  $\gamma$  is the width of that feature.

The values of  $x_0$  and  $\gamma$  are not seen to vary widely among dust sight lines within the Local Group, and thus we opt to keep these parameters fixed at  $x_0 = 4.626$  and  $\gamma = 1.05$ . Furthermore, the  $c_4$  parameter which gives the far-UV extinction curvature at wavelengths  $\lambda < 1700$  Å is poorly constrained due to the lack of sufficiently blue filters in our data. As such, we fixed this parameter to the average value of  $c_4 \approx 0.43$  found from the sample of Schady et al. (2012). All other parameters were allowed to vary freely. The resultant fits are shown in Table 3.3. While the parameter values without the XRT data included in the fit are poorly constrained, the best-fit dust law including the X-ray flux (henceforth FMX) shows a marked improvement over the other extinction laws ( $\chi^2/\text{dof} = 8.85/4$ ; Table 3.2). The best-fit FMX curve is shown in Figure 3.4 and yields values of  $A_V = 1.09 \pm 0.16$  mag and  $\beta = -0.92 \pm 0.02$ .

The best-fit FMX curve indicates that a weak 2175 Å bump may be present ( $c_3 = 0.69 \pm 0.32$ ), which at  $z = 1.728$  would lie nearly coincident with our  $R$  band observations. However, it is of marginal significance, and re-fitting the SED after fixing the bump strength as zero produces no appreciable difference in the best-fit values of the other parameters nor the overall quality of fit. Further, no evidence for this feature is seen in our Gemini spectrum (Figure 3.1). This feature has been more securely detected in several other GRBs, such as

Table 3.2: Results of Extinction Fits

Dust Model	+XRT?	$\beta$	$A_V$ (mag)	$\chi^2 / \text{dof}$
LMC	N	$-2.05 \pm 0.11$	$0.37 \pm 0.07$	135.8 / 7
LMC	Y	$-0.92 \pm 0.00$	$1.14 \pm 0.01$	230.1 / 8
LMC2	N	$-1.03 \pm 0.16$	$1.09 \pm 0.11$	69.5 / 7
LMC2	Y	$-0.92 \pm 0.00$	$1.16 \pm 0.01$	70.0 / 8
MW	N	$-2.50 \pm 0.09$	$0.07 \pm 0.06$	160.5 / 7
MW	Y	$-0.94 \pm 0.00$	$1.26 \pm 0.02$	464.6 / 8
SMC	N	$-1.39 \pm 0.11$	$0.62 \pm 0.06$	23.5 / 7
SMC	Y	$-0.89 \pm 0.00$	$0.88 \pm 0.01$	44.0 / 8
FM	N	$-1.04 \pm 3.27$	$0.97 \pm 3.26$	8.9 / 3
FM	Y	$-0.92 \pm 0.02$	$1.09 \pm 0.16$	8.9 / 4

Table 3.3: Best-Fit Fitzpatrick (1999) Dust Parameters for GRB 120119A

Dust Model	$A_V$ (mag)	$\beta$ (s)	$R_V$ (mag)	$c_1$	$c_2$	$c_3$	$c_4$	$\chi^2 / \text{dof}$
FM	$0.97 \pm 3.26$	$-1.04 \pm 3.27$	$4.13 \pm 1.32$	$-3.76 \pm 12.17$	$2.29 \pm 4.91$	$0.75 \pm 1.82$	0.43(fixed)	8.9 / 3
FMX	$1.09 \pm 0.16$	$-0.92 \pm 0.02$	$4.11 \pm 1.03$	$-3.36 \pm 0.59$	$2.13 \pm 0.27$	$0.69 \pm 0.32$	0.43(fixed)	8.9 / 4

GRB 070802 (Krühler et al. 2008; Elíasdóttir et al. 2009), GRB 080603A (Guidorzi et al. 2011), GRB 080605 (Zafar et al. 2012), GRB 080607 (Perley et al. 2011), and GRB 080805 (Zafar et al. 2012).

The closure relations of standard afterglow theory (e.g., Granot & Sari 2002; Piran 2005) can be used to infer the temporal decay index  $\alpha$  and spectral index  $\beta$  under various conditions through their relations with the electron spectral index  $p$ , allowing for a consistency check of our derived values for these two parameters. Under the assumption of an adiabatic expansion of the blast wave into a homogeneous external medium ( $n = \text{constant}$ ) in the slow-cooling regime, there are two possibilities for the spectral index  $\beta$  in the temporally decaying part of the light curve:  $\beta = -(p - 1)/2$  for  $\nu_m < \nu < \nu_c$ , and  $\beta = -p/2$  for  $\nu_c < \nu$ . The two possible values for  $\alpha$  in these regimes are  $\alpha = -3(p - 1)/4$  and  $\alpha = -3(p - 2)/4$ , respectively, leading to the closure relations  $\beta = 2\alpha/3$  for  $\nu$  between the peak frequency and the cooling break, and  $\beta = 2(\alpha - 1)/3$  for  $\nu > \nu_c$ . Adopting  $\alpha \approx -1.30$  at the SED extrapolation time, we derive  $\beta \approx -0.87$  for the  $\nu_m < \nu < \nu_c$  closure relation, consistent with our more secure determination of  $\beta = -0.92 \pm 0.02$  from the SED fit. In this interpretation, the cooling break has not yet passed through our bandpasses and the electron energy distribution index is  $p \approx 2.7$ .

We can further check our derived value of  $A_V$  by comparing it to the neutral hydrogen absorption excess as derived from X-ray data. Using the photon-counting mode (PC) data from the XRT, we measure  $N_H = 1.03_{-0.39}^{+0.46} \times 10^{22} \text{ cm}^{-2}$ . Watson & Jakobsson (2012) found that in addition to the general trend of a high  $A_V$  requiring large values of X-ray absorption (Schady et al. 2010), there is also a redshift trend indicating a dearth of low- $z$  events with low  $A_V$  and high  $N_H$ . This was expanded recently by Covino et al. (2013). While there

is significant scatter in this relation, our derived values of X-ray absorption and optical extinction are in general agreement with the  $N_{\text{H}}/A_V$  trend of events at similar redshifts.

### 3.3.3 Construction of Early-time SEDs

Our early-time observations are from a variety of telescopes and filters, at irregular times, and often rather sparsely sampled. In order to model color change as a function of time, we built up a series of SEDs at different temporal epochs using the PAIRITEL, PROMPT, Liverpool, and SMARTS photometry. PROMPT clear-filter observations were not included in the SED constructions due to complications in accurate color corrections with a changing sky background, and approximate redundancy with the equally well-sampled  $R$  filter.

One option for exploring color change as a function of time is to identify epochs where data through multiple filters were obtained nearly simultaneously. We explored this option, but coincident temporal alignment of images was only achievable six times within the first 20 min after the burst, leaving most of the data unused.

To circumvent this problem, interpolation was performed to create denser temporal sampling. Because the PAIRITEL observations had the highest time resolution, these were chosen for interpolation. We use a nonparametric light-curve estimate to interpolate the GRB brightness (and measurement errors) in epochs of incomplete photometric coverage. By using a flexible, nonparametric interpolation model, we avoid assuming an overly restrictive GRB template model and allow the data to determine the appropriate smooth light-curve shape.

To perform interpolation, we fit a natural cubic regression spline (Ruppert et al. 2003; Wasserman 2006) separately to the data from each of the three PAIRITEL bandpasses. We utilize regression splines because they are particularly adept at estimating smooth functions that may have complicated behavior such as periods of rapid decline and allow a straightforward estimate of both the brightness and model uncertainty of the brightness at each interpolation epoch (see, e.g., Richards et al. 2012 for usage in the context of SN light curves). Using a cubic spline model, the estimate of the magnitude in photometric band  $b$  at time  $t$  is

$$\widehat{m}_b(t) = \sum_{j=1}^{N+4} \widehat{\beta}_b(t) B_j(t), \quad (3.1)$$

where  $N$  is the number of spline knots,  $B_j$  is the  $j^{\text{th}}$  natural cubic spline basis, and the  $\widehat{\beta}_b(t)$  are estimates of the spline coefficients that are found by minimizing the weighted least-squares statistic of the spline-model magnitudes against the observed magnitudes  $m_b(t)$  with weights  $(1/\sigma_b(t))^2$ . Here,  $\sigma_b(t)$  is the observational error in the measurement of  $m_b(t)$ .

When fitting a regression spline, one must choose the quantity,  $N$ , and the locations of the knots, which correspond to points of discontinuity of the third derivative of the interpolated spline function. In this work, we follow convention and place the knots uniformly over the observed time points, which have been converted to logarithmic space. To choose  $N$ , we pick the value that minimizes the generalized cross-validation (GCV) score, which balances

the bias and variance of the fitted interpolation function with an explicit penalty to avoid overfitting to the observed data (see, e.g., Richards et al. 2012). The GCV criterion is defined as

$$\text{GCV}_b(N) = \frac{1}{n_b} \sum_{k=1}^{n_b} \left( \frac{m_b(t_k) - \widehat{m}_b(t_k)}{\sigma_b(t_k)(1 - N/n_b)} \right)^2, \quad (3.2)$$

where  $\widehat{m}_b(t_k)$  is the fitted value, at time  $t_k$ , of a spline with  $N$  knots, computed using Equation (3.1);  $t_1, t_2, \dots, t_{n_b}$  is the grid of epochs of observation in the light curve for photometric band  $b$ ; and  $n_b$  is the number of observed epochs of the light curve. In this formulation, the observational uncertainties in the measured magnitudes,  $\sigma_b(t_k)$ , are used to compute both the interpolated light-curve magnitude estimates,  $\widehat{m}_b(t)$ , and the model uncertainty in those estimates. Using the GCV criterion, we search for the optimal number of spline knots over the range 1–50, finding the optimal value to be 14 for each of the  $J$  and  $H$  bands, and 8 for  $K_s$ .

The spline regression provides a model uncertainty for each interpolation point, which must be combined in quadrature with an estimate of what the photometric uncertainty would have been had an observation taken place at that time. To approximate the latter, we performed another spline fit to the photometric uncertainties for each PAIRITEL filter as a function of time, assuming that each photometric uncertainty (§3.2.3) itself was uncertain at roughly the 10% level. The resultant fit is shown in the bottom panel of Figure 3.5; the optimal number of knots was 12, 6, and 7 for  $J$ ,  $H$ , and  $K_s$ , respectively. For each interpolated point, the associated uncertainty at a particular point in time was the mean approximate instrumental uncertainty inferred from this interpolation added in quadrature with the model uncertainty at that time.

The end result of the interpolation is a series of 4-7 color SEDs, finely sampled in time. While some bluer filters are occasionally included in these SEDs, the majority are 5-color  $RIJHK_s$  SEDs from PROMPT and PAIRITEL. While these alone cannot strongly break the intrinsic degeneracy between  $A_V$  and  $\beta$ , the longer lever arm afforded by the more secure late-time SED (3.3.2) gives us strong constraints on both these parameters and the type of dust. These SEDs can now be used to model the color change as a function of time.

### 3.3.4 Modelling Color Change

The simplest way to model the color change is to assume that the dust properties in the GRB environment are fixed and that only the spectral index  $\beta$  is causing the change. Each interpolated SED was fit under this assumption, with  $\beta$  left free and the dust parameters fixed at the inferred late-time values from the best-fit dust extinction law (FMX; see §3.3.2). The parameter  $\beta$  is fit independently at each SED, and no constraints are imposed on how it is allowed to vary with time. The results are shown in the left panel of Figure 3.6.

A second possibility is that the color change results from a superposition of two different emission components of different intrinsic spectral indices. In particular, a decaying reverse shock superimposed on a rising forward shock might qualitatively explain the ob-

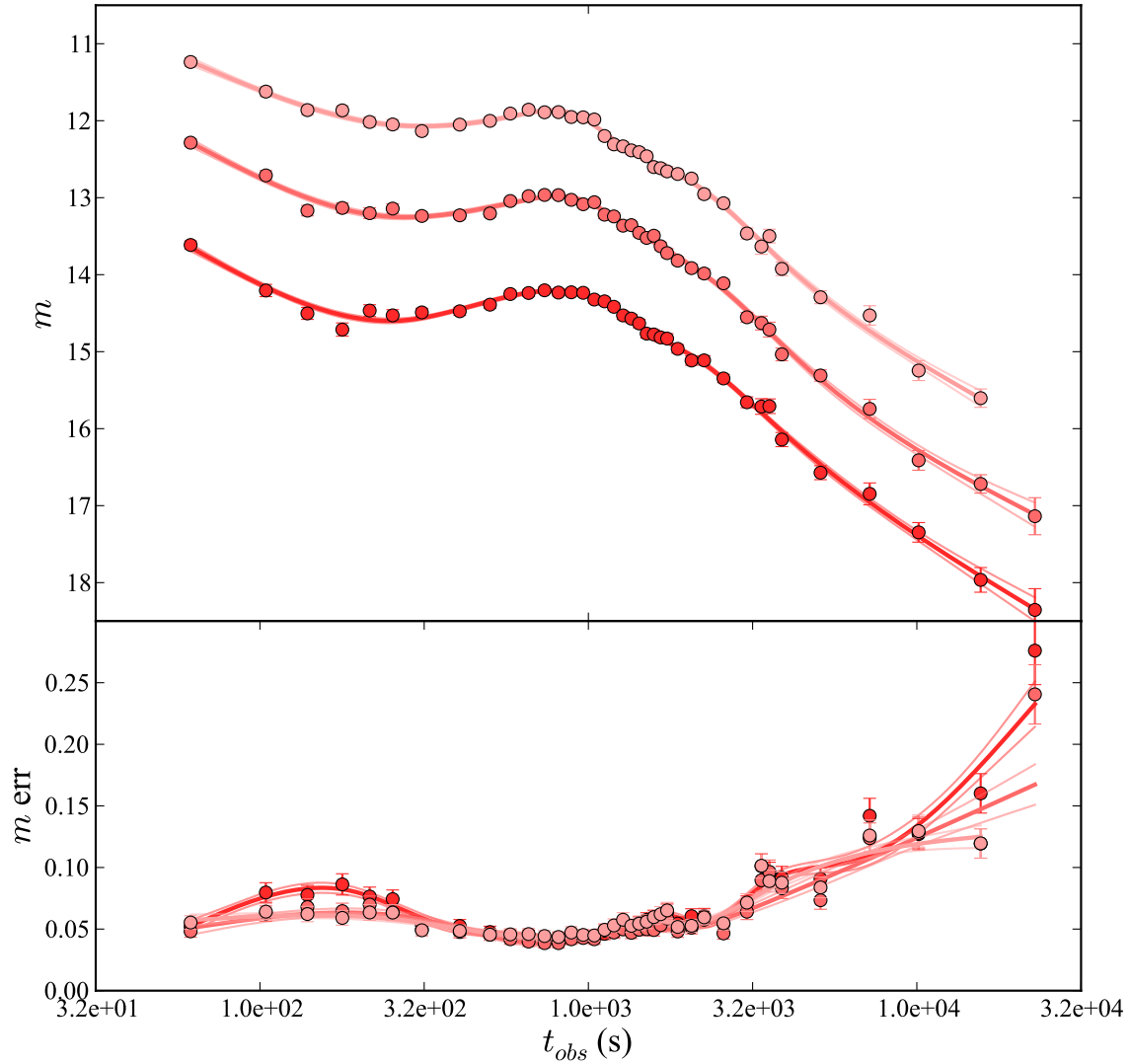


Figure 3.5: Natural cubic regression spline fits to the PAIRITEL data for use in interpolation. The upper plot shows the fit to the light curves, found via the GCV criterion to have an optimal number of 8 spline knots for  $K_s$ , and 14 for each of  $J$  and  $H$ . The bottom plot shows a fit to the photometric uncertainties, assuming each point was uncertain at the 10% level, in order to estimate these values at the interpolation points. The central lines show the optimal model fit, and the lighter outer lines show the model uncertainty. The plot colors are the same as in Figure 3.2.



served features (as previously seen in GRBs 061126, 080319B, and 130427A: Perley et al. 2008c; Bloom et al. 2009; Racusin et al. 2008b; Perley et al. 2014). We fixed the extinction to its late-time value and fit the light curve using the empirical model of Perley et al. (2008b), allowing the spectral indices of the early-time power-law component to differ from the late-time component. The fit at early times is poor and results in a spectral index change ( $\Delta\beta = 0.93$ ) that is much larger than seen in previous reverse/forward shock transitions, and larger than expected by theory. The presence of a bright reverse shock is also disfavored by the CARMA/VLA nondetections (§3.5).

We next explored whether time varying dust extinction signatures could be contributing to the color change. The photodestruction of dust is expected to alter both the extinction  $A_V$  and selective reddening  $R_V$  (e.g., Perna et al. 2003). There is also the possibility that the dust in the local environment of the GRB that would be affected has a significantly different extinction signature than the dust causing the observed late-time absorption. For simplicity we search for a change in the dust parameters by allowing only  $A_V$  to change and keeping all other extinction parameters fixed.

We refit each interpolated SED, allowing both  $A_V$  and  $\beta$  to vary freely, under no constraints as to how they are allowed to vary as a function of time. The results are shown in the right panel of Figure 3.6; they exhibit a drastic change compared with the left panel of this figure in both behavior and overall quality of fit (total  $\chi^2/\text{dof} = 146.7/108$  vs.  $\chi^2/\text{dof} = 277.7/171$ ). The fact that  $\beta$  alone is not the dominant source of color change in this fit gives a preliminary indication that a decrease in absorption may be present.

However, as this simple illustration imposes no constraints regarding how the parameters are allowed to change, the variations in  $A_V$  and  $\beta$  between epochs are often unphysically large and rapid. To account for this, simple, monotonic functional forms for  $A_V(t)$  and  $\beta(t)$  were assumed:

$$A_V(t) = A_{V,0} + \Delta A_V e^{-t/\tau_{A_V}}, \quad (3.3)$$

and

$$\beta(t) = \beta_0 + \Delta\beta e^{-t/\tau_\beta}. \quad (3.4)$$

In these parameterizations,  $A_{V,0}$  and  $\beta_0$  represent the late-time values of extinction and spectral index, and  $\Delta A_V$  and  $\Delta\beta$  correspond to the total change from the early-time values ( $t = 0$ ). No change in the total amount of extinction would thus be consistent with  $\Delta A_V = 0$ . In these fits,  $\Delta A_V$  was required to be positive; that is, we did not allow for an increase in extinction with time.

In fitting this model to the  $N$  SEDs constructed from  $M$  flux measurements as described in §3.3.3, we fixed the dust extinction model as well the late-time values of  $A_V$  and  $\beta$  inferred from that model for a variety of the late-time extinction curves shown in Table 3.2. In addition to the 4 remaining parameters  $\Delta A_V$ ,  $\Delta\beta$ ,  $\tau_{A_V}$ , and  $\tau_\beta$ , a flux normalization parameter was fit for each SED, leading to a total of  $M - (N + 4)$  degrees of freedom. The results are shown in Table 3.4. While the precise results are dependent on the assumed late-time extinction model, we note that in all cases,  $\Delta A_V$  is found to be positive to a statistically significant level. In other words, under the model assumptions, dust destruction is favored

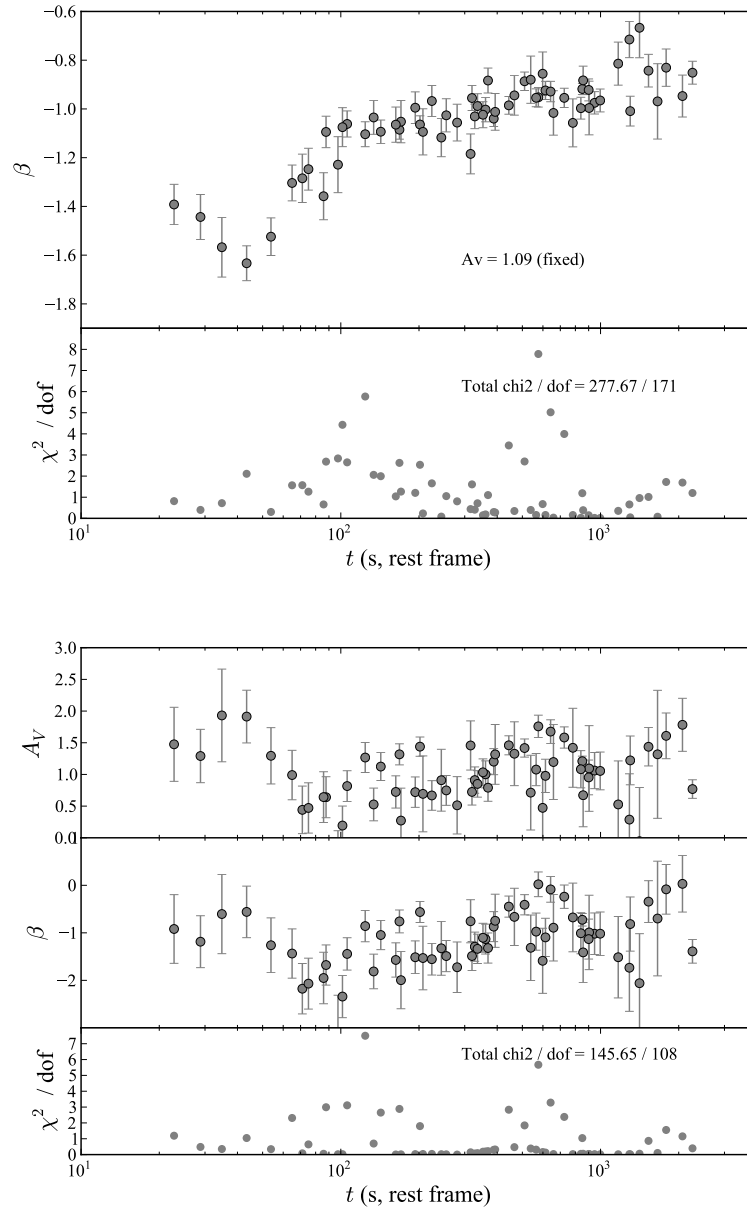


Figure 3.6: *Top panel:* The best-fit values of  $\beta$  for each interpolated SED as a function of time. The extinction  $A_V$  was fixed to the late-time value of 1.09 and FMX-like dust was assumed (see §3.3.2). Plotted below is the reduced  $\chi^2$  statistic for each individual fit. *Bottom panel:* Same as the top panel, but where both  $A_V$  and  $\beta$  were allowed to vary freely.

Table 3.4: Results of Color Change Fits

Dust Model	$A_{V,0}$ (mag)	$\Delta A_V$ (mag)	$\tau_{A_V}$ (s)	$\beta_0$	$\Delta\beta$	$\tau_\beta$ (s)	$\chi^2 / \text{dof}$
LMC2	-1.16 (fixed)	$0.47 \pm 0.72$	$57.51 \pm 63.09$	-0.92 (fixed)	$-0.33 \pm 0.81$	$65.32 \pm 121.31$	587.5 / 230
SMC	-0.88 (fixed)	$0.60 \pm 0.10$	$44.19 \pm 9.86$	-0.89 (fixed)	$-0.28 \pm 0.05$	$513.56 \pm 104.17$	383.5 / 230
FMX	-1.09 (fixed)	$0.61 \pm 0.15$	$39.00 \pm 13.34$	-0.92 (fixed)	$-0.28 \pm 0.09$	$258.90 \pm 71.18$	365.6 / 230

for each extinction law. The change in spectral index  $\beta$ , on the other hand, is less favored as the dominant source of color change, and its behavior with time is more dependent on the assumed extinction law.

As with the fits to the late-time dust, the extinction model that yielded the best fit to the color change was FMX, giving further support for this model over a simple SMC law. The behaviors of  $A_V$  and  $\beta$  with time using the best-fit values from this model are presented in Figure 3.7. To give a sense of the variance and covariance among the fit parameters, we drew 1500 samples from the resultant best-fit multivariate normal distribution (light-grey curves) with confidence contours overplotted (dashed lines contain 68% of the curves, dotted 95%).

Unlike the degeneracy typically seen between  $A_V$  and  $\beta$  in dust-model fits to optical/NIR SEDs, the parameters describing the change in  $A_V$  and  $\beta$  with time ( $\Delta A_V$  and  $\Delta\beta$ ) exhibit only mild covariance. After marginalizing over all other parameters the covariance is shown in Figure 3.8. Subject to all of the model assumptions outlined above, extinction change is expected with about  $4\sigma$  confidence, with a mean value of  $\Delta A_V = 0.61 \pm 0.15$  mag.

To guard against the fit falling into a local minimum, we fit each model 1000 times to the data over a randomly selected set of initial conditions for each fit parameter over the following ranges:  $0 \leq \Delta A_V \leq 2$  mag,  $-2 \leq \Delta\beta \leq 0$ ,  $0 \leq \tau_{A_V} \leq 1000$  s, and  $0 \leq \tau_\beta \leq 1000$  s. Each initial normalization parameter value was also randomly selected from a range encompassing all possible physical values. The fits given in Table 3.4 had both the best fits (lowest  $\chi^2$ ) as well as the plurality of convergences for each presented dust model.

### 3.3.5 Optical Rise and Shock Constraints

The color-change modelling described in §3.3.4 was performed free from assumptions of an underlying light-curve model; each time slice was treated independently and was fit with flux normalization as a free parameter. The analysis above indicates that this color change is likely caused at least in part by dust destruction (as will be discussed further in §3.4). As such, model-dependent absorption corrections would need to be performed in order to infer the intrinsic light curve, which itself could be produced by multiple emission components, including prompt emission from the central engine.

The second peak at  $\sim 800$  s (observer frame) is more straightforward to interpret. The lack of significant color change across the peak immediately rules out some possibilities for the optical rise. For instance, the passage of the peak frequency  $\nu_m$  of the forward-shock

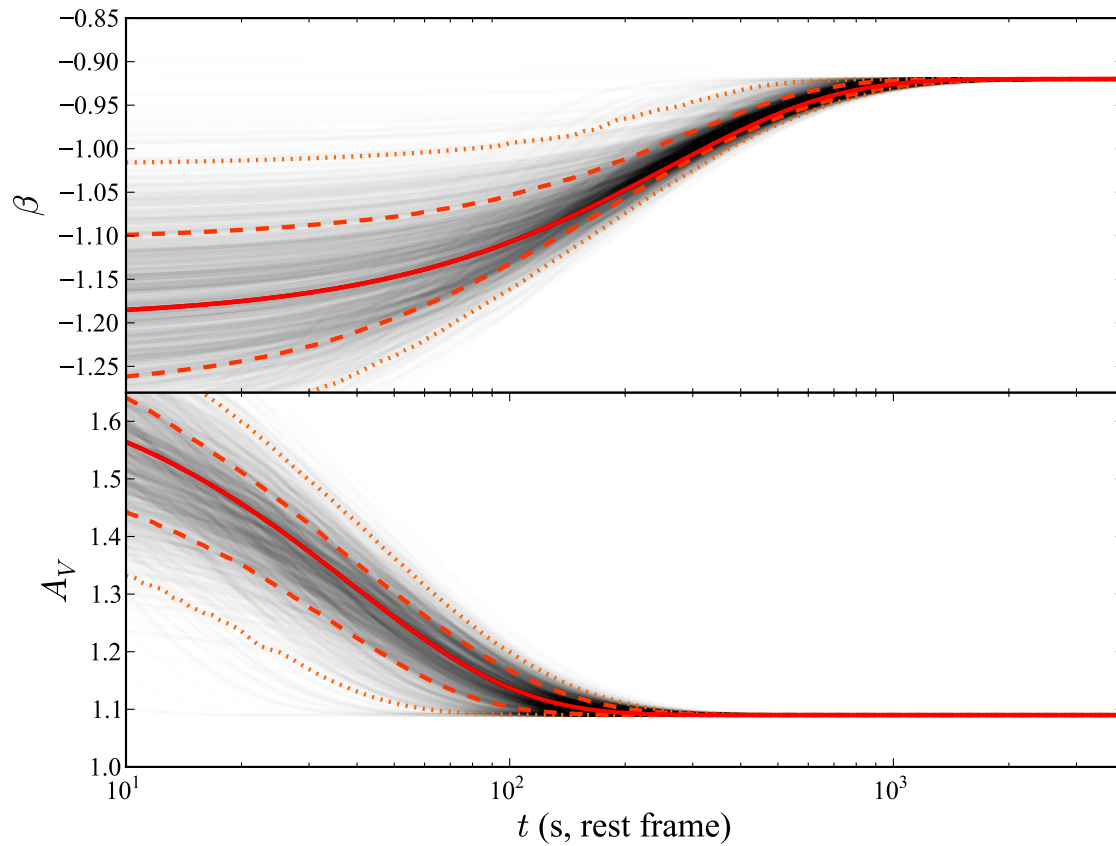


*Figure 3.7:* Best-fit values for  $A_V(t)$  (mag) and  $\beta(t)$  according to the functional forms of Equations 3.3 and 3.4, simultaneously fit to all available data at each SED interpolation point. FMX-type dust was assumed (§3.3.2). Light-grey lines show the resultant curve from one of the 1500 samples drawn from the multivariate normal distribution from the best-fit model. The mean value is plotted in red, with confidence contours overplotted with dashed lines (containing 68% of the curves) and dotted lines (containing 95% of the curves).

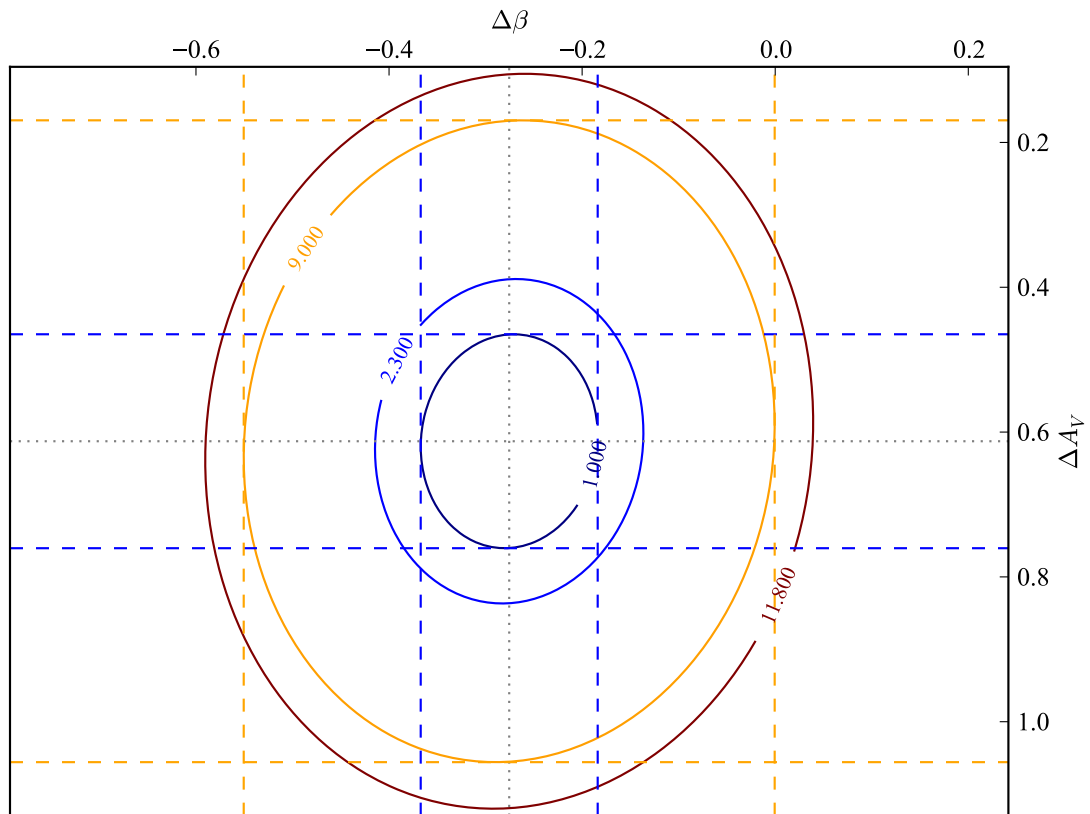


*Figure 3.8:* Covariance between parameters  $\Delta A_V$  and  $\Delta\beta$  from Equations 3.3 and 3.4. These parameters correspond to the total change in the values of  $A_V$  and  $\beta$  over the course of the light curve (i.e., a value of  $\Delta A_V = 0$  would be consistent with no change in the amount of dust). The outer blue ellipse ( $\Delta\chi^2 = 2.3$ ) and the outermost red ellipse ( $\Delta\chi^2 = 11.8$ ) show the 68.3% and 99.73% confidence intervals for two degrees of freedom. The dotted blue and orange lines show the projections for a further marginalization to a single parameter of interest, corresponding to the  $1\sigma$  and  $3\sigma$  confidence intervals for  $\Delta A_V$  and  $\Delta\beta$  alone.

synchrotron emission through the observed bands would produce a temporal rise if it occurred after the initial fireball deceleration. However, this would result in a blue-to-red color change as  $\nu_m$  passes from high to low frequencies; for instance, for expansion into a homogeneous external medium in the slow-cooling regime, the intrinsic spectral index should pass from  $\beta \approx \nu^{1/3}$  to  $\beta \approx \nu^{-(p-1)/2}$ , where  $p$  is the electron energy index (Sari et al. 1998).

The achromatic steep rise and slow decay of the afterglow at this stage shows some of the hallmarks of the onset of the forward shock as the fireball sweeps through the external medium. If this is the reason for the peak, we can use the time of the peak to obtain an estimate of the initial Lorentz factor  $\Gamma$ . Following the methodology of Mészáros (2006) and Rykoff et al. (2009), and assuming a constant circumburst density profile such as that of the interstellar medium (hereafter “ISM-like”), we have

$$\begin{aligned} \Gamma_0 \approx 2\Gamma_{\text{dec}} &= 2 \left( \frac{3E_{\text{iso}}}{32\pi n m_p c^5 \eta t_{\text{pk},z}^3} \right)^{1/8} \\ &\approx 560 \left( \frac{3E_{\text{iso},52}}{n_0 \eta_{0.2} t_{\text{pk},z,10}^3} \right)^{1/8}. \end{aligned} \quad (3.5)$$

In this equation,  $E_{\text{iso},52}$  is the isotropic  $\gamma$ -ray energy release in units of  $10^{52}$  erg,  $n_0$  is the circumburst density in units of  $\text{cm}^{-3}$ ,  $\eta_{0.2} = \eta/0.2$  is the radiative efficiency, and  $t_{\text{pk},z,10}$  is the rest-frame afterglow peak time in units of 10 s.

This determination requires an estimate of  $E_{\text{iso}}$ , as derived from the spectral model of the gamma-ray data. For consistency with the analysis of Rykoff et al. (2009), we adopt the value of  $E_{\text{iso}}$  derived from the methodology of Butler et al. (2007), utilizing a Bayesian analysis with BATSE spectral priors to estimate  $E_{\text{iso}}$  using the relatively narrow range of (15–150 keV) from the BAT. However, the estimate of  $\Gamma$  is only weakly dependent on  $E_{\text{iso}}$  (1/8<sup>th</sup> power), so the slightly different estimates (by a factor of  $< 2$ ) from *Konus-Wind* (Golenetskii et al. 2012) and *Fermi* GBM (Gruber 2012) does not significantly alter the result. Using  $E_{\text{iso}} = 2.1 \times 10^{53}$  erg and  $t_{\text{pk},z} \approx 300$  s, we find  $\Gamma_0 \approx 260(n_0 \eta_{0.2})^{-1/8}$ .

The redshift of GRB 120119A is comparable to that of GRB 990123, for which a bright radio flare from the reverse shock was detected. The reverse-shock emission observed for GRB 990123 peaked at  $\sim 1$  day since burst, at a flux level of  $\sim 100$ – $260 \mu\text{Jy}$  (Galama et al. 1999; Kulkarni et al. 1999) in the GHz range. Our CARMA upper limit on GRB 120119A (§3.2.12) does not allow us to exclude a radio flare as bright as the one of GRB 990123. However, GRB 120119A was also observed with the EVLA beginning 2012 January 21.2 (2.0 days after the burst) at a mean frequency of 5.8 GHz (Zauderer & Berger 2012). No significant radio emission was detected to a  $3\sigma$  upper limit of  $34 \mu\text{Jy}$ . This upper limit is below the  $\sim 5$  GHz flux of  $164 \pm 100 \mu\text{Jy}$  measured by Galama et al. (1999) at  $\sim 2$  day since GRB 990123. A reverse-shock contribution as bright as the one observed in GRB 990123 is thus disfavored in the case of GRB 120119A.

Hereafter, we check whether the CARMA upper limit can constrain the forward-shock parameters when combined with the optical-to-X-ray observations of GRB 120119A. The

similarity of the optical/NIR and X-ray temporal slopes, starting from  $\sim 3 \times 10^3$  s since the burst, suggests that the synchrotron frequency  $\nu_m$  is below the optical/NIR band ( $\nu_m \propto t^{-3/2}$ ; Sari et al. 1998), which allows for a determination of an upper limit on  $\nu_m$ . A lower limit can be placed on  $\nu_m$  by extrapolating the *R*-band optical flux to the time of the CARMA observation with our light-curve model (§3.3.1), under the assumption that the synchrotron self-absorption frequency  $\nu_a$  is below the CARMA band at the time of our observation, using

$$F_{95\text{ GHz}} = F_{\text{opt}} \left( \frac{\nu_{\text{opt}}}{\nu_m} \right)^{-\beta_{\text{opt}}} \left( \frac{\nu_m}{95\text{ GHz}} \right)^{-1/3} \lesssim 0.99\text{ mJy}. \quad (3.6)$$

This gives the bounds  $5.49 \times 10^{11} < \nu_m < 4.07 \times 10^{12}$  Hz and  $3.3 \times 10^2 \mu\text{Jy} < F_m < 1.8 \times 10^3 \mu\text{Jy}$ . In addition, since no strong evidence for a break is observed in the X-ray light curve up to  $\sim 1$  day since the burst, we can constrain the cooling-break frequency to be  $\nu_c(1\text{ day}) \gtrsim 1$  keV.

These constraints can be used to make estimates of the circumburst density  $n$ , the fraction of energy imparted to swept-up electrons  $\eta_e$ , and the fraction of energy going into magnetic fields  $\eta_B$ . Using the formalism of Yost et al. (2003) and assuming an adiabatically expanding fireball and a constant (ISM-like) circumburst matter density, a solution satisfying our constraints (using  $p = 2.7$  as estimated above) is  $n \approx 0.1\text{ cm}^{-3}$ ,  $\epsilon_B \approx 5 \times 10^{-4}$ , and  $\epsilon_e \approx 0.1$ , consistent with values found for other *Swift* events (Liang et al. 2008; Melandri et al. 2010). We note, however, that this set of parameters would imply a slightly higher flux at the time and frequency of the EVLA observation ( $\sim 100 \mu\text{Jy}$ ) than the upper limit of Zauderer & Berger (2012), under the assumptions outlined above.

### 3.3.6 Host-Galaxy Properties

The detection of a nonfading, extended source coincident with the GRB afterglow days to months after the GRB indicates that we have detected the GRB host galaxy. Given the negligible offset and relative brightness of the source ( $< 0.2''$  and  $R = 24.8$  mag), we calculate a very small probability of chance coincidence:  $P_{\text{chance}} = 4 \times 10^{-3}$  (Bloom et al. 2002).

The negligible fading in the *K* band relative to the late-time data (and only very marginal fading of the optical counterpart at 1–7 days) indicates that contribution of an afterglow to our photometry of the host galaxy at 4 days and later is essentially negligible, allowing us to categorize the properties of the host photometrically. Our host photometry is given in Table 3.5 and our *HST* imaging is shown in Fig. 3.9. The host color is observed to be quite red (although not quite as red as the afterglow), with  $R - K = 3.6$  mag (2.0 mag AB) after correction for Galactic reddening. This value is much redder than typical unobscured GRB hosts (Le Flocc’h et al. 2003; Hjorth et al. 2012) and fairly characteristic of the “dark” GRB host population (Perley et al. 2013; Rossi et al. 2012; Krühler et al. 2011b).

We fit the combined dataset to a range of simple population-synthesis models with Calzetti et al. (2000) extinction and constant star-formation history. Importantly, our models include an empirical treatment of nebular emission lines based on the relations of Kennicutt (1998), Kewley & Dopita (2002), and Kewley et al. (2004).



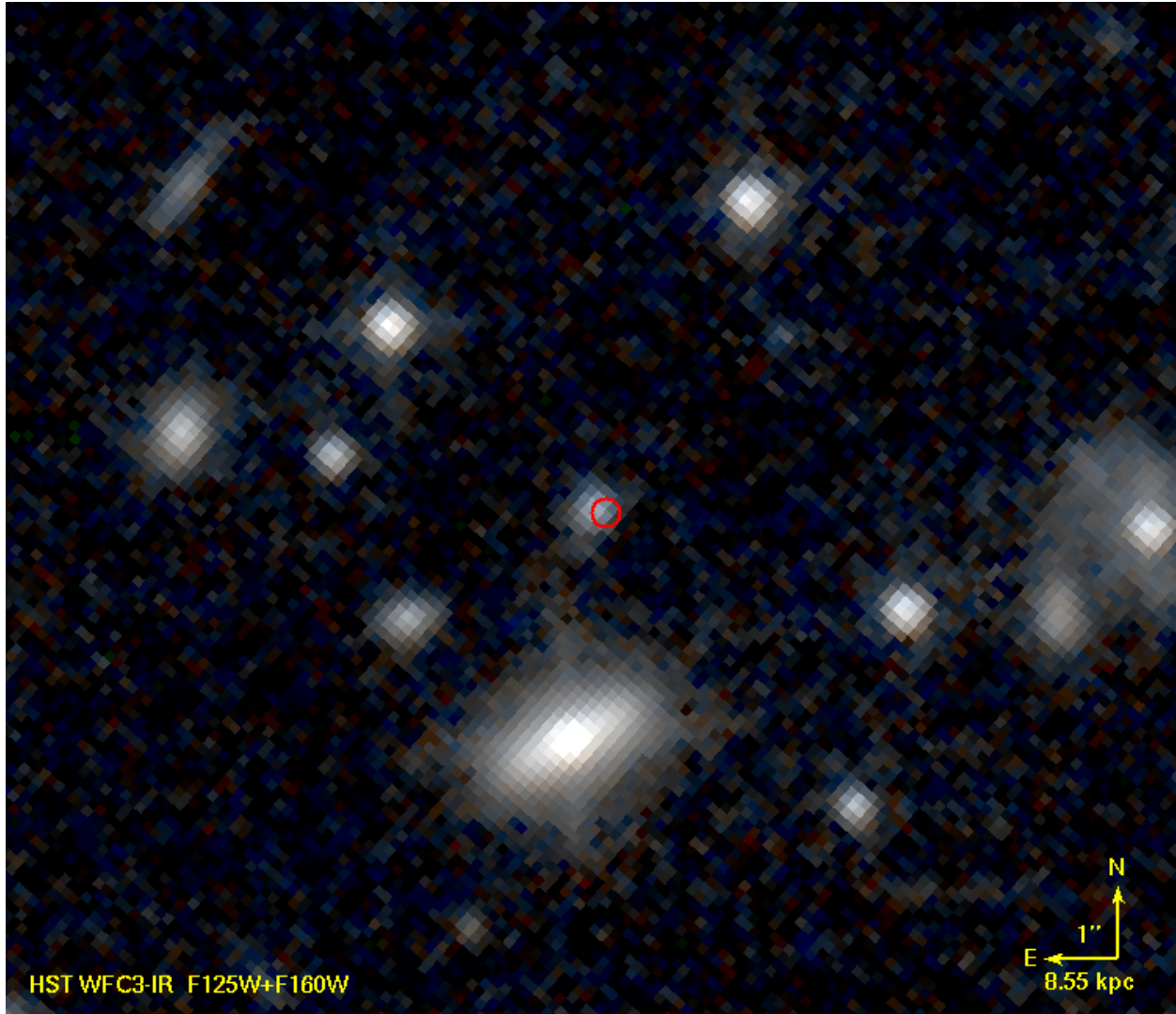


*Figure 3.9:* False-color NIR *HST* imaging of the field of GRB 120119A using the F125W and F160W filters of WFC3-IR, taken 9 months after the GRB. The host galaxy appears as a compact source centered slightly east of the optical position (red circle) with some extension in the NW and SSE directions. Given the redshift of the host, the blue color suggests substantial line contribution to the *J* band and a very large specific star-formation rate. There are no obvious signs of ongoing interaction at this resolution. The limiting magnitudes of the image are  $F125W = 25.6$  and  $F160W = 25.4$  (AB).



Table 3.5: GRB 120119A Host Photometry

Filter	Magnitude	$1\sigma$ Uncertainty
<i>B</i>	25.50	0.13
<i>g'</i>	25.27	0.05
<i>R</i>	24.60	0.17
<i>R</i>	24.68	0.11
<i>I</i>	23.65	0.13
<i>z'</i>	24.12	0.13
<i>K</i>	20.91	0.13
<i>F125W</i>	23.13	0.04
<i>F160W</i>	23.34	0.07

Note. — Values in this table have not been corrected for Galactic extinction.

The resulting SED is nearly flat in  $\nu F_\nu$ , with no evidence of a Balmer break, indicating a young population. A large upturn is evident in the F125W filter relative to all other bands; this feature is highly significant (given the excellent quality of the *HST* photometry) and cannot be explained by any model invoking the stellar continuum alone. This feature probably results from the [O III] and  $H\beta$  emission lines falling within the F125W bandpass — which, given the strength of the upturn, would imply that these features contribute approximately a third of the flux in the F125W broadband filter. This implies an extremely young stellar population. Based on our SED fitting procedure, we estimate a current star-formation rate of  $\sim 200 M_\odot \text{ yr}^{-1}$  and a stellar mass of only  $M \approx 2 \times 10^9 M_\odot$ . The mean attenuation is  $A_V \approx 1.8$  mag, indicating a quite dusty galaxy.

These properties suggest a young, vigorously star forming, dusty galaxy, with a star-formation rate one hundred times larger than that of the Milky Way despite a mass comparable to that of the LMC. Given the extreme inferred star-formation rate, we predict that the nebular lines of this host should be easily detectable with NIR spectroscopy, and the host should be detectable with current radio and millimeter/submillimeter facilities as well. The small size of the galaxy and the concentration of most of the light in the core indicates that much of this star formation is occurring within a very small volume ( $\lesssim 1''$  in diameter, corresponding to 8 kpc) and over a very short timescale ( $\sim 10^7$  yr) without an obvious merger trigger apparent in our imaging, although it is possible that even higher-resolution observations (with *HST* WFC3-UVIS or ACS, or ALMA) will resolve the core into a late-stage merger.

### 3.4 Discussion and Conclusions

The photodestruction of dust in the environments of GRBs is expected to occur at early times after the initial blast of high-energy radiation (Perna & Loeb 1998; Waxman & Draine 2000; Draine & Hao 2002). Simultaneous, multi-color imaging of the afterglow (especially during the high-intensity, high-energy emission) is necessary to observe both the decrease in

opacity and red-to-blue color change associated with dust destruction (Fruchter et al. 2001; Perna et al. 2003). Perley et al. (2010b) tested for this in the case of GRB 071025 with simultaneous  $JHK_s$  and unfiltered optical data (which resembled the  $I$  band due to the redness of the afterglow). They binned the optical and NIR measurements to temporally match, and dust models were fit at each four-point SED, allowing both the extinction and intrinsic spectral index  $\beta$  to vary. No evidence for a change in absorption was seen, notably during the the first bin, which coincides with the end of the prompt X-ray emission, ruling out dust destruction after the start of the NIR observations ( $\sim 150$  s).

We extended upon this methodology for GRB 120119A by performing interpolation via natural cubic regression splines to the densely sampled PAIRITEL data, which could then be combined with our other photometry (most notably the usually simultaneous PROMPT  $R$  and  $I$  filters) to create a dense temporal series of early-time SEDs (§3.3.3). The extinction properties inferred from late-time data were held as fixed (Fig. 3.4), and  $\beta$  was fit to each SED. We then explored whether allowing the extinction to vary with time could improve the fit (Fig. 3.4).

Both  $A_V$  and  $R_V$  (the latter of which we left fixed in our modelling) are expected to change with time in nontrivial ways under the influence of a high-intensity, high-energy radiation field. Detailed dust-destruction simulations by Perna et al. (2003) present the time evolution of extinction and reddening for a variety of environments (density and radius), dust distributions, and dust-to-gas ratios. These simulations highlight the complex interplay between changes in extinction and reddening with time and are highly dependent on the local environment. Note also that these simulations assume a constant luminosity from the X-ray source, and a fixed spectral index ( $\beta = 0.5$ ). A changing luminosity of the photoionizing radiation and a changing spectral index, as are present in GRB prompt emission, further complicate the issue. Choosing a rigorous parametric model to fit (and inferring meaningful constraints on its parameters) would be very difficult without detailed simulations allowing for the effects of changing luminosities and spectral indices.

Regardless, our relatively simplistic choice of functional forms for how  $A_V(t)$  and  $\beta(t)$  could vary (Equations 3.3 and 3.4) did in fact cause a statistically significant improvement in the overall fit compared to a fixed  $A_V$ . While not definitively implying dust destruction in GRB 120119A, simultaneous changes in  $A_V$  and  $\beta$  can account for the variations in the SED much better than a changing  $\beta$  alone.

Within the assumptions of the model, and by fixing the late-time extinction parameters to the best-fit values derived in §3.3.2, the extinction  $A_V$  is expected to decrease by an average of  $0.61 \pm 0.15$  mag (Fig. 3.7), with at least  $\sim 0.15$  mag of extinction change to a 99.73% level ( $3\sigma$ ; Fig. 3.8). Alternative parametric models may be more appropriate, but the limited spectral coverage at each temporal point prevents stringent model selection. Moreover, the inference of dust destruction appears to be robust against the exact choice of assumed late-time extinction curve, as all reasonable tested dust models resulted in this conclusion (after fixing the late-time  $A_V$  and  $\beta$  to their best-fit values for each particular model). In further support of the general conclusion of dust destruction, we note that the bulk of the color change is ongoing during the tail end of the high-intensity X-ray emission,

during which dust destruction is expected to occur (Fruchter et al. 2001).

Finally, we note that this work highlights the importance of well-sampled, multi-color early-time observations afforded by small and nimble fully robotic telescopes quickly training on the GRB location. Delays of seconds matter at this stage of the evolution of the GRB, and the importance of observation speed outweighs that of observation depth. The combination of shallow-and-fast robotic follow-up observations with deep late-time observations across the electromagnetic spectrum is necessary to illustrate the full story behind the evolution of GRB afterglows, which still to this day are revealing new insights.

## Acknowledgments

PAIRITEL is operated by the Smithsonian Astrophysical Observatory (SAO) and was made possible by a grant from the Harvard University Milton Fund, a camera loan from the University of Virginia, and continued support of the SAO and UC Berkeley. The PAIRITEL project is further supported by NASA/*Swift* Guest Investigator grants NNX10AI21G and NNX12AD73G. We utilized observations obtained at the Gemini Observatory, which is operated by the Association of Universities for Research in Astronomy, Inc., under a cooperative agreement with the NSF on behalf of the Gemini partnership: the NSF (United States), the Science and Technology Facilities Council (United Kingdom), the National Research Council (Canada), CONICYT (Chile), the Australian Research Council (Australia), Ministério da Ciência, Tecnologia e Inovação (Brazil), and Ministerio de Ciencia, Tecnología e Innovación Productiva (Argentina). The Liverpool Telescope is operated on the island of La Palma by Liverpool John Moores University in the Spanish Observatorio del Roque de los Muchachos of the Instituto de Astrofísica de Canarias with financial support from the UK Science and Technology Facilities Council. KAIT and its ongoing operation were made possible by donations from Sun Microsystems, Inc., the Hewlett-Packard Company, AutoScope Corporation, Lick Observatory, the NSF, the University of California, the Sylvia and Jim Katzman Foundation, and the TABASGO Foundation. Some of the data presented herein were obtained at the W. M. Keck Observatory, which is operated as a scientific partnership among the California Institute of Technology, the University of California, and NASA; the Observatory was made possible by the generous financial support of the W. M. Keck Foundation. We wish to extend special thanks to those of Hawaiian ancestry on whose sacred mountain we are privileged to be guests. We are grateful to the staffs at the Gemini, Keck, and Lick Observatories for their assistance. This publication has made use of data obtained from the *Swift* interface of the High-Energy Astrophysics Archive (HEASARC), provided by NASA's Goddard Space Flight Center. We sincerely thank the *Swift* team for the rapid public dissemination, calibration, and analysis of the *Swift* data. We also thank Scott Barthelmy for his invaluable efforts in creating and maintaining the GCN system.

We thank the anonymous referee for their useful comments on this paper. We also thank Alex Kann for providing helpful suggestions to the text. C.G.M. acknowledges support from the Royal Society. A.V.F.Õs group at UC Berkeley has received generous financial assistance

---

from Gary and Cynthia Bengier, the Christopher R. Redlich Fund, the Richard and Rhoda Goldman Fund, the TABASGO Foundation, NSF grant AST-1211916, and NASA/*Swift* grants NNX10AI21G and NNX12AD73G. A.G. acknowledges funding from the Slovenian Research Agency and from the Centre of Excellence for Space Science and Technologies SPACE-SI, an operation partly financed by the European Union, the European Regional Development Fund, and the Republic of Slovenia. Support for this work was provided by NASA to D.A.P. through Hubble Fellowship grant HST-HF-51296.01-A awarded by the Space Telescope Science Institute, which is operated for NASA by AURA, Inc., under contract NAS 5-26555. We dedicate this paper to the memory of Weidong Li, who developed the software for KAIT automatic follow-up observations of GRBs; we deeply miss his friendship and collaboration, which were tragically taken away from us much too early.

Table 3.6: Photometry of GRB 120119A

Instrument (UT)	Filter	$t_{\text{mid}}^1$ (s)	Exposure Time (s)	Magnitude <sup>2</sup>	Mag. Uncertainty
KAIT	clear	299.00	20.0	16.96	0.07
KAIT	clear	399.00	20.0	17.02	0.09
KAIT	clear	498.00	20.0	16.87	0.06
KAIT	clear	598.00	20.0	16.76	0.10
KAIT	clear	698.00	20.0	16.75	0.06
KAIT	clear	796.00	20.0	16.75	0.07
KAIT	clear	896.00	20.0	16.70	0.07
KAIT	clear	995.00	20.0	16.68	0.07
KAIT	clear	1095.00	20.0	16.95	0.06
KAIT	clear	1195.00	20.0	17.04	0.06
KAIT	clear	1293.00	20.0	17.00	0.06
KAIT	clear	1403.00	40.0	17.15	0.06
KAIT	clear	1600.00	40.0	17.37	0.05
KAIT	clear	1733.00	40.0	17.35	0.05
KAIT	clear	1867.00	40.0	17.37	0.06
KAIT	clear	2004.00	40.0	17.56	0.08
KAIT	clear	2157.00	80.0	17.58	0.06
KAIT	clear	2422.00	80.0	17.65	0.06
KAIT	clear	2686.00	80.0	18.01	0.04
KAIT	clear	3289.00	200.0	18.42	0.07
KAIT	clear	3954.00	200.0	18.61	0.06
KAIT	clear	4620.00	200.0	18.87	0.09
KAIT	clear	5203.00	200.0	19.09	0.09
KAIT	clear	5463.00	180.0	19.11	0.09
KAIT	<i>I</i>	266.00	20.0	16.17	0.11
KAIT	<i>I</i>	365.00	20.0	16.12	0.10
KAIT	<i>I</i>	465.00	20.0	16.04	0.08
KAIT	<i>I</i>	565.00	20.0	16.03	0.11
KAIT	<i>I</i>	665.00	20.0	16.03	0.08
KAIT	<i>I</i>	765.00	20.0	15.91	0.07
KAIT	<i>I</i>	862.00	20.0	16.09	0.11
KAIT	<i>I</i>	962.00	20.0	15.98	0.10
KAIT	<i>I</i>	1072.00	40.0	16.13	0.07
KAIT	<i>I</i>	1271.00	40.0	16.28	0.07
KAIT	<i>I</i>	1469.00	40.0	16.33	0.09
KAIT	<i>I</i>	1633.00	40.0	16.41	0.08
KAIT	<i>I</i>	1797.00	100.0	16.70	0.09
KAIT	<i>I</i>	2134.00	100.0	16.95	0.10
KAIT	<i>I</i>	2465.00	100.0	17.06	0.11
KAIT	<i>I</i>	3191.00	200.0	17.32	0.06
KAIT	<i>I</i>	3854.00	200.0	17.49	0.09
KAIT	<i>I</i>	4522.00	200.0	18.09	0.14
KAIT	<i>V</i>	252.00	60.0	18.15	0.22
KAIT	<i>V</i>	552.00	60.0	18.29	0.20
KAIT	<i>V</i>	859.00	80.0	18.49	0.35
KAIT	<i>V</i>	1258.00	80.0	18.11	0.19
Liverpool	<i>i'</i>	1210.26	120.0	16.83	0.03
Liverpool	<i>i'</i>	1834.44	120.0	17.23	0.04
Liverpool	<i>i'</i>	1966.26	120.0	17.30	0.04
Liverpool	<i>i'</i>	2892.54	120.0	17.98	0.06
Liverpool	<i>i'</i>	3024.42	120.0	18.03	0.03
Liverpool	<i>i'</i>	3157.32	120.0	18.07	0.05
Liverpool	<i>r'</i>	193.98	80.0	17.78	0.11

Table 3.6 (cont'd): Photometry of GRB 120119A

Instrument (UT)	Filter	$t_{\text{mid}}^1$ (s)	Exposure Time (s)	Magnitude <sup>2</sup>	Mag. Uncertainty
Liverpool	$r'$	276.84	80.0	17.61	0.08
Liverpool	$r'$	360.48	80.0	17.58	0.08
Liverpool	$r'$	444.12	80.0	17.57	0.08
Liverpool	$r'$	527.76	80.0	17.44	0.07
Liverpool	$r'$	611.40	80.0	17.34	0.07
Liverpool	$r'$	694.80	80.0	17.36	0.08
Liverpool	$r'$	872.76	10.0	17.32	0.05
Liverpool	$r'$	894.60	10.0	17.43	0.05
Liverpool	$r'$	916.50	10.0	17.39	0.05
Liverpool	$r'$	961.86	10.0	17.48	0.06
Liverpool	$r'$	984.12	10.0	17.47	0.05
Liverpool	$r'$	1005.96	10.0	17.34	0.05
Liverpool	$r'$	1058.16	120.0	17.59	0.02
Liverpool	$r'$	1541.10	120.0	17.93	0.02
Liverpool	$r'$	1673.88	120.0	17.98	0.02
Liverpool	$r'$	2455.56	120.0	18.43	0.03
Liverpool	$r'$	2587.44	120.0	18.57	0.03
Liverpool	$r'$	2719.68	120.0	18.64	0.03
Liverpool	$z'$	1373.46	120.0	16.33	0.04
Liverpool	$z'$	2128.26	120.0	16.78	0.04
Liverpool	$z'$	2260.20	120.0	16.82	0.03
P60	$g'$	12834.03	540.0	21.86	0.09
P60	$g'$	19187.24	540.0	22.09	0.12
P60	$g'$	99870.00	3600.0	>22.24	...
P60	$i'$	13427.89	540.0	20.28	0.05
P60	$i'$	19781.24	540.0	20.48	0.05
P60	$i'$	97870.00	3240.0	>22.02	...
P60	$r'$	14021.61	540.0	21.01	0.07
P60	$r'$	20375.23	540.0	21.57	0.11
PAIRITEL	$H$	61.50	15.6	12.29	0.05
PAIRITEL	$H$	104.24	23.4	12.71	0.06
PAIRITEL	$H$	139.49	23.4	13.17	0.07
PAIRITEL	$H$	178.15	23.4	13.13	0.06
PAIRITEL	$H$	215.84	23.4	13.20	0.07
PAIRITEL	$H$	253.58	23.4	13.14	0.06
PAIRITEL	$H$	311.13	46.8	13.24	0.05
PAIRITEL	$H$	405.83	46.8	13.23	0.05
PAIRITEL	$H$	501.56	46.8	13.20	0.05
PAIRITEL	$H$	578.52	46.8	13.04	0.04
PAIRITEL	$H$	657.70	46.8	12.98	0.04
PAIRITEL	$H$	735.34	46.8	12.96	0.04
PAIRITEL	$H$	810.72	46.8	12.97	0.04
PAIRITEL	$H$	887.10	46.8	13.03	0.04
PAIRITEL	$H$	964.24	46.8	13.08	0.04
PAIRITEL	$H$	1042.36	46.8	13.06	0.04
PAIRITEL	$H$	1119.79	46.8	13.22	0.05
PAIRITEL	$H$	1195.71	46.8	13.24	0.05
PAIRITEL	$H$	1274.87	46.8	13.36	0.05
PAIRITEL	$H$	1351.51	46.8	13.36	0.05
PAIRITEL	$H$	1427.32	46.8	13.46	0.05
PAIRITEL	$H$	1504.41	46.8	13.52	0.05
PAIRITEL	$H$	1582.05	46.8	13.49	0.05
PAIRITEL	$H$	1659.23	46.8	13.63	0.05

Table 3.6 (cont'd): Photometry of GRB 120119A

Instrument (UT)	Filter	$t_{\text{mid}}^1$ (s)	Exposure Time (s)	Magnitude <sup>2</sup>	Mag. Uncertainty
PAIRITEL	H	1736.67	46.8	13.72	0.06
PAIRITEL	H	1870.31	117.0	13.82	0.05
PAIRITEL	H	2060.75	117.0	13.91	0.05
PAIRITEL	H	2250.71	117.0	13.98	0.06
PAIRITEL	H	2578.47	280.8	14.11	0.05
PAIRITEL	H	3038.34	280.8	14.55	0.06
PAIRITEL	H	3364.40	117.0	14.63	0.09
PAIRITEL	H	3556.40	117.0	14.71	0.10
PAIRITEL	H	3880.96	280.8	15.04	0.08
PAIRITEL	H	5090.76	702.0	15.31	0.07
PAIRITEL	H	7186.38	1357.2	15.74	0.12
PAIRITEL	H	10125.95	2152.8	16.41	0.13
PAIRITEL	H	15645.71	4305.6	16.72	0.12
PAIRITEL	H	22881.03	4258.8	17.14	0.24
PAIRITEL	J	61.50	15.6	13.61	0.05
PAIRITEL	J	104.24	23.4	14.21	0.08
PAIRITEL	J	139.49	23.4	14.50	0.08
PAIRITEL	J	178.15	23.4	14.71	0.09
PAIRITEL	J	215.84	23.4	14.47	0.08
PAIRITEL	J	253.58	23.4	14.53	0.07
PAIRITEL	J	311.13	46.8	14.49	0.05
PAIRITEL	J	405.83	46.8	14.48	0.05
PAIRITEL	J	501.56	46.8	14.39	0.05
PAIRITEL	J	578.52	46.8	14.25	0.04
PAIRITEL	J	657.70	46.8	14.24	0.04
PAIRITEL	J	735.34	46.8	14.20	0.04
PAIRITEL	J	810.72	46.8	14.23	0.04
PAIRITEL	J	887.10	46.8	14.23	0.04
PAIRITEL	J	964.24	46.8	14.24	0.04
PAIRITEL	J	1042.36	46.8	14.32	0.04
PAIRITEL	J	1119.79	46.8	14.35	0.05
PAIRITEL	J	1195.71	46.8	14.42	0.05
PAIRITEL	J	1274.87	46.8	14.53	0.05
PAIRITEL	J	1351.51	46.8	14.57	0.05
PAIRITEL	J	1427.32	46.8	14.63	0.05
PAIRITEL	J	1504.41	46.8	14.77	0.06
PAIRITEL	J	1582.05	46.8	14.78	0.06
PAIRITEL	J	1659.23	46.8	14.81	0.06
PAIRITEL	J	1736.67	46.8	14.83	0.06
PAIRITEL	J	1870.31	117.0	14.96	0.05
PAIRITEL	J	2060.75	117.0	15.12	0.06
PAIRITEL	J	2250.71	117.0	15.11	0.06
PAIRITEL	J	2578.47	280.8	15.35	0.05
PAIRITEL	J	3038.34	280.8	15.66	0.07
PAIRITEL	J	3364.40	117.0	15.71	0.10
PAIRITEL	J	3556.40	117.0	15.71	0.09
PAIRITEL	J	3880.96	280.8	16.14	0.09
PAIRITEL	J	5090.76	702.0	16.57	0.09
PAIRITEL	J	7186.38	1357.2	16.85	0.14
PAIRITEL	J	10125.95	2152.8	17.35	0.13
PAIRITEL	J	15645.71	4305.6	17.96	0.16
PAIRITEL	J	22881.03	4258.8	18.35	0.28
PAIRITEL	K	61.50	15.6	11.24	0.06

Table 3.6 (cont'd): Photometry of GRB 120119A

Instrument (UT)	Filter	$t_{\text{mid}}^1$ (s)	Exposure Time (s)	Magnitude <sup>2</sup>	Mag. Uncertainty
PAIRITEL	<i>K</i>	104.24	23.4	11.62	0.06
PAIRITEL	<i>K</i>	139.49	23.4	11.86	0.06
PAIRITEL	<i>K</i>	178.15	23.4	11.87	0.06
PAIRITEL	<i>K</i>	215.84	23.4	12.02	0.06
PAIRITEL	<i>K</i>	253.58	23.4	12.05	0.06
PAIRITEL	<i>K</i>	311.13	46.8	12.13	0.05
PAIRITEL	<i>K</i>	405.83	46.8	12.05	0.05
PAIRITEL	<i>K</i>	501.56	46.8	12.00	0.05
PAIRITEL	<i>K</i>	578.52	46.8	11.91	0.05
PAIRITEL	<i>K</i>	657.70	46.8	11.86	0.05
PAIRITEL	<i>K</i>	735.34	46.8	11.89	0.04
PAIRITEL	<i>K</i>	810.72	46.8	11.89	0.04
PAIRITEL	<i>K</i>	887.10	46.8	11.95	0.05
PAIRITEL	<i>K</i>	964.24	46.8	11.96	0.05
PAIRITEL	<i>K</i>	1042.36	46.8	11.98	0.04
PAIRITEL	<i>K</i>	1119.79	46.8	12.20	0.05
PAIRITEL	<i>K</i>	1195.71	46.8	12.31	0.05
PAIRITEL	<i>K</i>	1274.87	46.8	12.33	0.06
PAIRITEL	<i>K</i>	1351.51	46.8	12.39	0.05
PAIRITEL	<i>K</i>	1427.32	46.8	12.41	0.05
PAIRITEL	<i>K</i>	1504.41	46.8	12.46	0.06
PAIRITEL	<i>K</i>	1582.05	46.8	12.60	0.06
PAIRITEL	<i>K</i>	1659.23	46.8	12.62	0.06
PAIRITEL	<i>K</i>	1736.67	46.8	12.66	0.07
PAIRITEL	<i>K</i>	1870.31	117.0	12.69	0.05
PAIRITEL	<i>K</i>	2060.75	117.0	12.75	0.05
PAIRITEL	<i>K</i>	2250.71	117.0	12.95	0.06
PAIRITEL	<i>K</i>	2578.47	280.8	13.07	0.05
PAIRITEL	<i>K</i>	3038.34	280.8	13.46	0.07
PAIRITEL	<i>K</i>	3364.40	117.0	13.63	0.10
PAIRITEL	<i>K</i>	3556.40	117.0	13.50	0.09
PAIRITEL	<i>K</i>	3880.96	280.8	13.92	0.09
PAIRITEL	<i>K</i>	5090.76	702.0	14.29	0.08
PAIRITEL	<i>K</i>	7186.38	1357.2	14.53	0.13
PAIRITEL	<i>K</i>	10125.95	2152.8	15.25	0.13
PAIRITEL	<i>K</i>	15645.71	4305.6	15.60	0.12
PAIRITEL	<i>K</i>	22881.03	4258.8	>16.41	...
PROMPT	<i>B</i>	241.06	40.0	19.46	0.37
PROMPT	<i>B</i>	290.30	40.0	19.06	0.28
PROMPT	<i>B</i>	338.69	40.0	19.05	0.26
PROMPT	<i>B</i>	388.80	40.0	19.11	0.29
PROMPT	<i>B</i>	458.78	80.0	19.13	0.17
PROMPT	<i>B</i>	551.23	80.0	19.37	0.20
PROMPT	<i>B</i>	1209.60	160.0	19.09	0.12
PROMPT	<i>B</i>	1391.04	160.0	19.23	0.14
PROMPT	<i>B</i>	1570.75	160.0	19.42	0.15
PROMPT	<i>B</i>	1753.06	160.0	19.76	0.23
PROMPT	<i>B</i>	1977.70	240.0	19.86	0.18
PROMPT	<i>B</i>	2276.64	240.0	19.84	0.18
PROMPT	<i>B</i>	3547.58	560.0	20.74	0.28
PROMPT	<i>B</i>	4161.02	480.0	20.87	0.35
PROMPT	<i>B</i>	5577.98	480.0	21.09	0.41
PROMPT	<i>g'</i>	88095.17	14400.0	>23.45	...



Table 3.6 (cont'd): Photometry of GRB 120119A

Instrument (UT)	Filter	$t_{\text{mid}}^1$ (s)	Exposure Time (s)	Magnitude <sup>2</sup>	Mag. Uncertainty
PROMPT	<i>I</i>	44.06	5.0	15.69	0.11
PROMPT	<i>I</i>	62.21	10.0	15.64	0.06
PROMPT	<i>I</i>	78.62	5.0	15.90	0.13
PROMPT	<i>I</i>	93.31	5.0	16.26	0.17
PROMPT	<i>I</i>	118.37	20.0	16.29	0.06
PROMPT	<i>I</i>	146.88	20.0	16.39	0.07
PROMPT	<i>I</i>	177.12	20.0	16.23	0.06
PROMPT	<i>I</i>	202.18	10.0	16.25	0.11
PROMPT	<i>I</i>	239.33	40.0	16.21	0.04
PROMPT	<i>I</i>	288.58	40.0	16.17	0.04
PROMPT	<i>I</i>	338.69	40.0	16.11	0.04
PROMPT	<i>I</i>	388.80	40.0	16.14	0.04
PROMPT	<i>I</i>	458.78	80.0	16.08	0.03
PROMPT	<i>I</i>	550.37	80.0	15.99	0.02
PROMPT	<i>I</i>	1209.60	160.0	16.12	0.03
PROMPT	<i>I</i>	1391.04	160.0	16.24	0.02
PROMPT	<i>I</i>	1571.62	160.0	16.33	0.03
PROMPT	<i>I</i>	1753.06	160.0	16.46	0.03
PROMPT	<i>I</i>	1977.70	240.0	16.63	0.03
PROMPT	<i>I</i>	2337.98	240.0	16.88	0.03
PROMPT	<i>I</i>	3523.39	560.0	17.43	0.04
PROMPT	<i>I</i>	4178.30	560.0	17.75	0.04
PROMPT	<i>I</i>	4879.87	560.0	17.95	0.05
PROMPT	<i>I</i>	5641.06	640.0	18.26	0.06
PROMPT	<i>I</i>	6498.14	800.0	18.43	0.06
PROMPT	<i>I</i>	7437.31	800.0	18.64	0.08
PROMPT	<i>I</i>	8589.02	800.0	18.83	0.09
PROMPT	<i>I</i>	9838.37	880.0	18.95	0.12
PROMPT	<i>I</i>	11219.04	800.0	19.18	0.14
PROMPT	<i>I</i>	12553.92	800.0	19.39	0.17
PROMPT	<i>I</i>	14552.35	1360.0	19.35	0.11
PROMPT	<i>I</i>	16818.62	1040.0	20.01	0.32
PROMPT	Open	39.74	5.0	16.93	0.07
PROMPT	Open	62.21	10.0	16.86	0.04
PROMPT	Open	76.90	5.0	17.09	0.07
PROMPT	Open	94.18	10.0	17.41	0.06
PROMPT	Open	118.37	20.0	17.47	0.04
PROMPT	Open	146.88	20.0	17.60	0.04
PROMPT	Open	176.26	20.0	17.45	0.04
PROMPT	Open	203.90	20.0	17.35	0.04
PROMPT	Open	241.06	40.0	17.31	0.02
PROMPT	Open	288.58	40.0	17.23	0.02
PROMPT	Open	338.69	40.0	17.19	0.02
PROMPT	Open	388.80	40.0	17.26	0.02
PROMPT	Open	458.78	80.0	17.19	0.01
PROMPT	Open	550.37	80.0	17.05	0.01
PROMPT	Open	1208.74	160.0	17.13	0.01
PROMPT	Open	1390.18	160.0	17.29	0.01
PROMPT	Open	1570.75	160.0	17.40	0.01
PROMPT	Open	1752.19	160.0	17.49	0.01
PROMPT	Open	1975.10	240.0	17.65	0.01
PROMPT	Open	2274.91	240.0	17.87	0.01
PROMPT	Open	3555.36	560.0	18.56	0.02

Table 3.6 (cont'd): Photometry of GRB 120119A

Instrument (UT)	Filter	$t_{\text{mid}}^1$ (s)	Exposure Time (s)	Magnitude <sup>2</sup>	Mag. Uncertainty
PROMPT	Open	4172.26	560.0	18.90	0.02
PROMPT	Open	4873.82	560.0	19.09	0.02
PROMPT	Open	5643.65	40.0	19.34	0.03
PROMPT	Open	6492.96	800.0	19.59	0.03
PROMPT	Open	7464.10	880.0	19.97	0.04
PROMPT	Open	8590.75	960.0	19.88	0.04
PROMPT	Open	9906.62	1200.0	20.22	0.06
PROMPT	Open	11922.34	2320.0	20.40	0.05
PROMPT	Open	14434.85	2000.0	20.60	0.06
PROMPT	Open	16656.19	1440.0	20.50	0.10
PROMPT	R	78.62	10.0	17.08	0.14
PROMPT	R	95.04	5.0	17.58	0.44
PROMPT	R	118.37	20.0	17.82	0.13
PROMPT	R	146.88	20.0	17.70	0.14
PROMPT	R	176.26	20.0	17.55	0.11
PROMPT	R	204.77	20.0	17.41	0.10
PROMPT	R	234.14	20.0	17.55	0.11
PROMPT	R	288.58	40.0	17.36	0.06
PROMPT	R	338.69	40.0	17.49	0.06
PROMPT	R	388.80	40.0	17.38	0.05
PROMPT	R	458.78	80.0	17.30	0.03
PROMPT	R	551.23	80.0	17.18	0.03
PROMPT	R	1209.60	160.0	17.34	0.03
PROMPT	R	1391.04	160.0	17.39	0.03
PROMPT	R	1570.75	160.0	17.62	0.03
PROMPT	R	1752.19	160.0	17.70	0.03
PROMPT	R	1975.97	240.0	17.83	0.03
PROMPT	R	2291.33	320.0	18.03	0.03
PROMPT	R	3549.31	560.0	18.77	0.04
PROMPT	R	4173.98	560.0	18.90	0.04
PROMPT	R	4877.28	560.0	19.16	0.06
PROMPT	R	5640.19	640.0	19.53	0.08
PROMPT	R	6494.69	800.0	19.68	0.08
PROMPT	R	7383.74	720.0	19.89	0.11
PROMPT	R	8616.67	880.0	20.04	0.12
PROMPT	R	9908.35	1040.0	20.18	0.15
PROMPT	R	11163.74	1040.0	20.29	0.16
PROMPT	R	12500.35	1040.0	20.55	0.18
PROMPT	R	14442.62	2080.0	20.64	0.14
PROMPT	R	16687.30	1520.0	20.67	0.20
PROMPT	R	88782.91	15200.0	>22.50	...
PROMPT	z'	89494.85	13040.0	>21.38	...
SMARTS	B	2320.78	180.0	19.89	0.06
SMARTS	H	2320.78	120.0	14.01	0.02
SMARTS	I	2320.78	180.0	16.93	0.06
SMARTS	I	6163.78	900.0	18.53	0.05
SMARTS	I	10678.79	900.0	19.36	0.05
SMARTS	I	80477.78	900.0	>21.70	...
SMARTS	J	2320.78	180.0	15.11	0.01
SMARTS	J	6163.78	720.0	16.85	0.02
SMARTS	J	10678.79	720.0	17.76	0.05
SMARTS	J	80477.78	720.0	>19.20	...
SMARTS	K	2320.78	180.0	12.92	0.08

*Table 3.6 (cont'd):* Photometry of GRB 120119A

Instrument (UT)	Filter	$t_{\text{mid}}^1$ (s)	Exposure Time (s)	Magnitude <sup>2</sup>	Mag. Uncertainty
SMARTS	<i>K</i>	6163.78	720.0	14.52	0.09
SMARTS	<i>K</i>	10678.79	720.0	15.55	0.08
SMARTS	<i>K</i>	80477.78	720.0	>17.00	...
SMARTS	<i>R</i>	2320.78	180.0	17.96	0.05
SMARTS	<i>V</i>	2320.78	120.0	18.83	0.03
SMARTS	<i>V</i>	6163.78	720.0	20.45	0.04
SMARTS	<i>V</i>	10678.79	900.0	21.21	0.06
SMARTS	<i>V</i>	80477.78	900.0	>23.00	...

<sup>1</sup>Time since the *Swift* trigger of the midpoint of the exposure.

<sup>2</sup>Magnitudes in this table have not been corrected for Galactic extinction ( $E(B - V) = 0.093$  mag). Observations in the  $g'$ -,  $r'$ -,  $i'$ -, and  $z'$ -bands are reported on the AB magnitude system.  $B$ -,  $V$ -,  $R$ -,  $I$ -,  $J$ -,  $H$ -, and  $K$ -band observations are referenced to Vega.

## Chapter 4

# The PAIRITEL Early-time Near-infrared GRB Afterglow Catalog

### 4.1 Introduction

The November 2004 launch of the *Swift* Gamma-Ray Burst Explorer (Gehrels et al. 2004) began a new era in the study of gamma-ray bursts (GRBs), the most energetic known explosions in the universe. The combination of the high detection rate ( $\sim 100/\text{yr}$ ) of the Burst Alert Telescope (BAT; Barthelmy et al. 2005) with precise localizations from the X-Ray Telescope (XRT; Burrows et al. 2005) and Ultraviolet/Optical Telescope (UVOT; Roming et al. 2005) allowed a global network of robotic follow-up facilities on the ground to begin observations within minutes of the burst. The rise of small and nimble robotic facilities not only served to inform deeper follow-up through rapid localization, but also opened a new window into understanding the properties of early-time UVOIR afterglows themselves.

While most *Swift* GRBs that are rapidly observed by its narrow-field instruments resulted in the detection of an X-ray afterglow, a far smaller fraction than expected of optical afterglows were detected with the UVOT (Roming et al. 2006). This was in part due to the intrinsically fainter and more distant GRB population selected by the sensitive *Swift* satellite compared to previous missions (Jakobsson et al. 2006b), but the additional suppression of optical flux relative to X-rays was necessary both to fully explain the observed optical detection rates and for the afterglows of some bursts to be compatible with standard synchrotron afterglow theory. While high-redshift origins leading to the suppression of optical flux from absorption in the IGM can be invoked to explain some events, the large number of optically suppressed GRBs with low measured redshift (e.g., Cenko et al. 2009a) necessitate alternative explanations.

Deep imaging surveys of GRB host galaxies (Perley et al. 2009b, 2013) and deep multi-color afterglow imaging surveys (Greiner et al. 2011) have revealed the primary cause of optical suppression of GRB afterglows to be moderate-to-large extinction columns along GRB sightlines. This suggests observational biases in conclusions drawn from surveys of afterglows selected for optical brightness. In contrast, because they are less affected by dust

extinction than their optical counterparts, near-infrared filters provide a less biased view of the distribution of UVOIR afterglow properties.

The robotic Peters Automatic Infrared Imaging Telescope (PAIRITEL; Bloom et al. 2006b) was designed explicitly for the follow-up of *Swift* GRBs and other transients with the northern (2MASS; Skrutskie et al. 2006) 1.3 m telescope. From its commissioning in late 2004 to its closure in August 2013, this completely automated system routinely responded to *Swift* GRB triggers for simultaneous  $J$ ,  $H$ , and  $K_s$ <sup>a</sup> imaging (see §4.2.1). Unlike many other facilities which are limited to imaging with a single filter at a time, PAIRITEL’s simultaneous multi-color imaging can capture color evolution free of assumptions regarding temporal behavior. This capability has been instrumental in thorough studies of individual events, particularly during the early-time afterglow where significant color-change has been seen to occur (e.g., Bloom et al. 2009; Morgan et al. 2014).

Newer facilities GROND (Greiner et al. 2008) and RATIR (Butler et al. 2012) now offer both larger apertures and a broader spectrum of simultaneous color observations. Nevertheless, what PAIRITEL lacked in size it made up for in speed, and remains unsurpassed in response time for multi-color NIR imaging<sup>b</sup>. Furthermore, prior to the commissioning of GROND in 2007, PAIRITEL provided the only rapid, simultaneous multi-color NIR imaging of GRB afterglows, and remained the only such facility in the northern hemisphere until the commissioning of RATIR in 2012. In this chapter, we present a catalog of observations of the earliest-time afterglows captured during PAIRITEL operations – those which were observed within three minutes of the *Swift* trigger. An overview of the data collection, reduction, and photometry is provided in §4.2, followed by the presentation of our observations in §4.3 and a discussion in §4.4.

## 4.2 Methodology

### 4.2.1 Data Collection

PAIRITEL consisted of the 1.3 m Peters Telescope at Mt. Hopkins, Arizona, which was formerly used for the Two Micron All Sky Survey (2MASS; Skrutskie et al. 2006) but was subsequently refurbished with the southern 2MASS camera. Upon receiving positional information from the BAT for a new *Swift* GRB trigger from GCN Notices<sup>c</sup>, the system automatically slewed the telescope to the trigger location if it did not violate observing constraints. The system further refined its pointing upon receiving updated positional information from XRT afterglow detections. Targets which were beyond observability constraints were placed in the schedule for later observation, when possible. Over 150 *Swift* GRBs were observed with this automated system within 24 hours of their triggers (Fig. 4.1).

<sup>a</sup> $J$ ,  $H$ , and  $K_s$  filters have effective wavelengths of  $1.24\mu\text{m}$ ,  $1.66\mu\text{m}$ , and  $2.16\mu\text{m}$ , respectively.

<sup>b</sup>We note, however, that the 60 cm REM (Covino et al. 2004) has achieved several instances of sub-minute response times with simultaneous imaging in two filters: one optical and one NIR.

<sup>c</sup><http://gcn.gsfc.nasa.gov/>

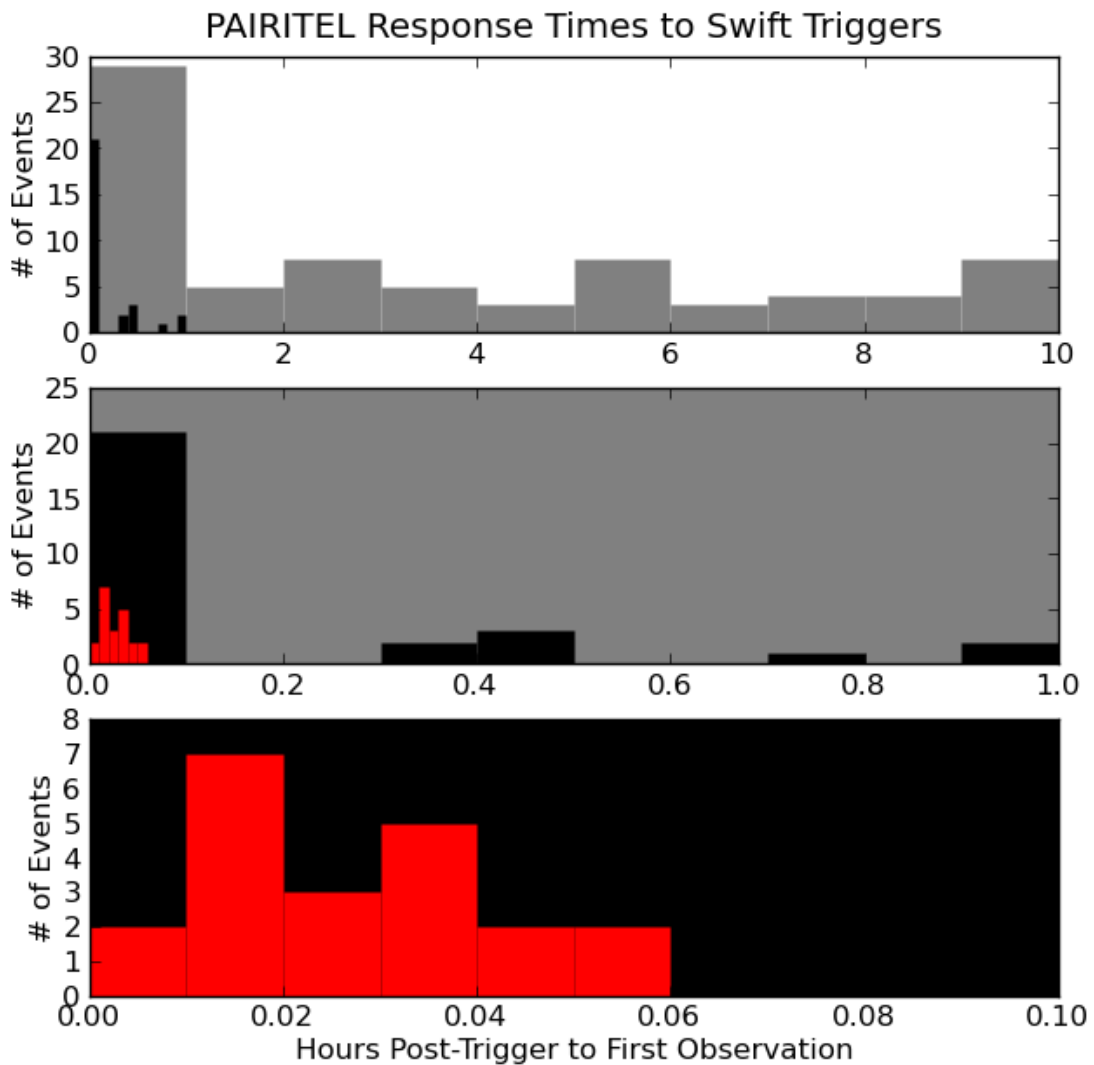


Figure 4.1: Histogram of PAIRITEL response times to *Swift* triggers, showing the duration of time from the BAT trigger to the beginning of PAIRITEL image acquisition. Each of the lower two panels shows an enlargement of the first bin of the panel above it.

PAIRITEL’s field of view was  $8.5' \times 8.5'$ , large enough to encompass BAT uncertainty regions, which are typically of order  $3'$ . The imaging and readout procedure utilized by the system was in part dictated by the reuse of the 2MASS camera and readout electronics. PAIRITEL used two dichroics to image in the NIR  $J$ ,  $H$ , and  $K_s$  filters simultaneously with an exposure of 7.8 s, preceded by a short exposure of 0.051 s which served as a bias read. Three images were taken at each dither position and then median combined into 23.4 s “triplestacks” (see §4.2.2). Data collection continued in this manner until observing constraints were met, or a higher priority target interrupted the observations.

### 4.2.2 Data Reduction

We have reduced and photometered the PAIRITEL data for all GRBs presented in this work with improved pipelines. The new software improved both the quality of the reduced images and the speed with which they were produced, which was particularly important for the rapid analysis of new events. Image reductions were performed with the third and final incarnation of the PAIRITEL reduction pipeline<sup>d</sup>. The reduction procedure is described in detail in Klein & Bloom (2014), but we provide an abridged description here for completeness.

First, the 0.051 s bias reads were subtracted from each of the longer 7.8 s exposures. Due to the brightness of the sky in the NIR, median sky background images were created over a 5-10 minute integration window, to be subtracted from the raw exposures. This sky subtraction procedure was performed twice for each image, once utilizing a coarse pixel mask to exclude flux from astrophysical sources, and again with a more refined mask utilizing the results from the first sky subtraction. Each image was then divided by a standard flat image for the relevant filter, resulting in the final reduced images.

As the telescope jitter between subsequent exposures was small compared to the  $2''$  pixel scale, the three images at each dither position are next simply directly summed into a 23.4 s “triplestack”. The deepest  $J$ -band triplestack is identified using SExtractor and serves as the reference image to which others are subsequently aligned. We utilize a normalized cross-correlation image alignment algorithm to determine the relative offsets between the triplestacks. Typically, a 9 pixel search radius around the rough position known to the telescope control system was sufficient, but on occasion this needed to be increased in sparse fields. Before coadding, we verified the images by eye to check the quality of the reductions and the success of the alignment procedure. Occasional manual intervention is required when images are misaligned due to too few reference stars, or when varying the masking parameters is necessary. On occasion, large backgrounds prevented salvageable reductions of the  $K_s$ -band images.

After alignment, images were resampled to  $1''$  pixel<sup>-1</sup> from the native  $2''$  pixel scale and median-combined using SWarp (Bertin et al. 2002). A minimum of two triplestacks was required for each photometric measurement (see §4.2.3). In order to achieve high time-resolution while maintaining significant detections, we iteratively coadded images for the

<sup>d</sup>[https://github.com/ckleinastro/pairitel\\_reduction\\_pipeline](https://github.com/ckleinastro/pairitel_reduction_pipeline)

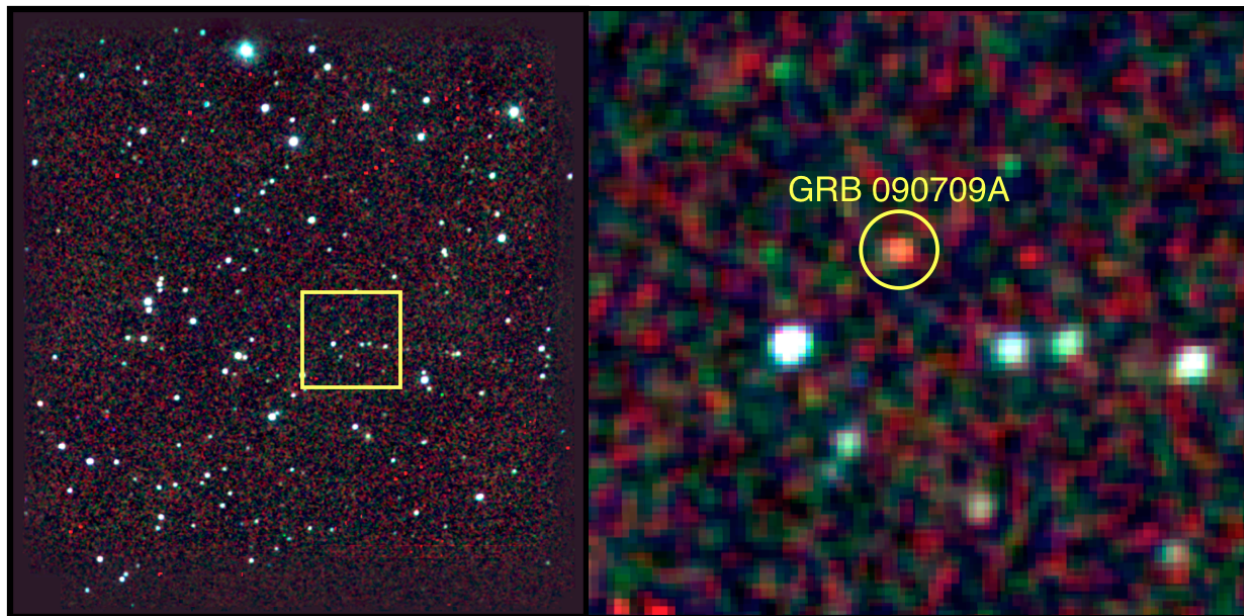


*Figure 4.2:* False color ( $J,H,K_s$ ) PAIRITEL image of the field of GRB 090709A, showing the full  $8.5' \times 8.5'$  field of view (left) and detail (right). The afterglow is centered in the yellow circle ( $5''$  radius) and is clearly much redder than the surrounding field stars. This 5 minute mosaic, beginning  $\sim 2$  minutes post trigger, highlights PAIRITEL’s ability to rapidly identify bursts of interest.

afterglows in this study until a photometric uncertainty of about 0.2 mag was achieved for each data point. As the last step in the reduction procedure, each final mosaic was astrometrically calibrated with *Astrometry.net* (Lang et al. 2010). An example mosaic of one of the events in our sample, GRB 090709A, is presented in Figure 4.16.

### 4.2.3 Photometry

Aperture photometry was performed using custom Python software<sup>e</sup>, utilizing Source Extractor (SExtractor; Bertin & Arnouts 1996) as a back end. An initial selection of calibration stars was determined automatically for each image through comparison of the 2MASS catalog with the SExtractor output. Stars with brightnesses near the saturation limit for each filter and those suffering from confusion with nearby sources were automatically detected and excluded. Additional checks on potential calibration stars then performed, including examining plots of calibration star brightness over time to check for variation, and flagging large deviations from 2MASS values of derived calibration star magnitudes.

The choice of aperture size for photometry requires a balance between capturing as much of the source signal as is possible without being overtaken by background noise. While in principle this is calculable from the point-spread function of each image, the non-trivial noise

<sup>e</sup><https://github.com/qmorgan/qsoft/tree/master/Software/Phot>



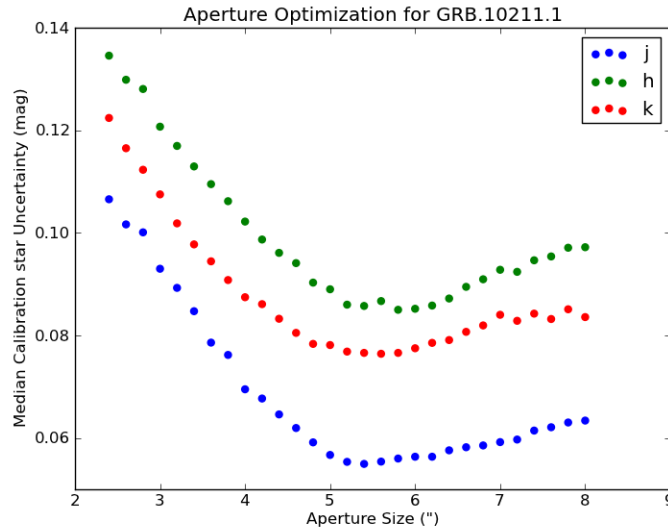


Figure 4.3: Example of the optimal aperture determination for an afterglow. For each filter, the aperture which minimizes the median standard deviation of the magnitude for all calibration stars is chosen. The x-axis is the *diameter* of the circular aperture in arcseconds.

properties of the detector led us to a more brute-force approach: we determined the optimal aperture for each afterglow by recalculating the photometry using a number of different apertures and determining which one minimizes the median deviation of the calibration star magnitudes from the 2MASS catalog across all images. An example of this measurement is shown in Figure 4.3. The optimal photometric aperture for each afterglow can vary for each filter due to differing observing conditions, but typically ranged from  $\sim 5 - 6''$  in diameter.

The zeropoint and associated uncertainty  $\sigma_{zp}$  was calculated for each image individually through comparison of the calibration stars with 2MASS magnitudes. In the process of resampling from PAIRITEL’s native pixel scale of  $2''/\text{pixel}$  to  $1''/\text{pixel}$ , the nominal statistical uncertainty in the instrumental magnitude  $\sigma_{inst}$  is underestimated by about a factor of  $2^f$  relative to what the standard deviation of the sky pixels would indicate. In addition, the large plate scale and variable response function of the PAIRITEL detectors create an additional source of systematic uncertainty, estimated to be about 3 percent by Blake et al. (2008) and  $\sim 0.02$  mag per position by Perley et al. (2010a), which decreases with the square root of the number of dither positions  $N_{dither}$ . We re-measured this value by calculating standard deviation of the magnitude variations of bright calibration stars across high-quality images in all filters. We found this additional per-dither uncertainty  $\sigma_{dither}$  to be about 0.02 mag in  $J$ , and 0.03 mag in  $H$  and  $K_s$ . The final uncertainty was calculated from the sum of all of these sources in quadrature:  $\sigma_{total} = \sqrt{\sigma_{zp}^2 + (2.4\sigma_{inst})^2 + (\sigma_{dither}/\sqrt{N_{dither}})^2}$ .

<sup>f</sup>For PAIRITEL, this was measured by Perley et al. (2010a) to be a factor of about 2.4.

## 4.3 Observations

The catalog presented here includes all *Swift* GRBs that PAIRITEL observed within 3 minutes of the trigger between November 2005 and March 2010<sup>g</sup>. A total of 17 GRBs in this timeframe triggered the system early enough for observations to begin within 3 minutes, but three of them suffered from bad initial telescope pointing and are not included here. The remaining 14 GRBs comprise our sample of simultaneous early-time multi-color NIR observations. While all 14 events have reliable *J*-band and *H*-band imaging, poor observing conditions prevented good reductions of the more troublesome *K<sub>s</sub>*-band images for three events (GRBs 070208, 090530, and 090618). While the PAIRITEL data for several of the bursts in this catalog has been published previously, we have re-reduced and analyzed the images with the newest pipelines to produce updated light-curves<sup>h</sup>.

Table 4.1 presents a summary of the properties of these GRBs obtained from the literature. Eight events in the sample have spectroscopic redshift measurements from afterglow observations, two have measured redshifts of their likely host galaxy from emission spectra, and the remainder have redshift estimates or limits from photometric fits. In addition, 11 of the 14 events have some estimate of the extent of host galaxy line-of-sight extinction from SED fits. We also include a sample of *Swift* high-energy properties from Butler & Kocevski (2007) and Butler et al. (2007).

### 4.3.1 GRB 051109A

GRB 051109A (*Swift* trigger 163136) was detected by the BAT on 2005-11-09 01:12:21 (Tagliaferri et al. 2005). PAIRITEL autonomously responded to the GCN notices and observations began at 2005-11-09 01:13:55, 1.57 minutes after the trigger. This well-observed (e.g., Yost et al. 2007) afterglow from early in the *Swift* mission was at a moderate redshift of 2.346 (Quimby et al. 2005). Fits to its early-time *JHK<sub>s</sub>* SED imply a spectral index of  $\beta = 0.70 \pm 0.21$ . Our photometry is presented in Table 4.4 and the light curve is shown in Figure 4.4.

### 4.3.2 GRB 061126

GRB 061126 (*Swift* trigger 240766) was detected by the BAT on 2006-11-26 08:47:56 (Sbarufatti et al. 2006). PAIRITEL autonomously responded to the GCN notices and observations began at 2006-11-26 08:48:54, 0.97 minutes after the trigger. An emission spectrum from the likely host galaxy of this event reveals that it is at a redshift of  $z = 1.1588$  (Perley et al. 2008c). Highly variable cloud cover plagued the transmission in the early PAIRITEL

<sup>g</sup>A few additional events, including GRB120119A (Chapter 3 and Morgan et al. 2014) were observed between the end of our catalog and the closure of PAIRITEL, though the overall rate decreased due to complications in triggering and pointing with the aging system.

<sup>h</sup>The exception is GRB 080319B, for which the extreme brightness of the afterglow required special treatment. For that event, we use the PAIRITEL photometry published in Bloom et al. (2009).

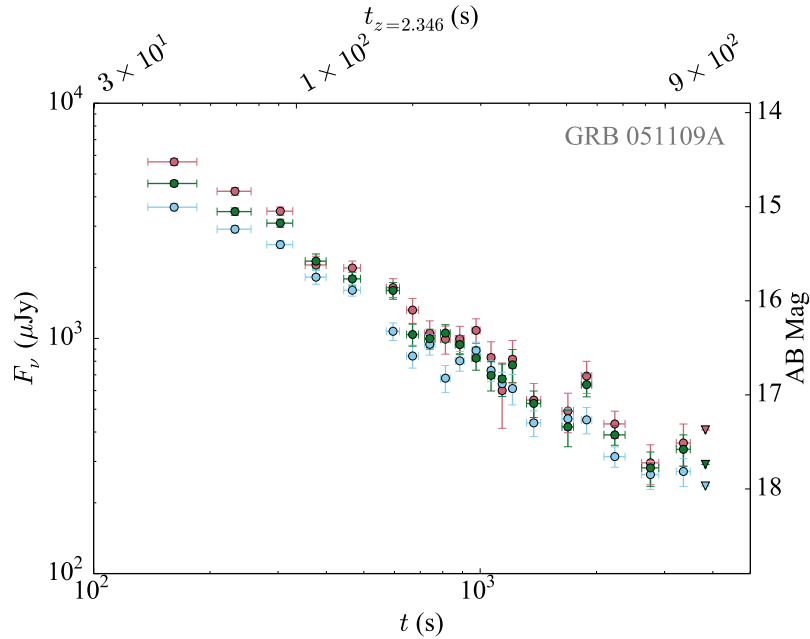


Figure 4.4: PAIRITEL Light Curve of GRB 051109A

observation, but the afterglow was bright enough to remain easily detected. PAIRITEL photometry for this event was first published in (Perley et al. 2008c), who demonstrated a large discrepancy between the optical and X-ray fluxes at late times. No standard dust extinction law can explain this discrepancy, but the authors explored the possibility of “grey dust” resulting in the suppression of the optical flux. Our photometry is presented in Table 4.5 and the light curve is shown in Figure 4.5.

### 4.3.3 GRB 061222A

GRB 061222A (*Swift* trigger 252588) was detected by the BAT on 2006-12-22 03:28:52 (Grupe et al. 2006). PAIRITEL autonomously responded to the GCN notices and observations began at 2006-12-22 03:31:04, 2.20 minutes after the trigger. While very bright at high-energies, this event was extremely suppressed in the optical, and the only previously reported afterglow detections were in the  $K_s$ -band with NIRI on Gemini South (Cenko & Fox 2006a,b). Deep optical observations revealed a blue host galaxy at a redshift of  $z = 2.088$  (Perley et al. 2009b, 2013). SED fits to the afterglow which include X-ray data imply a huge absorption column ( $A_V > 6.6$ , Perley et al. 2013). Here we report for the first time the PAIRITEL photometry for this event, which include a single  $K_s$ -band detection at about 5 minutes after the burst. Consistent with a highly dust-extinguished afterglow, we do not detect any flux in the  $J$  or  $H$  bands. Our photometry is presented in Table 4.6 and the light curve is shown in Figure 4.6.

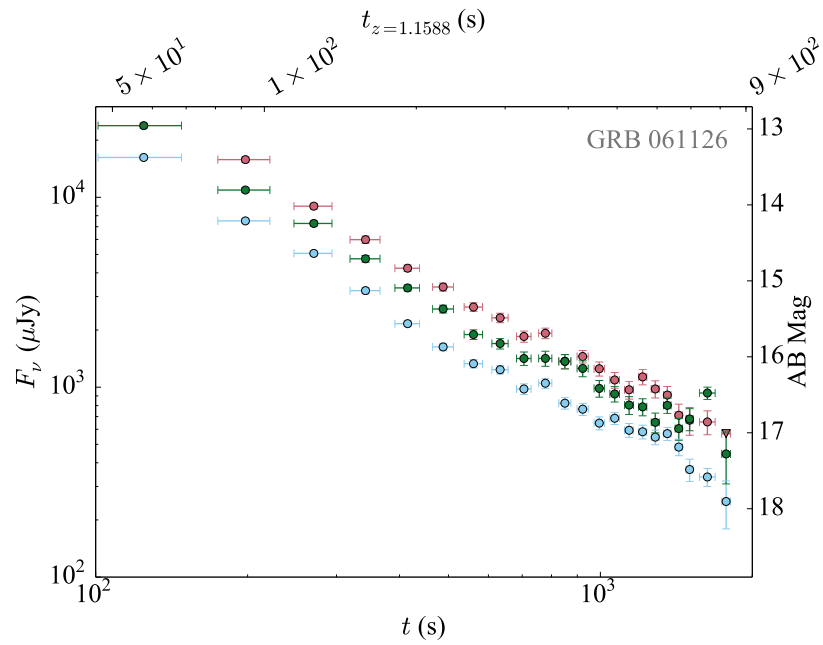


Figure 4.5: PAIRITEL Light Curve of GRB 061126

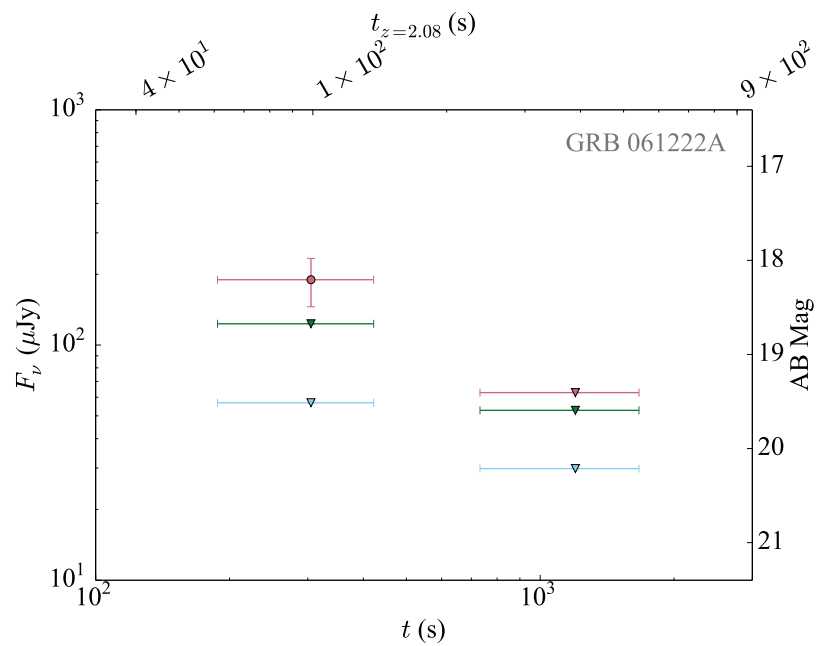


Figure 4.6: PAIRITEL Light Curve of GRB 061222A

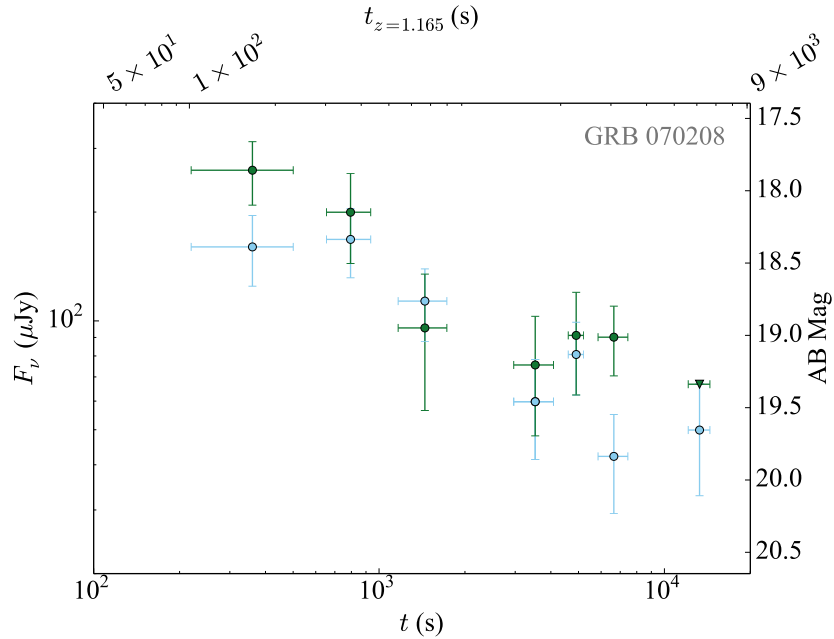


Figure 4.7: PAIRITEL Light Curve of GRB 070208

#### 4.3.4 GRB 070208

GRB 070208 (*Swift* trigger 259714) was detected by the BAT on 2007-02-08 09:10:34 (Sato et al. 2007). PAIRITEL autonomously responded to the GCN notices and observations began at 2007-02-08 09:12:26, 1.87 minutes after the trigger. Afterglow spectroscopy revealed the event to be at  $z = 1.165$  (Cucchiara et al. 2007b), and fits to the optical SED of this event show a moderate column of SMC-like dust with  $A_V = 0.96 \pm 0.09$  (Cenko et al. 2009a). PAIRITEL images for this burst suffered from reduction problems and  $K$ -band photometry could not be obtained. Our  $J$  and  $H$  photometry is presented in Table 4.7 and the light curve is shown in Figure 4.7.

#### 4.3.5 GRB 071025

GRB 071025 (*Swift* trigger 295301) was detected by the BAT on 2007-10-25 04:08:54 (Pagani et al. 2007). PAIRITEL autonomously responded to the GCN notices and observations began at 2007-10-25 04:11:00, 2.10 minutes after the trigger. Photometry of the PAIRITEL imaging for this event was first published by Perley et al. (2010a) where it was used in conjunction with optical data to show evidence for dust extinction incompatible with any locally observed dust laws. They show instead that the SED is well-fit by models by Maiolino et al. (2004) of dust formed by supernovae used to explain the extinction seen along the line of sight to a high redshift ( $z = 6.2$ ) quasar. Perley et al. (2010a) further estimates a photometric redshift of this event of  $z = 4.8 \pm 0.2$ . Our photometry is presented in Table

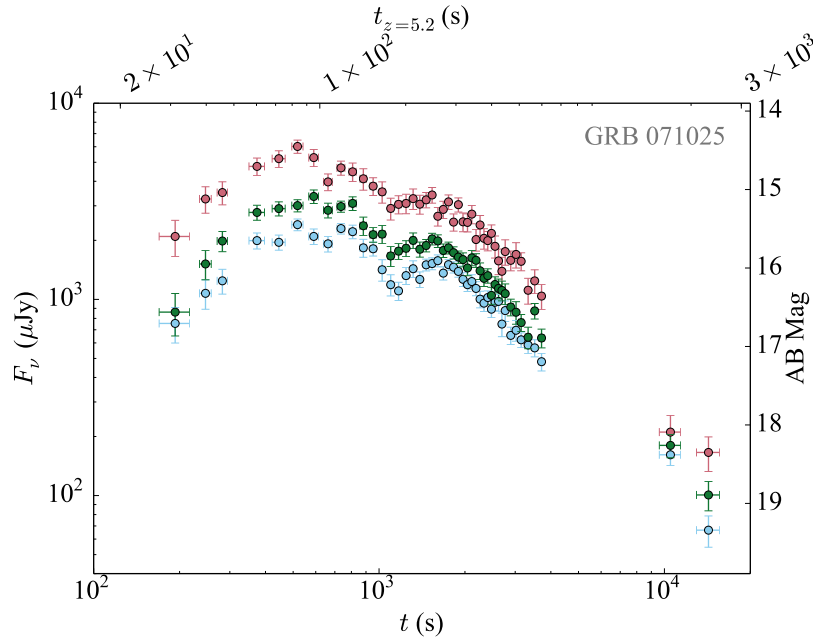


Figure 4.8: PAIRITEL Light Curve of GRB 071025

4.8 and the light curve is shown in Figure 4.8.

### 4.3.6 GRB 080319A

GRB 080319A (*Swift* trigger 306754) was detected by the BAT on 2008-03-19 05:45:42 (Pagani et al. 2008a). PAIRITEL autonomously responded to the GCN notices and observations began at 2008-03-19 05:48:19, 2.62 minutes after the trigger. Due to the intense focus by the community on GRB 080319B which occurred only 27 minutes after this event, follow-up was limited for GRB 080319A. Limits from the host spectroscopy indicate a redshift of  $1.1 < z < 2.1$  (Perley 2014). At the maximum allowed redshift and assuming an intrinsic spectral slope  $\beta < 1.2$ , the lower-limit on the absorption is  $A_V > 0.25$  (Perley et al. 2009b). Our photometry for this event is presented in Table 4.9 and the light curve is shown in Figure 4.9.

### 4.3.7 GRB 080319B

GRB 080319B (*Swift* trigger 306757) was detected by the BAT on 2008-03-19 06:12:49 (Racusin et al. 2008a). PAIRITEL autonomously responded to the GCN notices and observations began at 2008-03-19 06:13:39, 0.83 minutes after the trigger. This extremely bright “naked-eye” burst occurred at a redshift of  $z = 0.9382$  (Vreeswijk et al. 2008c,e) and the SED indicates only small amounts of extinction, if any ( $A_V = 0.07 \pm 0.07$ ; Bloom et al. 2009). The

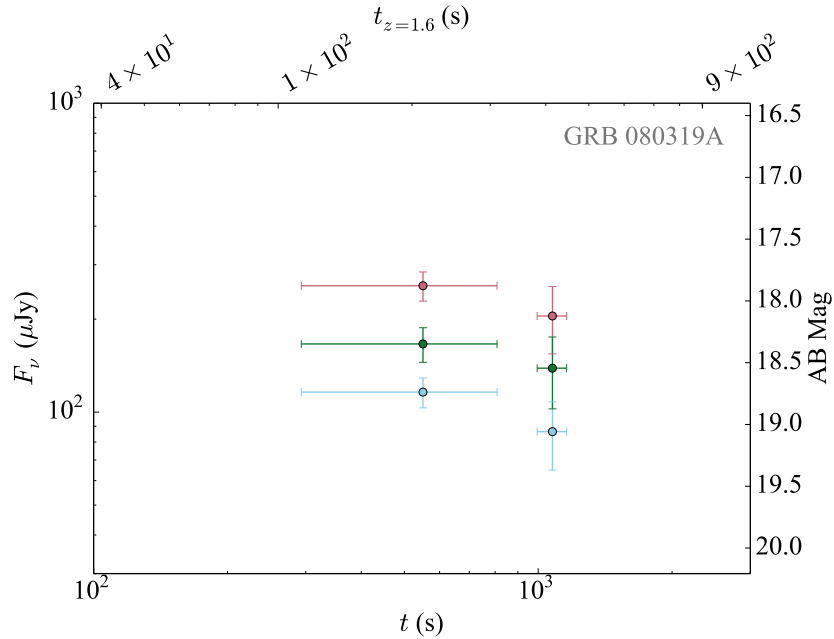


Figure 4.9: PAIRITEL Light Curve of GRB 080319A

PAIRITEL photometry for this event was first published in [Bloom et al. \(2009\)](#) and reveals significant color change over time. The photometry for this event was taken from ([Bloom et al. 2009](#)) due to the special treatment required to obtain the early-time PAIRITEL fluxes of this extremely bright afterglow. The light curve is shown in [Figure 4.10](#).

### 4.3.8 GRB 080319C

GRB 080319C (*Swift* trigger 306778) was detected by the BAT on 2008-03-19 12:25:56 ([Pagani et al. 2008b](#)). PAIRITEL autonomously responded to the GCN notices and observations began at 2008-03-19 12:27:07, 1.18 minutes after the trigger. Spectroscopy of the afterglow revealed its redshift to be  $z = 1.9492$  ([Wiersema et al. 2008b](#)), and SED fits by [Kann et al. \(2010\)](#) suggest a moderate column of SED-like dust with  $A_V = 0.59 \pm 0.12$ . Our early-time light curve of this event shows a rise peaking at about 100 s in the rest frame. Our photometry is presented in [Table 4.10](#) and the light curve is shown in [Figure 4.11](#).

### 4.3.9 GRB 080320

GRB 080320 (*Swift* trigger 306858) was detected by the BAT on 2008-03-20 04:37:38 ([Grupe et al. 2008](#)). PAIRITEL autonomously responded to the GCN notices and observations began at 2008-03-20 04:39:45, 2.11 minutes after the trigger. Due the focus on GRB 080319B from the previous night and a nearly-full moon, follow-up of this event was

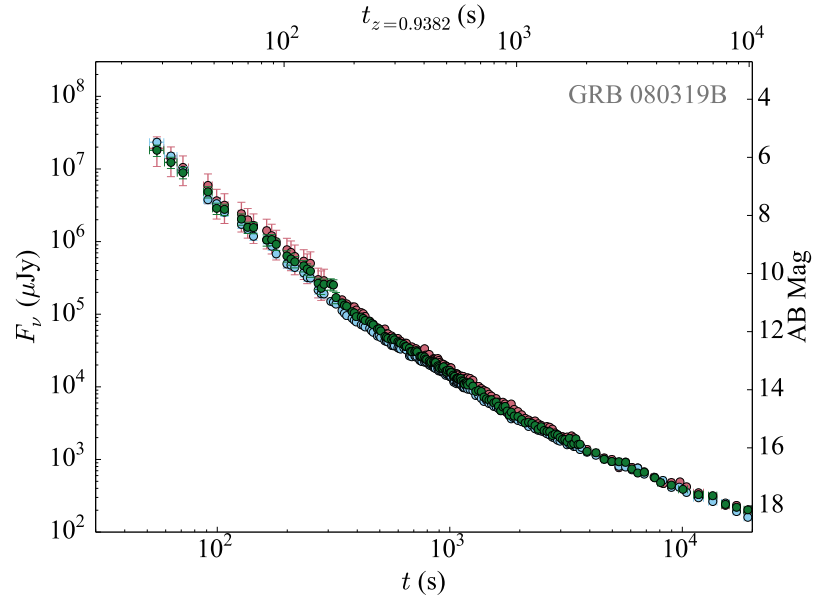


Figure 4.10: PAIRITEL Light Curve of GRB 080319B. Data from (Bloom et al. 2009).

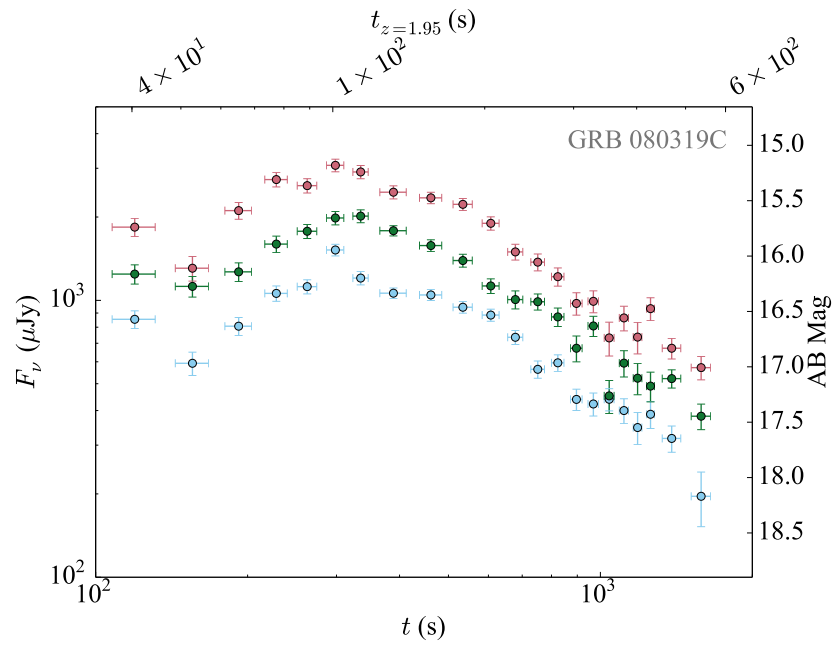


Figure 4.11: PAIRITEL Light Curve of GRB 080319C



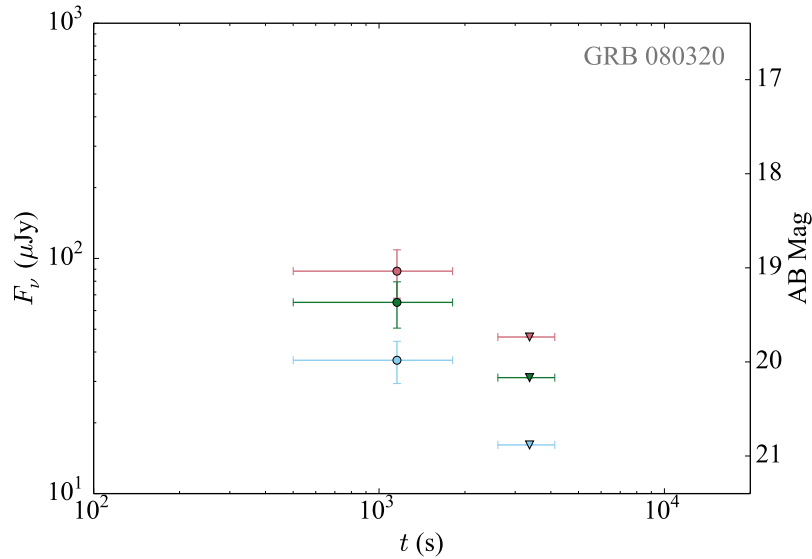


Figure 4.12: PAIRITEL Light Curve of GRB 080320

limited. The afterglow nevertheless was shown to be suppressed in the optical compared to the X-rays, either due to high-redshift, large amounts of dust extinction, or both (Perley et al. 2009b). No redshift is available for this event, though an  $i$ -band detection places an upper-limit of  $z < 7$ . A lack of host detection to deep limits gives further credence to a high-redshift event (Perley et al. 2009b). Here we report an early-time PAIRITEL detection of the afterglow for the first time. We find a faint detection in all three filters which quickly fades beyond our detection limits. The  $JHK_s$  SED implies a spectral index of  $\beta \simeq 1.6$ , suggesting that dust extinction also plays a significant role in the optical suppression of this event. Our photometry is presented in Table 4.11 and the light curve is shown in Figure 4.12.

#### 4.3.10 GRB 080604

GRB 080604 (*Swift* trigger 313116) was detected by the BAT on 2008-06-04 07:27:01 (La Parola et al. 2008). PAIRITEL autonomously responded to the GCN notices and observations began at 2008-06-04 07:29:34, 2.55 minutes after the trigger. This is the only burst in our sample for which we do not detect the afterglow. However, a faint optical afterglow was reported by other facilities, and the redshift of the event was found to be  $z = 1.416$  (Wiersema et al. 2008a). Our upper limits for this event are presented in Table 4.12.

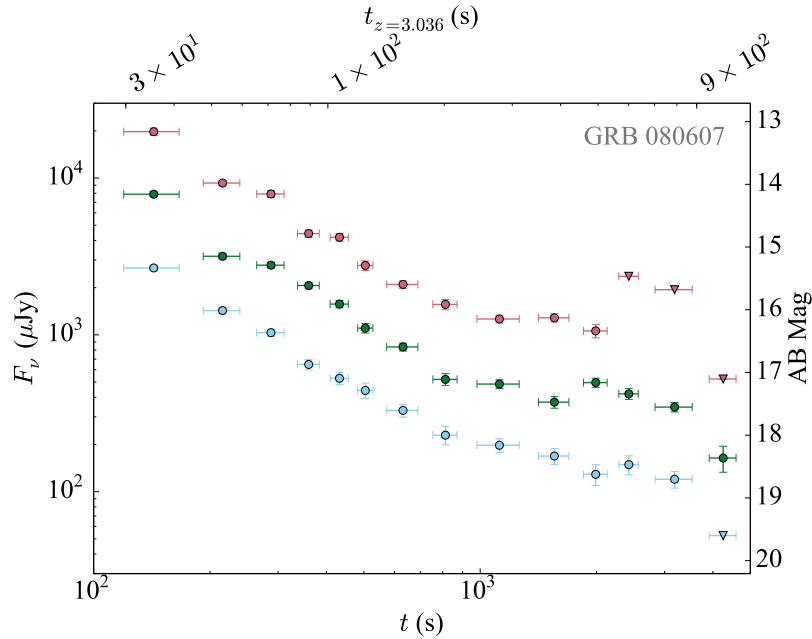


Figure 4.13: PAIRITEL Light Curve of GRB 080607

### 4.3.11 GRB 080607

GRB 080607 (*Swift* trigger 313417) was detected by the BAT on 2008-06-07 06:07:27 (Mangano et al. 2008). PAIRITEL autonomously responded to the GCN notices and observations began at 2008-06-07 06:09:20, 1.88 minutes after the trigger. The PAIRITEL observations for this event were first published in Perley et al. (2011) which details the extinction properties of this  $z = 3.036$  event (Prochaska et al. 2009). The extinction properties are unlike those seen along local sightlines, and were best fit with a generalized FM parameterization. A very large dust column was found ( $A_V \simeq 3.3$ ), which, once corrected for, revealed this event to be one of the most optically luminous GRBs observed. Our photometry is presented in Table 4.13 and the light curve is shown in Figure 4.13.

### 4.3.12 GRB 090530

GRB 090530 (*Swift* trigger 353567) was detected by the BAT on 2009-05-30 03:18:18 (Cannizzo et al. 2009). PAIRITEL autonomously responded to the GCN notices and observations began at 2009-05-30 03:20:06, 1.8 minutes after the trigger. PAIRITEL images for this burst suffered from reduction problems and  $K$ -band photometry could not be obtained. This event occurred at a redshift of  $z = 1.266$  (Goldoni et al. 2013) SED fits to the afterglow imply a small column of dust extinction ( $A_V \sim 0.15$ ; Krühler et al. 2011a). Our  $J$  and  $H$  photometry is presented in Table 4.14 and the light curve is shown in Figure 4.14.

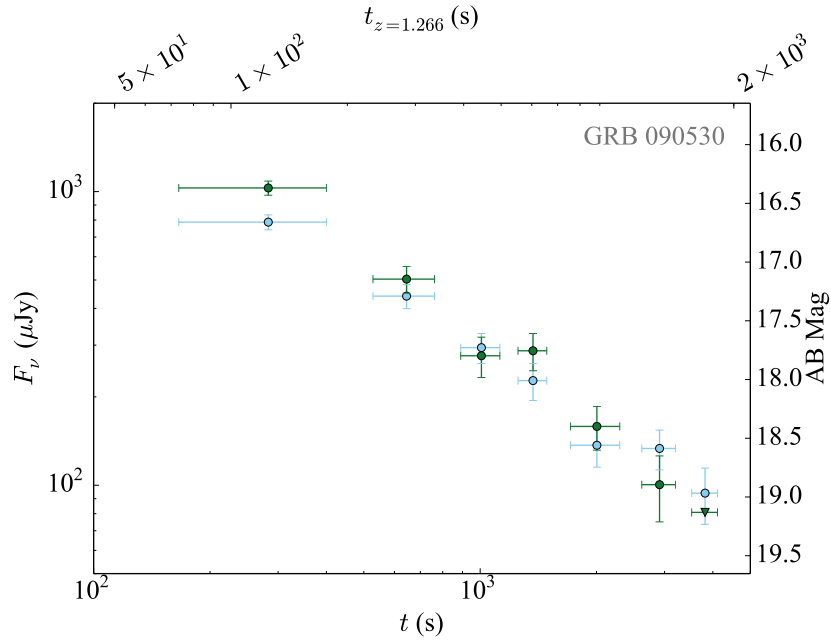


Figure 4.14: PAIRITEL Light Curve of GRB 090530

### 4.3.13 GRB 090618

GRB 090618 (*Swift* trigger 355083) was detected by the BAT on 2009-06-18 08:28:29 (Schady et al. 2009). PAIRITEL autonomously responded to the GCN notices and observations began at 2009-06-18 08:30:16, 1.78 minutes after the trigger. Intermittent clouds led to highly variable transmission and sky brightnesses during the PAIRITEL observations, causing reduction problems for the *K*-band images. This low-redshift burst ( $z = 0.54$ ; Cenko et al. 2009a, Fatkhullin et al. 2009) was found to have an associated supernova from deep late-time photometry (Cano et al. 2011). Our *J* and *H* photometry is presented in Table 4.15 and the light curve is shown in Figure 4.15.

### 4.3.14 GRB 090709A

GRB 090709A (*Swift* trigger 356890) was detected by the BAT on 2009-07-09 07:38:34 (Morris et al. 2009). PAIRITEL autonomously responded to the GCN notices and observations began at 2009-07-09 07:40:22, 1.80 minutes after the trigger. The afterglow was very red, and with an estimated redshift of  $z \simeq 1.8$  from photometry of the likely host galaxy, the dust extinction along the line of sight is quite high at roughly  $A_V \simeq 3.4$  (Perley et al. 2013). The PAIRITEL observations of this GRB were first published in Cenko et al. (2010c), and our updated photometry is presented in Table 4.16 with the light curve shown in Figure 4.16.

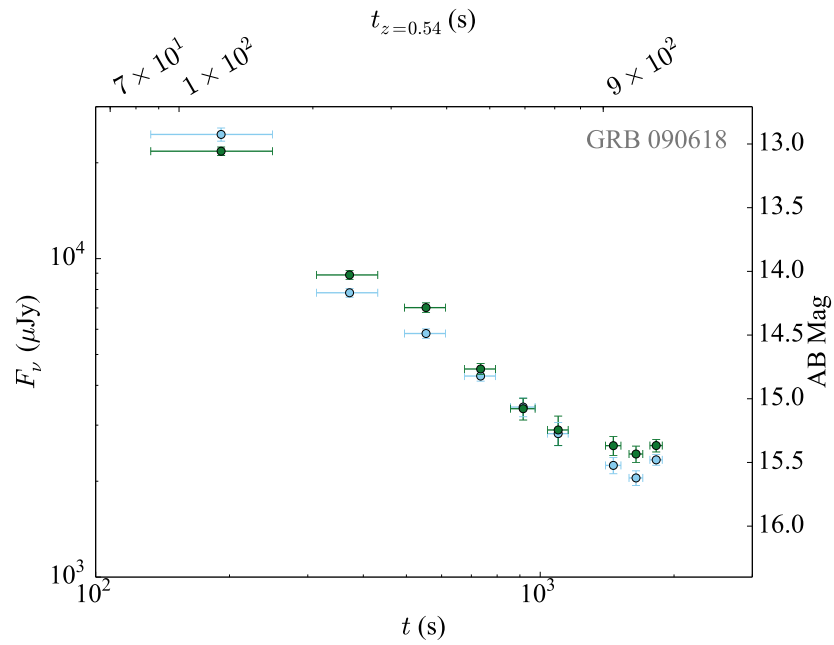


Figure 4.15: PAIRITEL Light Curve of GRB 090618

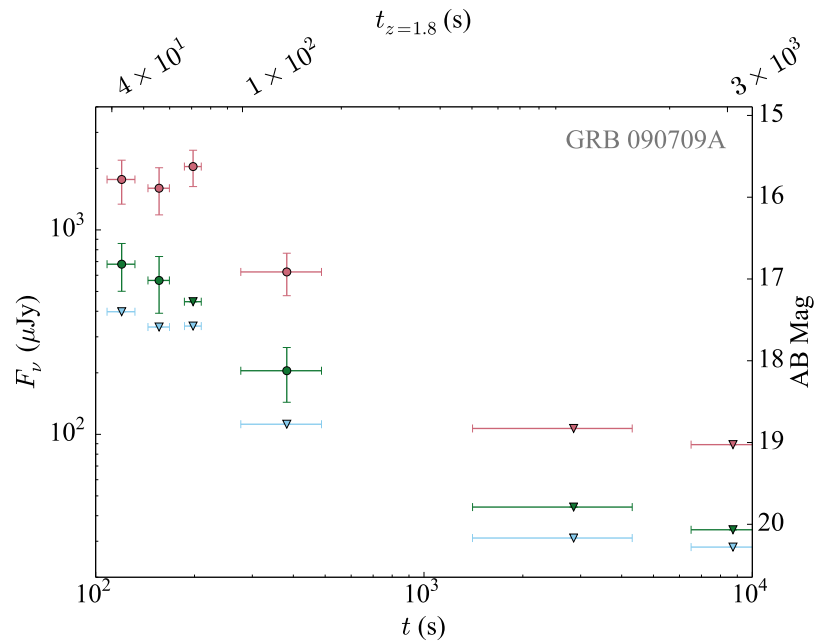


Figure 4.16: PAIRITEL Light Curve of GRB 090709A

Table 4.1: Summary of GRB Properties

GRB	$z$	$z$ type <sup>a</sup>	$z$ ref	$\beta$	$A_V$ (mag)	Dust type	SED ref	$E_{peak}$ (keV)	$S$ (erg cm <sup>-2</sup> )	$N_{H,pc}$ (10 <sup>22</sup> cm <sup>-2</sup> )	$T_{90}$ (s)
051109A	2.346	ab	1	$0.70 \pm 0.21^e$	...	...	...	1.05e+02	1.54e-06	5.00e-02	4.90e+00
061126	1.1588	hem	2	< 1.0	< 0.8	Grey? <sup>b</sup>	2	3.89e+02	1.39e-05	1.33e-01	2.68e+01
061222A	2.088	hem	3	0.6? <sup>c</sup>	> 6.6	SMC	3,17	2.30e+02	1.45e-05	3.07e-01	8.17e+01
070208	1.165	ab	4	0.6? <sup>c</sup>	$0.96 \pm 0.09$	SMC	5	6.60e+01	5.67e-07	1.82e-01	5.25e+01
071025	$4.8 \pm 0.2$	ph	6,7	$0.96 \pm 0.14$	$1.09 \pm 0.20^d$	Maiolino	7,8	1.65e+02	1.10e-05	7.30e-02	1.61e+02
080319A	$1.6 \pm 0.5$	hem	24	0.6? <sup>c</sup>	> 0.25	SMC	3	1.05e+02	7.19e-06	9.40e-02	4.56e+01
080319B	0.9382	ab	9,10,6	$0.50 \pm 0.12^f$	$0.07 \pm 0.07$	SMC	22	1.22e+03	4.11e-04	5.30e-02	1.47e+02
080319C	1.9492	ab	11,6	$0.98 \pm 0.42$	$0.59 \pm 0.12$	SMC	19	1.57e+02	5.38e-06	7.30e-02	3.29e+01
080320	< 7	ph	3	...	...	...	...	9.51e+01	5.64e-07	5.30e-02	2.14e+01
080604	1.416	ab	21	...	...	...	...	2.23e+02	2.23e-05	-1.80e-02	1.25e+02
080607	3.0363	ab	12,6	0.7? <sup>c</sup>	$3.3 \pm 0.3$	FM	23	9.03e+02	5.12e-05	1.42e-01	8.37e+01
090530	1.266	ab	13, 14	$0.4 \pm 0.3$	$0.15^{+0.15}_{-0.08}$	SMC	14	9.05e+01	1.84e-06	8.10e-02	4.08e+01
090618	0.54	ab	15,16	$0.64 \pm 0.02$	$0.24 \pm 0.09$	SMC	20	1.38e+02	1.48e-04	9.70e-02	1.15e+02
090709A	$1.8^{+0.46}_{-0.71}$	hph	17	0.7? <sup>c</sup>	$3.4 \pm 0.3$	SMC	17	3.00e+02	4.59e-05	1.83e-01	3.45e+02

<sup>a</sup>ab: Afterglow absorption spectrum; hem: Emission spectrum from likely host galaxy; ph: Photometric redshift from afterglow colors; hph: Photometric redshift from colors of likely host galaxy

<sup>b</sup>Standard extinction laws provide poor fits to the data for GRB 061126. See [Perley et al. \(2008c\)](#) for details.

<sup>c</sup>For these bursts,  $\beta$  was assumed, since a large amount of dust extinction prevents good fits to the intrinsic spectral index.

<sup>d</sup>The Maiolino extinction curve ([Maiolino et al. 2004](#)) is normalized to  $A_{3000}$  instead of  $A_V$ , since the  $V$  band at  $z > 5$  is shifted into the mid-IR. See [Perley et al. \(2010a\)](#) for details.

<sup>e</sup>A more accurate determination of  $\beta$  was unavailable from the literature for this event, so we calculated its value from a linear fit to the  $JHK_s$  SED at 3 minutes in the observer frame (see [Table 4.2](#)).

<sup>f</sup>The value of  $\beta$  for GRB 080319B was observed to vary at early times; we took the value it was at closest to our interpolation time of 3 minutes in the rest frame.

References. — (1) [Quimby et al. 2005](#); (2) [Perley et al. 2008c](#); (3) [Perley et al. 2009b](#); (4) [Cucchiara et al. 2007b](#); (5) [Cenko et al. 2009a](#); (6) [Fynbo et al. 2009b](#); (7) [Perley et al. 2010a](#); (8) [Jang et al. 2011](#); (9) [Vreeswijk et al. 2008c](#); (10) [Vreeswijk et al. 2008e](#); (11) [Wiersema et al. 2008b](#); (12) [Prochaska et al. 2009](#); (13) [Goldoni et al. 2013](#); (14) [Krühler et al. 2011a](#); (15) [Cenko et al. 2009a](#); (16) [Fatkhullin et al. 2009](#); (17) [Perley et al. 2013](#); (19) [Kann et al. 2010](#); (20) [Cano et al. 2011](#); (21) [Wiersema et al. 2008a](#); (22) [Bloom et al. 2009](#) (23) [Perley et al. 2011](#); (24) [Perley 2014](#)

## 4.4 Discussion

### 4.4.1 Detection Rates and the Role of Dust Extinction

Perhaps the most immediately noticeable feature of the PAIRITEL early-time catalog when compared to other studies is its large detection rate. Of the fourteen bursts included in the sample, only one (GRB 080604) was not detected. This detection rate of  $\sim 93\%$  is higher than that of any published optical afterglow catalog and rivals that of the XRT (96%, Burrows et al. 2007). While this is of course in part due to limiting the sample to only the earliest observed events, the NIR filters also play a big role. For instance, the detection rate of the UVOT, with the  $V$  band as its reddest filter, was only 26% for the first UVOT catalog of 229 GRBs (Roming et al. 2009)<sup>i</sup>. The detection rate from Melandri et al. (2008), who cataloged a total of 63 GRBs from a network of three robotic 2-meter telescopes, was higher at ( $\sim 38\%$ ). An additional 10 GRBs ( $\sim 16\%$ ) from their sample were detected by other telescopes, mostly in the IR. Since most undetected events in their catalog were observed within a few minutes after the trigger, they rule out poor sensitivity and response time as the reason for the nondetections. The detection fraction was yet higher still for the catalog of 29 GRBs from Cenko et al. (2009a) observed with the robotic 1.5-meter P60 telescope. Their survey revealed detections for a much higher fraction of events ( $\sim 80\%$ ), likely due to the use of redder filters including  $i'$  and  $z'$  in their automated follow-up sequence. Following in this trend, the 2.2 m GROND with the capability for imaging in 7-simultaneous bands, including  $J$ ,  $H$ , and  $K$ , detected 20 out of 22 afterglows ( $\sim 91\%$ ) observed within 30 minutes of the burst (Greiner et al. 2011). That the 1.3 m PAIRITEL was able to match<sup>j</sup> the detection rate of a telescope with nearly 3 times its collecting area is a testament to the importance of speed in early-time afterglow observations. The mean delay between the *Swift* trigger and the start of PAIRITEL observations for the fourteen bursts in this catalog was  $1.85 \pm 0.48$  minutes, which is nearly a factor of three times faster than the  $5.25 \pm 1.59$  minute average delay of the fourteen most rapidly observed GROND bursts from Greiner et al. (2011).

Another clear property of our sample is the prevalence of highly dust-extinguished events. Due in part to the PAIRITEL observations, 11 of the 14 bursts have at least an estimate of their host galaxy extinction along the line-of-sight from multi-wavelength afterglow observations (Table 4.1). Three of these eleven bursts with measured extinction have  $A_V > 3.0$  (GRB 061222A, GRB 080607, and GRB 090709A), and an additional 2 have  $A_V \simeq 1.0$  (GRB 070208 and GRB 071025). The predominance of low average host extinction implied by other studies (Kann et al. 2006, 2010; Starling et al. 2007; Schady et al. 2007, 2010) are likely biased strongly against dusty hosts by their selection criteria (Fynbo et al. 2009b). For instance, in the large sample of 85 bursts with derived host extinction from Kann et al.

<sup>i</sup>However, this fraction increases when more optimal coaddition techniques are implemented (Morgan et al. 2008; Swenson et al. 2013).

<sup>j</sup>Small number statistics of course are an important consideration with a sample size of only fourteen, where each event counts for  $\sim 7\%$  of the quoted rate. However, we note that that the two earliest non-detections of Greiner et al. (2011) were within their fourteen most rapidly observed events, indicating consistency with our rates.

(2010), only two bursts have  $A_V \simeq 1.2$  and the remainder (98%) have  $A_V < 0.8$ . As they conclude, NIR observations, being less affected by extinction, are necessary for good SED fits.

This combination of a high detection rate and the prevalence of highly extinguished bursts in our sample further supports the findings of other studies (Gehrels et al. 2008; Zheng et al. 2009; Cenko et al. 2009a; Perley et al. 2009b; Greiner et al. 2011; Melandri et al. 2012) that optical extinction due to dust, rather than intrinsic faintness, is responsible for the majority of optically “dark” GRBs. Indeed, two of the thirteen bursts in our sample (GRB 061222A and GRB 090709A) were undetected with PAIRITEL’s bluest (but most sensitive)  $J$ -band filter and would have been missed without the observations using the redder filters.

#### 4.4.2 Brightness and Luminosity Distributions

For 10 of the 14 events in our sample, we were able to interpolate the flux<sup>k</sup> to  $t = 3$  minutes after the GRB trigger in the observer frame to obtain the early-time NIR brightness distribution of these events. The interpolation was performed using the light curve fitting code described in Perley (2011). The remaining four events (GRBs 061222A, 080319A, 080320, and 080604) had two or fewer detections per filter, preventing a robust estimate of the flux. Table 4.2 shows the resultant flux estimates for each of the three filters across all applicable bursts, and the distribution is plotted in Figure 4.17. While the distribution appears to be more weighted toward the faint-end than previous studies (e.g., Akerlof & Swan 2007; Cenko et al. 2009a), a more direct comparison would require extrapolation to the same observed time (typically 1000 s) to estimate whether our sample is drawn from the same distribution.

Eight of the ten events in 4.2 had spectroscopic redshifts from either the afterglow or likely host (see Table 4.1), and the remaining two have redshift estimates from photometric fits to the afterglow (GRB 071025:  $z = 4.8 \pm 0.2$  Perley et al. 2010a) and the host galaxy (Perley et al. 2013, GRB 090709A:  $z = 1.8^{+0.46}_{-0.71}$ ), respectively. We can thus estimate the luminosities of all ten events at a common rest-frame time. We re-interpolated the light-curves to a rest-frame time of  $t_z = 3$  minutes using the method above (Table 4.2).

For all but one of these bursts, fits to the SED of the event were available in the literature to give estimates of the dust extinction and intrinsic spectral index of the afterglows (Table 4.1). We used the best-fit dust law<sup>l</sup> to correct for the rest-frame extinction. For the remaining burst, GRB 051109A, we fit for  $\beta$  from our  $JHK_s$  SED at the interpolation time (obtaining  $\beta = 0.70 \pm 0.21$ ) and assumed  $A_V = 0^m$ .

<sup>k</sup>Flux values were corrected for Galactic extinction along the line-of-sight using the recalibration by Schlafly & Finkbeiner (2011) of the Schlegel et al. (1998) Milky Way extinction maps.

<sup>l</sup>The majority of events were well fit with SMC-like dust, but three bursts showed strong evidence for different extinction laws: GRB 080607 (Perley et al. 2011), GRB 071025 (Perley et al. 2010a), and GRB 061126 (Perley et al. 2008c). GRB 061126 showed evidence for a dust law where the degeneracy between  $A_V$  and  $\beta$  was difficult to break. For this event, we assumed the case of  $A_V = 0$  and  $\beta = 0.93$  for our modeling.

<sup>m</sup>We note, however, that the best-fit value of  $\beta$  for this event implies that any present dust extinction is unlikely to be large enough to affect our calculations.

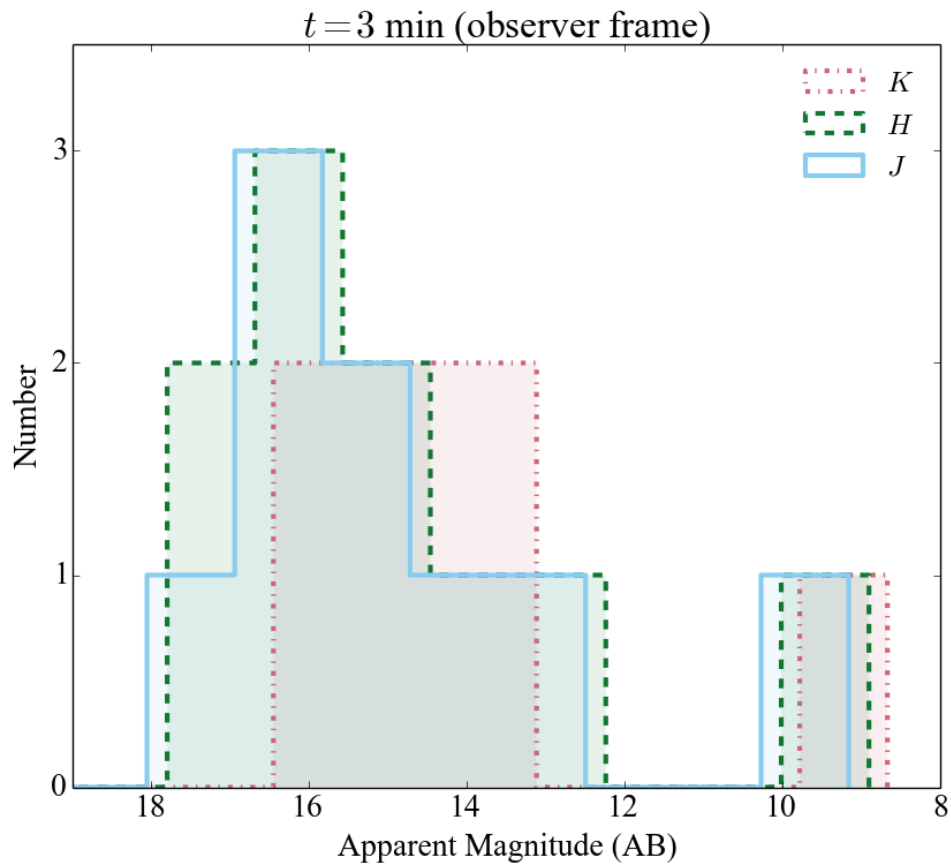


*Figure 4.17:* PAIRITEL Brightness Distribution at  $t = 3$  minutes (observer frame). The bins were set to a fixed width, and the slight offsets between the three histograms were set to roughly account for the average flux difference seen in the different colors.



Table 4.2: Interpolated Flux values for PAIRITEL Catalog

GRB	$z$	$E(B - V)^a$ (mag)	$F_J(t = 3\text{m})$ ( $\mu\text{Jy}$ )	$F_H(t = 3\text{m})$ ( $\mu\text{Jy}$ )	$F_{K_s}(t = 3\text{m})$ ( $\mu\text{Jy}$ )	$F_J(t_z = 3\text{m})$ ( $\mu\text{Jy}$ )	$F_H(t_z = 3\text{m})$ ( $\mu\text{Jy}$ )	$F_{K_s}(t_z = 3\text{m})$ ( $\mu\text{Jy}$ )
051109A	2.346	0.1568	3.2e+03	4.0e+03	4.7e+03	9.9e+02	1.2e+03	1.5e+03
061126	1.1588	0.099	8.1e+03	1.2e+04	1.6e+04	2.3e+03	3.5e+03	4.5e+03
070208	1.165	0.0635	2.3e+02	3.2e+02	...	1.7e+02	2.4e+02	...
071025	$\sim 5.0$	0.0336	7.1e+02	9.6e+02	1.6e+03	1.3e+03	1.8e+03	3.0e+03
080319B	0.9382	0.0223	7.8e+05	9.9e+05	1.2e+06	1.1e+05	1.3e+05	1.6e+05
080319C	1.9492	0.014	1.4e+03	2.1e+03	3.1e+03	9.1e+02	1.4e+03	1.9e+03
080607	3.0363	0.0191	1.9e+03	4.8e+03	1.3e+04	2.9e+02	7.4e+02	2.0e+03
090530	1.266	0.0198	1.1e+03	1.2e+03	...	6.2e+02	7.3e+02	...
090618	0.54	0.0753	2.3e+04	2.3e+04	...	1.1e+04	1.3e+04	...
090709A	$\sim 1.8$	0.0742	...	4.7e+02	1.3e+03	...	1.6e+02	4.9e+02

<sup>a</sup>Average Galactic extinction in the line-of-sight to the GRB from [Schlafly & Finkbeiner \(2011\)](#). Flux values in this table have not been corrected for extinction.

Finally, k-corrections were performed on each of the extinction-corrected fluxes to convert them all to the rest-frame  $V$  band. Using the  $J$ -band as an example, the observed flux at time  $t$  is equal to the same flux at some other frequency in the rest frame at a corrected time  $t/(1+z)$ :

$$f_{obs,J}(t_0) = f_{rest,\nu_{rest}}[t_0/(1+z)],$$

where the corresponding rest frame frequency is  $\nu_{rest} = (1+z)\nu_J$ . This rest frame flux at frequency  $\nu_{rest}$  was converted to a common frequency of the  $V$  band, under the assumption of  $f_\nu \propto \nu^\beta$ :

$$f_{rest,V} = f_{rest,\nu_{rest}} \left[ \frac{\nu_V}{\nu_{rest}} \right]^\beta.$$

However, since  $\nu_{rest} = (1+z)\nu_J$ , the specific flux at rest-frame  $V$ -band is:

$$f_{rest,V} = f_{rest,\nu_{rest}} \left( \frac{\nu_V}{(1+z)\nu_J} \right)^\beta.$$

To evaluate this at a time  $t_0$  in the rest frame,  $f_{rest,\nu_{rest}}(t_0) = f_{obs,J}[t_0(1+z)]$ , so

$$f_{rest,V}(t_0) = f_{obs,J}[t_0(1+z)] \left[ \frac{\nu_V}{(1+z)\nu_J} \right]^\beta.$$

To convert this specific flux to a specific luminosity, we assume standard  $\Lambda$ CDM with  $H_0 = 72$  km/s/Mpc,  $\Omega_M = 0.27$ , and  $\Omega_\Lambda = 0.73$  to obtain the luminosity distance  $D_L$ . The specific luminosity is then

$$L_{rest,V}(t_0) = \frac{4\pi D_L^2}{(1+z)} f_{rest,V}(t_0),$$

which is converted into an absolute  $V$ -band magnitude (AB) using: converted to an absolute magnitude:

$$M_V = -2.5 \log_{10} \left[ \frac{L_{rest,V}(t_0)}{4\pi(10\text{pc})^2} \right] - 48.6.$$

The resultant values are shown in Table 4.3 and plotted in Figure 4.18. Each of the three PAIRITEL filters yields consistent values of rest-frame  $M_V$  for each burst, generally varying less than 0.1 mag between the filters. All events in the resultant luminosity distribution had  $H$ -band detections. We note that the missing  $K_s$ -band values for three bursts is due to reduction problems with these images, rather than intrinsic faintness at this color. The non-detection in  $J$  of GRB 090709A, on the other hand, is indeed due to the extreme redness of that afterglow.

In contrast to the single log-normal luminosity distributions from other single-instrument homogenous samples of GRBs (Melandri et al. 2008; Cenko et al. 2009a; Oates et al. 2009), the PAIRITEL sample appears bimodal and is weighted more towards faint events. This could in part be due to our distribution being calculated at an earlier time in the rest frame than most previous studies. Kann et al. (2011) measured the luminosities for 48 afterglows

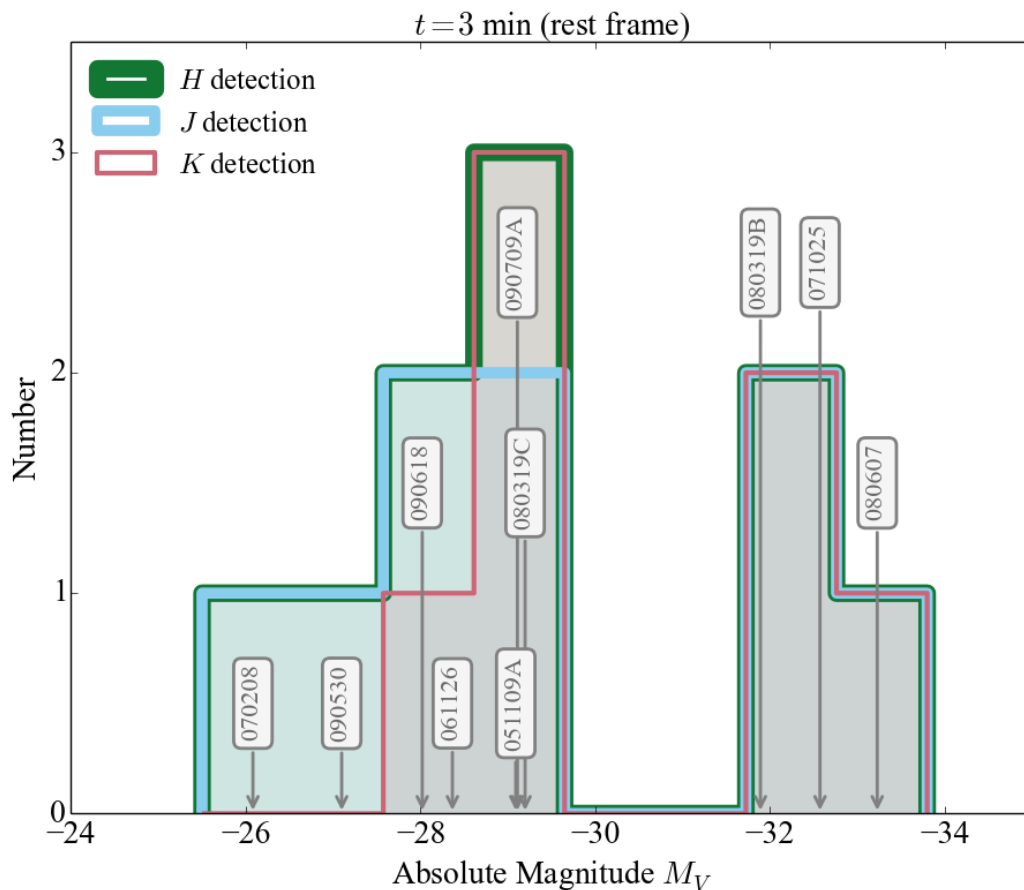


Figure 4.18: PAIRITEL Luminosity Distribution at  $t = 3$  minutes (rest frame)

at 86 s in the rest frame and found a distribution best-fit by three overlapping gaussians, indicating that the early-time luminosities may be dominated by three different classes of early-time behavior.

## Acknowledgments

PAIRITEL was operated by the Smithsonian Astrophysical Observatory (SAO) and was made possible by a grant from the Harvard University Milton Fund, a camera loan from the University of Virginia, and support of the SAO and UC Berkeley. The PAIRITEL project was further supported by NASA/Swift Guest Investigator grants NNG06GH50G and NNX08AN84G.

Table 4.3: Dust-Corrected PAIRITEL Absolute Magnitudes ( $M_V$ ) at  $t = 3$  Minutes (Rest Frame)

GRB	$M_V$ ( $J$ images)	$M_V$ ( $H$ images)	$M_V$ ( $K_s$ images)	$M_V$ (Average)
051109A	-29.12	-29.09	-29.04	-29.08
061126	-28.24	-28.37	-28.38	-28.33
070208	-26.26	-26.08	...	-26.17
071025	-32.50	-32.57	-32.75	-32.61
080319B	-31.86	-31.89	-31.97	-31.91
080319C	-29.39	-29.20	-29.13	-29.24
080607	-33.17	-33.23	-33.28	-33.23
090530	-27.10	-27.10	...	-27.10
090618	-28.12	-28.02	...	-28.07
090709A	...	-29.11	-29.10	-29.11

Table 4.4: Photometry of GRB 051109A

$t_{\text{mid}}$ (s)	Exp (s)	$J$ (mag)	$J$ Err $1\sigma$	$H$ (mag)	$H$ Err $1\sigma$	$K_s$ (mag)	$K_s$ Err $1\sigma$
161.5	46.8	14.24	0.04	13.46	0.03	12.74	0.04
232.0	46.8	14.47	0.04	13.76	0.04	13.05	0.04
304.0	46.8	14.64	0.04	13.88	0.04	13.26	0.05
376.0	46.8	14.98	0.07	14.28	0.08	13.83	0.10
467.0	46.8	15.12	0.06	14.47	0.07	13.87	0.08
595.0	46.8	15.56	0.09	14.59	0.09	14.07	0.10
668.5	46.8	15.82	0.12	15.06	0.12	14.31	0.13
740.5	46.8	15.69	0.11	15.11	0.11	14.56	0.14
813.0	46.8	16.06	0.14	15.05	0.09	14.62	0.15
885.5	46.8	15.87	0.10	15.17	0.10	14.62	0.14
976.0	46.8	15.76	0.09	15.31	0.12	14.53	0.13
1067.0	46.8	15.97	0.11	15.50	0.15	14.82	0.18
1140.0	46.8	16.11	0.13	15.54	0.17	15.17	0.33
1212.5	46.8	16.17	0.16	15.39	0.17	14.84	0.22
1376.0	117.0	16.53	0.14	15.80	0.14	15.27	0.19
1686.5	117.0	16.49	0.12	16.04	0.19	15.39	0.21
1885.5	117.0	16.50	0.14	15.60	0.12	15.01	0.17
2230.5	280.8	16.89	0.11	16.13	0.10	15.52	0.14
2758.0	280.8	17.08	0.15	16.48	0.18	15.94	0.21
3356.5	280.8	17.05	0.15	16.28	0.16	15.73	0.22
3826.5	46.8	> 17.20	...	> 16.44	...	> 15.59	...

Note. — Photometric observations of GRB 051109A. Time is presented as the time since GRB trigger. Values in this table have not been corrected for the expected Galactic extinction of  $E(B - V) = 0.155$ . All magnitudes are given in the Vega system, calibrated to 2MASS.

Table 4.5: Photometry of GRB 061126

$t_{\text{mid}}$ (s)	Exp (s)	$J$ (mag)	$J$ Err $1\sigma$	$H$ (mag)	$H$ Err $1\sigma$	$K_s$ (mag)	$K_s$ Err $1\sigma$
124.5	46.8	12.61	0.03	11.66	0.03	10.86	0.04
198.0	46.8	13.44	0.03	12.51	0.03	11.62	0.04
270.5	46.8	13.87	0.03	12.95	0.03	12.23	0.04
342.5	46.8	14.36	0.04	13.41	0.04	12.67	0.05
415.0	46.8	14.80	0.04	13.80	0.04	13.05	0.04
488.0	46.8	15.10	0.05	14.08	0.05	13.30	0.05
560.5	46.8	15.32	0.06	14.41	0.06	13.56	0.06
633.0	46.8	15.40	0.06	14.53	0.07	13.70	0.06
705.5	46.8	15.66	0.07	14.73	0.09	13.95	0.07
778.0	46.8	15.58	0.07	14.73	0.10	13.90	0.07
850.5	46.8	15.84	0.08	14.77	0.09	14.27	0.09
922.5	46.8	15.92	0.08	14.86	0.10	14.21	0.08
995.0	46.8	16.11	0.08	15.12	0.11	14.37	0.09
1067.5	46.8	16.04	0.08	15.19	0.10	14.52	0.10
1140.0	46.8	16.20	0.09	15.34	0.12	14.65	0.12
1212.5	46.8	16.22	0.09	15.36	0.11	14.48	0.10
1284.5	46.8	16.29	0.10	15.57	0.13	14.64	0.11
1357.0	46.8	16.24	0.09	15.34	0.10	14.72	0.12
1430.0	46.8	16.42	0.11	15.65	0.14	14.98	0.16
1502.5	46.8	16.72	0.14	15.52	0.14	15.05	0.18
1629.5	117.0	16.82	0.12	15.18	0.08	15.07	0.16
1774.5	70.2	17.14	0.30	15.98	0.33	> 15.23	...

Note. — Photometric observations of GRB 061126. Time is presented as the time since GRB trigger. Values in this table have not been corrected for the expected Galactic extinction of  $E(B - V) = 0.157$ . All magnitudes are given in the Vega system, calibrated to 2MASS.

Table 4.6: Photometry of GRB 061222A

$t_{\text{mid}}$ (s)	Exp (s)	$J$ (mag)	$J$ Err $1\sigma$	$H$ (mag)	$H$ Err $1\sigma$	$K_s$ (mag)	$K_s$ Err $1\sigma$
304.99	234.0	> 18.70	...	> 17.35	...	16.40	0.25
1200.0	936.0	> 19.40	...	> 18.27	...	> 17.60	...

Note. — Photometric observations of GRB 061222A. Time is presented as the time since GRB trigger. Values in this table have not been corrected for the expected Galactic extinction of  $E(B - V) = 0.099$ . All magnitudes are given in the Vega system, calibrated to 2MASS.

*Table 4.7: Photometry of GRB 070208*

$t_{\text{mid}}$ (s)	Exp (s)	$J$ (mag)	$J$ Err $1\sigma$	$H$ (mag)	$H$ Err $1\sigma$
360.0	280.8	17.51	0.24	16.49	0.22
794.5	280.8	17.45	0.23	16.78	0.30
1447.5	561.6	17.88	0.25	17.58	0.43
3526.0	1123.2	18.58	0.33	17.84	0.39
3526.0	1123.2	18.58	0.33	17.84	0.39
4907.0	608.4	18.25	0.25	17.63	0.34
6649.5	1591.2	18.95	0.33	17.65	0.24
13277.0	2316.6	18.77	0.36	> 17.97	...

Note. — Photometric observations of GRB 070208. Time is presented as the time since GRB trigger. Values in this table have not been corrected for the expected Galactic extinction of  $E(B - V) = 0.014$ . All magnitudes are given in the Vega system, calibrated to 2MASS.

Table 4.8: Photometry of GRB 071025

$t_{\text{mid}}$ (s)	Exp (s)	$J$ (mag)	$J$ Err $1\sigma$	$H$ (mag)	$H$ Err $1\sigma$	$K_s$ (mag)	$K_s$ Err $1\sigma$
193.0	46.8	15.86	0.22	15.22	0.26	13.78	0.22
246.5	23.4	15.48	0.18	14.61	0.18	13.30	0.17
282.5	23.4	15.32	0.16	14.31	0.13	13.22	0.15
373.5	46.8	14.81	0.10	13.95	0.10	12.89	0.11
445.5	46.8	14.83	0.10	13.90	0.09	12.79	0.11
518.0	46.8	14.61	0.07	13.86	0.08	12.63	0.08
590.5	46.8	14.76	0.10	13.75	0.09	12.78	0.11
662.5	46.8	14.85	0.10	13.92	0.09	13.08	0.11
735.5	46.8	14.66	0.07	13.87	0.07	12.91	0.09
808.0	46.8	14.70	0.09	13.83	0.09	12.96	0.12
881.0	46.8	14.90	0.11	14.12	0.12	13.04	0.14
953.5	46.8	14.91	0.09	14.23	0.09	13.14	0.11
1025.5	46.8	15.18	0.14	14.23	0.11	13.21	0.13
1098.5	46.8	15.37	0.13	14.50	0.13	13.42	0.14
1170.5	46.8	15.45	0.12	14.44	0.10	13.37	0.11
1243.5	46.8	15.25	0.11	14.41	0.10	13.36	0.12
1316.5	46.8	15.17	0.11	14.31	0.10	13.30	0.13
1389.5	46.8	15.30	0.10	14.42	0.10	13.37	0.12
1462.5	46.8	15.12	0.08	14.37	0.08	13.31	0.10
1534.5	46.8	15.10	0.08	14.29	0.07	13.25	0.10
1607.0	46.8	15.06	0.08	14.31	0.08	13.52	0.12
1679.5	46.8	15.22	0.08	14.43	0.09	13.44	0.11
1751.5	46.8	15.12	0.07	14.40	0.08	13.34	0.09
1824.5	46.8	15.15	0.07	14.46	0.08	13.60	0.11
1896.5	46.8	15.20	0.07	14.52	0.08	13.38	0.09
1969.0	46.8	15.30	0.09	14.55	0.09	13.59	0.12
2041.5	46.8	15.37	0.08	14.66	0.09	13.60	0.11
2114.0	46.8	15.33	0.09	14.53	0.10	13.50	0.12
2187.0	46.8	15.42	0.09	14.56	0.09	13.82	0.14
2259.5	46.8	15.55	0.11	14.69	0.10	13.63	0.13
2332.0	46.8	15.61	0.10	14.79	0.10	13.80	0.13
2404.5	46.8	15.53	0.09	14.76	0.09	13.83	0.12
2476.5	46.8	15.68	0.10	15.01	0.11	13.74	0.11
2549.5	46.8	15.59	0.10	14.87	0.10	13.91	0.14
2622.5	46.8	15.58	0.12	14.92	0.13	14.09	0.16
2695.0	46.8	15.87	0.15	14.94	0.12	14.22	0.19
2767.5	46.8	15.70	0.13	14.98	0.13	13.97	0.16
2894.0	117.0	16.02	0.11	15.16	0.11	14.08	0.13
3020.5	46.8	15.95	0.13	15.22	0.14	14.01	0.16
3148.0	117.0	16.07	0.09	15.35	0.11	14.10	0.11
3329.5	117.0	16.14	0.10	15.54	0.14	14.47	0.16
3511.0	117.0	16.18	0.11	15.20	0.10	14.35	0.15
3710.5	140.4	16.35	0.11	15.55	0.12	14.54	0.16
10499.0	1801.8	17.54	0.13	16.92	0.15	16.27	0.23
14269.5	2620.8	18.50	0.20	17.55	0.18	16.53	0.22

Note. — Photometric observations of GRB 071025. Time is presented as the time since GRB trigger. Values in this table have not been corrected for the expected Galactic extinction of  $E(B - V) = 0.064$ . All magnitudes are given in the Vega system, calibrated to 2MASS.

Table 4.9: Photometry of GRB 080319A

$t_{\text{mid}}$ (s)	Exp (s)	$J$ (mag)	$J$ Err $1\sigma$	$H$ (mag)	$H$ Err $1\sigma$	$K_s$ (mag)	$K_s$ Err $1\sigma$
550.5	514.8	17.86	0.12	16.98	0.14	16.04	0.12
1076.5	163.8	18.18	0.27	17.18	0.28	16.29	0.26

Note. — Photometric observations of GRB 080319A. Time is presented as the time since GRB trigger. Values in this table have not been corrected for the expected Galactic extinction of  $E(B - V) = 0.015$ . All magnitudes are given in the Vega system, calibrated to 2MASS.

Table 4.10: Photometry of GRB 080319C

$t_{\text{mid}}$ (s)	Exp (s)	$J$ (mag)	$J$ Err $1\sigma$	$H$ (mag)	$H$ Err $1\sigma$	$K_s$ (mag)	$K_s$ Err $1\sigma$
83.5	23.4	15.37	0.06	14.34	0.06	13.34	0.06
119.5	23.4	15.70	0.08	14.80	0.09	13.91	0.08
155.5	23.4	16.09	0.10	14.91	0.09	14.28	0.11
192.0	23.4	15.76	0.08	14.78	0.08	13.76	0.08
228.0	23.4	15.46	0.07	14.53	0.07	13.48	0.06
262.5	23.4	15.40	0.06	14.41	0.06	13.53	0.06
298.5	23.4	15.07	0.05	14.29	0.06	13.35	0.06
335.0	23.4	15.32	0.06	14.28	0.06	13.41	0.06
389.0	46.8	15.46	0.05	14.41	0.05	13.59	0.06
461.5	46.8	15.48	0.05	14.54	0.05	13.64	0.05
534.0	46.8	15.59	0.05	14.68	0.06	13.70	0.05
606.5	46.8	15.66	0.05	14.91	0.07	13.87	0.06
678.5	46.8	15.86	0.06	15.03	0.08	14.13	0.07
751.5	46.8	16.15	0.08	15.05	0.07	14.22	0.08
823.5	46.8	16.09	0.07	15.19	0.08	14.35	0.08
896.5	46.8	16.42	0.10	15.47	0.12	14.60	0.10
968.5	46.8	16.46	0.10	15.27	0.09	14.58	0.10
1041.0	46.8	16.42	0.10	15.90	0.15	14.91	0.15
1113.5	46.8	16.52	0.11	15.60	0.12	14.73	0.11
1185.0	46.8	16.67	0.14	15.74	0.14	14.90	0.14
1257.0	46.8	16.55	0.12	15.81	0.13	14.64	0.10
1384.5	117.0	16.77	0.12	15.74	0.08	15.00	0.09
1583.5	140.4	17.29	0.24	16.08	0.11	15.18	0.10

Note. — Photometric observations of GRB 080319C. Time is presented as the time since GRB trigger. Values in this table have not been corrected for the expected Galactic extinction of  $E(B - V) = 0.022$ . All magnitudes are given in the Vega system, calibrated to 2MASS.



*Table 4.11: Photometry of GRB 080320*

$t_{\text{mid}}$ (s)	Exp (s)	$J$ (mag)	$J$ Err $1\sigma$	$H$ (mag)	$H$ Err $1\sigma$	$K$ (mag)	$K$ Err $1\sigma$
1155.5	1310.4	19.10	0.22	18.00	0.24	17.20	0.25
3368.5	1521.0	> 20.00	...	> 18.80	...	> 17.90	...

Note. — Photometric observations of GRB 080320. Time is presented as the time since GRB trigger. Values in this table have not been corrected for the expected Galactic extinction of  $E(B - V) = 0.014$ . All magnitudes are given in the Vega system, calibrated to 2MASS.

*Table 4.12: Photometry of GRB 080604*

$t_{\text{mid}}$ (s)	Exp (s)	$J$ (mag)	$J$ Err $1\sigma$	$H$ (mag)	$H$ Err $1\sigma$	$K_s$ (mag)	$K_s$ Err $1\sigma$
2447.5	2925.0	> 20.0	...	> 18.8	...	> 17.9	...

Note. — Photometric observations of GRB 080604. Time is presented as the time since GRB trigger. Values in this table have not been corrected for the expected Galactic extinction of  $E(B - V) = 0.050$ . All magnitudes are given in the Vega system, calibrated to 2MASS.

*Table 4.13: Photometry of GRB 080607*

$t_{\text{mid}}$ (s)	Exp (s)	$J$ (mag)	$J$ Err $1\sigma$	$H$ (mag)	$H$ Err $1\sigma$	$K_s$ (mag)	$K_s$ Err $1\sigma$
143.0	46.8	14.46	0.04	12.79	0.04	11.33	0.06
215.5	46.8	15.14	0.05	13.78	0.04	12.15	0.04
287.5	46.8	15.49	0.06	13.93	0.04	12.32	0.05
360.0	46.8	15.99	0.08	14.25	0.05	12.95	0.06
432.5	46.8	16.21	0.10	14.55	0.06	13.01	0.06
504.5	46.8	16.41	0.12	14.93	0.07	13.46	0.08
631.5	117.0	16.73	0.10	15.23	0.06	13.76	0.06
813.0	117.0	17.12	0.14	15.75	0.09	14.08	0.08
1121.5	280.8	17.28	0.11	15.82	0.07	14.31	0.06
1556.0	280.8	17.45	0.13	16.11	0.09	14.29	0.07
1990.5	280.8	17.75	0.16	15.80	0.07	14.50	0.11
2424.5	280.8	17.59	0.15	15.98	0.09	> 13.63	...
3185.0	702.0	17.82	0.13	16.19	0.07	> 13.85	...
4253.5	678.6	> 18.72	...	17.00	0.20	> 15.27	...

Note. — Photometric observations of GRB 080607. Time is presented as the time since GRB trigger. Values in this table have not been corrected for the expected Galactic extinction of  $E(B - V) = 0.019$ . All magnitudes are given in the Vega system, calibrated to 2MASS.

*Table 4.14:* Photometry of GRB 090530

$t_{\text{mid}}$ (s)	Exp (s)	$J$ (mag)	$J$ Err $1\sigma$	$H$ (mag)	$H$ Err $1\sigma$
283.0	234.0	15.78	0.06	15.00	0.06
645.0	234.0	16.41	0.10	15.78	0.11
1007.5	234.0	16.85	0.13	16.43	0.17
1370.0	234.0	17.13	0.16	16.39	0.16
2004.5	585.0	17.68	0.17	17.04	0.18
2911.5	585.0	17.71	0.17	17.53	0.27
3818.5	585.0	18.09	0.23	> 17.77	...

Note. — Photometric observations of GRB 090530. Time is presented as the time since GRB trigger. Values in this table have not been corrected for the expected Galactic extinction of  $E(B - V) = 0.020$ . All magnitudes are given in the Vega system, calibrated to 2MASS.

*Table 4.15:* Photometry of GRB 090618

$t_{\text{mid}}$ (s)	Exp (s)	$J$ (mag)	$J$ Err $1\sigma$	$H$ (mag)	$H$ Err $1\sigma$
191.5	117.0	12.09	0.05	11.72	0.03
372.5	117.0	13.34	0.03	12.69	0.04
553.5	117.0	13.66	0.04	12.95	0.04
734.5	117.0	13.99	0.04	13.43	0.04
915.5	117.0	14.23	0.07	13.74	0.09
1097.5	117.0	14.44	0.09	13.91	0.11
1460.5	117.0	14.69	0.06	14.03	0.07
1642.5	117.0	14.79	0.06	14.10	0.06
1823.5	117.0	14.65	0.04	14.03	0.05

Note. — Photometric observations of GRB 090618. Time is presented as the time since GRB trigger. Values in this table have not been corrected for the expected Galactic extinction of  $E(B - V) = 0.075$ . All magnitudes are given in the Vega system, calibrated to 2MASS.

*Table 4.16:* Photometry of GRB 090709A

$t_{\text{mid}}$ (s)	Exp (s)	$J$ (mag)	$J$ Err $1\sigma$	$H$ (mag)	$H$ Err $1\sigma$	$K_s$ (mag)	$K_s$ Err $1\sigma$
120.0	23.4	> 16.57	...	15.48	0.28	13.97	0.26
156.0	23.4	> 16.75	...	15.68	0.33	14.08	0.28
198.0	23.4	> 16.74	...	> 15.94	...	13.81	0.22
382.0	210.6	> 17.94	...	16.79	0.32	15.10	0.25
2856.5	2901.6	> 19.33	...	> 18.45	...	> 17.01	...
8732.0	4446.0	> 19.45	...	> 18.73	...	> 17.21	...

Note. — Photometric observations of GRB 090709A. Time is presented as the time since GRB trigger. Values in this table have not been corrected for the expected Galactic extinction of  $E(B - V) = 0.074$ . All magnitudes are given in the Vega system, calibrated to 2MASS.

# Bibliography

- Ackermann, M., Ajello, M., Asano, K., et al. 2014, [Science](#), **343**, 42
- Aihara, H., Allende Prieto, C., An, D., et al. 2011, [ApJS](#), **193**, 29
- Akerlof, C. W., & Swan, H. F. 2007, [ApJ](#), **671**, 1868
- Amati, L., Frontera, F., Tavani, M., et al. 2002, [A&A](#), **390**, 81
- Antonelli, L. A., Maund, J. R., Palazzi, E., et al. 2010, GCN Circular, 10620
- Bailey, S., Aragon, C., Romano, R., et al. 2007, *The Astrophysical Journal*, 665, 1246
- Band, D. L., Norris, J. P., & Bonnell, J. T. 2004, [ApJ](#), **613**, 484
- Barkana, R., & Loeb, A. 2004, [ApJ](#), **601**, 64
- Barthelmy, S. D., Barbier, L. M., Cummings, J. R., et al. 2005, [Space Sci. Rev.](#), **120**, 143
- Berger, E. 2006, GCN Circular, 5962
- Berger, E., Cenko, S. B., Steidel, C., Reddy, N., & Fox, D. B. 2005, GCN Circular, 3368
- Berger, E., Foley, R., Simcoe, R., & Irwin, J. 2008a, GCN Circular, 8434
- Berger, E., Fox, D. B., & Cucchiara, A. 2007, GCN Circular, 6470
- Berger, E., Fox, D. B., Cucchiara, A., & Cenko, S. B. 2008b, GCN Circular, 8335
- Berger, E., & Gladders, M. 2006, GCN Circular, 5170
- Berger, E., Kulkarni, S. R., Rau, A., & Fox, D. B. 2006, GCN Circular, 4815
- Berger, E., & Mulchaey, J. 2005, GCN Circular, 3122
- Berger, E., & Rauch, M. 2008, GCN Circular, 8542
- Berger, E., & Shin, M.-S. 2006, GCN Circular, 5283
- Bertin, E., & Arnouts, S. 1996, *A&AS*, 117, 393
- Bertin, E., Mellier, Y., Radovich, M., et al. 2002, in *Astronomical Society of the Pacific Conference Series*, Vol. 281, *Astronomical Data Analysis Software and Systems XI*, ed. D. A. Bohlender, D. Durand, & T. H. Handley, 228
- Beuermann, K., Hessman, F. V., Reinsch, K., et al. 1999, *A&A*, 352, L26
- Blake, C. H., Bloom, J. S., Latham, D. W., et al. 2008, [PASP](#), **120**, 860
- Bloom, J. S., Kulkarni, S. R., & Djorgovski, S. G. 2002, [AJ](#), **123**, 1111
- Bloom, J. S., Perley, D. A., & Chen, H. W. 2006a, GCN Circular, 5826
- Bloom, J. S., & Richards, J. W. 2012, *Data Mining and Machine Learning in Time-Domain Discovery and Classification*, ed. M. J. Way, J. D. Scargle, K. M. Ali, & A. N. Srivastava, 89
- Bloom, J. S., Starr, D. L., Blake, C. H., Skrutskie, M. F., & Falco, E. E. 2006b, in *Astronomical Society of the Pacific Conference Series*, Vol. 351, *Astronomical Data Analysis*

- Software and Systems XV, ed. C. Gabriel, C. Arviset, D. Ponz, & S. Enrique, 751
- Bloom, J. S., Perley, D. A., Li, W., et al. 2009, [ApJ](#), **691**, 723
- Bloom, J. S., Giannios, D., Metzger, B. D., et al. 2011, [Science](#), **333**, 203
- Bouwens, R. J., Illingworth, G. D., Oesch, P. A., et al. 2010, [ApJ](#), **709**, L133
- Bouwens, R. J., Illingworth, G. D., Labbe, I., et al. 2011, [Nature](#), **469**, 504
- Breiman, L. 1984, *Classification and Regression Trees* (Chapman & Hall/CRC)
- . 2001, *Machine Learning*, **45**, 5
- Burrows, D. N., Hill, J. E., Nousek, J. A., et al. 2005, [Space Sci. Rev.](#), **120**, 165
- Burrows, D. N., Kennea, J. A., Abbey, A. F., et al. 2007, in [Society of Photo-Optical Instrumentation Engineers \(SPIE\) Conference Series](#), Vol. 6686
- Butler, N., Klein, C., Fox, O., et al. 2012, in [Society of Photo-Optical Instrumentation Engineers \(SPIE\) Conference Series](#), Vol. 8446
- Butler, N. R., Bloom, J. S., & Poznanski, D. 2010, [ApJ](#), **711**, 495
- Butler, N. R., & Kocevski, D. 2007, [ApJ](#), **663**, 407
- Butler, N. R., Kocevski, D., & Bloom, J. S. 2009, [ApJ](#), **694**, 76
- Butler, N. R., Kocevski, D., Bloom, J. S., & Curtis, J. L. 2007, [ApJ](#), **671**, 656
- Cabrera Lavers, A., de Ugarte Postigo, A., Castro-Tirado, A. J., et al. 2011, *GCN Circular*, 12234
- Calzetti, D., Armus, L., Bohlin, R. C., et al. 2000, [ApJ](#), **533**, 682
- Campana, S., Tagliaferri, G., Malesani, D., et al. 2007, [A&A](#), **464**, L25
- Cannizzo, J. K., Barthelmy, S. D., Baumgartner, W. H., et al. 2009, *GCN Circular*, 9438
- Cano, Z., Bersier, D., Guidorzi, C., et al. 2011, [MNRAS](#), **413**, 669
- Cardelli, J. A., Clayton, G. C., & Mathis, J. S. 1989, [ApJ](#), **345**, 245
- Carliles, S., et al. 2010, *The Astrophysical Journal*, **712**, 511
- Carroll, R. J., Ruppert, D., Stefanski, L. A., & Crainiceanu, C. 2006, *Measurement Error in Nonlinear Models: A Modern Perspective*, second edition edn. (Chapman & Hall/CRC)
- Cenko, S. B., Berger, E., Djorgovski, S. G., Mahabal, A. A., & Fox, D. B. 2006a, *GCN Circular*, 5155
- Cenko, S. B., Bloom, J. S., Perley, D. A., et al. 2010a, *GCN Circular*, 10389
- Cenko, S. B., & Fox, D. B. 2006a, *GCN Circular*, 5978
- . 2006b, *GRB Coordinates Network*, 5975, 1
- Cenko, S. B., Gezari, S., Small, T., Fox, D. B., & Chornock, R. 2007, *GCN Circular*, 6322
- Cenko, S. B., Hora, J. L., & Bloom, J. S. 2011, *GCN Circular*, 11638
- Cenko, S. B., Kulkarni, S. R., Gal-Yam, A., & Berger, E. 2005, *GCN Circular*, 3542
- Cenko, S. B., Perley, D. A., Junkkarinen, V., et al. 2009a, *GCN Circular*, 9518
- Cenko, S. B., Perley, D. A., Morgan, A. N., et al. 2010b, *GCN Circular*, 10752
- Cenko, S. B., Fox, D. B., Moon, D.-S., et al. 2006b, [PASP](#), **118**, 1396
- Cenko, S. B., Kelemen, J., Harrison, F. A., et al. 2009b, [ApJ](#), **693**, 1484
- Cenko, S. B., Butler, N. R., Ofek, E. O., et al. 2010c, [AJ](#), **140**, 224
- Chawla, N. V., Japkowicz, N., & Kotcz, A. 2004, [SIGKDD Explor. Newsl.](#), **6**, 1
- Chen, C., Liaw, A., & Breiman, L. 2004, [Technical Report](#)
- Chen, H.-W., Helsby, J., Shtetman, S., Thompson, I., & Crane, J. 2009, *GCN Circular*,

10038

- Chen, H.-W., Prochaska, J. X., Bloom, J. S., & Thompson, I. B. 2005, *ApJ*, **634**, L25
- Chester, M. M., & Beardmore, A. P. 2012, GCN Circular, 12880
- Chornock, R., Berger, E., Fox, D., et al. 2010a, GCN Circular, 11164
- Chornock, R., Cenko, S. B., Griffith, C. V., et al. 2009a, GCN Circular, 9151
- Chornock, R., Cucchiara, A., Fox, D., & Berger, E. 2010b, GCN Circular, 10466
- Chornock, R., Perley, D. A., Cenko, S. B., & Bloom, J. S. 2009b, GCN Circular, 9243
- Chornock, R., Perley, D. A., & Cobb, B. E. 2009c, GCN Circular, 10100
- Chornock, R., Berger, E., Levesque, E. M., et al. 2010c, *ApJ*, submitted, [arXiv:1004.2262](https://arxiv.org/abs/1004.2262) [[astro-ph.HE](#)]
- Covino, S., Stefanon, M., Sciuto, G., et al. 2004, in *Ground-based Instrumentation for Astronomy*, ed. A. F. M. Moorwood & M. Iye, Vol. 5492, 1613
- Covino, S., Melandri, A., Salvaterra, R., et al. 2013, *MNRAS*, **432**, 1231
- Cucchiara, A., Bloom, J. S., & Cenko, S. B. 2011a, GCN Circular, 12202
- Cucchiara, A., Fox, D., Levan, A., & Tanvir, N. 2009a, GCN Circular, 10202
- Cucchiara, A., & Fox, D. B. 2008, GCN Circular, 7654
- . 2010, GCN Circular, 10624
- Cucchiara, A., Fox, D. B., & Berger, E. 2006a, GCN Circular, 4729
- Cucchiara, A., Fox, D. B., & Cenko, S. B. 2007a, GCN Circular, 7124
- Cucchiara, A., Fox, D. B., Cenko, S. B., & Berger, E. 2008a, GCN Circular, 8346
- . 2008b, GCN Circular, 8448
- . 2008c, GCN Circular, 8713
- . 2008d, GCN Circular, 8065
- Cucchiara, A., Fox, D. B., Cenko, S. B., & Price, P. A. 2007b, GCN Circular, 6083
- Cucchiara, A., Jones, T., Charlton, J. C., et al. 2009b, *ApJ*, **697**, 345
- Cucchiara, A., Marshall, F. E., & Guidorzi, C. 2007c, GCN Circular, 6419
- Cucchiara, A., Price, P. A., Fox, D. B., Cenko, S. B., & Schmidt, B. P. 2006b, GCN Circular, 5052
- Cucchiara, A., Levan, A. J., Fox, D. B., et al. 2011b, *ApJ*, **736**, 7
- D’Avanzo, P., D’Elia, V., & Covino, S. 2008a, GCN Circular, 8350
- D’Avanzo, P., Fiore, F., Piranomonte, S., et al. 2007, GCN Circular, 7152
- D’Avanzo, P., D’Elia, V., Adreuzzi, G., et al. 2008b, GCN Circular, 7997
- D’Avanzo, P., Perri, M., Fugazza, D., et al. 2010, *A&A*, **522**, A20
- de Ugarte Postigo, A., Castro-Tirado, A. J., & Gorosabel, J. 2011a, GCN Circular, 11978
- de Ugarte Postigo, A., Castro-Tirado, A. J., Tello, J. C., Cabrera Lavers, A., & Reverte, D. 2011b, GCN Circular, 11993
- de Ugarte Postigo, A., Gorosabel, J., Fynbo, J. P. U., Wiersema, K., & Tanvir, N. 2009a, GCN Circular, 9771
- de Ugarte Postigo, A., Gorosabel, J., Malesani, D., Fynbo, J. P. U., & Levan, A. J. 2009b, GCN Circular, 9383
- de Ugarte Postigo, A., Jakobsson, P., Malesani, D., et al. 2009c, GCN Circular, 8766
- de Ugarte Postigo, A., Thoene, C. C., Vergani, S. D., Milvang-Jensen, B., & Fynbo, J. 2010,

- GCN Circular, 10445
- de Ugarte Postigo, A., Goldoni, P., Milvang-Jensen, B., et al. 2011c, GCN Circular, 11579
- de Ugarte Postigo, A., Fynbo, J. P. U., Jakobsson, P., et al. 2011d, GCN Circular, 12258
- D’Elia, V., Covino, S., & D’Avanzo, P. 2008a, GCN Circular, 8438
- D’Elia, V., Thoene, C. C., de Ugarte Postigo, A., et al. 2008b, GCN Circular, 8531
- D’Elia, V., Piranomonte, S., Fiore, F., et al. 2005, GCN Circular, 4044
- D’Elia, V., Piranomonte, S., Covino, S., et al. 2006, GCN Circular, 5637
- D’Elia, V., Fiore, F., Meurs, E. J. A., et al. 2007, *A&A*, **467**, 629
- Della Valle, M., Chincarini, G., Panagia, N., et al. 2006, *Nature*, **444**, 1050
- Draine, B. T., & Hao, L. 2002, *ApJ*, **569**, 780
- Dubath, P., Rimoldini, L., Süveges, M., et al. 2011, *MNRAS*, **414**, 2602
- Efron, B. 1982, The jackknife, the bootstrap, and other resampling plans. (Society of Industrial and Applied Mathematics CBMS-NSF Monographs.)
- Elíasdóttir, Á., Fynbo, J. P. U., Hjorth, J., et al. 2009, *ApJ*, **697**, 1725
- Fatkhullin, T., Gorosabel, J., de Ugarte Postigo, A., et al. 2009, GCN Circular, 9712
- Filippenko, A. V., Li, W. D., Treffers, R. R., & Modjaz, M. 2001, in *Astronomical Society of the Pacific Conference Series*, Vol. 246, IAU Colloq. 183: Small Telescope Astronomy on Global Scales, ed. B. Paczynski, W.-P. Chen, & C. Lemme, 121
- Firmani, C., Ghisellini, G., Avila-Reese, V., & Ghirlanda, G. 2006, *MNRAS*, **370**, 185
- Fitzpatrick, E. L. 1999, *PASP*, **111**, 63
- Flores, H., Fynbo, J. P. U., de Ugarte Postigo, A., et al. 2010, GCN Circular, 11317
- Foley, R. J., Chen, H.-W., Bloom, J., & Prochaska, J. X. 2005, GCN Circular, 3483
- Friedman, A. S., & Bloom, J. S. 2005, *ApJ*, **627**, 1
- Fruchter, A., Krolik, J. H., & Rhoads, J. E. 2001, *ApJ*, **563**, 597
- Fugazza, D., Fiore, F., Patat, N., et al. 2005, GCN Circular, 3948
- Fugazza, D., D’Avanzo, P., Malesani, D., et al. 2006, GCN Circular, 5513
- Fynbo, J., Quirion, P.-O., Malesani, D., et al. 2008a, GCN Circular, 7797
- Fynbo, J. P. U., Hjorth, J., Jensen, B. L., et al. 2005a, GCN Circular, 3136
- Fynbo, J. P. U., Malesani, D., Hjorth, J., Sollerman, J., & Thoene, C. C. 2008b, GCN Circular, 8254
- Fynbo, J. P. U., Malesani, D., Jakobsson, P., & D’Elia, V. 2009a, GCN Circular, 9947
- Fynbo, J. P. U., Malesani, D., & Milvang-Jensen, B. 2008c, GCN Circular, 7949
- Fynbo, J. P. U., Malesani, D., Thoene, C. C., et al. 2006a, GCN Circular, 5809
- Fynbo, J. P. U., Sollerman, J., Jensen, B. L., et al. 2005b, GCN Circular, 3749
- Fynbo, J. P. U., Starling, R. L. C., Ledoux, C., et al. 2006b, *A&A*, **451**, L47
- Fynbo, J. P. U., Jakobsson, P., Prochaska, J. X., et al. 2009b, *ApJS*, **185**, 526
- Galama, T. J., Briggs, M. S., Wijers, R. A. M. J., et al. 1999, *Nature*, **398**, 394
- Gehrels, N., Chincarini, G., Giommi, P., et al. 2004, *ApJ*, **611**, 1005
- Gehrels, N., Barthelmy, S. D., Burrows, D. N., et al. 2008, *ApJ*, **689**, 1161
- Gendre, B., Stratta, G., Atteia, J. L., et al. 2013, *ApJ*, **766**, 30
- Ghirlanda, G., Ghisellini, G., & Lazzati, D. 2004, *ApJ*, **616**, 331
- Goldoni, P., de Ugarte Postigo, A., & Fynbo, J. P. U. 2013, GCN Circular, 15571

- Goldoni, P., Flores, H., Malesani, D., et al. 2010, GCN Circular, 10684
- Golenetskii, S., Aptekar, R., Frederiks, D., et al. 2012, GCN Circular, 12872
- Gomboc, A., Kobayashi, S., Guidorzi, C., et al. 2008, [ApJ](#), **687**, 443
- Gordon, K. D., Clayton, G. C., Misselt, K. A., Landolt, A. U., & Wolff, M. J. 2003, [ApJ](#), **594**, 279
- Graham, J. F., Fruchter, A. S., Levan, A. J., et al. 2007, GCN Circular, 6836
- Granot, J., & Sari, R. 2002, [ApJ](#), **568**, 820
- Grazian, A., Fernandez-Soto, A., Testa, V., et al. 2006, GCN Circular, 4545
- Greiner, J., Bornemann, W., Clemens, C., et al. 2008, [PASP](#), **120**, 405
- Greiner, J., Krühler, T., McBreen, S., et al. 2009a, [ApJ](#), **693**, 1912
- Greiner, J., Krühler, T., Fynbo, J. P. U., et al. 2009b, [ApJ](#), **693**, 1610
- Greiner, J., Krühler, T., Klose, S., et al. 2011, [A&A](#), **526**, A30
- Gruber, D. 2012, GCN Circular, 12874
- Grupe, D., Nousek, J. A., vanden Berk, D. E., et al. 2007, [AJ](#), **133**, 2216
- Grupe, D., Barbier, L. M., Brown, P. J., et al. 2006, GCN Circular, 5954
- Grupe, D., Burrows, D. N., Chester, M. M., et al. 2008, GCN Circular, 7473
- Guidorzi, C., Monfardini, A., Gomboc, A., et al. 2006, [PASP](#), **118**, 288
- Guidorzi, C., Kobayashi, S., Perley, D. A., et al. 2011, [MNRAS](#), **417**, 2124
- Hjorth, J., Malesani, D., Jakobsson, P., et al. 2012, [ApJ](#), **756**, 187
- Hodapp, K. W., Jensen, J. B., Irwin, E. M., et al. 2003, [PASP](#), **115**, 1388
- Hook, I. M., Jørgensen, I., Allington-Smith, J. R., et al. 2004, [PASP](#), **116**, 425
- Hughes, G. 1968, Information Theory, IEEE Transactions on, **14**, 55
- Jakobsson, P., de Ugarte Postigo, A., Gorosabel, J., et al. 2009, GCN Circular, 9797
- Jakobsson, P., Fynbo, J. P. U., Malesani, D., Hjorth, J., & Milvang-Jensen, B. 2008a, GCN Circular, 7757
- Jakobsson, P., Fynbo, J. P. U., Malesani, D., et al. 2007a, GCN Circular, 7117
- Jakobsson, P., Fynbo, J. P. U., Vreeswijk, P. M., & de Ugarte Postigo, A. 2008b, GCN Circular, 8077
- Jakobsson, P., Levan, A., Chapman, R., et al. 2006a, GCN Circular, 5617
- Jakobsson, P., Malesani, D., Thoene, C. C., et al. 2007b, GCN Circular, 6283
- Jakobsson, P., Vreeswijk, P. M., de Ugarte Postigo, A., et al. 2008c, GCN Circular, 8062
- Jakobsson, P., Vreeswijk, P. M., Malesani, D., et al. 2008d, GCN Circular, 7286
- Jakobsson, P., Vreeswijk, P. M., Xu, D., & Thoene, C. C. 2008e, GCN Circular, 7832
- Jakobsson, P., Levan, A., Fynbo, J. P. U., et al. 2006b, [A&A](#), **447**, 897
- Jakobsson, P., Fynbo, J. P. U., Ledoux, C., et al. 2006c, [A&A](#), **460**, L13
- Jakobsson, P., Fynbo, J. P. U., Andersen, M. I., et al. 2007c, GCN Circular, 6398
- Jakobsson, P., Malesani, D., Vreeswijk, P. M., et al. 2008f, GCN Circular, 7998
- Jang, M., Im, M., Lee, I., et al. 2011, [ApJ](#), **741**, L20
- Jaunsen, A. O., Fynbo, J. P. U., Andersen, M. I., & Vreeswijk, P. 2007a, GCN Circular, 6216
- Jaunsen, A. O., Malesani, D., Fynbo, J. P. U., Sollerman, J., & Vreeswijk, P. M. 2007b, GCN Circular, 6010



- Jaunsen, A. O., Rol, E., Watson, D. J., et al. 2008, *ApJ*, **681**, 453
- Jester, S., Schneider, D. P., Richards, G. T., et al. 2005, *AJ*, **130**, 873
- Kalberla, P. M. W., Burton, W. B., Hartmann, D., et al. 2005, *A&A*, **440**, 775
- Kann, D. A., Klose, S., & Zeh, A. 2006, *ApJ*, **641**, 993
- Kann, D. A., Klose, S., Zhang, B., et al. 2010, *ApJ*, **720**, 1513
- . 2011, *ApJ*, **734**, 96
- Kawai, N. 2008, in *Astronomical Society of the Pacific Conference Series*, Vol. 399, *Panoramic Views of Galaxy Formation and Evolution*, ed. T. Kodama, T. Yamada, & K. Aoki, 37
- Kawai, N., Yamada, T., Kosugi, G., Hattori, T., & Aoki, K. 2005, *GCN Circular*, 3937
- Kelson, D., & Berger, E. 2005, *GCN Circular*, 3101
- Kennicutt, Jr., R. C. 1998, *ARA&A*, **36**, 189
- Kewley, L. J., & Dopita, M. A. 2002, *ApJS*, **142**, 35
- Kewley, L. J., Geller, M. J., & Jansen, R. A. 2004, *AJ*, **127**, 2002
- Klein, C. R., & Bloom, J. S. 2014, *MNRAS*, submitted, [arXiv:1404.4870](https://arxiv.org/abs/1404.4870) [[astro-ph.SR](#)]
- Kocevski, D., & Petrosian, V. 2013, *ApJ*, **765**, 116
- Koen, C. 2009, *MNRAS*, **396**, 1499
- . 2010, *MNRAS*, **401**, 1369
- Kohavi, R. 1995, in *International Joint Conferences on Artificial Intelligence*, Vol. 14, 1137
- Krühler, T., Küpcü Yoldaş, A., Greiner, J., et al. 2008, *ApJ*, **685**, 376
- Krühler, T., Schady, P., Greiner, J., et al. 2011a, *A&A*, **526**, A153
- Krühler, T., Greiner, J., Schady, P., et al. 2011b, *A&A*, **534**, A108
- Kuin, N. P. M., Landsman, W., Page, M. J., et al. 2009, *MNRAS*, **395**, L21
- Kulkarni, S. R., Frail, D. A., Sari, R., et al. 1999, *ApJ*, **522**, L97
- La Parola, V., Evans, P. A., Gehrels, N., et al. 2008, *GCN Circular*, 7800
- Lamb, D. Q., & Reichart, D. E. 2000, *ApJ*, **536**, 1
- Landolt, A. U. 1992, *AJ*, **104**, 340
- Lang, D., Hogg, D. W., Mierle, K., Blanton, M., & Roweis, S. 2010, *AJ*, **139**, 1782
- Le Floch, E., Duc, P.-A., Mirabel, I. F., et al. 2003, *A&A*, **400**, 499
- Ledoux, C., Jakobsson, P., Jaunsen, A. O., et al. 2007, *GCN Circular*, 7023
- Ledoux, C., Vreeswijk, P., Smette, A., Jaunsen, A., & Kaufer, A. 2006, *GCN Circular*, 5237
- Ledoux, C., Vreeswijk, P., Ellison, S., et al. 2005, *GCN Circular*, 3860
- Levan, A. J., Fynbo, J. P. U., Hjorth, J., et al. 2009a, *GCN Circular*, 9958
- Levan, A. J., Wiersema, K., & Tanvir, N. R. 2011a, *GCN Circular*, 12429
- Levan, A. J., Jakobsson, P., De Cia, A., et al. 2009b, *GCN Circular*, 9409
- Levan, A. J., Tanvir, N. R., Cenko, S. B., et al. 2011b, *Science*, **333**, 199
- Levesque, E. M., Bloom, J. S., Butler, N. R., et al. 2010, *MNRAS*, **401**, 963
- Li, W., Filippenko, A. V., Chornock, R., & Jha, S. 2003a, *ApJ*, **586**, L9
- . 2003b, *PASP*, **115**, 844
- Liang, E.-W., Racusin, J. L., Zhang, B., Zhang, B.-B., & Burrows, D. N. 2008, *ApJ*, **675**, 528
- LSST Science Collaboration, Abell, P. A., Allison, J., et al. 2009, *LSST Science Book*, [arXiv:0912.0201](https://arxiv.org/abs/0912.0201) [[astro-ph.IM](#)]



- Maiolino, R., Schneider, R., Oliva, E., et al. 2004, *Nature*, **431**, 533
- Malesani, D., Fynbo, J. P. U., Christensen, L., et al. 2009a, GCN Circular, 9761
- Malesani, D., Fynbo, J. P. U., D’Elia, V., et al. 2009b, GCN Circular, 9457
- Malesani, D., Fynbo, J. P. U., Jakobsson, P., Vreeswijk, P. M., & Niemi, S.-M. 2008, GCN Circular, 7544
- Malesani, D., Jakobsson, P., Fynbo, J. P. U., Hjorth, J., & Vreeswijk, P. M. 2007, GCN Circular, 6651
- Malesani, D., Fugazza, D., D’Avanzo, P., et al. 2011, GCN Circular, 11977
- Mangano, V., Cummings, J. R., Cusumano, G., et al. 2008, GCN Circular, 7847
- McQuinn, M., Lidz, A., Zaldarriaga, M., Hernquist, L., & Dutta, S. 2008, *MNRAS*, **388**, 1101
- Melandri, A., Grazian, A., Guidorzi, C., et al. 2006, GCN Circular, 4539
- Melandri, A., Mundell, C. G., Kobayashi, S., et al. 2008, *ApJ*, **686**, 1209
- Melandri, A., Kobayashi, S., Mundell, C. G., et al. 2010, *ApJ*, **723**, 1331
- Melandri, A., Sbarufatti, B., D’Avanzo, P., et al. 2012, *MNRAS*, **421**, 1265
- Mészáros, P. 2006, *Reports on Progress in Physics*, **69**, 2259
- Milne, P. A., & Cenko, S. B. 2011, GCN Circular, 11708
- Milvang-Jensen, B., Goldoni, P., Tanvir, N. R., et al. 2010, GCN Circular, 10876
- Mirabal, N., & Halpern, J. P. 2006, GCN Circular, 4792
- Mirabal, N., Halpern, J. P., & O’Brien, P. T. 2007, *ApJ*, **661**, L127
- Miralda-Escude, J. 1998, *ApJ*, **501**, 15
- Misselt, K. A., Clayton, G. C., & Gordon, K. D. 1999, *ApJ*, **515**, 128
- Morgan, A. N., Vanden Berk, D. E., Roming, P. W. A., et al. 2008, *ApJ*, **683**, 913
- Morgan, A. N., Perley, D. A., Cenko, S. B., et al. 2014, *MNRAS*, **440**, 1810
- Morris, D. C., Beardmore, A. P., Evans, P. A., et al. 2009, GCN Circular, 9625
- Mortlock, D. J., Warren, S. J., Venemans, B. P., et al. 2011, *Nature*, **474**, 616
- Murakami, T., Yonetoku, D., Izawa, H., & Ioka, K. 2003, *PASJ*, **55**, L65
- Oates, S. R., Page, M. J., Schady, P., et al. 2009, *MNRAS*, **395**, 490
- O’Brien, P. T., Willingale, R., Osborne, J., et al. 2006, *ApJ*, **647**, 1213
- Oke, J. B., Cohen, J. G., Carr, M., et al. 1995, *PASP*, **107**, 375
- O’Keefe, P., Gowanlock, M., McConnell, S., & Patton, D. 2009, in *Astronomical Society of the Pacific Conference Series*, Vol. 411, 318
- O’Meara, J., Chen, H.-W., & Prochaska, J. X. 2010, GCN Circular, 11089
- Osip, D., Chen, H.-W., & Prochaska, J. X. 2006, GCN Circular, 5715
- Pagani, C., Baumgartner, W. H., Burrows, D. N., et al. 2007, GCN Circular, 6986
- Pagani, C., Evans, P. A., Gehrels, N., et al. 2008a, GCN Circular, 7426
- Pagani, C., Barthelmy, S. D., Baumgartner, W. H., et al. 2008b, GCN Circular, 7442
- Panaitescu, A., & Vestrand, W. T. 2008, *MNRAS*, **387**, 497
- Pei, Y. C. 1992, *ApJ*, **395**, 130
- Perley, D. A. 2011, PhD thesis, University of California, Berkeley
- . 2014, Private comm.
- Perley, D. A., Chornock, R., & Bloom, J. S. 2008a, GCN Circular, 7962

- Perley, D. A., Foley, R. J., Bloom, J. S., & Butler, N. R. 2006, GCN Circular, 5387
- Perley, D. A., Prochaska, J. X., Kalas, P., et al. 2009a, GCN Circular, 10272
- Perley, D. A., Li, W., Chornock, R., et al. 2008b, *ApJ*, 688, 470
- Perley, D. A., Bloom, J. S., Butler, N. R., et al. 2008c, *ApJ*, 672, 449
- Perley, D. A., Cenko, S. B., Bloom, J. S., et al. 2009b, *AJ*, 138, 1690
- Perley, D. A., Bloom, J. S., Klein, C. R., et al. 2010a, *MNRAS*, 406, 2473
- . 2010b, *MNRAS*, 406, 2473
- Perley, D. A., Morgan, A. N., Updike, A., et al. 2011, *AJ*, 141, 36
- Perley, D. A., Levan, A. J., Tanvir, N. R., et al. 2013, *ApJ*, 778, 128
- Perley, D. A., Cenko, S. B., Corsi, A., et al. 2014, *ApJ*, 781, 37
- Perna, R., Lazzati, D., & Fiore, F. 2003, *ApJ*, 585, 775
- Perna, R., & Loeb, A. 1998, *ApJ*, 501, 467
- Piran, T. 2005, *Rev. Mod. Phys.*, 76, 1143
- Piranomonte, S., Covino, S., Malesani, D., et al. 2006a, GCN Circular, 5626
- Piranomonte, S., Vergani, S. D., Malesani, D., et al. 2011, GCN Circular, 12164
- Piranomonte, S., D’Elia, V., Fiore, F., et al. 2006b, GCN Circular, 4520
- Price, P. A. 2006, GCN Circular, 5104
- Price, P. A., Berger, E., & Fox, D. B. 2006a, GCN Circular, 5275
- Price, P. A., Cowie, L. L., Minezaki, T., et al. 2006b, *ApJ*, 645, 851
- Prochaska, J. X., Foley, R., Tran, H., Bloom, J. S., & Chen, H.-W. 2006, GCN Circular, 4593
- Prochaska, J. X., Foley, R. J., Holden, B., et al. 2008a, GCN Circular, 7397
- Prochaska, J. X., Perley, D., Howard, A., et al. 2008b, GCN Circular, 8083
- Prochaska, J. X., Thoene, C. C., Malesani, D., Fynbo, J. P. U., & Vreeswijk, P. M. 2007, GCN Circular, 6698
- Prochaska, J. X., Sheffer, Y., Perley, D. A., et al. 2009, *ApJ*, 691, L27
- Prochter, G. E., Prochaska, J. X., & Burles, S. M. 2006, *ApJ*, 639, 766
- Quimby, R., Fox, D., Hoefflich, P., Roman, B., & Wheeler, J. C. 2005, GCN Circular, 4221
- Racusin, J. L., Gehrels, N., Holland, S. T., et al. 2008a, GCN Circular, 7427
- Racusin, J. L., Karpov, S. V., Sokolowski, M., et al. 2008b, *Nature*, 455, 183
- Rau, A., Fynbo, J., & Greiner, J. 2010, GCN Circular, 10350
- Reichart, D. E. 2001, *ApJ*, 553, 235
- Richards, J. W., Homrighausen, D., Freeman, P. E., Schafer, C. M., & Poznanski, D. 2012, *MNRAS*, 419, 1121
- Richards, J. W., Starr, D. L., Butler, N. R., et al. 2011, *ApJ*, 733, 10
- Roming, P. W. A., Kennedy, T. E., Mason, K. O., et al. 2005, *Space Sci. Rev.*, 120, 95
- Roming, P. W. A., Schady, P., Fox, D. B., et al. 2006, *ApJ*, 652, 1416
- Roming, P. W. A., Koch, T. S., Oates, S. R., et al. 2009, *ApJ*, 690, 163
- Rossi, A., Kloke, S., Ferrero, P., et al. 2012, *A&A*, 545, A77
- Ruiz-Velasco, A. E., Swan, H., Troja, E., et al. 2007, *ApJ*, 669, 1
- Ruppert, D., Wand, M., & Carroll, R. 2003, *Semiparametric Regression*, Cambridge Series on Statistical and Probabilistic Mathematics (Cambridge University Press)

- Rykoff, E. S., Smith, D. A., Price, P. A., et al. 2004, [ApJ](#), **601**, 1013
- Rykoff, E. S., Aharonian, F., Akerlof, C. W., et al. 2009, [ApJ](#), **702**, 489
- Salvaterra, R., Campana, S., Chincarini, G., Tagliaferri, G., & Covino, S. 2007, [MNRAS](#), **380**, L45
- Salvaterra, R., Della Valle, M., Campana, S., et al. 2009, [Nature](#), **461**, 1258
- Sari, R., Piran, T., & Narayan, R. 1998, [ApJ](#), **497**, L17
- Sato, G., Barthelmy, S. D., Campana, S., et al. 2007, GCN Circular, 6074
- Savaglio, S., Palazzi, E., Ferrero, P., & Kloze, S. 2007, GCN Circular, 6166
- Sbarufatti, B., Barthelmy, S. D., Mangano, V., et al. 2006, GCN Circular, 5854
- Schady, P., & Moretti, A. 2006, GCN Circular, 5296
- Schady, P., Mason, K. O., Page, M. J., et al. 2007, [MNRAS](#), **377**, 273
- Schady, P., Baumgartner, W. H., Beardmore, A. P., et al. 2009, GCN Circular, 9512
- Schady, P., Page, M. J., Oates, S. R., et al. 2010, [MNRAS](#), **401**, 2773
- Schady, P., Dwelly, T., Page, M. J., et al. 2012, [A&A](#), **537**, A15
- Schaefer, B. E. 2007, [ApJ](#), **660**, 16
- Schlaflly, E. F., & Finkbeiner, D. P. 2011, [ApJ](#), **737**, 103
- Schlegel, D. J., Finkbeiner, D. P., & Davis, M. 1998, [ApJ](#), **500**, 525
- Seaton, M. J. 1979, [MNRAS](#), **187**, 73P
- Shahmoradi, A., & Nemiroff, R. J. 2011, [MNRAS](#), **411**, 1843
- Skrutskie, M. F., Cutri, R. M., Stiening, R., et al. 2006, [AJ](#), **131**, 1163
- Starling, R., Thoene, C. C., Fynbo, J. P. U., Vreeswijk, P., & Hjorth, J. 2006, GCN Circular, 5131
- Starling, R. L. C., Wijers, R. A. M. J., Wiersema, K., et al. 2007, [ApJ](#), **661**, 787
- Stekhoven, D. J., & Bühlmann, P. 2011, [Bioinformatics](#)
- Swenson, C. A., Roming, P. W. A., De Pasquale, M., & Oates, S. R. 2013, [ApJ](#), **774**, 2
- Tagliaferri, G., Barthelmy, S., Burrows, D., et al. 2005, GCN Circular, 4213
- Tanvir, N. R., & Jakobsson, P. 2007, [Royal Society of London Philosophical Transactions Series A](#), **365**, 1377
- Tanvir, N. R., Wiersema, K., Fynbo, J. P. U., Levan, A. J., & Perley, D. 2010a, GCN Circular, 11116
- Tanvir, N. R., Wiersema, K., & Levan, A. J. 2010b, GCN Circular, 11230
- Tanvir, N. R., Wiersema, K., Levan, A. J., Cenko, S. B., & Geballe, T. 2011, GCN Circular, 12225
- Tanvir, N. R., Fox, D. B., Levan, A. J., et al. 2009, [Nature](#), **461**, 1254
- Tanvir, N. R., Vergani, S., Hjorth, J., et al. 2010c, GCN Circular, 11123
- Thoene, C. C., de Ugarte Postigo, A., Vreeswijk, P. M., Malesani, D., & Jakobsson, P. 2008a, GCN Circular, 8058
- Thoene, C. C., Fynbo, J. P. U., Jakobsson, P., Vreeswijk, P. M., & Hjorth, J. 2006a, GCN Circular, 5812
- Thoene, C. C., Jakobsson, P., Fynbo, J. P. U., et al. 2007a, GCN Circular, 6499
- Thoene, C. C., Jaunsen, A. O., Fynbo, J. P. U., Jakobsson, P., & Vreeswijk, P. M. 2007b, GCN Circular, 6379

- Thoene, C. C., Malesani, D., Vreeswijk, P. M., et al. 2008b, *GCN Circular*, 7602
- Thoene, C. C., Perley, D. A., Cooke, J., et al. 2007c, *GCN Circular*, 6741
- Thoene, C. C., Levan, A., Jakobsson, P., et al. 2006b, *GCN Circular*, 5373
- Totani, T., Kawai, N., Kosugi, G., et al. 2006, *PASJ*, 58, 485
- Ukwatta, T. N., Sakamoto, T., Dhuga, K. S., et al. 2009, in *American Institute of Physics Conference Series, Vol. 1133, American Institute of Physics Conference Series*, ed. C. Meehan, C. Kouveliotou, & N. Gehrels, 437
- Ukwatta, T. N., Stamatikos, M., Dhuga, K. S., et al. 2010, *ApJ*, 711, 1073
- Ukwatta, T. N., Dhuga, K. S., Stamatikos, M., et al. 2011, *MNRAS*, 1618
- van Dokkum, P. G. 2001, *PASP*, 113, 1420
- vanden Berk, D. E., Grupe, D., Racusin, J., Roming, P., & Koch, S. 2008, in *American Institute of Physics Conference Series, Vol. 1000, American Institute of Physics Conference Series*, ed. M. Galassi, D. Palmer, & E. Fenimore, 80
- Vergani, S. D., Petitjean, P., Ledoux, C., et al. 2009, *A&A*, 503, 771
- Vergani, S. D., D'Avanzo, P., Malesani, D., et al. 2010, *GCN Circular*, 10495
- Vestrand, W. T., Wren, J. A., Panaitescu, A., et al. 2014, *Science*, 343, 38
- Vreeswijk, P., Jakobsson, P., Ledoux, C., Thoene, C., & Fynbo, J. 2006, *GCN Circular*, 5535
- Vreeswijk, P., Malesani, D., Fynbo, J., et al. 2008a, *GCN Circular*, 8301
- Vreeswijk, P. M., Fynbo, J. P. U., Malesani, D., Hjorth, J., & de Ugarte Postigo, A. 2008b, *GCN Circular*, 8191
- Vreeswijk, P. M., Milvang-Jensen, B., Smette, A., et al. 2008c, *GCN Circular*, 7451
- Vreeswijk, P. M., Thoene, C. C., Malesani, D., et al. 2008d, *GCN Circular*, 7601
- Vreeswijk, P. M., Ledoux, C., Smette, A., et al. 2007, *A&A*, 468, 83
- Vreeswijk, P. M., Smette, A., Malesani, D., et al. 2008e, *GCN Circular*, 7444
- Wasserman, L. 2006, *All of Nonparametric Statistics*, Springer Texts in Statistics (Springer)
- Watson, D., & Jakobsson, P. 2012, *ApJ*, 754, 89
- Waxman, E., & Draine, B. T. 2000, *ApJ*, 537, 796
- Wiersema, K., Graham, J., Tanvir, N., et al. 2008a, *GCN Circular*, 7818
- Wiersema, K., Levan, A., Kamble, A., Tanvir, N., & Malesani, D. 2009, *GCN Circular*, 9673
- Wiersema, K., Tanvir, N., Vreeswijk, P., et al. 2008b, *GCN Circular*, 7517
- Wiersema, K., Flores, H., D'Elia, V., et al. 2011, *GCN Circular*, 12431
- Wijers, R. A. M. J., Bloom, J. S., Bagla, J. S., & Natarajan, P. 1998, *MNRAS*, 294, L13
- Xiao, L., & Schaefer, B. E. 2009, *ApJ*, 707, 387
- . 2011, *ApJ*, 731, 103
- Xu, D., Fynbo, J. P. U., Tanvir, N. R., et al. 2009, *GCN Circular*, 10053
- Yost, S. A., Harrison, F. A., Sari, R., & Frail, D. A. 2003, *ApJ*, 597, 459
- Yost, S. A., Swan, H. F., Rykoff, E. S., et al. 2007, *ApJ*, 657, 925
- Zafar, T., Watson, D., Elíasdóttir, Á., et al. 2012, *ApJ*, 753, 82
- Zauderer, A., & Berger, E. 2012, *GCN Circular*, 12895
- Zhang, Z., Deng, J., Lu, R., & Gao, H. 2006, *Chinese J. Astron. Astrophys.*, 6, 312
- Zheng, W.-K., Deng, J.-S., & Wang, J. 2009, *Research in Astronomy and Astrophysics*, 9, 1103

## Appendix A

# Software and Web Products for GRB Follow-Up and Analysis

The rapid dissemination of information is critical for the study of astronomical transients. For GRBs, even delays as small as seconds matter at the early stages of evolution, making the speed of both data analysis and the distribution thereof of the utmost importance. To this end, we have endeavored to streamline and automate much of the software developed for this dissertation work<sup>a</sup>. Tools developed that were thought to be useful to the broader community were ported into web services for public use. In this appendix, we provide brief descriptions and screenshots of these products. The RATE GRB- $z$  project, outlined in Chapter 2, parses rapidly available metrics for *Swift* GRBs from GCN notices and online tables to calculate a quantitative follow-up decision parameter,  $\hat{Q}$ . The main page for the RATE GRB- $z$  project is shown in Figure A.1 and contains a table of  $\hat{Q}$  values for the newest available GRBs, along with links to methodology explanations and auto-generated GRB summary pages (e.g. Figure A.2). The function `Signal.SwiftGRBFlow()`<sup>b</sup> continuously monitors an RSS feed of *Swift* triggers, and upon identification of a new event, triggers a sequence of events including downloading and parsing data from several websites, creating finding charts and region files based on positional information, generating a summary page (e.g. Figure A.2), and emailing a link to that page to interested parties. A full list of summary pages is available at <http://swift.qmorgan.com>. Finally, we have created an interface for the manual generation of finding charts, shown in Figure A.3 and available at <http://fc.qmorgan.com>. The underlying functionality can easily be accessed with a PHP URL query string for integration with other web products.

<sup>a</sup>The full codebase of software developed in the preparation of this dissertation is open source and available at <https://github.com/qmorgan/qsoft>.

<sup>b</sup><https://github.com/qmorgan/qsoft/blob/master/Software/AutoRedux/Signal.py>



# RATE GRB-z

110531A  
RATE GRB-z  
090423

- About RATE GRB-z
- How it Works
- The Paper
- Contact Us
- Swift GRB Pages
- RSS Feed
- Finding Chart Generator
- A. N. Morgan's Webpage

## Introduction

As the discovery rate of potentially interesting transients dwarfs the available resources with which to perform follow-up observations, it becomes necessary to have tools to inform whether or not to spend resources on each new event.

We have developed the Random forest Automated Triage Estimator for GRB redshifts (RATE GRB-z) to assist in rapidly identifying high-redshift ( $z > 4$ ) candidates using early-time metrics from the three telescopes onboard *Swift*.

**The method reduces this decision of whether or not to follow-up a new GRB to a single parameter:  $Q_{\hat{}}$ . If a user wishes to devote 20% of telescope observing time to chasing high- $z$  GRB candidates, then we recommend follow-up for all events with  $Q_{\hat{}} < 0.2$ .**

See [How it Works](#) for more information on the methodology and expected performance metrics, or read [the paper](#) for the full details. The latest available predictions are shown below, and real-time alerts are available by subscribing to our [RSS Feed](#). We also provide our data products for all past [Swift GRBs](#). We welcome questions/comments/suggestions: please [contact us](#).

## Predictions for Latest GRBs

GRB	Region File	Finding Chart	z	$Q_{\hat{}}$
<a href="#">120404A</a>	<a href="#">Link</a>	<a href="#">Link</a>	2.876	0.637
<a href="#">120403B</a>	<a href="#">Link</a>	<a href="#">Link</a>		0.622
<a href="#">120403A</a>	<a href="#">Link</a>	<a href="#">Link</a>		
<a href="#">120401A</a>	<a href="#">Link</a>	<a href="#">Link</a>		0.496
<a href="#">120328A</a>	<a href="#">Link</a>	<a href="#">Link</a>		0.563
<a href="#">120327A</a>	<a href="#">Link</a>	<a href="#">Link</a>	2.813	0.444
<a href="#">120326A</a>	<a href="#">Link</a>	<a href="#">Link</a>	1.798	0.948
<a href="#">120324A</a>	<a href="#">Link</a>	<a href="#">Link</a>		0.607
<a href="#">120320A</a>	<a href="#">Link</a>	<a href="#">Link</a>		0.0

Figure A.1: Screenshot of the main page of the RATE GRB- $z$  website (<http://rate.grbz.info>). Links to auto-generated GRB summary pages (e.g. Figure A.2), DS9 region files, and finding charts are provided in addition to  $Q_{\hat{}}$  values and redshifts, when available.

# Swift Trigger 519043

**Q**

Swift GRB Pages

RSS Feed

Finding Chart Generator

A. N. Morgan's Webpage

Temporal Information

Burst Time: ('12/04/01 05:24:15.94')

Spatial Information

**BAT:** RA = 58.068, Dec = -17.671, Uncertainty: 180."  
(RA = 03:52:16.32, Dec = -17:40:15.6)

**XRT:** RA = 58.0835, Dec = -17.6349, Uncertainty: 5.4"  
(RA = 03:52:20.04, Dec = -17:38:05.6399999999)

**Extinction:** E\_(B-V) = Unknown

[DS9 Region File](#)

Useful Links

[GRAASP ToO Page](#)

[Caltech React Page](#)

[NVO DataScope Query](#)

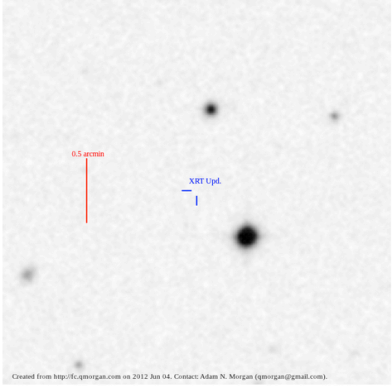
[GCN Notices for this Trigger](#)

Finding Charts

SDSS Finding Chart (May not be available)

DSS Finding Chart:

Swift\_519043-GRB120401A: Finding Chart



XRT Upd. Pos. (J2000)  
RA = 03:52:19.68  
Dec = -17:38:08.88  
Uncertainty = 2.5  
(arcseconds)

Image from:  
DSS2 (red)

Image is 3.0  
arcmin/side

Created from <http://cqmorgan.com> on 2012 Jun 04. Contact Adam N. Morgan ([qmorgan@gmail.com](mailto:qmorgan@gmail.com)).

Figure A.2: Screenshot of a GRB summary page that is automatically generated for each new *Swift* event. Information provided includes trigger time, burst position from each of the three *Swift* telescopes (if available), links to other burst-specific webpages, and an auto-generated finding chart using the best available position. A full list of summary pages is available at <http://swift.qmorgan.com>

### Q's Finding Chart Generator

Instructions: Fill out the following fields and click "Submit":

Source RA:  (Decimal Degrees or hh:mm:ss, J2000 coordinates)

Source Dec:  (Decimal Degrees or +dd:mm:ss, J2000 coordinates)

Source Uncertainty:  arcseconds (error circle to be drawn around the source location)

Error circle shape:

Include Scale Bar?

Desired Sky Region Size:  (arcminutes/side or AUTO)

Source Name:  (Label at top of finding chart)

Instrument Name:  (Label above the source error circle)

Contact:  (Optional, placed below the Finding Chart)

Survey Name:  (SDSS not available for all locations)

[Contact](#)

### MyObject: Finding Chart

SDSS DR7  
ra: 137.397 dec: 33.119  
scale: 0.4000 arcsec/pix  
image zoom: 1:1

Pos Pos. (J2000)  
RA = 09:09:35.28  
Dec = +33:07:09.12  
Uncertainty = 3.0  
(arcseconds)

Image from:  
SDSS

Image is 4.0  
arcmin/side

Created from <http://fc.qmorgan.com> on 2014 May 04. Contact: Adam N. Morgan ([qmorgan@gmail.com](mailto:qmorgan@gmail.com)).

Contact: Anon User ([email@address.com](mailto:email@address.com))

Figure A.3: Screenshot of finding chart generator page <http://fc.qmorgan.com>. The interface accepts user inputs of position, positional uncertainty, and several cosmetic options to generate a finding chart such as the example above.